Ph.D. Thesis

Université de Limoges

University of Limoges

ED 653 - Sciences et Ingénierie (SI)

XLIM Research Institute

A thesis submitted to University of Limoges
in partial fulfillment of the requirements of the degree of

Doctor of Philosophy

High Frequency Electronics, Photonics and Systems

Presented and defensed by

Manal AIT ASSOU

On January 31, 2024

Synthetic Aperture Imaging and Spectroscopy in the Terahertz Range Using Time Domain Spectroscopy System

Thesis supervisor: Cyril Decroze, Georges Humbert, Aurelian Crunteanu

JURY:

President of jury
Ms. Michèle Lalande, Professor at the University of Limoges

Reporters
Ms. Claire Migliaccio, Professor at Nice university, LEAT-Nice Laboratory
Mr. Patrick Mounaix, DR-CNRS, IMS Bordeaux

Examiners
Mr. Emmanuel Perrin, Ph.D. engineer, CRT CISTEME
Mr. Sebastian Engelbrecht, Ph.D. engineer, Saint-Louis institute
Mr. Georges Humbert, CR-CNRS, XLIM research institute
Mr. Aurelian Crunteanu, DR-CNRS, XLIM research institute
Mr. Cyril Decroze, Professor at the University of Limoges

To my family

“There are always flowers for those who want to see them”
Henri Matisse

Acknowledgements

My PhD journey is coming to an end, and I couldn’t be prouder. This thesis would not have been possible without the guidance and the help of numerous people and entities who, in one way or another, contributed and extended their valuable assistance in the preparation and completion of this study. I would like to express my deepest gratitude to these exceptional individuals who supported and guided me throughout this transformative journey, enabling me to successfully obtain my doctorate. First and foremost, I want to begin by recognizing the University of Limoges for funding my entire PhD, a crucial support that made this achievement possible.

My sincere gratitude goes to my PhD supervisors, Cyril DECROZE, Georges HUMBERT, and Aurelian CRUNTEANU. Their constant support, guidance, and encouragement have been invaluable throughout the entire process. From the initial stages to the final submission of my thesis, their unwavering presence and wealth of wisdom have been instrumental in shaping my academic growth. I am profoundly grateful for the immeasurable contributions they made to my development.

I would also like to express my gratitude to the members of my thesis jury for being part of my PhD defense.

Special thanks are due to Françoise COSSET, Claire DARRAUD, and Catherine DI BIN, professors at the University of Limoges, for granting me the opportunity to teach during my second and third years of study. Teaching under their guidance was an incredibly rewarding experience.

My heartfelt thanks extend to all the members of the "Fiber Photonics," "MINT," and "Antennas and Signals" teams at XLIM for warmly welcoming me, despite our different research focuses. I'm also grateful to everyone I interacted with at the XLIM laboratory during my PhD, for creating a joyful and motivating working atmosphere.

On a personal note, I want to express my deep appreciation to my friends who started as colleagues but became close companions under the shared circumstances. Thank you, Clara ABBOUAB, Ceren YILDIRIM, Ruoxue HE and Nadia TIABI for being such good and supportive friends. I will cherish our shared laughter and tears. It was such a breath of fresh air to have a strong, funny, and ambitious group of friends around to encourage and motivate each other during challenging times. To Khadija BEN LAHCEN, whose enduring friendship and support transcended geographical boundaries, I extend heartfelt gratitude. Our decade-long bond, marked by shared accomplishments and pivotal moments, has been a source of strength and joy.

Words could not express my gratitude to my parents for their trust, patience, and unwavering encouragement. They instilled in me a love for learning, ambition, and the perpetual pursuit of improvement. Thank you for getting me to where I am today. I also thank my siblings, Laila, Maroua, and Acile, and Soulaimane, for their unconditional love and support. This work is dedicated to all of you.

Lastly, my deepest appreciation goes to my husband. His support was pivotal in maintaining my resilience throughout this journey, enabling me to persevere and finally reach the end of this academic tunnel.

Rights

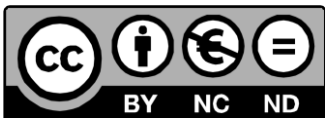

Table of Contents

List of Figures

List of Tables

Introduction

It never sees to amaze me how humans have harnessed electromagnetic (EM) waves to meet their needs. Starting with the use of light emitted from fire around 400 000 BC, this journey has evolved into the utilization of remarkably advanced sources to generate waves beyond our five senses, paving the way for diverse and equally sophisticated applications. From communication to exploring the unknown, EM waves have not only enhanced everyday life but also opened doors for the boldest among us to conquer uncharted territories.

Looking ahead to the present, humans persist in their ongoing quest for discovery. Although we have come a long way since 1888 when the German physicist Heinrich Hertz produced and detected EM waves for the first time, we still have much to learn about the EM spectrum. One particularly challenging portion of this spectrum lies in the range of frequencies between 0.3×10^{12} Hz and 10×10^{12} Hz, also known as the Terahertz (THz) wave band (1 THz = 10^{12} Hz), equivalent to wavelengths between 0.03 mm to 1 mm. Historically, this band has been referred to as the THz gap due to the difficulties associated with generating and detecting waves in this range. Tightly lodged between the microwaves and the far-infrared regions of the EM spectrum, this THz gap has long been considered a high-frequency barrier from the microwave perspective or a low-frequency limit from the light perspective. However, recent research has focused on THz waves as an independent field, recognizing their properties and potential applications. THz waves have properties that are shared with both neighboring bands, such as the ability to penetrate certain materials and produce high-resolution images, as well as the ability to generate molecular vibrations, which forms the basis of spectroscopy and imaging applications.

The emergence of THz time-domain spectroscopy (THz-TDS) system in the 1980s provided an unprecedented access to the previously unattainable frequency band, and it was not surprising that the first THz imaging demonstrations followed soon after. In 1995, researchers from AT&T Bell Laboratories successfully developed the first imaging system based on a THz-TDS system, which produced a transmission image of a packaged electronic chip. The demonstrated system relied on using multiple focusing lenses on the THz beam path and moving an object in the focal point of the THz beam. This imaging configuration remained the same for a long time until the development of flexible THz-TDS systems, with compact laser fiber sources and fiber-pigtailed antennas.

The newfound flexibility offered by the development of flexible THz-TDS systems has led to the exploration of adapting other imaging techniques in THz range, such as Synthetic Aperture (SA) imaging. SA imaging is a well-established technique in the microwave frequency region that is typically used in radar applications and non-destructive sensing and security. Essentially, SA is a radar imaging technique that produces two-dimensional images or three-dimensional reconstructions of target objects. To do this, it processes the data received to improve resolution. SA imaging has revolutionized imaging in the microwave domain, as it enables the scanning of large areas and the reconstruction of high-resolution images.

A first demonstration of SA imaging in the THz frequency range was achieved in 2001, by K. McClatchey, M. T. Reiten, and R. A. Cheville, using a conventional THz-TDS system in reflection configuration, which produced images of a rotating object under test from the reflected waves. This initial attempt at THz imaging using the SA technique eliminated the focusing lenses, typical to a TDS classical imaging set-up, and relied on a divergent beam and numerical post-processing treatment to produce the object's image. Since then, large efforts

have been made to further the development of SA imaging technique using THz-TDS systems, and multiple configurations have been proposed offering optimized performances for different scenarios.

However, instead of moving the antennas to generate the SA, most proposed systems require moving the object under test, which can be unsuitable for many test subjects that need a minimal amount of displacement. Fine historical art and archeological finds is a relevant example of these objects under test. The level of fragility in which the objects are found requires a special set of conditions in order to be analyzed. Moreover, due to variations in size, shape, and characteristics among archaeological finds and artworks, an adaptable imaging setup is required to cater to their diverse requirements.

In addition, there is a noticeable focus of the research efforts on reflection-based imaging configurations, rather than transmission configurations. Reflection configurations have been useful in interrogating high-density or reflective objects. However, the reflected beam from low density and almost transparent objects is not sufficient to generate an image using the reflection configuration. Some proposed systems rely on an additional metallic surface behind low density objects (thin mail packaging inspection, chocolate bar inspection, etc) in order to gather reflected beams that propagated through the object under test. However, this approach adds complexities to the system (calibration for example) and reduces its versatility.

Moreover, the development of SA-based THz imaging systems did not incorporate spectroscopy applications, which is a missed opportunity to fully exploit the potential of THz waves. Existing SA-based imaging systems concentrate on resolving obstacles associated with optimizing the SA, including the field of view and resolution, but have yet to explore the potential of utilizing information extracted from the produced image to deduce the properties of the material being inspected. Medicine tablet inspection is a good example of an application that would benefit greatly from this proposition. In addition to imaging, there has been an interest in accessing the exact characteristics of the different components of the tablet, which is useful for homogeneity of the chemical components and quality inspection.

Finally, the acquisition time to generate an image in THz range is still significant. In fact, the reported necessary acquisition time for previously established imaging approaches and SA approach is equally high, which hinders the development of real-time THz imaging. The acquisition time is a significant point of an imaging system as many industries require fast acquisition to accommodate a large number of samples in a limited time. “Conveyor belt” based inspection systems are a good example of the need for a fast and efficient imaging system. This calls for an adaptable imaging and spectroscopy approach that optimizes acquisition time.

The main objective of this work is to provide a different imaging and spectroscopy approach in THz range through the combination of SA imaging with a TDS system in transmission configuration. This configuration is supposed to allow the interrogation of a stationary object in transmission configuration. Moreover, the proposed approach aims to extract not only object’s structure via imaging but also information on its properties. This work will demonstrate the extraction of material characteristics from the reconstructed data, enabling a comprehensive analysis of the object under test based on a single set of measurements. Finally, to reduce acquisition time, we demonstrate an approach based on sparse sampling the SA.

Finally, THz fibers (or waveguides) are gaining more momentum as research demonstrates their utility in different applications such as communication and material characterization. However, beam profile imaging and modal content characterization of THz fibers are still in

development. Experimental approaches have been proposed on the subject, but multiple challenges are still persistent as they are mainly based on near-field microscopy imaging. Consequently, a more flexible imaging approach adapted to THz fibers is necessary to ensure deeper understanding of the components and facilitating future advancements. In this work, we aim to provide an initial demonstration of the SA-THz for beam profiling and modal characterization of a THz fiber. However, further research and optimization are required to enhance the efficiency of various parameters related to THz propagation, generation, detection, and numerical process. These efforts are necessary to develop a robust system capable of effectively addressing the applications outlined earlier.

This manuscript will be organized as follows, the first chapter lays the ground for the general notions and facts around THz band and the state of the art of the technology developed in this range. We start by listing different application areas of THz imaging and spectroscopy with illustrated examples. Then, a brief listing of THz generation and detection technologies is provided, and subsequently elaborating further on photoconductive antennas which are the components used in our work. After that, we present the TDS system and its different elements and characteristics which will lead us finally to detailing two THz imaging methods, which are raster scanning and SA imaging. The later section will allow the identification of the differences between the imaging methods and highlighting the contributions of our work. Next, we lay the ground for sparse sampling, and how it is expected to reduce the acquisition time of our proposed approach. And finally, we elaborate on the spectroscopy section of the study, providing essential notions on how to extract the materials characteristics in a typical context and how the process of material characterization should be affected by the introduction of SA imaging.

The second chapter will detail the process of application of the SA imaging approach to a TDS system in transmission configuration. We start the chapter by giving a short recall of SA imaging and the algorithm used to reconstruct images. The effectiveness of this imaging method is demonstrated through the examination of three distinct samples, each selected to illustrate different aspects of the approach's capabilities. Following the demonstration of 3D imaging, one of the samples is used to demonstrate the approach's spectroscopic capacities. Using the reconstructed image, we calculate the characteristics of the different materials of a multi-material sample. We conclude on the efficacy of the approach in providing a novel context for THz imaging and spectroscopy, which is different from the classical configuration, without compromising the primary objective of utilizing THz waves. Moreover, within this chapter, we evaluate the performance of sparse spatial sampling for both imaging and spectroscopy, quantifying its impact on minimizing acquisition time. A comprehensive comparison between imaging and spectroscopy results obtained using sparse arrays and full synthetic arrays is conducted. This quantitative assessment serves to conclude on the contributions of sparse arrays to the proposed approach.

And on the final chapter, we demonstrate an interesting application of SA imaging and spectroscopy. The setup is used to characterize a THz anti-resonant hollow core fiber. By following the same previously detailed procedure, we image the beam profile at the output of the fiber at different frequencies of the THz band. Furthermore, we introduce a new approach to modal characterization of THz fibers. Even though this new approach faces some challenges, we demonstrate its potential and provide an elaborate analysis of its future perspectives.

Chapter I. Terahertz radiation for active imaging and spectroscopy

I.1. Terahertz radiation

THz radiation refers to EM waves that fall within the frequency range of 0.3 THz to 10 THz (Figure I-1), corresponding to wavelengths ranging from 30 µm to 1 mm. This specific band resides between the infrared and microwave regions of the EM spectrum. While it was once considered a gap in the spectrum, significant advancements over the past two decades have led to a thorough comprehension of THz waves properties. Consequently, these properties have proven immensely advantageous for diverse applications across multiple domains.

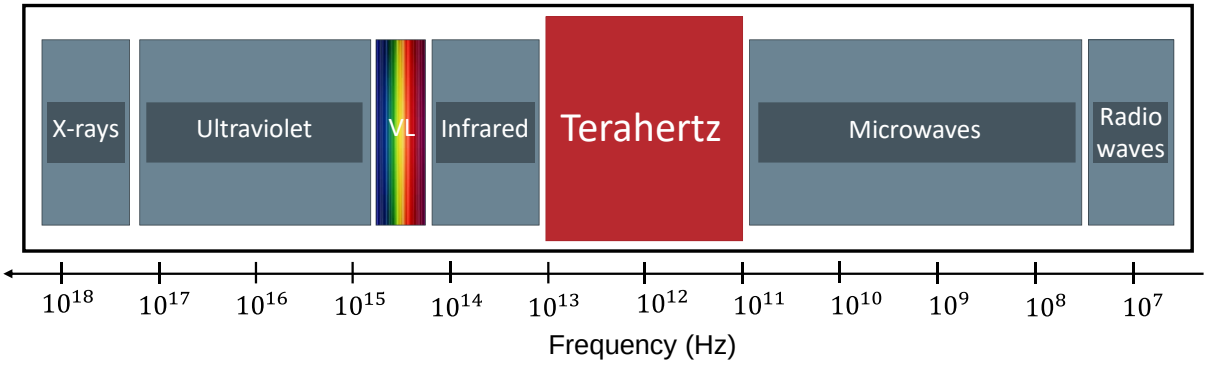

Figure I-1. THz region in the EM spectrum.

I.1.1. Terahertz characteristics

THz photons possess low energy levels, which ensures that THz waves do not cause ionization in biological tissues [1]. Ionization occurs when radiation carries enough photon energy to detach electrons from atoms or molecules. An exposure of a human body to a high dose of ionizing radiation may cause damage to its DNA, increasing the possibility of developing cancer afterwards. The radiation is described as ionizing when the energy is larger than approximately 10 eV. Typical X-ray imaging systems for medical purpose involves photon energies close to 100 keV which is surely harmful for humans. In contrast, the energy corresponding to THz waves falls on the order of tens of meV, far from the energy range of concern. Therefore, THz imaging is considered a safe modality for both samples and operators.

Another notable property is that most dielectric materials, such as cloth, paper, wood, leather, and plastic, are transparent to THz waves. Paired with high reflectivity when incident on metallic surfaces and dielectrics with high permittivity, THz waves enable a high contrast between metallic and non-metallic surfaces in imaging applications, making them highly suitable for nondestructive evaluation applications in security and production chains quality inspection, for example.

In terms of imaging capabilities, the higher frequencies of THz waves offer enhanced resolution in comparison to millimeter waves (mmW), while also providing a wider bandwidth, which results in a 3D image with better range and cross-range resolution. Moreover, THz waves experience reduced scattering due to their longer wavelength compared to visible and IR waves as scattering depends on the wavelength of the radiation. When combined with spectroscopic capabilities, THz wave-based inspections yield valuable information regarding the profile and composition of the sample [2].

Unlike microwaves, THz waves exhibit significant water absorption characteristics [3]. This property has hindered the advancement of THz analysis of the Earth atmosphere and limited its applications to astronomy and research in the upper atmosphere in high altitude observatories in very limited available frequency windows. Regardless, that does not mean that THz radiation did not find its market in the bio-sensing field. On the contrary, research has been conducted to either base the diagnostic on the water content or dehydrate samples in order to access additional information. Similar to water molecules, other molecules exhibit strong absorption and dispersion peaks in the THz range due to rotational and vibrational transitions. These transitions are unique to each molecule, enabling spectroscopic fingerprinting i.e., signature of molecules, in the THz range.

I.1.2. Terahertz applications

In the following sections, we will focus on three key points that exemplify the wide range of possible applications of THz waves.

I.1.2.1. Material characterization and identification

THz radiation finds a number of industrial applications in material characterization. In the paper manufacturing industries [4], the production of the finished goods is being controlled using the THz systems monitoring the thickness as well as the moisture content of the paper during the production process. The differentiation between two different paper samples was also demonstrated experimentally using THz waves [5].

In addition, the THz systems also find its utility in the polymer manufacturing industry such as regulation of polymeric processes using a real-time paint meter [6], quality-control check of the plastic weld joints [7], conductive properties of polyaniline films [8], estimation of the moisture level [9], fiber orientation [10], and glass-transition temperature of polymers [11].

Likewise, in the food items manufacturing industry, it is important to detect the unwanted and harmful objects in food before its final packaging. THz systems play a crucial role in detecting both metallic and nonmetallic contamination in the food items like chocolate bars [12] [13] or ground meat [14]. Pesticide residue was detected in rice powder with a 99.78 % efficiency [15], benzoic acid was successfully identified in wheat flour [16] and melanin in milk powder [17].

Moreover, the medical industry benefits significantly from the material characterization capabilities offered by THz waves. In the case of Traditional Chinese Medicine (TCM) for example, herbal sources serve as the primary providers of active ingredients for various treatments. Multiple demonstrations have proven that THz spectroscopy and imaging enable the detection of foreign elements in TCM herbs and facilitate differentiation between active healing ingredients and potentially harmful substances [18]. Furthermore, THz technology has achieved remarkable success in identifying the geographical origin of plants with an impressive accuracy of 96% [19]. In the realm of Western medicine, THz waves have been successfully employed to investigate the structure and homogeneity of tablets of medicines [20], as well as to assess their density and substance concentration levels [21] (Figure I-2).

Additionally, THz systems have applications in the detection of liquid explosives. This is attributed to the distinct dielectric response exhibited by various liquids in the THz band, which enables differentiation from other alcohol-based substances [32].

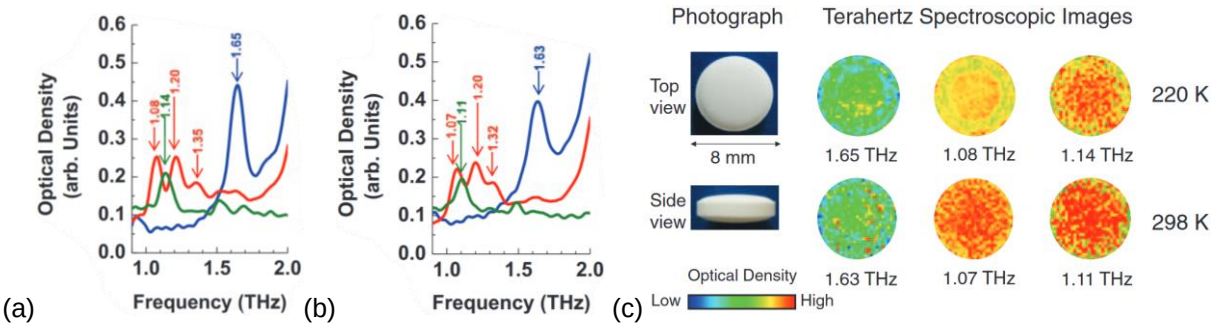

Figure I-2. Temperature-dependent THz spectra of three forms of famotidine. The measurement temperatures were (a) 220, (b) 298. The spectra show the resonant peaks of the substrates. (c) Temperature-dependent THz images of an over-the-counter tablet containing 10 mg of the three forms of famotidine, measured at 220 K (upper row) and 298 K (lower row). The images are taken at the resonance frequencies of the three types of famotidine for each temperature. Higher intensity pixels of each image indicate the presence of famotidine [22].

I.1.2.2. Non-destructive sensing

A notable example of a field in need of non-destructive sensing is the fine art conservation and restoration field, which is one of the first domains to benefit from utilization of the THz waves. As the deterioration or damage of cultural heritage objects is inevitable, the conservator-restorer of artworks is responsible for their examination, conservation, and restoration, as well as for preserving their aesthetic and historical integrity against the natural aging, atmospheric conditions, insects, and human contact. The evaluation of the materials of the object is necessary before carrying out the conservation and restoration work to avoid further damage to the object. The evaluation starts with a visual inspection and then non-destructive or non-contact observation with imaging techniques including THz methods [23], [24]. THz waves could be used for heritage and art conservation for two specific objectives: spectroscopy of material constituents and imaging the internal structure of the objects.

A typical cross-sectional structure of a western painting is shown in Figure I-3, along with various EM waves being used over the years for various analyses depending on their characteristics. X-rays have shown to be able to penetrate all levels in contrast to THz waves that cannot reach further than the preparation level. However, THz radiation offers a compromise of non-destructive and fully safe cross-sectional imaging.

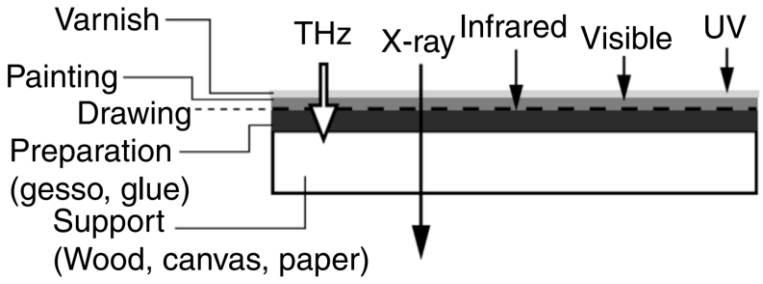

Figure I-3. Typical structure of a painting and the depth of penetration of different EM waves [25].

Using a commercial THz TDS spectroscopy system, two white pigments (lead white and calcite) were clearly distinguished on a painting based on their reflection spectra (Figure I-4).

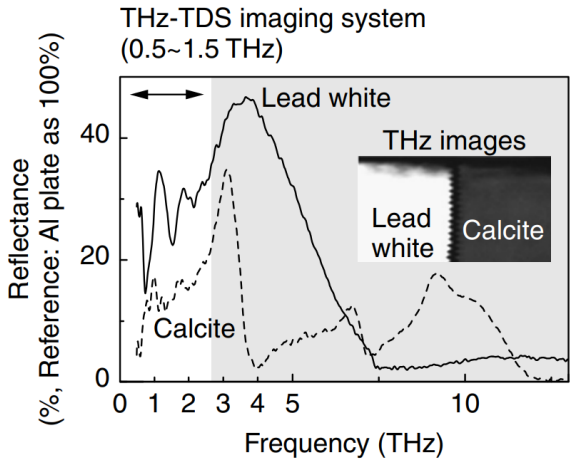

Figure I-4. Reflection spectra and imaging result of two white pigments made of Lead white and calcite using THz-TDS system [25].

Another example of application concerned the assessment of the state of conservation of a medallion stone object has been assessed [26]. A number of internal fractures that were not possible to detect by other imaging methods were found in certain areas of this highly deteriorated object, as shown in Figure I-5. It is easy to see that the areas located at points (a) to (c) are presenting an internal air gap that generates an echo 35 ps to 45 ps from the surface, which corresponds to a depth of 2.3 mm to 3.4 mm from the surface. The measurement at the point (d) shows that the stone is solid at that position and has no internal structure.

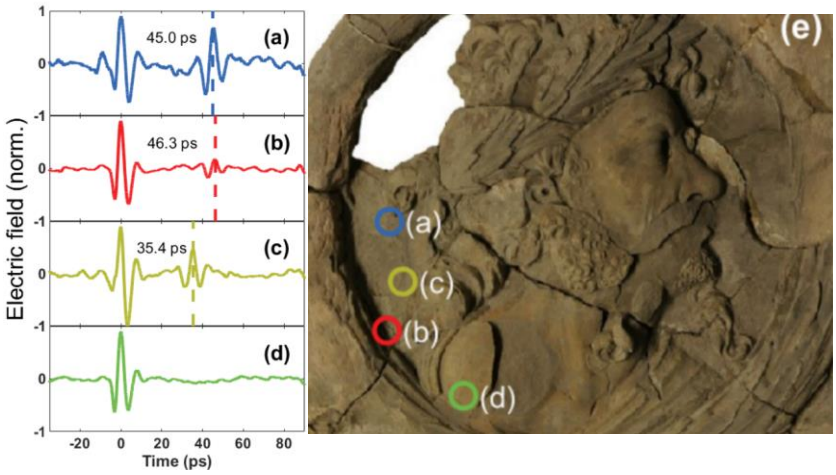

Figure I-5. (a) to (d) Reflected THz pulses from various locations on the medallion photographed in (e), the positions that correspond to each measurement are marked on the photograph [26].

I.1.2.3. Security screening

The detection of powder, liquids, explosives, and other potential threats within small packages and mail has gained significant importance in recent times [27]. Following the discovery of letters containing chemical, biological, and radiological elements over the years, threats has generated the need for new and efficient detection methods to address them. In response, the latest THz imaging scanner has been specifically designed to inspect compact items such as envelopes, letters, and small packages [28]. This technology provides an additional approach to security screening, offering advantages in terms of safety, accessibility, and detection capabilities. Figure I-6 shows an example of rapid screening of mail packages for noninvasive inspection in a reflection setup.

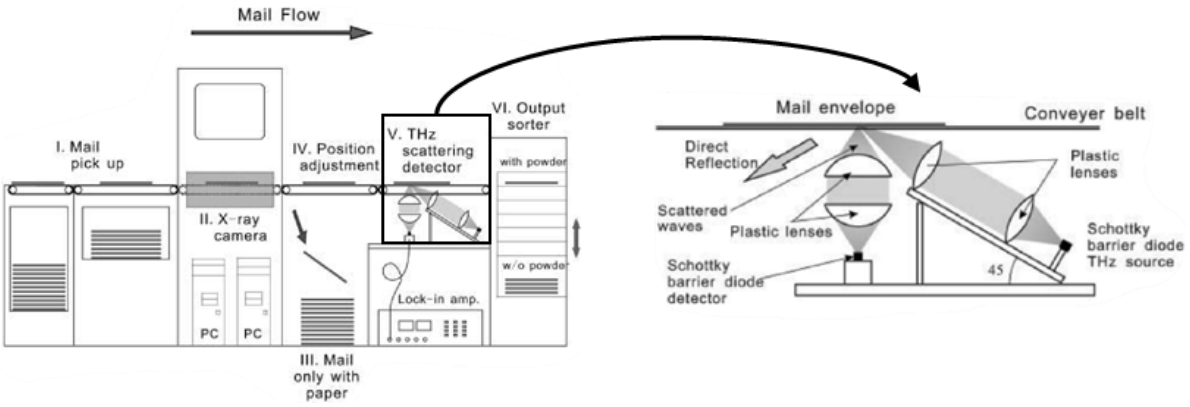

Figure I-6. THz rapid screening noninvasive mail inspection system and the THz detector setup [27].

The main goal is to be able to detect the existence of foreign elements to the usual content of packages and ideally identify the dangerous among the detected substances. Figure I-7 shows the experimental result of successful recognition of small quantities of powders hidden in an envelope.

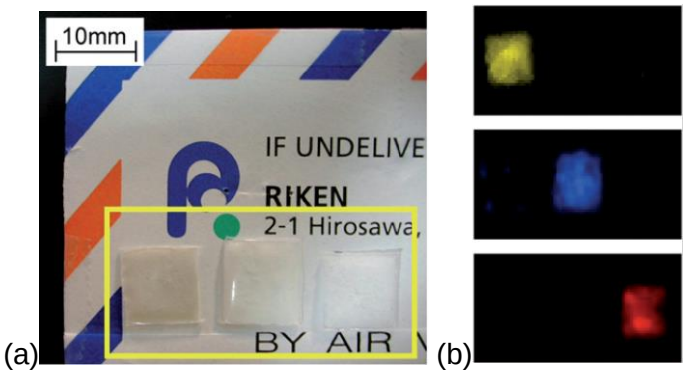

Figure I-7. Recognition of powders hidden in an envelope. (a) Photograph of envelope and plastic bags, from left to right, in yellow box: MDA (methylenedioxyamphetamine), aspirin and methamphetamine. (b) THz images at different frequencies (false colors) to identify the three powders [29].

On another note, there is a need for robust security measures, including full-body scanners, in highly sensitive facilities and public areas such as airports, train platforms, government offices, and open grounds during festive celebrations. Traditionally, security screening in these areas has relied on metal detectors, X-ray screening, or mmW passive and/or active imaging systems. However, the utilization of THz radiation-based security systems offers a safer alternative compared to X-rays [30] and demonstrates potential for noninvasive full-body security scanning in airports [31], [32].

I.1.2.4. Biomedical applications

The field of medical and biomedical imaging holds great promise for the application of THz imaging techniques [33]. Notably, an exposure to the THz wave with intensities of sub hundred milliwatt per square centimeter or even greater does not show any significant variation at a cellular and molecular level of the living substance [34], [35]. Consequently, THz imaging enables safer medical imaging for human subjects [36]. However, because of the high-water absorption of the THz waves (300 cm^{-1} at frequency 1.5 THz), biomedical applications have focused on in vitro diagnosis where a water-removing pre-treatment is necessary to dehydrate cancer tissues for example [37]. Figure I-8 shows the spectroscopy results of an in vitro sample

of brain tissue in four different states and the difference detected in the THz range allows for a preliminary identification of the state of the tissue.

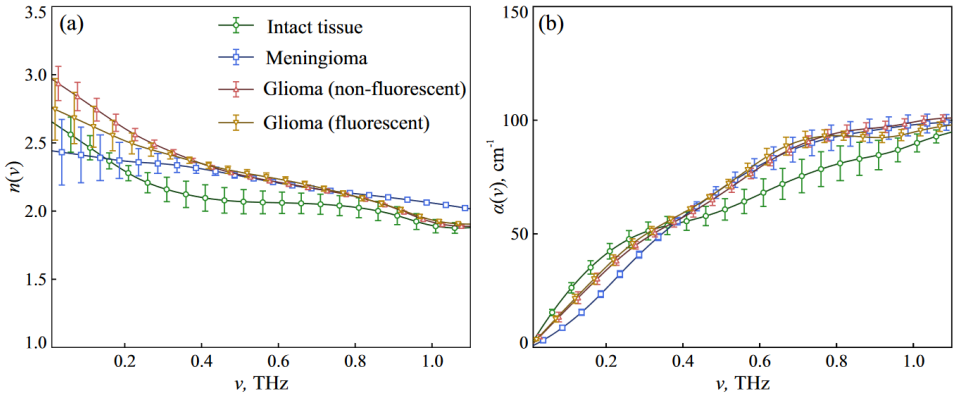

Figure I-8. Results of the in vitro THz spectroscopy of the gelatin-embedded brain tissues: healthy intact tissue and three types of brain tumors (Meningioma, Glioma (non-fluorescent) and Glioma (fluorescent)). (a) Refractive index and (b) absorption coefficient [37].

Another example of in vitro diagnosis is presented in Figure I-9, where the refractive index map of the malignant tissue is assembled for a visual identification.

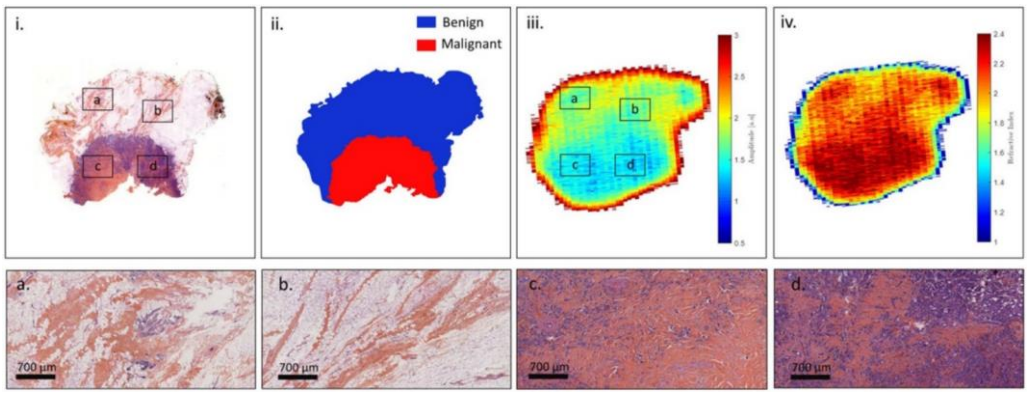

Figure I-9. (i) Pathology image and correlated view of the respective zones (a)–(d); (ii) pathology mask; (iii) raw THz image at 550 GHz; (iv) refractive index map at 550 GHz [38].

In vivo applications are immerging nowadays to find solutions for medical imaging that could be used for living body diagnosis [36]. The potential applications of in vivo THz imaging encompass the analysis of breast tumors [39], [40], evaluation of skin hydration and detection of skin cancer [41] or early cancer diagnosis [42], [43].

I.1.2.5. Next-generation telecommunication

To meet the increasing demand for high data rate communication [44], it is imperative to employ higher operating frequencies within the THz range of the EM spectrum [45]. However, the implementation of a communication link using higher THz frequencies requires careful consideration of various design aspects. The THz domain of the EM spectrum is characterized by high signal attenuation and low power levels, requiring the use of highly directive wireless communication systems that enable point-to-point connectivity over short distances [46]. This facilitates the establishment of secure short-range links for high-speed exchange of confidential information. Ongoing active research in the field of THz communication systems focuses particularly on indoor applications, particularly for point-to-point communication

spanning several meters [47], [48]. It is important to note that THz communication systems primarily operate over short distances due to limitations imposed by atmospheric attenuation and scattering caused by buildings and surrounding materials [49], [50].

I.2. Terahertz generation and detection technologies

THz sources can be categorized into several types, including vacuum electronic sources, solid-state sources, and sources driven by lasers such as Quantum Cascade Laser (QCL), optically pumped gas laser, photomixing and photoconductive switches, etc. The following sections will provide examples for some of these categories.

I.2.1. Vacuum electronic devices

Electron beam sources, such as gyrotrons [51], free electron lasers (FELs) [52], and backward wave oscillators (BWOs) [53] are capable of generating relatively high-power signals at the THz frequency range. These devices operate based on the interaction of a high-energy electron beam with a strong magnetic field inside resonant cavities or waveguides, which results in an energy transfer between the electron beam and an EM wave. Gyrotrons with 5 kW power at 1 THz have been successfully developed [54]. An FEL provides very high operating frequencies and wider frequency tuning range (0.1-10 THz) [55]. However, Gyrotrons are much more compact than FELs and can operate at relatively small accelerating voltages, usually about several tens of kilovolts [54]. It is important to note that complete systems are typically large and heavy and need high bias voltage and a temperature-controlled environment usually with a water-cooling system.

I.2.2. Solid state sources

Solid-state sources include diode-based sources, transistor-based sources, and frequency multiplication-based sources. Among them are resonant tunneling diodes (RTD) [56], Gunn or transferred electron devices (TED) [57], and transit time devices [58] such as impact avalanche transit time (IMPATT) diodes, tunnel injection transit time (TUNNETT) diodes and UTC-PD (Uni-Travelling Carrier) photodiodes [59], [60]. These solid-state sources can emit frequencies from several hundred of GHz up to several THz, although they typically generate sub-THz frequencies. It should be noted that the performance of these electronic THz sources tends to degrade at higher frequencies, with generating around 100 mW at 200 GHz to less than 0.05 mW at 2 THz. This is a work in progress specifically on the front of semiconductor technologies.

In the case of THz frequency multipliers [61], a nonlinear device is employed to multiply the frequency of a driver source, resulting in the generation of higher-order harmonic frequencies. Planar Schottky varactor diodes are commonly used in frequency multipliers [62]. The most efficient THz frequency multipliers are employing series chains of frequency doublers and frequency triplers with generated signals reaching up to 2 THz. However, the power is still an aspect of improvement (~20 µW).

I.2.3. Quantum Cascade Laser

One of the promising semiconductor lasers in the THz range is the quantum cascade laser (QCL) [63]. The QCL operates as a unipolar laser (a type of laser that operates based on one type of charge carrier rather than two, either electrons or holes), consisting of multiple layers of semiconductor materials arranged in alternating fashion, creating quantum energy wells that confine electrons to specific energy states. As the electrons traverse the lasing medium, they

transition from one quantum well to the next under the influence of an applied voltage (Figure I-10). Within specially engineered regions called the "active region," the electron undergoes a transition from a higher energy state to a lower one, releasing a photon in the process. This cycle repeats as the electron progresses through the multilayered structure, emitting multiple photons at each active region. A single QCL can include up to 75 active regions, resulting in a corresponding number of photon emissions by each electron as it traverses the device. Notably, QCLs have been demonstrated to achieve output powers of approximately 10 mW at a frequency of 2 THz. Various QCL lasers can cover the wavelength range from 1.2 to 5 THz. While these lasers are compact in size, they typically require low-temperature operation and employ cryogenic cooling systems. Some THz quantum cascade lasers have reported operational temperatures as high as 199.5 K for a pulsed system at a frequency of 3.22 THz [64]. QCLs can be used either for continuous wave (CW) or pulsed wave generation.

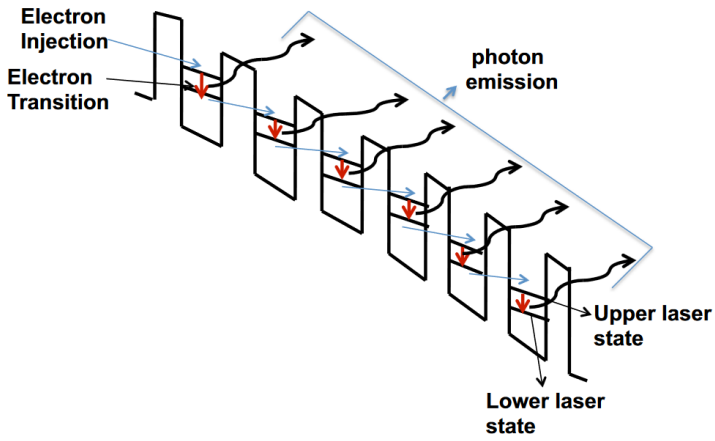

Figure I-10. General scheme of the active region of QCL with multiple stages. At each stage, the electron drops down the energy levels (straight red arrow) and emits a photon (curved arrow) [65].

I.2.4. Optically pumped gas laser

Another type of THz laser is the optically pumped far-infrared gas laser [66]. These lasers operate by using a CO_2 laser pumping a cavity containing a gas (Figure I-11), which undergoes lasing at THz frequencies through the rotational state transitions of specific molecules. The precise lasing frequency is determined by the type of gas used. Various type of media for THz gas laser have been exploited such as CH_3F, CH_3OH, NH_3, COOH and CH_2F_2, giving thousands of THz lines in the 0.1 to 8 THz range [67]. Optically pumped gas lasers provide powerful THz radiation either in pulsed or CW mode. Typically, these lasers generate power levels ranging from several µW up to 100 mW, while the laser-pump power reaching values of 20 to 100 W. However, these lasers suffer from the large size due to the bulky CO_2 laser and also from the long gas cell necessary for enough gain. Measures have been taken to overcome these problems such as a compact NH_3 gas laser pumped with a QCL giving tens of microwatts at 1.07 THz [68]. Hollow-core optical fibers and photonic crystal fibers, which are light, flexible and show low confinement loss, have been also theoretically investigated working as the gas cell, showing the possibility of more compact THz gas lasers [69].

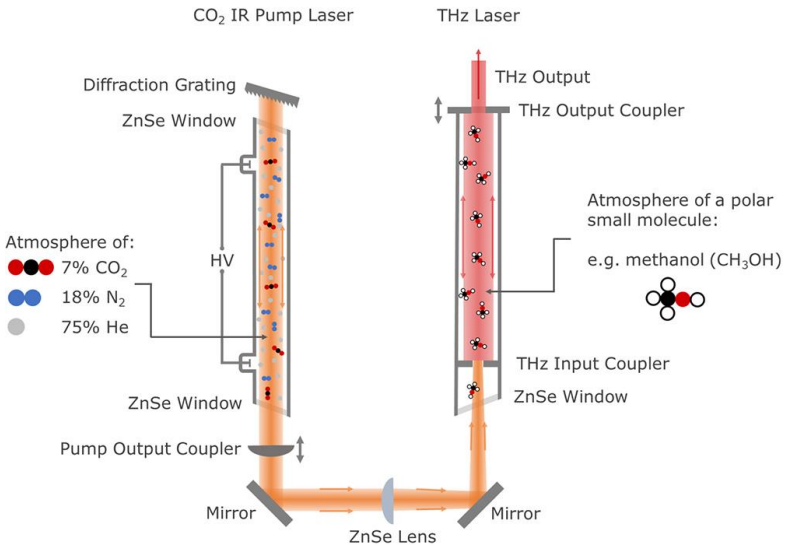

Figure I-11. Schematic of an optically pumped THz molecular laser based on an Edinburgh Instruments FIRL-100. A pump laser is used to optically excite a vapor of polar molecules to a higher energy level from which they relax with the emission of THz radiation. The system generates THz radiation between 0.25 THz to 7 THz [70].

I.2.5. Photomixing

Photomixing is the generation of CW THz radiation from two lasers. The beams, with frequency ω_1 and ω_2 are spatially overlapped and focused onto a photomixer device which generates the THz radiation (Figure I-12). A typical photomixer device is made from low-temperature grown semiconductor structure such as gallium arsenide (GaAs) or indium gallium arsenide (In GaAs), with a patterned metalized layer which is used to form an electrode array and radiating antenna [71]. The photonic absorption of the laser beams in the semiconductor material with a short charge carrier lifetime result in the modulation of the conductivity at the desired THz frequency $\omega_{THz} = \omega_1 - \omega_2$. An applied electric field allows the conductivity variation to be converted into a current which is radiated by the metallic antenna. A variation of the time delay between the laser beams enables the generation of a tunable THz wave and controlling both the phase and frequency of the generated THz wave. A tunable frequency up to 5 THz has been demonstrated [72]. However, the achievable power is on the order of 10^{-8} W.

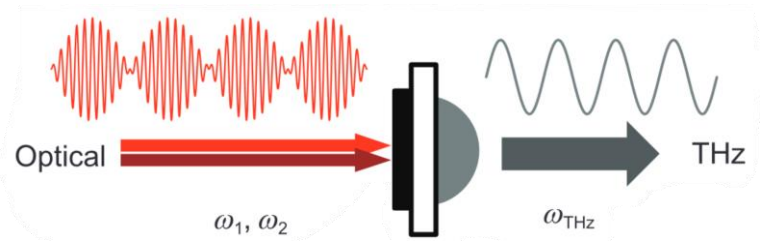

Figure I-12. Schematic diagram of photomixing.

I.2.6. Optical rectification

Optical rectification (OR) is a nonlinear optical phenomenon that was initially demonstrated in 1962 [73], shortly after the development of lasers. It relies on the inverse second-order electro-optical effect in a nonlinear crystal. This nonlinear process involves the creation of a quasi-DC polarization using a sinusoidal driving field in a nonlinear medium when exposed to a high-intensity optical beam, resulting in the emission of EM waves in the THz frequency range.

I.2.7. Terahertz generation by photoconductive switches

The concept of photoconductive switches or photoconductive antennas (PCAs) was first introduced in the early 1980s [74]. A typical PCA (Figure I-13) consists of two metallic electrodes on a semiconductor with high carrier mobility [75]. When the semiconductor material is subjected to an intense and short laser pulse, the incident light excites the electrons from the valence band to the conduction band, which generates a transient population of charge carriers within the semiconductor. The generated charge carriers are subsequently accelerated by a bias voltage, resulting in a rapid transient current between the two electrodes. The coupling of the THz wave to free space occurs through the metallic electrodes which acts as an antenna, whose parameters and geometry heavily influences the frequency of the emitted THz short pulse.

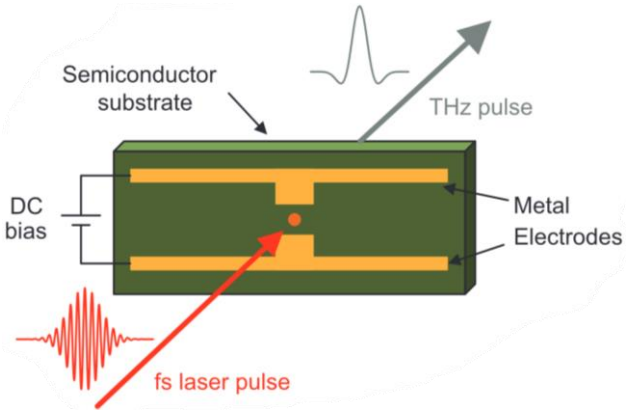

Figure I-13. THz pulse emission from a photoconductive switch excited by a femtosecond laser pulse.

Significant advancements have been made in photoconductive switches, leading to notable improvements in THz pulse energy and frequency response. These advancements have been achieved through the use of novel semiconductor materials and optimized geometries [76], [77]. Various antenna geometries have been explored (Figure I-14), such as the bow-tie antenna, interdigitated structures, spiral antenna, and more designs derived from the microwave theory.

Recent research has focused on enhancing THz generation by incorporating interdigitated geometries for example. Compared to the conventional large gap dipole PCA or bowtie PCA, interdigitated geometry shows better performance in generating THz pulses because it takes advantage of both the small gap and large gap aspects. As the gap between the PCA electrodes is filled with metal teeth-like structure, most of the generated photocarriers get collected at the respective electrodes with less carrier drift time and leads to a higher optical-to-THz conversion efficiency up to 7.5%, with maximum output power exceeding a milliwatt. Interdigitated PCA have also proven to shift the resonant frequency toward higher THz frequencies [78].

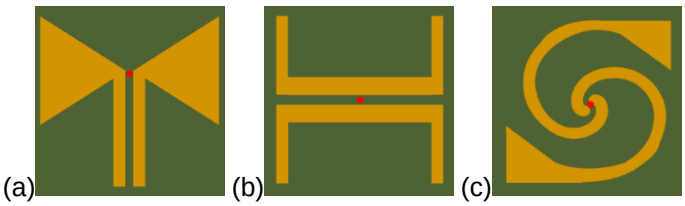

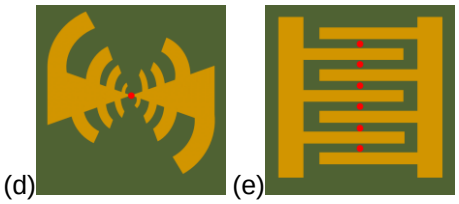

Figure I-14. Four planar PCAs. The yellow indicates the metallic part and the green indicates the photoconductive substrate. (a) Butterfly antenna, (b) dual U-shaped antenna, (c) spiral antenna, (d) log periodic antenna and (e) interdigitated antenna. The red dote indicates the fs laser excitation. (Adapted from [79] and [80]).

I.2.8. Terahertz detector technologies

In this section, we review some of the common THz detection techniques which are thermal detectors and optoelectronic detectors specifically electro-optical crystals and PCAs.

Thermal detectors, such as bolometers, are thermal sensors that absorb EM radiation resulting in an increase of their temperature [81]. Thermal detectors are incoherent as they are not phase sensitive and only provide signal amplitude detection. Bolometers can be very broadband detectors as thermal conversion is typically wavelength independent [82].

Optoelectronic detection encompasses non-linear electro-optical detectors [83] and PCAs [84]. These techniques are coherent due to time domain signal sampling, which means that they enable the extraction of both amplitude and phase information from incident THz signals by controlling the timing of a gating laser beam relative to the incidence of the THz signal. In the electro-optic detection scheme, the incident THz wave and gating laser beam co-propagate within an electro-optic crystal, resulting in a change in the polarization state of the laser beam. The change in polarization is detected as a voltage at the output of balanced photodiode detectors and is proportional to the amplitude of the THz electric field.

In the PCA detection scheme (Figure I-15), an optical probe pulse illuminates a photoconductive switch while the THz wave to be detected passes through. The generated voltage between the switch electrodes is proportional to the electric field of the received THz wave which is measured as a photocurrent in the time domain.

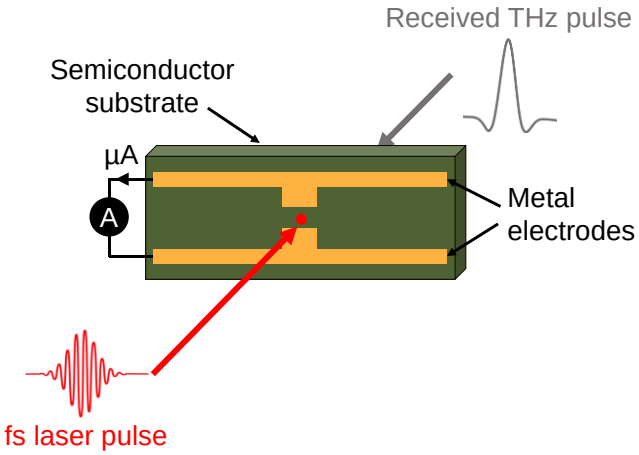

Figure I-15. THz pulse detection using a dipole PCA excited by a femtosecond laser pulse.

For more detailed information on the functioning of PCA antennas, the following sections will provide a comprehensive overview, as they serve as the primary technology for THz generation and detection used in this work.

I.3. Optoelectronic techniques, based on PCAs, for the generation and detection of pulsed THz waves

As detailed in the previous section, optoelectronic methods for THz generation and detection involve non-linear electro-optical devices and PCAs. These techniques can serve for both pulsed and CW generation. While both non-linear electro-optical devices and PCAs technologies have their respective benefits and limitations, we have chosen to focus on PCAs for pulsed THz wave generation in this work since they are integrated in the THz Time Domain Spectroscopy system which was used for the research presented in the manuscript.

I.3.1. Pulsed terahertz signal generation in photoconductive antenna

PCAs are widely utilized for both THz generation and detection. These antennas operate by inducing transient photocarriers in a semiconductor substrate using ultrafast laser pulses. A typical PCA consists of a semi-insulating semiconductor substrate with two DC biased metal electrodes separated by a gap. To generate THz pulses, voltage is applied across the electrodes. Since the substrate is semi-insulating, electric energy is stored in the gap area. The ultrafast laser pulses serve as transient switches, opening this reservoir of electric energy and releasing it in the form of picosecond (ps) short pulses, containing spectral content within the THz range. The brief duration of the laser pulse is essential for producing a short pulse containing spectral information within the THz spectrum. The polarization of the radiated THz wave aligns parallel to the biased field, which is perpendicular to the strip lines formed by the electrodes. For efficient generation, the laser pulses must have enough photon energy to create photoinduced free carriers within the substrate. Generally, the photon energy of the excitation optical pulse should exceed the band gap of the substrate. Free carriers are driven by the bias field across the gap and generate a photocurrent. Since electrons usually have much higher mobility than holes, the contribution of holes can be ignored in most cases. The current density is described as: [25]

Eq. 1

$$J(t) = N(t)e\mu E_b$$

where N(t) is density of photocarriers, e denotes the elementary charge, μ is the mobility of electron, and E_b is the bias electric field. The photocarrier density N(t) is a function of time, whose format is determined by the laser pulse shape and the carrier lifetime. Since the photocurrent varies in time, it generates EM pulse, whose electric field is approximately:

Eq. 2

$$E_{THz} = \frac{1}{4\pi\varepsilon_0}\frac{A}{c^2 z}\frac{\partial J(t)}{\partial t} = \frac{Ae}{4\pi\varepsilon_0 c^2 z}\frac{\partial N(t)}{\partial t}\mu E_b$$

where A is the area in the gap illuminated by the laser light, ε_0 is the vacuum permittivity, c is the speed in vacuum, and z is the distance between the field point and the THz source. The energy of the generated THz pulse originates from the electric energy stored in the gap of the PCA, rather than directly from the energy of the optical pulse. However, there is a direct correlation between the energy of the THz radiation pulse and the energy of the excitation laser pulse. The excitation laser pulse serves as a trigger that facilitates the release of the stored energy, converting it into THz radiation. As more photocarriers are generated within the antenna, a larger amount of the stored energy is transformed into THz radiation.

It is important to note that when the PCA's substrate is excited, it transitions from being a semi-insulating material to a conductive medium. As a result, the photo current is modified from Eq. 1 to:

Eq. 3

$$J(t) = \frac{\sigma(t)E_b}{\frac{\sigma(t)\eta_0}{1+n} + 1}$$

where σ is the conductivity of the substrate, η_0 denotes the impedance of air, which is $\eta_0 = 377$, and n is the refractive index of the substrate. The substrate conductivity σ is induced by the excitation laser, and can be considered as $\sigma \propto I_0$, where I_0 is the laser intensity. Combining Eq. 2 with Eq. 3, the THz field is:

Eq. 4

$$E_{THz} \propto \frac{d\sigma(t)}{dt} \frac{1}{\left[1 + \frac{\sigma(t)\eta_0}{1+n}\right]^2} \propto \frac{I_0}{(1+kI_0)^2}$$

Where $k = \frac{\kappa(t)\eta_0}{1+n}$, and κ(t) is the ratio between σ(t) and I_0. From Equation [4], it is evident that the THz field reaches a saturation point relative to the power of the excitation laser when it reaches a certain level of intensity.

There are also limitations to increasing the biased field in a PCA, as a high electric field can result in dielectric breakdown of the substrate. The dielectric breakdown of the semiconductor material integrated in a PCA can be categorized into two types: field-induced breakdown and thermal-induced breakdown. Field-induced breakdown occurs when the biased field exceeds the breakdown field of the semiconductor material, typically around 4×10^5 V/cm for GaAs. Field-induced break down usually happens instantly when reaching the limit field excitation. Thermal-induced breakdown, on the other hand, is caused by the heating of the substrate due to photocurrent flow and absorption of the excitation laser. Heating reduces the substrate's resistance, leading to even higher current flow. Thermal-induced breakdown is a relatively slow process, taking seconds to minutes. In most cases, breakdown in PCAs during THz wave generation is thermal induced. The thermal-induced breakdown introduces a tradeoff between the intensity of the excitation laser and the maximum biased voltage. Applying appropriate treatment or coatings to the substrate surface can increase the threshold of breakdown field, thereby enhancing THz wave generation from the PCA.

I.3.2. Pulsed terahertz signal detection in photoconductive antenna

Using a PCA as a THz detector is quite similar to using it as a THz emitter. The main distinction lies in that the two electrodes are connected to an ampere-meter instead of a DC power supply. In the detection mode, an optical probe pulse is employed to generate transient photocarriers in the semiconductor substrate submitted to the incident THz field. These photoinduced carriers are consequently driven by the THz field, leading to the generation of a current between the two electrodes. By controlling the time delay between the optical probe pulse and the THz pulse, it is possible to sample the electric field at any specific time and enabling the assembly of the photocurrent over time. The THz field induced current is: [25]

Eq. 5

$$\bar{J} = \bar{N} e \mu E_{THz}(\tau)$$

Here $\bar{N}$ denotes the average electron density, and τ is the temporal delay between probe pulse and the THz pulse. By modifying the temporal delay, the THz pulse waveform as a function of τ is recorded. The THz oscillation has a period of approximately 1 ps. As shown in Eq. 4, the detection of THz pulses directly records its field rather than intensity, meaning that the access not only amplitude, but also phase information of the THz pulse, while the latter (i.e., phase) is rather difficult to be directly measured in optics.

I.3.3. Performance of the PCA

The performance of a PCA relies mainly on the following factors: the substrate material, geometry of the active area, geometry of the antenna, and the excitation laser pulse [85], [86], [87]. Materials with a short carrier lifetime, such as low-temperature GaAs (LT-GaAs) or doped silicon, are usually selected as the substrate in order to increase the response speed of the PCA. The response speed is essential to generate and detect short THz pulses containing high frequency components. Higher carrier mobility of the semiconductor substrate is also a desired character since it results in the high efficiency of THz wave generation. High dark resistance is required for the substrate in order to have sufficiently high breakdown voltage across the antenna. The gap area between the electrodes with laser excitation is another crucial aspect of a PCA and the distribution of the excitation light within the gap is also important. It was demonstrated that concentrating the excitation beam close to the anode, where the electric potential has the highest slope since the mobility of electrons is higher than that of the holes, leads to higher THz wave generation [79]. PCAs with smaller gaps have higher efficiency, especially when low excitation power is used. However, larger gaps allow higher excitation power and bias voltage to be applied on the PC antenna, thus generating higher power THz radiation [88]. The shape of the antenna is crucial to optimize coupling of THz waves between the PCA device and the free space. In terms of frequency response, various antennas are divided into two groups: resonant and non-resonant antennas. The former has a resonant frequency, which emits THz waves around a certain central frequency. The dipole-antenna is the most widely used resonant antenna, which emits THz wave with a central wavelength of $\lambda_n = \frac{2L}{m}$ where L denotes the width of the antenna from one side of the anode to the other side of the cathode and m can be any positive integer. A resonant antenna does not provide a naturally large bandwidth. A non-resonant antenna has a variable width and leads to a broader frequency response range. Geometries of a non-resonant antenna include spiral and logarithmic periodic antennas (Figure I-14).

In most cases, the THz emission using PCAs has been described using the approximation of an ideal dipole, producing linearly polarized radiation perpendicular to the strip lines formed by the electrodes. However, the dipoles used in real THz systems are not ideal, and so the polarization state of the radiation is not, in general, purely perpendicular to the strip lines formed by the electrodes and could take a direction in between while still being linear. That is because a typical emitter generates a cross-polarized component which is on the order of a few percent as large as the component polarized along the dipole. Roughly 7% large amplitude of the cross-polarization was found in comparison to the dominant polarization component, although no explanation was provided for the origin of this small component [89].

I.4. THz time domain spectroscopy (THz-TDS) system

In order to generate and detect broadband THz pulses using PCAs, two antennas are integrated in a TDS system as emitter and detector, respectively.

A typical fiber-coupled THz-TDS system using PCA is shown in Figure I-16. The system consists of a femtosecond laser, a computer-controlled optical delay line, an optically gated fiber pig-tailed THz transmitter, optics for collimating and focusing the THz beam, an optically gated fiber pig-tailed THz receiver, a current pre-amplifier, and a digital signal processor (DSP) controlled by a personal computer.

The THz-TDS approach is based on the coherent detection of THz pulses by sampling the electric field as a function of temporal delay. Experimentally this is achieved by splitting up a laser pulse into two beams, one to pump the transmitter and one to gate the receiver (Figure I-16). When the laser pulse illuminates the gap of the emitter PCA, free charge carriers are injected. With an electric bias on the electrodes, a THz wave is generated and coupled into free space by a silicon lens. A similar antenna serves as a receiver if the bias is replaced by a lock-in amplifier and the current of nano-amperes, proportional to the THz electric field, can be detected. By changing the timing between the two laser pump beams, the detection gate is reconstructing the THz pulse as a function of delay (Figure I-16). Typically, the delay is generated using a retro-reflective mirror positioned on a linear stage moving in one of the laser beams, usually the emission laser source.

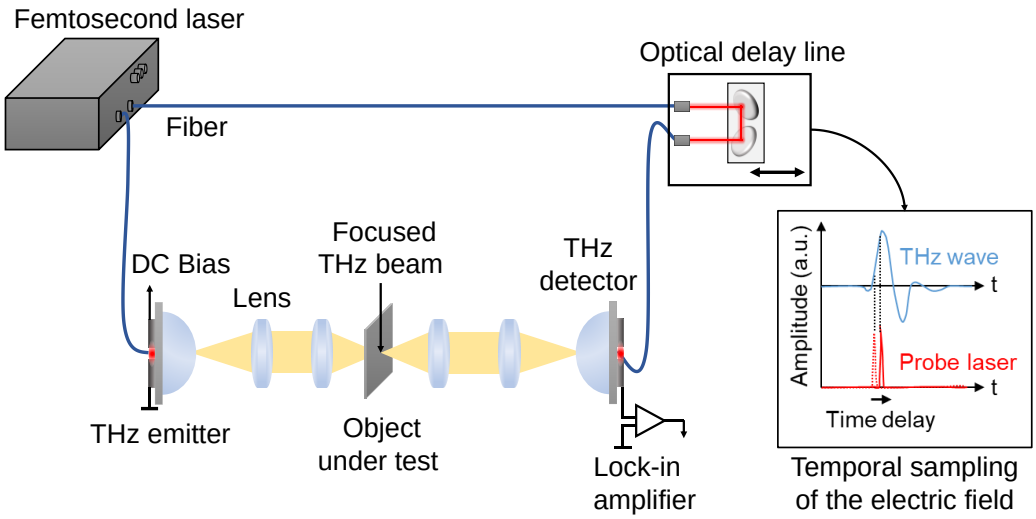

Figure I-16. Typical fiber-coupled THz-TDS system in transmission configuration, and the illustration of the principle of detection based on temporal sampling of the electrical field by moving the optical delay line.

The features of this setup have not been substantially altered since the initial report of the first THz-TDS system in 1989. However, there have been a number of significant advances, which have enabled the imaging applications such as the use of a rapid scanning optical delay line.

Historically, a standard laboratory THz-TDS system is based on free-space propagation of the laser beam between bulky mirrors guiding the gating laser pulses to the transmitter and receiver PCAs [90], [91]. However, this configuration has proven to be space consuming and lacks flexibility. Also, in terms of eye safety, precautionary measures have to be taken against the laser light. Even more, its experimental layout is mostly limited to geometries working in transmission or reflection under one particular fixed angle (Figure I-17).

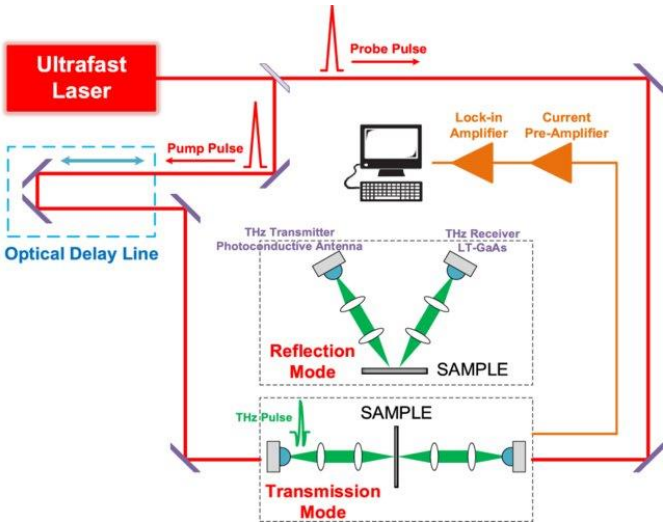

Figure I-17. Schematic diagram of TDS system in both reflection and transmission. The pump beams are delivered to the PCAs through free space guided propagation, using mirrors and beam slitters [92].

In contrast, antennas receiving the optical excitation through optical fibers offers a huge advantage in flexibility, which makes all-fiber TDS system the currently most popular configuration. As laser pulses are guided in fibers, the system is inherently eye safe. Less free-space propagation also increases the system's mechanical and thermal stability [74]. We should note that the switch from free space propagation to fiber coupled radiating components resulted in a necessary adaptation of the optical pump wavelength from 800 nm to around 1550 nm as it is the wavelength most adapted to fiber-guided propagation. Consequently, the composition in the semiconductor materials of the PCAs are adapted to match the change in the wavelength of the optical pump following the use of fibers.

Using the TDS system not only is the intensity measured, but the electric field of the THz pulse is resolved in the coherent detection scheme. The result of a typical measurement under laboratory conditions can be seen in Figure I-18.a. This shows the reference electric field, acquired in ambient temperature air. The transient field consists of a single-cycle pulse with a duration of around 2 ps. If a sample is inserted in the THz beam path, the pulse is delayed due to the slightly higher refractive index of the sample. The pulse peak amplitude is also reduced, and secondary echo modulations can appear after the main peak. The Fourier Transform of the measured signal leads to the complex spectrum (Figure I-18.b). The reference amplitude extends from 0.1 THz to 6 THz. The polar water molecules from the air moisture absorb some discreate narrowband frequencies, which could be eliminated using a purge box to purify the air and reduce the humidity level.

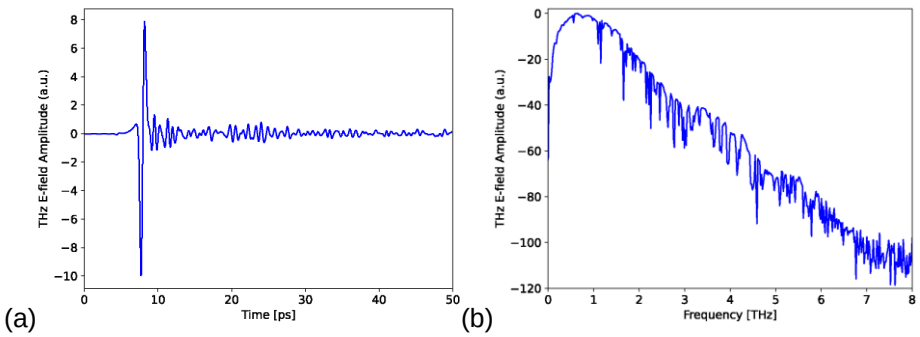

Figure I-18. Measured THz electric field (a) as a function of time (b) Normalized magnitude of the corresponding frequency spectrum.

Here, a brief comment on the state of the art of each component is presented.

Femtosecond laser source

The invention of the ultra-short lasers allowed a very fast surge in TDS systems. The short duration of the pulse is necessary for the generation of a short pulse of whom the spectral information falls into the THz range. Historically, the vast majority of the work in this field has been carried out using mode locked Ti: sapphire lasers, operating near a wavelength of 800 nm. These are the most widespread femtosecond laser sources, and the laser parameters (pulse duration, wavelength, and output power) are all ideally suited for driving GaAs-based THz emitters and detectors. However, these lasers were quite sensitive to small changes in optical alignment and are thus not stable against mechanical vibrations. In order to update the TDS system, a more robust femtosecond laser is desired. An excellent alternative is the mode locked lasers, in which the light pulses propagate entirely within an optical fiber. The wavelength of these fiber sources is usually 1550 nm which are adapted to the maxima of optical transparency of silica fibers occurring at 1.3 and 1.55 µm [93]. One can no longer use GaAs, since this wavelength is below the band gap of the material. So, antennas based on materials such as InGaAs/InAlAs are used instead as they are more compatible with the wavelength, offering a solution for flexible and all fiber TDS systems. The 1550 nm laser are erbium doped and achieve ultra-short pulse width through nonlinear pulse compression and by managing the effects of dispersion and nonlinearity in the fiber [94].

Optical delay line

One of the key elements of THz TDS systems is the optical delay line or ODU (optical delay unit). Usually, it consists of a motorized translation stage and two corner reflectors mounted on its top. In order to move the sampling gate across the waveform to be sampled, the TDS system requires a means for varying the delay of one optical beam relative to a second. In nearly all cases, this is accomplished by varying the optical path length traversed by one of the beams. Often, the alignment of the optical beam onto the detector is more sensitive than the alignment of the generating beam as the sensitivity must be optimized, although this depends on the details of the antenna structures employed. In these cases, it makes more sense to place the variable delay in the path illuminating the generating antenna. The mechanical scanner can either be a slow stepper motor or a rapidly oscillating device such as a galvanometer. The speed of the scanner dictates the arrangement for the data acquisition. In many imaging applications, it is desirable to scan the optical delay as rapidly as possible, in order to increase the waveform acquisition rate. The optical delay line provides a delay range which reflects the maximum optical path (free space separation distance) between the antennas [95]. The longer the delay line the longer is the distance between the antenna modules.

Terahertz beam optics

The first category of lenses are the lenses directly attached to the antenna. In general, the lens has a plano-convex structure with a spherical or elliptical side [96], while the flat side is attached to the planar antenna from the substrate side. The lens’s primary objective is to compact the beam for easy coupling with other optical elements. Additionally, the lens facilitates the transition of the generated or detected THz beam across from a media to the other. It works to minimize reflection loss at the frontier between the substrate and the lens, ensuring efficient transfer. Moreover, the lens aims to maximize the Gaussian form of the beam by preventing the excitation of slab modes caused by total reflection at the substrate's surface.

That is why substrate and lens are made from the same low loss material, or from materials with close dielectric constants to the photo-excited substrate, a silicon (Si) lens is used with a GaAs based antenna for example. An antireflection coating is applied to the lens-air interface to minimize the reflection loss since usually the material of the lens and substrate has a high dielectric constant (n = 3.41 for silicon). Both semiconducting emitters and detectors in TDS systems are coupled with integrated antennas. This is quite natural because the generation and detection mechanism of this system involves planar antennas.

The designs of the lenses in the lens-antenna systems are most often elliptical or hemispherical lenses with a cylindrical extension (Figure I-19). There are several design considerations, mainly the form of the coupled beam compared to a gaussian beam, and secondly the directivity or divergence of the beam. In principle, there are many combinations of surface shape and extension length possible but to give a general idea, increasing the extension decreases the divergence of the beam and eventually leads to a collimated beam with astigmatism. Also, the effective lens aperture decreases, and more radiation is lost, due to internal reflection at the lens-air interface. In terms of the Gaussian beam form, increasing the extension length leads to a less Gaussian beam with higher side lobes and an increased directivity. In terms of the bandwidth of a TDS system, it was found that the hyper hemispherical lens restricts the bandwidth because it exhibits large interference fringes. In contrast, the collimating lens offers less restriction bandwidth wise. The preferable approach depends on many details, notably the design of the optical systems integrating the antenna-lens composition.

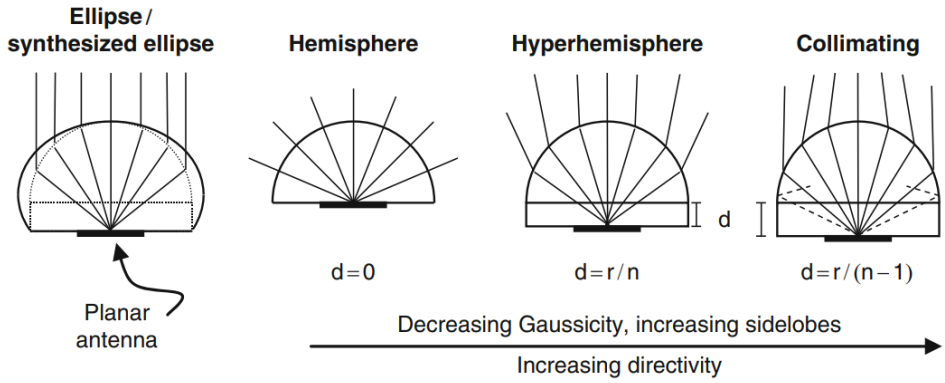

Figure I-19. Common shapes of a typical lens attached to a PCA. Lenses are made of Si (n = 3.42) with a radius of 3 mm. Solid lines represent emerging rays while dashed lines represent trapped rays. The evolution of the qualitative properties in terms of Gaussian optics are indicated by the arrow [67].

A second category of optical lenses are the independent elements that are placed away from the source in order to collimate or focus the THz beam (such as the four lenses used in the TDS system presented in Figure I-16 to focus the THz beam on the object under test). The lenses can be made from polymer materials such as HDPE, Tsurupica, TPX or Teflon. These materials have in common a relatively low refractive index of about 1.4 to 1.7 which varies slowly across the THz range, which is useful since they are coupling THz radiation from and to air (n = 1). Normally, antireflection coatings are not necessary as the reflection losses of these materials are between 3% and 7% per interface. Regarding the surface accuracy, optical polishing is not required in many applications. This makes polymer lenses fairly cheap. Besides polymers, crystalline materials are frequently employed. Those used most often are quartz, Si and Ge which are expensive compared to polymer lenses and more demanding regarding fabrication. Therefore, they are mainly used in specialized systems such as quasi-optical lens–antenna systems.

Mirrors can also be used instead of lenses to collimate the THz beam. Mirrors are usually made of solid metal or glass with the front surface metallized into an ellipsoidal or paraboloidal form. The mirrors are usually used for off axis focalization, which generates forms of distortion of the amplitude and phase as well as cross polarization upon reflection (Figure I-20). This is particularly troublesome because systems are normally designed for fundamental Gaussian propagation, and such distortion degrades the beam coupling, especially when multiple mirrors are used.

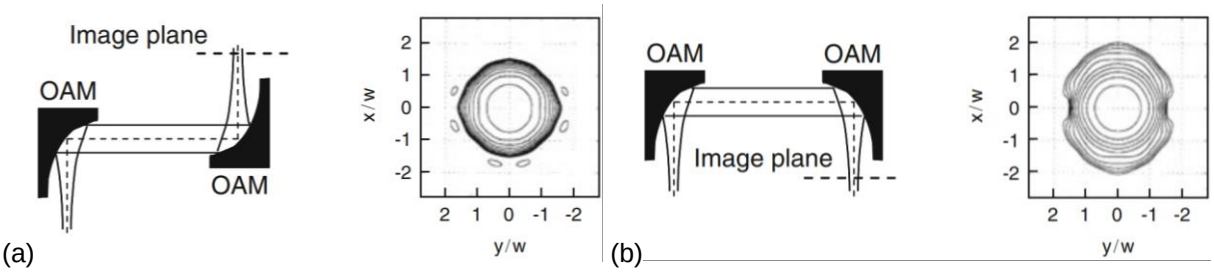

Figure I-20. Two configurations of off-axis ellipsoidal mirrors illuminated with a fundamental Gaussian beam, and their respective measured beam profiles after collimation. Note that in configuration (a) the beam profile in the image plane is more symmetric, because aberrations are corrected by the differently oriented mirrors (adapted from [97]).

Dynamic range of THz-TDS

Lenses and mirrors are usually used to improve the intrinsically low sensitivity of the PCAs. However, one might wonder on the limitations imposed by a change in the classical structure of the TDS system, such as eliminating the focusing lenses and mirrors. For that reason, it is necessary to predict the variation of the characteristics of the systems, and most importantly predict the change of perspective when choosing the materials and objects under test when not relying on the classical configuration. This analysis could be done through the dynamic range of the detected signal. In fact, the dynamic range is measured from the ratio between the generated electric field $E(f)$ and the intrinsic noise of the detector $N(f)$ as follows: [98]

Eq. 6

$$D(f) = \frac{E(f)}{N(f)}$$

The noise floor is normally independent of frequency and corresponds to the spectrum recorded with a completely blocked THz beam path. The origin of this noise is mostly electronic.

When a TDS system is used to measure the spectral response of an object under test, the reduction of the amplitude of the THz wave caused by the object is associated with the spectral features of the object. Generally, the losses associated with the spectral features of the object are frequency dependent and could be quantified using the absorption parameter $\alpha(f)$. For a measured material, the detected THz field using the TDS system is:

Eq. 7

$$E_D(f) = E(f)L\, e^{-\alpha(f)d}$$

Where L is frequency-independent loss that is also independent from the spectral features of the object under test. In order to identify the absorption feature, the modulation of the THz field caused by this absorption line at f_0 must be higher than the noise level of the system as follows:

Eq. 8

$$E(f)Le^{-\alpha d} > N(f)$$

When αd << 1, Eq. 8 yields:

Eq. 9

$$D(f) \approx \frac{E(f)}{N(f)} > \frac{1}{\alpha(f)d}\frac{1}{L}$$

Eq. 9 shows that the detection and analysis of a material using the TDS depends on its thickness, intrinsic frequency-independent losses, and spectral loss in the THz range. As the choice of these parameters for a known dynamic range of the utilized system will enable the retrieval of the THz field through the object and identify spectral features of the target.

In fact, the limits of the measurable absorption coefficient in transmission and reflection configuration TDS systems was successfully quantified [99]. They show that the largest absorption coefficient that can be measured reliably with a given dynamic range is determined by the following equation:

Eq. 10

$$\alpha_{max}(f) = \frac{2}{e}\ln\left(D(f)\frac{4n(f)}{(n(f)+1)^2}\right)$$

With e the thickness of the sample, and n(f) being the frequency dependent refractive index of the material. As the dynamic range of a TDS system decreases for higher frequencies and the absorption coefficient of materials is known to increase with frequency, this relation sets a limit on the effective useful bandwidth for each material to be measured as illustrated in Figure I-21. Using model data in Figure I-21. a, the dynamic range curve is illustrated. α_{max} is calculated from Eq. 10 assuming a thickness e = 1 mm and an index n = 2. The profiles of the absorptions α_1, α_2, and α_3 are commonly found in absorbing materials. For $\alpha_1 > \alpha_2 > \alpha_3$ the falling curve of α_{max} limits the bandwidth BW such that $BW_1 < BW_2 < BW_3$. The measured data confirms this observation by calculating α_{max} for two samples: fused silica (SiO_2) with a thickness e = 3 mm and index n = 2, and ceramic BIN77 (BN: AlN) with thickness e = 2 mm and refractive index n = 2.5. α_{max} is larger for the thinner sample. It is seen that the measured absorption (dark blue for SiO_2 and pink for BN: AIN in Figure I-21.b) cannot be measured beyond their respective α_{max}, and that limits the measurement bandwidth.

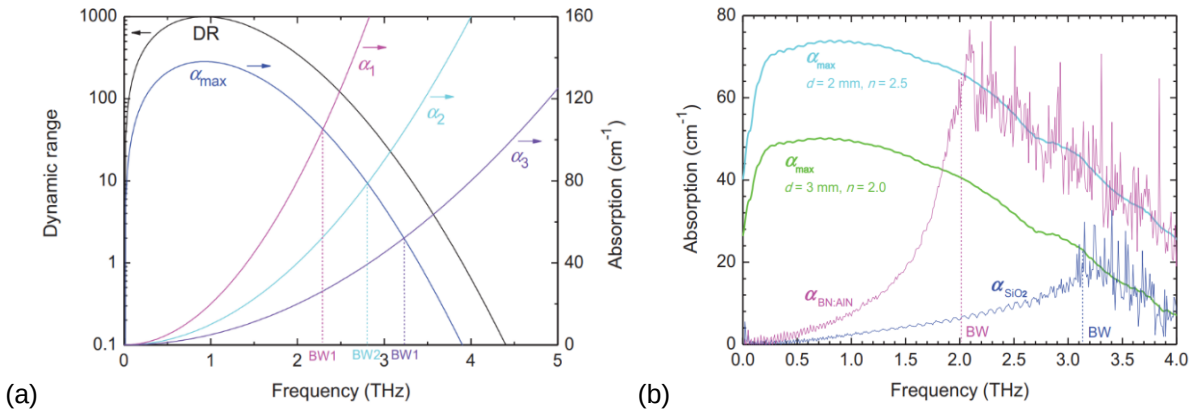

Figure I-21. Relationship between the dynamic range, measurement bandwidth and the absorption coefficient presented using model data in (a) and confirmed using experimental data in (b).

Note that the maximum measurable absorption is inversely proportional to the sample's thickness, meaning that to detect through a highly absorbent material, it is necessary to take it in a form of a thinner sample. In fact, the optimal sample thickness l_{opt} was investigate as a function of the absorption of a sample $\alpha(f)$ (independently from the limitation of the TDS system) and the following relationship was derived [100]:

Eq. 11

$$l_{opt} = \frac{2}{\alpha(f)}$$

Therefore, strongly absorbing material should be prepared as thin samples in order to improve the measurement accuracy as well as the bandwidth as $\alpha(f)$ varies with frequency.

The dynamic range can be improved by reducing random noise in measurement by averaging a series of signals obtained from multiple repeated measurements. The averaging is effective in the time domain, but not in the frequency domain [98]. The averaging effect is depicted in Figure I-22, where the noise floor reduces according to the number of averaged signals, in contrast to a single-shot measurement.

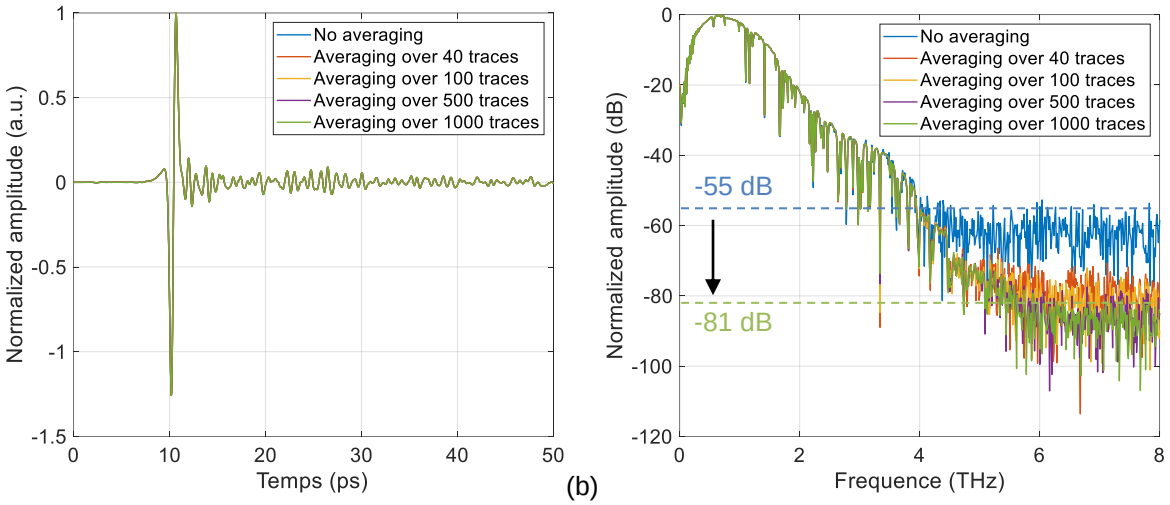

Figure I-22. Evolution of measured THz signal with the number of averaged signals. (a) in time domain and (b) in frequency domain. The signal is measured using the classical configuration of TDS using four focusing lenses.

Averaging over 1000 traces in time domain enhanced the amplitude of the frequency spectrum by 26 dB in dynamic range (Figure I-22.b.), thus expanding the available frequency band from 4 THz without averaging to 5.5 THz with 1000 averages.

The evolution of the measured signal from no averaging to averaging over 40 traces is substantial, resulting in an improvement of the dynamic range of 20 dB. However, increasing the number of traces to 100 or more does not yield the same effect, with only 6 dB improvement in dynamic range when averaging over 1000 traces. Since the averaging process contributes significantly to acquisition time, it is crucial to compromise between the number of averages and the acquisition time in relation to the gained dynamic range and available bandwidth.

The following section will provide details on available imaging possibilities using the TDS system.

I.5. Pulsed terahertz imaging

By far, most of the applications using THz waves can be sorted into the following two categories, spectroscopy, and imaging. If the requirements are a large bandwidth and coherent generation and detection, the chosen system is typically the pulsed THz-TDS.

To generate an image using a TDS system, a three-dimensional scan is necessary, the three dimensions being space (2D) and time scan (1D). The time scanning is executed through a delay line. The 2D space scan can be executed through multiple ways, the most prominent are raster scan imaging and SA imaging approaches, which will be detailed in the following sub-sections.

I.5.1. Raster scanning

Imaging by raster scanning or mechanical scanning is based on translating an object under test in the focal point of a focused THz beam. By translating the object and measuring the transmitted, or reflected, signal at each position, an image can be built pixel-by-pixel (Figure I-23). The resolution of the image is dictated by the size of the focal spot (generally between 1 mm and 0.5 mm). Each pixel of the assembled image contains amplitude and phase information about the scanned area of the object.

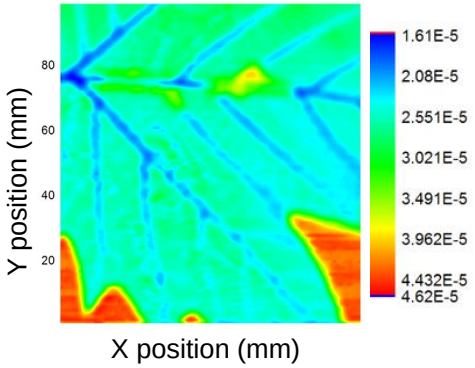

Figure I-23. Result of raster scan imaging of a tree leaf using a focused THz-TDS system (adapted from [101]).

The acquisition time to generate an image through raster scanning depends on the number of pixels and the averaging time of the transmitted signal of each pixel, and the averaging time depends on the speed of the ODU. The step of the mechanical scanning is usually equal to the estimated size of the focused THz beam, which is usually between 1 mm to 0.5 mm. We expect to spend seconds at each position to sufficiently average the acquired signal and generate an image with minimal noise. While some seconds do not seem to be a long acquisition time, when applied on each pixel during imaging, the acquisition time rises exponentially. For instance, accounting for 5s averaging time to average over 40 traces for each pixel, the acquisition time of an image with 50×50 pixels with 0.5 mm resolution (0.5 mm steps) is 3.5 hours. In addition to the time necessary for the mechanical translation platform to scan all the required positions.

A good alignment of the optical elements provides a small illuminating spot, thus resulting in a high-resolution image. However, the size of the spot is limited by the diffraction limit, which is proportional to the wavelength λ of the light used for imaging, and inversely proportional to the diameter of the radiating aperture D:

Eq. 12

$$\Delta \approx \frac{\lambda R}{D}$$

with R the range between the aperture and the object under test.

There are techniques such as near-field imaging for producing images that appear to have resolution higher than the diffraction limit [102]. Although these techniques improve the resolution, they generally come at an enormous amount of complexity and increase of cost. Usually, these techniques are only appropriate for a small subset of imaging problems.

In addition to the lateral resolution, the depth of focus (DOF) is also limited. The DOF is the distance in which the THz beam is appropriately focused before diverging again (Figure I-24) and a tightly focused THz beam that retains its size over a large DOF is highly desirable. The DOF of the focused beam using a standard lens is calculated using the following equation [103]:

Eq. 13

$$DOF = \frac{8\lambda}{\pi}\left(\frac{f}{w}\right)^2$$

With λ the wavelength, f the focal length of the lens and w the radius of the incident beam on the lens. In the case of a lens with a focal length f = 5 cm, a collimated beam with a radius w = 1.75 cm, the theoretical DOF of a TDS may vary from 2 cm at 300 GHz to 1,2 mm at 5 THz. This values of DOF are very limited and could not be overcome using standard lenses.

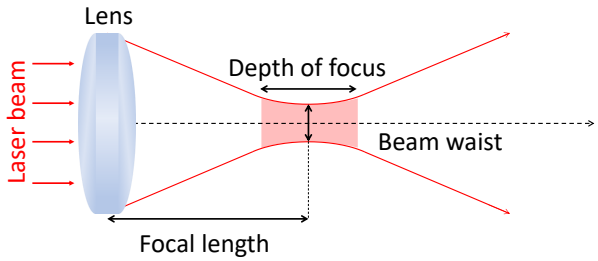

Figure I-24. Illustration of the DOF of a focusing lens.

Complex optical components such as extended DOF diffractive lenses [104] and components called Axions (Figure I-25.) could generate Bessel beams from an incident Gaussian beam in order to extend and significantly improve the DOF [105] [106].

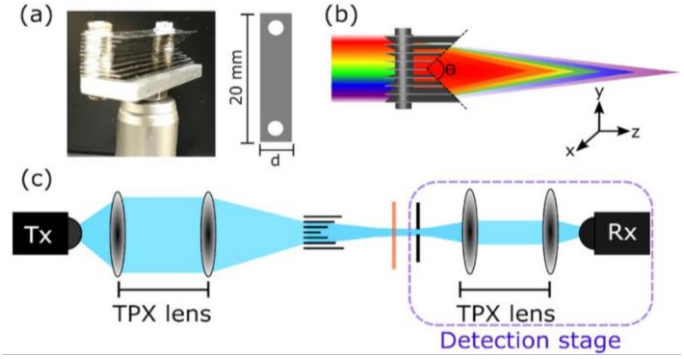

Figure I-25. (a) A triangular-shaped axicon. (b) False color diagram representing the variation of the focal length as a function of frequency. (c) Experimental setup for the investigation of focal depth and cross-section properties of the metallic axicon. The blue regions denote THz light. The sample is represented by the orange line [106].

However, the use of the axions comes with additional constraints such as the secondary lobes generated by focusing the THz beam and additional costs.

To conclude, this section discusses the current predominant method of THz imaging known as raster scanning, highlighting its effectiveness and widespread usage. Raster scanning involves moving the object being imaged incrementally in a lateral (side-to-side) manner to capture each individual pixel of the image. While this technique has proven effective, it does have a limitation: it requires the object under examination to be movable, which might not always be feasible or practical in certain scenarios.

To address this limitation, the proposed solution is the utilization of SA imaging. This technique aims to overcome the need for physical movement of the object by employing a different imaging approach. SA imaging involves using computational methods to create high-resolution images without requiring the object to be moved incrementally. Instead, it leverages signal processing algorithms to combine and synthesize information obtained from different angles or positions, allowing for the creation of detailed images without physical movement of the object.

In the next section, we introduce SA imaging and discuss its state-of-the-art application in the THz range.

I.5.2. Synthetic aperture approach for terahertz imaging

The need for more adaptable systems has led to the necessity of establishing a new approach to THz imaging. By looking at how similar problems were addressed in adjacent frequency bands, SA imaging seems like a noteworthy example of a technique originally developed for radio frequencies but transferred remarkably to the mm-waves and sub-THz region. The transfer to THz region is ongoing as a lot of recent work on the subject has been presented only in the last five years.

I.5.2.1. The concept of synthetic aperture imaging

SA imaging technique was developed originally for radar applications, and it was known more with the name Synthetic Aperture Radar (SAR) imaging. However, for the purposes of avoiding confusion, we will further on use the term SA for Synthetic Aperture, as it was detached long ago from exclusive radar applications and used as an imaging technique in many domains such as the medical domain, security, and safety control, etc.

Historically, SA radar systems were developed for radar imaging in the early 1950s under the sponsorship of U.S. Department of defense mainly for airborne radar applications. Over the years, SA radar has proven to be capable of high-resolution remote sensing, independent of flight attitude and weather as SA radar can select frequencies to avoid signal attenuation caused by the weather or other factors. SA radar imaging has day and night imaging capabilities, as it is active imaging, providing the source of illumination in addition to the detection. The imaging technique have a wide range of applications in outdoor remote sensing [107] and mapping of the surface of the Earth or other planets [108]. SA radar imaging was also used for defense applications [109], oceanography [110] and geology, for example in soil discrimination and subsurface imaging [111].

The basic principle of SA is based on using an antenna mounted on a moving platform (historically airplanes) [112]. As the antenna is translated along the movement trajectory, it transmits EM waves sequentially (Figure I-26). The configuration can be monostatic (use of

one antenna for both emission and detection of the scattered EM radiation) or bistatic (use of two antennas or more for the multi-static case, one for emitting and the other for detecting the radiation). In any case, the scattered waves are detected with meaningful time delays and stored for subsequent processing. The combination of the received signals from different incremental positions builds a virtual aperture that is much larger than the physical antenna used for the scanning, and that is the source of the term “synthetic aperture”.

The combination of the received signals is processed numerically through image reconstruction algorithms. One of the most popular image reconstruction algorithms is back-projection (BP) algorithm [113]. BP is commonly used because of its many benefits such as simple straightforward algorithm and its better performance for 3D imaging, compared to range migration algorithm for example, because it implements the calculations in spatial domain directly without interpolation or spatial FFT operations, which may generate numerical errors [114]. However, BP has been limited by the computational expense. Research on that front has been done and many computational solutions are proposed for executing fast and memory efficient BP algorithm for SA imaging [115], [116], [117].

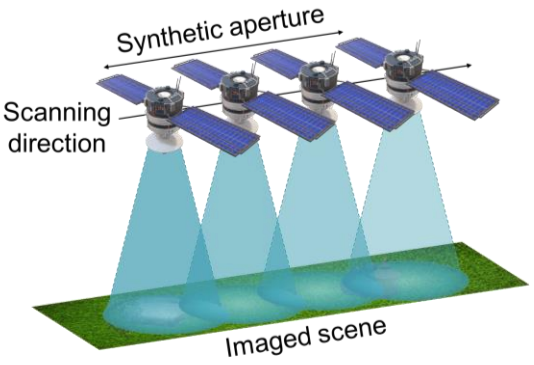

(a)

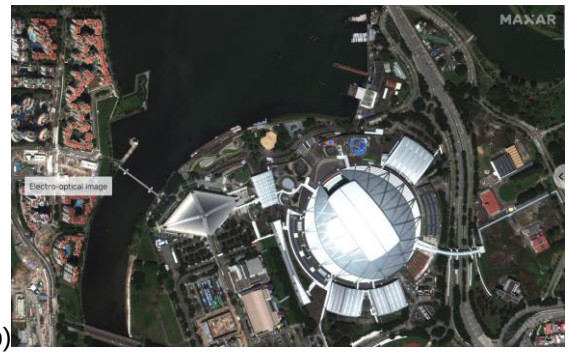

(b)

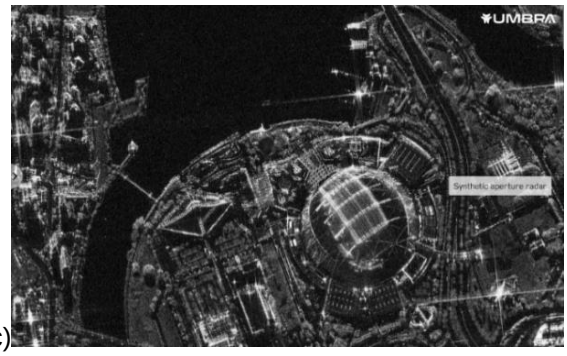

(c)

Figure I-26. (a) Basic principle of far-field SA radar imaging using a satellite. The map of the scanned ground is reconstructed from scattered waves collected from each position of the satellite. (b) Photograph of Singapore National Stadium and (c) its reconstructed image using SA radar with 25 cm resolution cross-range [118].

The spatial resolution of the resulted image is directly related to the ratio of the wavelength λ of the EM wave to the length of the traveled distance D by the mobile antenna [119], [120]:

Eq. 14

$$\delta_{CR} = \frac{\lambda R}{D}$$

with R the range distance between the mobile platform and the imaged scene.

The Field of View (FOV) is related to the wavelength and the size of the incremental steps d taken by the mobile antenna [121]:

Eq. 15

$$FOV = \frac{\lambda R}{d}$$

The movement of the antenna in one direction results in an image with two dimensions: the range direction (or depth) which is perpendicular to the movement direction, and the cross-range direction, which is along the direction of the movement of the antenna. The range resolution is limited by the available bandwidth of the signals used to reconstruct the image, described using the following equation in reflection configuration [119], [120]:

Eq. 16

$$\delta_R = \frac{c}{2B}$$

Using SA approach, the spatial resolution of the image is no longer limited by the aperture of each individual antenna/detector but is limited by the dimension of the virtual array and the antenna pattern, which has a certain directivity. In fact, a decrease in antenna directivity acts like a spatial filter, which also limits resolution. As a result, one can get high spatial resolution with small imaging elements.

In the following section, we provide an overview of the state-of-the-art THz-SA imaging before introducing our unique approach.

I.5.2.2. Terahertz synthetic aperture imaging

Adapting SA imaging for THz applications began as early as 2001 [122] when broad bandwidth imaging of cylindrical targets at THz frequencies using Inverse SA (known as ISAR) technique was demonstrated (Figure I-27). It is called inverse SA because the SA is created by moving the object under test rather than moving the antennas.

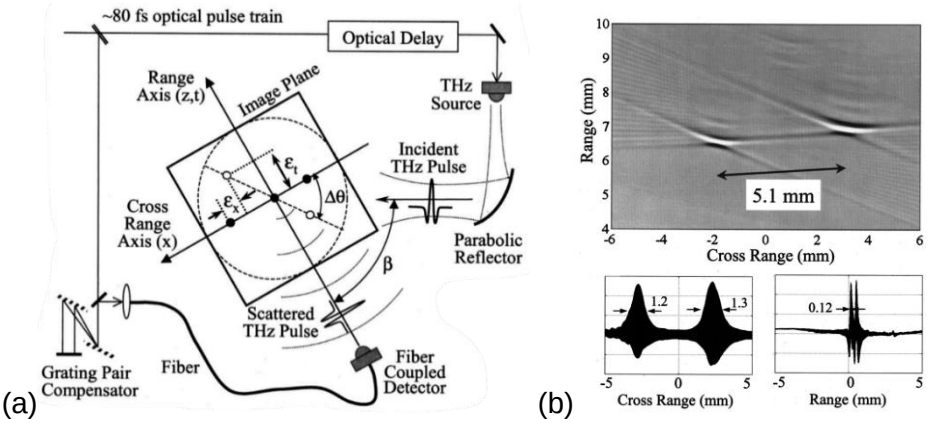

Figure I-27. (a) THz imaging setup. The emitter is illuminating the rotating object under test and the scattered pulse is detected by the detector at an angle β from the emitter. (b) Reconstructed image obtained from the data scattered from two metallic cylinders with 0.5 mm diameter. The figures show the reconstructed image peaks projected onto the cross-range axis and range axis. The projection shows a 10 times difference in resolution between range and cross-range resolutions (adapted from [122]).

The experiment employed a TDS system in a reflection configuration, with the object under test being rotated on a platform to capture signals reflected from all angles. The range

resolution achieved in this demonstration, determined by the THz pulse bandwidth ranging from 0.2 to 1.5 THz, was 0.12 mm, while the cross-range resolution was 1.2 mm.

After the first demonstration of SA imaging in THz domain using a TDS system, multiple reports have followed demonstrating SA imaging using electronic antennas and electronic-based devices that were able to generate signals in the THz range. A study reported utilizing a frequency modulated continuous wave (FMCW) radar operating at 600 GHz [123]. The experimental results demonstrated sub-centimeter resolution in all three spatial dimensions. The FMCW radar transceiver is built on a back end of commercial microwave components with a front-end of custom designed frequency multipliers and mixers. The optics consists of a 40 cm diameter ellipsoidal primary reflector with a 4 m focal length. Although this work successfully pushed the boundaries of microwave-based systems, it still fell short of fully capitalizing the immense potential of THz waves. Notably, the limitation of the system in terms of frequency bandwidth restricted the range resolution of the reconstructed image. To address this limitation, a stepped-frequency FMCW radar was developed, capable of generating a broader bandwidth ranging from 140 to 220 GHz. This advancement was employed to demonstrate a three-dimensional THz imaging system [124]. However, it is worth mentioning that the system's central frequency remained around 200 GHz, which is relatively low when considering the THz range.

Vector Network Analyzer (VNA) based electronic systems are also used for SA imaging in the THz rang. In 2020, a system employing a rail-based SA technique was demonstrated in the 220 GHz to 355 GHz and 500 GHz to 750 GHz bands with sub-millimeter resolution [125]. In the demonstrated setup (Figure I-28.a), the object is inclined with respect to the transmitter (horn antenna) and is scanned in azimuth using a motorized linear stage. The single-transceiver system is based on a frequency extender module coupled with a VNA to reach higher frequencies. The reflected data is processed according to an image reconstruction algorithm. The image of two screws behind a thick layer of a polymer was reconstructed (Figure I-28.b and .c).

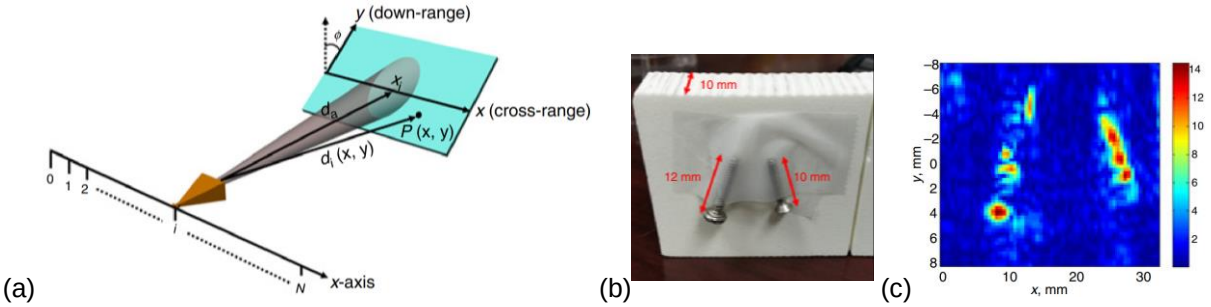

Figure I-28. (a) Rail-based SA geometry. (b) Object of demonstration: two metallic screws, one is 12 mm long and has a 2.8 mm diameter, and the second is 10 mm long and has 2 mm in diameter. The screws were taped a 10 mm thick Ecco stock Lok substrate (ε_r = 1.7). (c) THz SAR reconstructed image after thresholding (adapted from [125]).

In 2021, the electronic transceiver module-based system was able to achieve the 1.5 THz limit [126]. The imaging of a metallic sample was demonstrated at 1.5 THz using a system based on a horn antenna attached to a frequency extender and a VNA (Figure I-29). The object under test was attached to a mobile mechanical platform and moved in horizontal and vertical directions in order to create the SA, while the horn antenna is fixed. The image was reconstructed according to an image reconstruction algorithm, from reflected signals at the surface of the object under test.

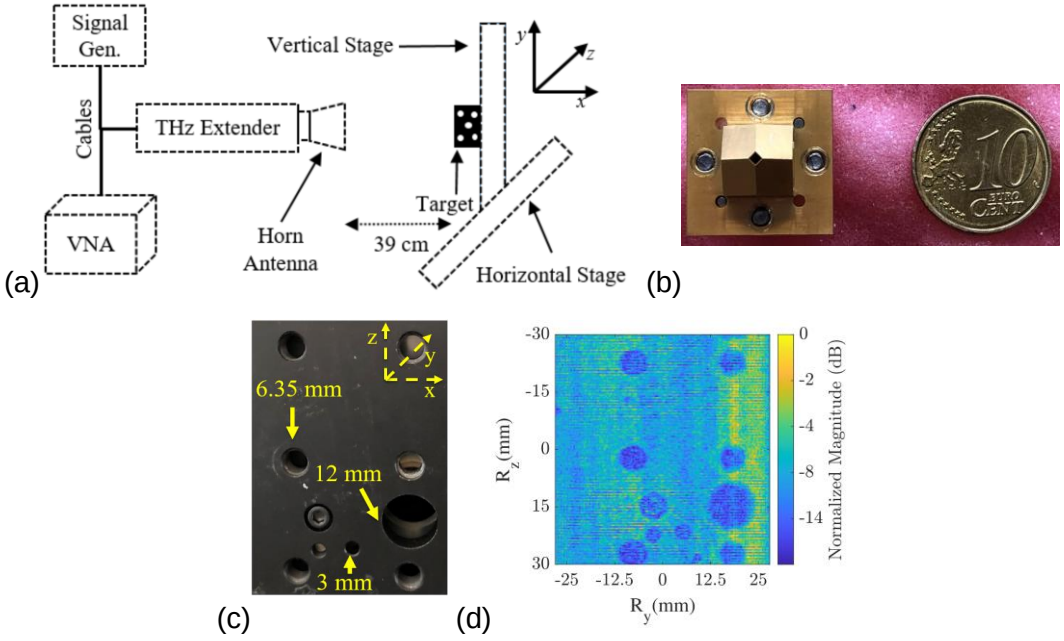

Figure I-29. (a) SA measurement setup. (b) The horn antenna next to 10 cent euro coin for reference. (c) Imaged object. (d) SA reconstructed image between 1.1 THz and 1.5 THz. (adapted from [126])

Nevertheless, these electronic-based systems encounter a common challenge, which is the necessity to physically move the object to create a SA. To move the antenna heads, extenders, and VNAs has proven to be complex, requiring ample space and meticulous technical considerations. Despite efforts to develop compact extenders, such as micro models weighing 1.8 kg and having lengths of 21 cm, employing this technique entails various other elements that can complicate its application at high frequencies. Factors like cable length and the precision of the mobile stage in relation to phase error can collectively present obstacles for users of the technology. Furthermore, although frequency extenders provide access to higher frequencies, the bandwidth remains limited to less than 0.4 THz. Consequently, a different frequency extender must be employed to shift from a frequency band to another, posing budgetary challenges. Moreover, each frequency extender requires a compatible antenna to access the desired frequency range. All of these factors indicate the need for an alternative approach that simplifies the application of the SA imaging technique in the THz range and enables access to frequencies exceeding 1.5 THz.

In order to achieve this goal, research has focused on utilizing opto-electronic systems for SA applications. A THz photomixing system has been employed to demonstrate THz image reconstruction [127]. In the study, a CW THz generation and detection method were used in the near-field region of the antennas to image a point source by compensating for the phase of the spherical incident wave. While successful reconstruction of a point source image was achieved at frequencies of 535 GHz and 1.6 THz, the CW system's limited bandwidth hinders range resolution capabilities.

Using a TDS system (Picometrix T-Ray 4000), 3D imaging was demonstrated in a reflection monostatic configuration [128]. The monostatic configuration was achieved by creating a virtual source using a lens. The lens is used to focus the emitted and reflected THz wave to and from the object under test. The object under test is placed bellow the focal point of the lens thus creating a single “monostatic” source/detector (Figure I-30.a.). The setup containing the emitter, detector and lens are all mobilized to create the SA, while the object under test stays fixed. A wide bandwidth of 900 GHz, spanning from 0.3 to 1.2 THz, was effectively

accessed. This extensive frequency range facilitated the reconstruction of detailed 3D images, including those of a ribbon electronic connector and various other objects. The broadband nature of the frequency band played a crucial role in achieving an impressive range resolution, enabling visualization at multiple depths within the object (Figure I-30.c. and .d).

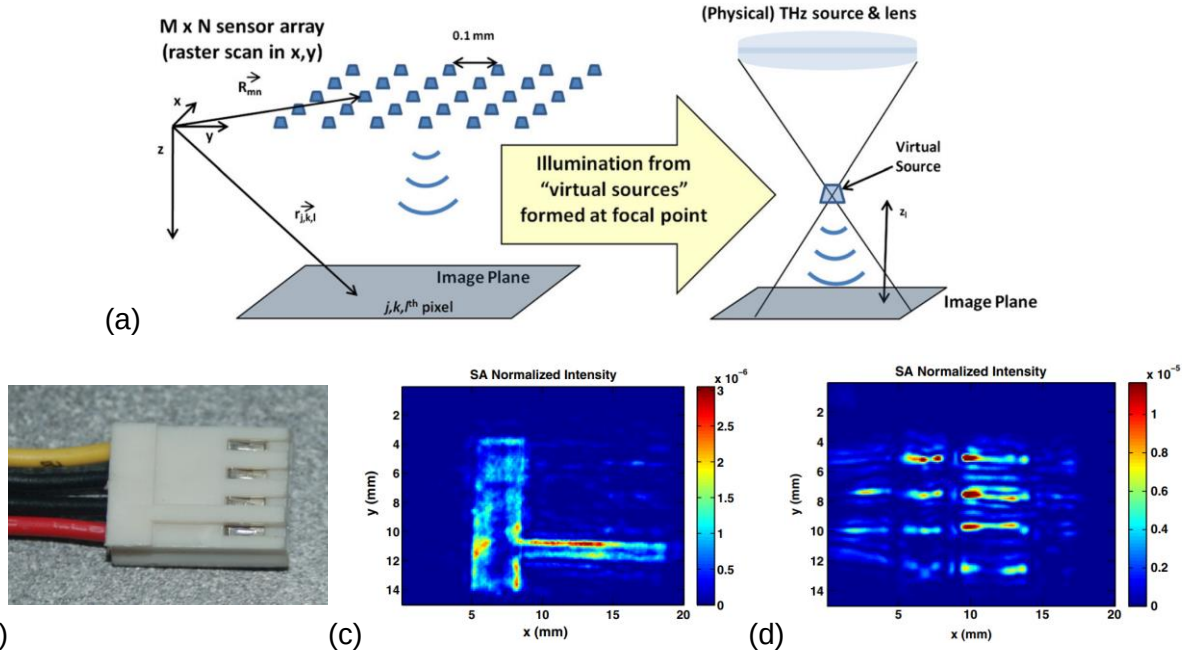

(a) (b) (c) (d)

Figure I-30. (a) 2D Synthetic array implemented with a Picometrix T-Ray 4000 pulsed system. SA was created by mobilizing the antennas and the lens to scan the fixed object under test. (b) Optical image of ribbon cable (c) SA image of ribbon plug. Focusing depth is 10.06 mm. (d) SA image of ribbon plug focused at 12.39 mm. Four hidden metal traces appear bright due to high reflectivity and sharp edges. The images were reconstructed between 0.4 and 1.2 THz (adapted from [128]).

After demonstrating the capabilities of 3D broadband THz SA imaging, the integration of 3D imaging techniques with chemical mapping was explored. Using the same setup in Figure I-30.a., along with a correlation treatment, the goal was to generate spectral images. The primary objective of a spectral image was to simultaneously depict the scene and differential substances by using false color representation to indicate the presence of specific chemical signatures. To demonstrate these findings, a pellet made with lactose and high-density polyethylene (Figure I-31.a) was scanned in reflection configuration [129]. The presented results showed 3D spectral surface profiling. Notably, in Figure I-31.b, the two sides of the pellet were clearly distinguishable. These results enabled the identification of the two distinct substances present in the pellet. It is important to note that this approach does not provide a comprehensive characterization of the substances but serves as a spectral imaging method that offers preliminary differentiation between different elements.

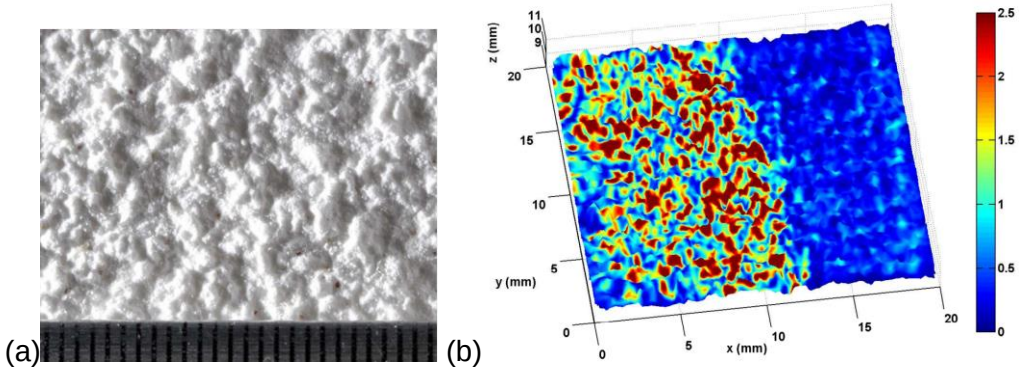

Figure I-31. (a) Pellet constructed with part lactose and part high-density polyethylene. (b) Spectral surface profile of a square section of the two-part pellet. The color scale was created using correlation processing, normalized by its standard deviation [129].

Another approach to THz SA imaging was demonstrated using a TDS system in reflection configuration, with a fixed angle between the antennas (Figure I-32). No external lenses were needed, and the approach demonstrated the possibility of reconstructing images of a reflective rotating object [130].

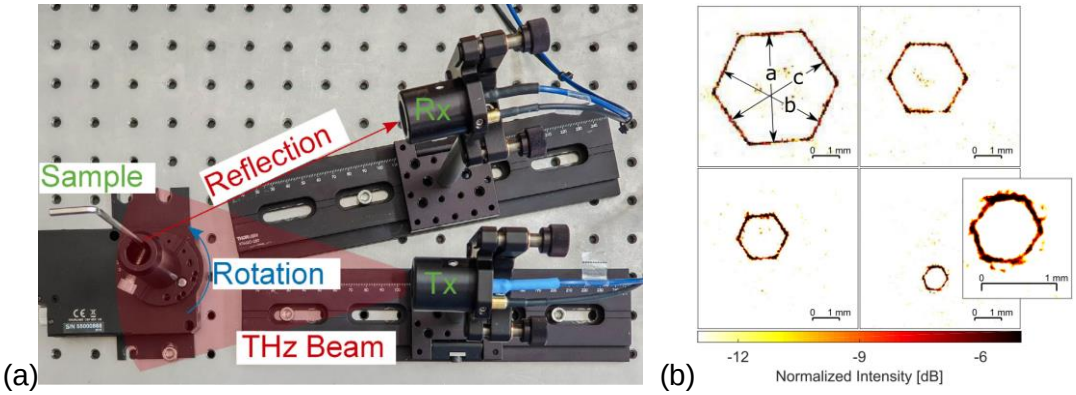

Figure I-32. (a) Top view of the 2D imaging measurement setup. The receiver and transmitter antennas are stationary while the sample is positioned on a rotation unit allowing a 360° circular scan of the sample. Images of hex-wrenches of different diameters: 4 mm (top left), 2.5 mm (top right), 1.5 mm (bottom left) and 750 µm (bottom right) [130].

Building upon that work, the researchers adapted the technique in 2023 for 3D imaging by creating a synthetic half-cylinder array of phased coherent apertures [131]. To create the cylindrical SA, an object under test is positioned on a rotation stage and a linear moving platform in the z-direction (Figure I-33), which simulates the movement of the detector and emitter. The rotational stage rotates from 0◦ to θ_{sa} resulting in a partial cylindrical SA. The image of two coins was reconstructed from reflected signals and a 2D projection in the x-y-plane demonstrates the 3D capabilities of the proposed approach.

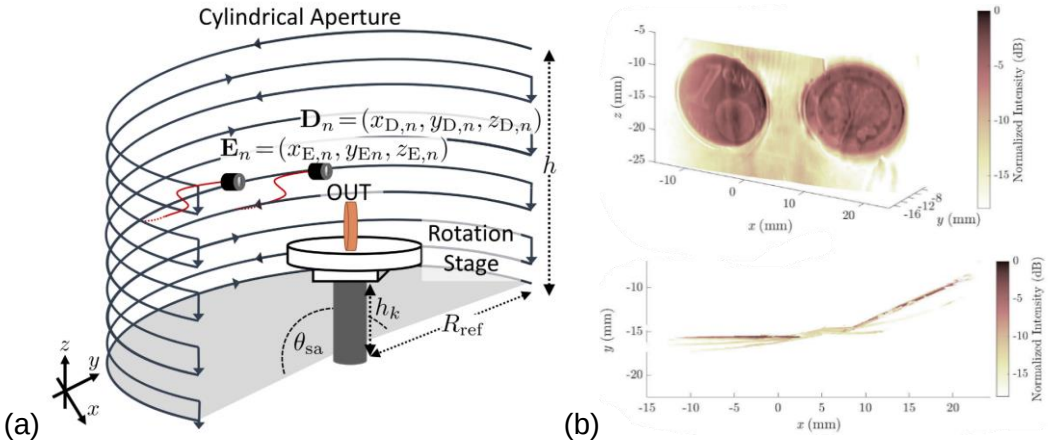

Figure I-33. (a) 3D cylindrical SA. (b) Reconstructed image of the two 1-euro cent coins inside a paper envelope. A 2D projection of the volume in the x-y-plane is shown demonstrating the different orientations and position of the two coins and the envelope in the x-y-plane (adapted from [131]).

I.5.2.3. Real PCA arrays for fast THz imaging

The results from literature demonstrate the efficiency of SA imaging in the THz range using electronic and optoelectronic-based systems. Nonetheless, the scanning time to create a synthetic array is a disadvantage of the method. In fact, just like raster scan, the averaging of the temporal signal at each position of the antenna results in hours of acquisition time. Thus, SA imaging is providing a useful different imaging configuration, however, it does not cut back the acquisition time. Consequently, in order to tackle the limitation of acquisition time, researchers have grown an interest in real photoconductive arrays. Some examples of successfully designed PCA arrays can be found in literature. One of the first proposed PCA arrays is an array of 16 dipole PCAs [132]. For the excitation of the whole array, a micro lens array with 16 lenses was used to create one spot laser for each antenna from a collimated large area optical beam (Figure I-34).

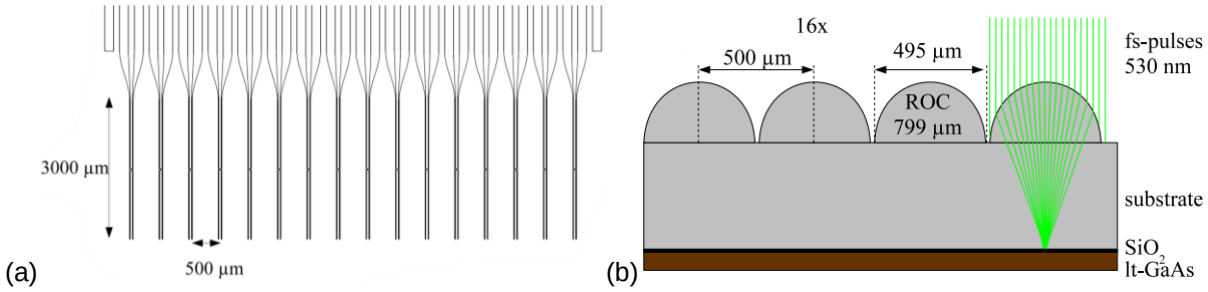

Figure I-34. (a) 16 channel photoconductive switch array. (b) Schematic of micro-lens array attached to the photoconductive switch array (Adapted from [132]).

The lens spacing was designed to match the antenna spacing. The micro-lens array is attached to the photoconductive antenna using optical adhesive. The resulting photocurrent of each photoconductive antenna is independently amplified by a multichannel lock-in amplifier (Figure I-35).

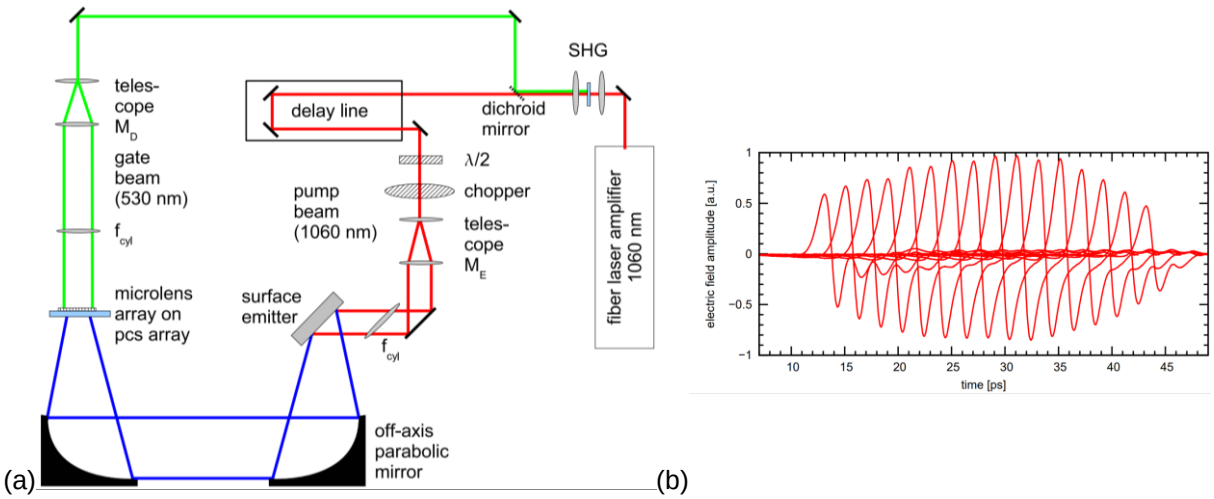

Figure I-35. (a) Schematic setup of the THz system for multichannel detection using an array of photoconductive switches. (b) Simultaneous measurement of 16 ultrashort THz pulses. Each pulse was shifted in time for 2 ps for a better overview. (Adapted from [132]).

The micro-lens eliminates the need of mechanical scanning thus giving the advantage of an instantaneous multiple acquisition. However, the collimated optical beam must have the size of the array in order to reach all antennas of the arrays. Moreover, due to imperfections, the portion of the unfocused laser power exciting zones far from the photoconductive gap of the antennas result in an increase in photocurrent leading to screening effects and a higher noise level. That is why, a spatial light modulator (SLM) was introduced instead of the micro-lens configuration to provide a more efficient optical excitation of the gap of each PCA of the array. An SLM is a transmissive or reflective device that's used to spatially modulate the amplitude and/or phase of an optical wave front in two dimensions. In the case of a PCA array, the SLM is used to modulate the laser beam to illuminate the gap of each element of the array simultaneously or successively. Algorithms are available in order to create the desired pattern to illuminate the desired locations on the array simultaneously. This allows for a non-mechanic fast optical steering with the possibility of using multiple focal spots to interrogate multiple antennas, and thus improving the acquisition time. An example using the SLM is proposed with an array containing 64 dipole antennas [133] (Figure I-36.a. and .b.). In order to optimize the wiring situation of the demonstrated component and to keep the cost at a reasonable amount, each row of 8 antennas is attached to one photocurrent amplifier creating 8 detection channels and each of the channels corresponds to a row of 8 PCA elements Figure I-36.c. The SLM is used to create a multifocal spot to interrogate all 8 channels simultaneously. The measured photocurrent from the 8 channels of the array was amplified using 8 dedicated low-noise transimpedance amplifiers. The SLM steers the optical beam with a rate of 60 Hz to scan each antenna of each row. Thus, speeding up the acquisition process and simplifying the on-ship wiring.

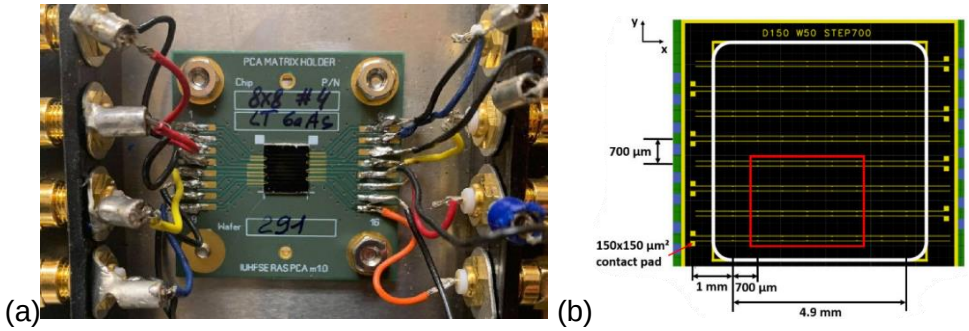

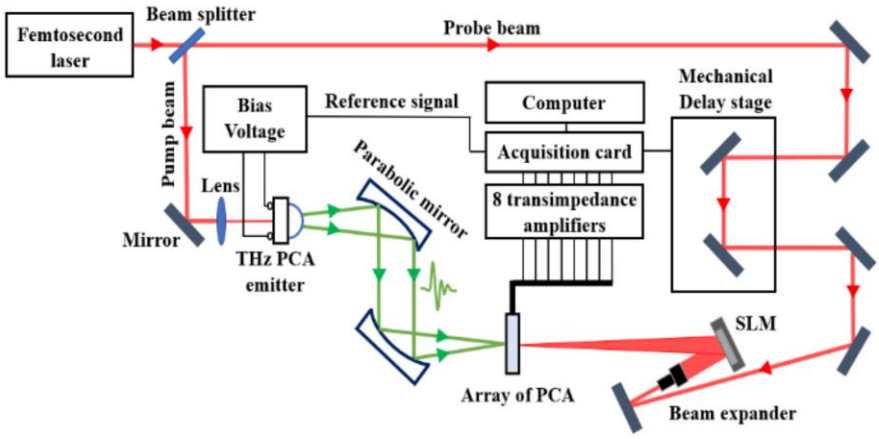

(c)

Figure I-36. PCA detector array for THz time-domain imaging system. (a) Photograph of the PCA array detector mounted on a printed circuit board (PCB). (b) Schematic of the 8×8 PCA array with dimension specifications. (c) Schematic of the THz time-domain system for characterizing the PCA Array. A spatial light modulator was used for focusing and steering the femtosecond laser beam on 8 PCAs of the Array simultaneously. (Adapted from [133]).

However, these proposed real photoconductive arrays were not demonstrated in the context of SA imaging. It was rather demonstrated in the context of pixel-by-pixel acquisition, mimicking the results of raster scanning. Figure I-37 shows the result of imaging a “binary” object made of metal and paper using the 8×8 array presented above, in transmission configuration. The resulted image shows a blue part where the waves were blocked by the metal and the yellow side is where the transmission of the THz wave was higher. However, the resulted image has 64 pixels as each antenna of the array was used to capture one pixel.

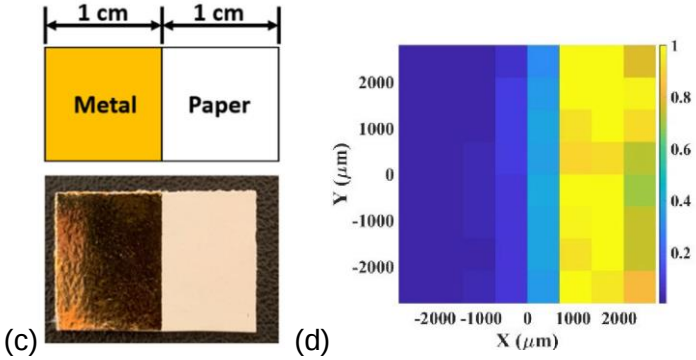

(c) (d)

Figure I-37. (c) Schematic and photograph of the binary amplitude mask which is fabricated using hot stamping technique. (d) Relative intensity image of the THz time domain pulse [133].

An on-chip real array of PCAs is an interesting prospect for real-time THz coherent imaging based on SA approach. Using a real array, the SA becomes a “real aperture”, but the numerical image reconstruction process will remain the same. The array could serve for either generation or detection of THz waves. For instantaneous generation, each PCA of an array is connected to a DC voltage. An SLM would modulate the optical beam into multiple beams in order to illuminate all antennas at once. For instantaneous detection, each row of the array would be connected to an amplifier and an SLM would scan one element of each row simultaneously. An array of emitters provides faster acquisition process because the configuration does not require any mechanical scanning, in contrast to the detection array configuration, where a mechanical scan is needed to adapt to the limited number of photocurrent amplifiers. In both

cases, the acquired data will be processed according to an image reconstruction algorithm to generate the image of the object under test.

The on-chip antenna array, illuminated through free space laser propagation modulated using an SLM, is an available option in the case of PCA arrays made with substrate with a bandgap that corresponds to around 800 nm laser excitation. However, for fiber coupled PCAs that has to be illuminated with a laser beam with a wavelength of 1550 nm, each antenna should be fiber coupled and connected to a photocurrent amplifier in order to acquire each THz signal independently from each antenna. This configuration achieves real-time acquisition, as the data acquisition is instantaneous for all antennas of the arrays and there is no need for an SLM to steer the antennas of the array. The acquisition time will only depend on the Optical Delay Unit (ODU) time. In addition to that, the fiber coupled array provides more flexibility. In fact, a detached antenna array is a more practical proposition, in contrast to on-chip antennas. The antennas constituting the array allow a flexibility in the size and separation between the antennas, which will provide the possibility to control the performance of the array, notably resolution and FOV. An array of transmitting antennas is more practical than an array of detectors. In fact, an array of detectors is the priciest configuration as each antenna has to have its own transimpedance amplifier in order to execute the simultaneous acquisition. Multi-channel, multi-frequency lock-in amplifiers can be used to replace the individual lock-in amplifiers required for each antenna and using software to decompose the signal input from the channels [134]. However, an experimental demonstration of a multi-channel multi-frequency lock-in amplifier in the THz range has yet to be available.

We will focus solely on utilizing 'synthetic' arrays in our work. Nonetheless, we address the challenge of acquisition time through alternative methods instead of creating an actual PCA array. We aim to accelerate the process by building on SA imaging and integrating sparse sampling. Although we do not anticipate achieving real-time imaging through sparse sampling, our objective is to decrease the time needed to scan an object under test. In the following section, we discuss forms of sparse sampling and explore its potential relevance to SA-THz imaging.

I.5.3. Sparse synthetic aperture imaging

Due to the increasing demand for high-resolution images across large fields of view, SA radar imaging has faced challenges associated with the growing amount of data. In 3D mmW SA imaging, the range and cross range resolutions depend on the synthesized planar aperture and the bandwidth of the transmitted signal, respectively. However, traditional imaging algorithms based on Fourier transforms, such as the range-Doppler (RD) algorithm [135] and range migration algorithm (RMA) [136], require subwavelength spatial sampling, leading to a high cost of signal acquisition. To address this issue, extensive research has been conducted on sparse imaging technology.

One popular technique in the field of sparse imaging is Compressed Sensing (CS). CS is a signal processing technique that efficiently acquires and reconstructs a signal by exploiting its sparsity. It leverages the principle that a signal can be recovered from far fewer acquisitions than dictated by the Nyquist-Shannon sampling theorem through an optimization procedure. In the context of THz imaging, CS provides a partial solution to significant challenges, including reducing image acquisition time. By using CS for THz imaging, a much smaller number of measurements should be acquired compared to the number of pixels in the reconstructed

image, which is not the case for full sampling where the number of samplings is the same as the number of pixels of the image.

A simple CS system, as shown in Figure I-38, can be employed to scan through an object and reconstruct its image. The setup consists of a THz transmitter and receiver, a planar screen with a random pattern of blocking pixels, and two lenses. The THz wave passes through the object, the screen illuminates the object in a pseudo-random but known manners, and the collected wave is then received. The pixelated screen acts as an optical filter, with "pixels" representing zeros and ones in the compressed sensing system's matrix. For each filter, the beam focus on a single point, providing one sample measurement. Multiple measurements using different masks are combined to reconstruct a reliable image of the object under test, enabling information gathering with a lower number of measurements compared to raster scanning.

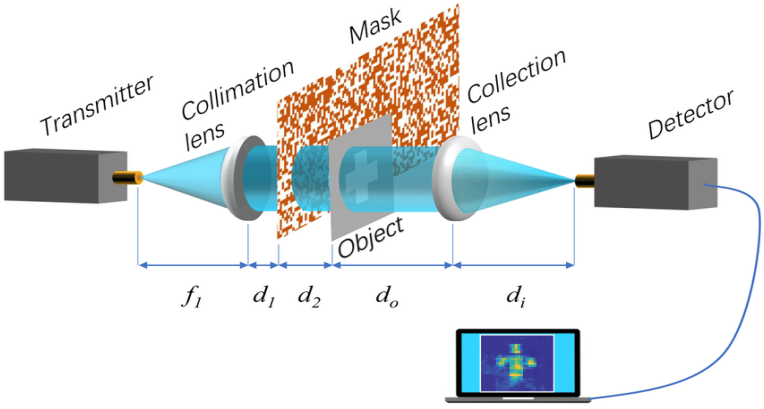

Figure I-38. Scheme architecture of THz CS imaging system [137].

While CS offers significant time savings by eliminating mechanical scanning, one challenge is how to switch between masks. Initial demonstrations of THz CS utilized manually constructed metal masks, resulting in slow image acquisition [138]. Subsequent techniques involved rotating masks, providing an imaging speed equivalent to a frame rate of 10 frames per second. [139]. However, this approach requires synchronization of emission, detection, and mask positioning for applying the CS algorithm. More sophisticated approaches have been developed, such as spatially distributed photoexcitation of charge carrier density in a semiconductor wafer or electronically programmable metamaterial masks.[140]. Nevertheless, these masks increase the size, complexity, and cost of the THz imaging setup. The performance of the CS method is still dependent on the design of the measurement mask, and accurate matching between the sparse basis and the target location is crucial for optimal image reconstruction.

Another approach to sparse sampling involves using a less dense SA antenna array to reconstruct a 3D image of the object under test. This approach eliminates random or targeted elements from a linear 2D array, resulting in a configuration with significantly fewer antennas than a fully dense array. Extensive research in the radar imaging and medical domains has been conducted on optimizing the sparse distribution of antennas, considering the minimum number of antennas required for reliable reconstruction [141]. The distribution of sparse elements also plays a role, as it affects the peak side lobe level (PSLL). The PSLL is the ratio, usually expressed in dB, of the amplitude at the peak of the main lobe to the amplitude at the peak of a side lobe, which is an important criterion for evaluating array performance that should ideally be minimized [142]. Genetic algorithms (GA) and modified genetic algorithms (MGA)

are widely employed to optimize sparse arrays and determine the optimum arrangement of sparsely spaced elements to achieve the lowest achievable PSLL [143] [144]. In the THz range, sparse arrays were explored in the Multiple Input Multiple Output (MIMO) configuration (Figure I-39) where, as the name indicates, multiple antennas are used for emission and multiple antennas are positioned for detection but distributed sparsely across the imaging plane [145], [146], [147]. The figure below is an example of an imaging MIMO sparse array geometry. The instruments used in the experiments mainly include a 2D mechanical scanner and a VNA [148]. To obtain the experimental data collected by a scanning 1D MIMO array, a pair of transceiver antennas are, respectively, installed on two independent horizontal tracks in the 2D scanner, and together scan along the vertical track. Through mechanical scanning point by point in a uniform pattern, the equivalent sparse array can be realized, and at the same time the VNA is used to record the echo data at different positions. An experimental confirmation to verify the performance of the MIMO array is provided in Figure I-39.d.

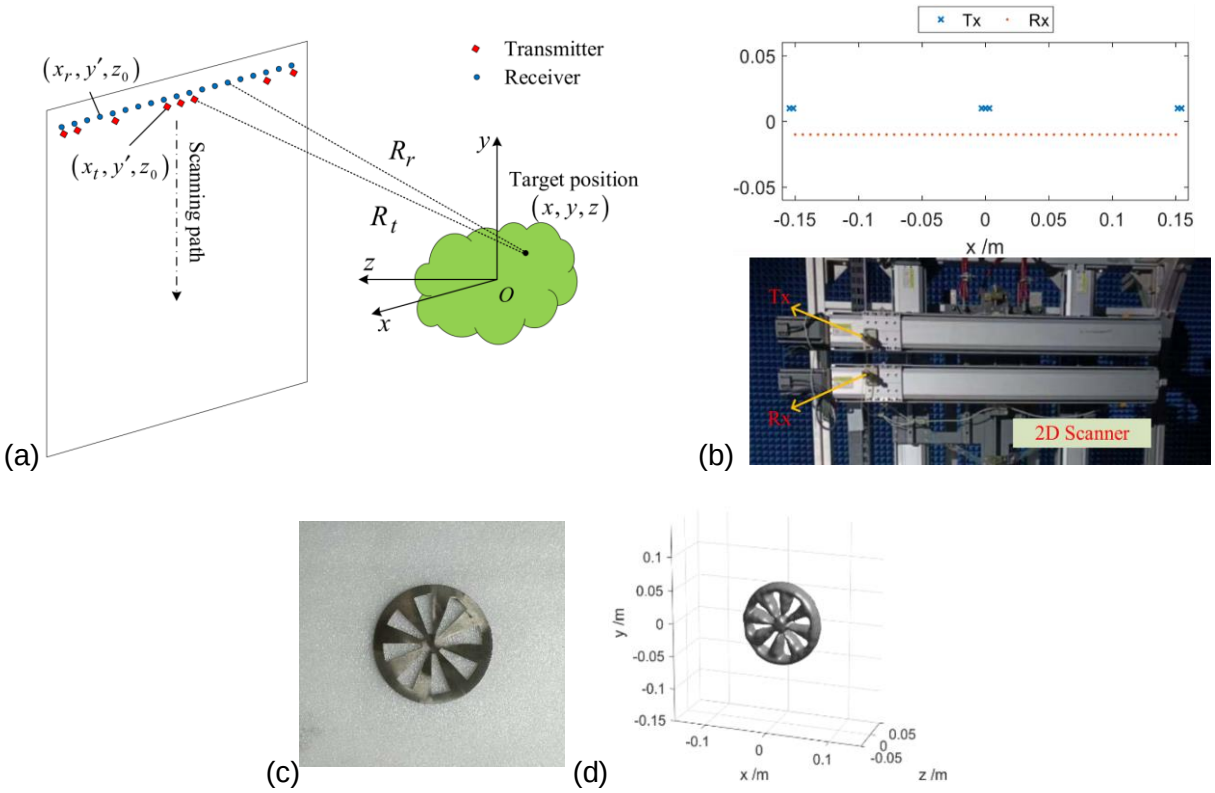

Figure I-39. Example of an imaging MIMO sparse array geometry. (a) Schematic of 1D MIMO sparse array imaging geometry and coordinate definitions. (b) MIMO array configuration used in an experimental demonstration, executed with the photographed experimental setup. (c) Photograph of a metallic object under test. (d) Experimental imaging result of the object. The image is reconstructed using the BP algorithm. [148].

In our work, we will be more interested in a sparse configuration resembling the Single Input Multiple Output (SIMO) approach where only one detector is used in contrast to multiple sparsely distributed synthetic PCA emitters.

After establishing THz imaging, the following section will offer insights and essential information regarding THz spectroscopy.

I.5.4. Terahertz spectroscopy

While microwave spectroscopy had its own applications, the drive for higher frequencies was inevitable in order to observe fundamental elements which have a strong presence at higher frequencies. The strong interaction of the THz waves with these small but fundamental molecules, that are also pervasive in many physical and chemical systems, have led to a number of important applications.

THz radiation, which corresponds to the wavelengths from 30 µm to 1 mm, has photons with energy varying from 0.42 to 41.5 meV and a temperature scaling from 5 K to 500 K. The low photon energy allows probing the molecular vibrations with the given level of energy without losing electrons. This safe and un-ionizing vibration results in changes on the level of the photon that can be quantified. These quantifiable changes reflect the nature of the material as they are unique to each material, which makes an interesting way of identifying materials through their unique fingerprint in the THz range.

With the growing recognition and interest in THz spectroscopy, significant advancements have been made in THz sources and detectors, and the TDS system is one of the most used systems now days for THz spectroscopy. The TDS system offers a coherent detection, which is the access to amplitude and phase, as described in the previous section, which is necessary for the extraction of a material's characteristics. This is a significant advantage of TDS compared to CW THz measurements and infrared and visible broadband spectroscopy.

Figure I-40.a. shows a schematic diagram of the TDS spectroscopy experiment in transmission configuration. Each time the pulse encounters an interface separating two materials of different refractive index, it splits in two, with a reflected and a transmitted part.

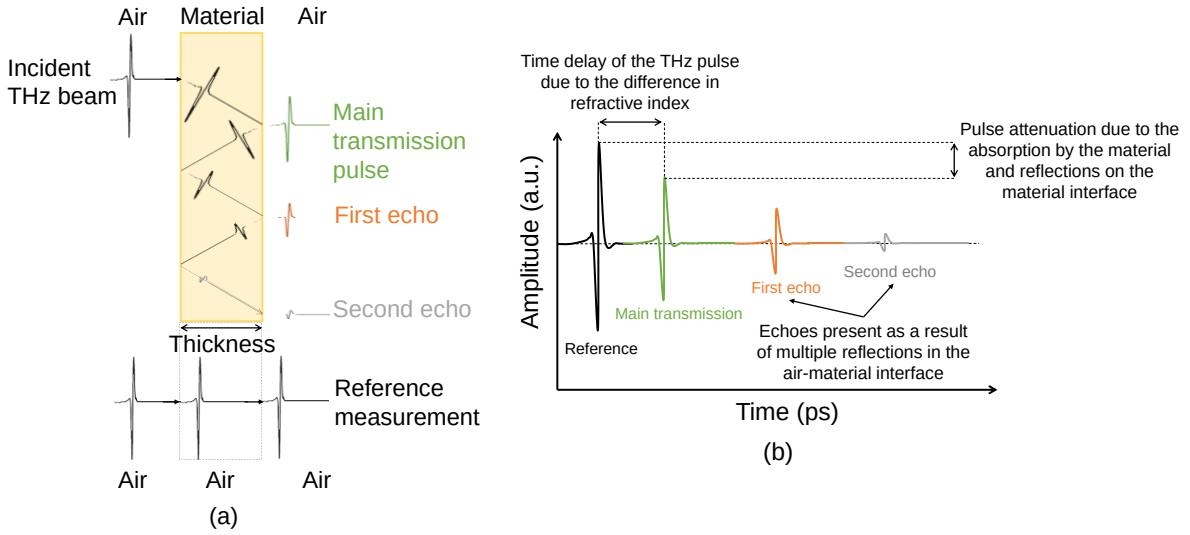

Figure I-40. Principle of THz spectroscopy. (a) The propagation of a THz incident pulse into a material and the detection of the transmitted pulse with its echoes. (b) Detected temporal THz pulse of a reference measurement and the transmitted pulse through the material showcasing the effect of the propagation in different media on the THz pulse.

In Figure I-40.b., the measurement after interaction with the sample may contain several time-shifted pulses of different amplitudes: the first pulse corresponds to direct transmission through the sample, while subsequent pulses are echoes from reflections at the air-material interfaces. The time difference between the pulse measured in the absence of a sample and the one measured with sample is related to the difference in the refractive index between the air and

the sample. The decrease in amplitude is related to both the reflection coefficients at the interfaces and to the absorption of the wave within the sample under test. The useful frequency band for the measurement is determined not only by that of the reference spectrum, but above all by that of the spectrum in the presence of the sample to be characterized, which is limited because the sample under test absorbs the waves and therefore degrades the signal-to-noise ratio. The transmission-based arrangement is very well suited to extracting parameters from transparent materials such as gases or polymers. For solid materials that are too absorbent, or have thicknesses that are too thick, it might be more adapted to carry out the experiment in reflection configuration rather than transmission.

Having the experimental value of the frequency-domain transfer function, the spectral properties of the sample, i.e., the refractive index and absorption coefficient, can be determined from the magnitude $\rho(f)$ and phase $\varphi(f)$ of the spectral ratio using the following equations:

Eq. 17

$$n(f) = 1 + c\frac{\varphi(f)}{2\pi e f}$$

Eq. 18

$$\alpha(f) = \frac{4\pi f}{c}\kappa(f)$$

Eq. 19

$$\text{With } \kappa(f) = -\frac{c}{4\pi f e}\ln\big(\tau(f)\rho(f)\big)$$

Eq. 20

$$\text{And } \tau(f) = 1 - \frac{(n(f)-1)^2}{(n(f)+1)^2}$$

The analytical equations of the refractive index and absorption coefficient are frequency dependent and deliver information only on the scanned region, which is the small spot illuminated with the focused THz beam of the TDS system.

Like any experimental measurement, uncertainties may occur and impact the measured material characteristics. Uncertainties in the determination of material properties can come from a variety of sources, including geometrical errors such as the lack of parallelism the faces of the sample and sample thickness measurement uncertainties, the optical quality of the surface of the sample faces, or sample inhomogeneity leading to diffraction and scattering. Sources of uncertainty might also be relating to the experimental setup such as problems of convergence and shaping of the THz beam and the lack of reproducibility in the measurement of the temporal profile of the field.

The error in determining the material's optical parameters is the sum of these different contributions. Accuracy in determining optical indices can range from 10% to 0.1% for the refractive index, and less than 1 cm^{-1} for the absorption value. Measurement of the absorption coefficient is also limited by the measurement dynamic range. It should be noted that the extraction procedure assumes a homogeneous sample with parallel faces. In the case of heterogeneous materials such as tissues, scattering and diffraction due to inhomogeneities play a major role, greatly disrupting the measurement technique and "invalidating" the extraction results, particularly with regard to absorption.

I.6. Conclusion and contributions of the research work

Significant progress has been made in SA imaging within the THz range, driven by the technology's potential applications. However, it is noteworthy that the previously demonstrated approaches, based on SA technique, have predominantly adopted the reflection configuration for illuminating and detecting THz waves with the object under test being in movement to generate the SA. This configuration enables the entire imaging system to be conveniently positioned on one side of the experimental setup with respect to the object under test. This arrangement offers space-saving benefits, particularly for electronic-based systems that tend to be bulkier compared to opto-electronic systems. Furthermore, the reflection setup is better suited for reflective solid materials, highly absorbent or objects with thicknesses exceeding the optimal range for TDS systems in transmission configuration. On the other hand, the transmission configuration is more appropriate for extracting parameters from transparent materials such as gases or polymers, as the low reflected beam from these materials creates a challenge in accurately capturing and utilizing the reflected signals for reconstruction and analysis.

Furthermore, the reported studies on SA imaging using coherent generation and detection systems have not extensively used the reconstructed amplitude and phase information to extract the real refractive index and absorption coefficient of the objects under test. While the amplitude of the reconstructed data may indicate variations indicating a transition from a substance to another, it is insufficient for comprehensive characterization or identification of the scanned materials. Even spectral imaging cannot identify the different constituting elements of the object under test but can only serve as an anomaly detection approach. This "anomaly detection" approach can indicate the presence of contaminants but requires further examination for detailed analysis.

To address these challenges, this work will present a SA aperture-based imaging approach using a THz-TDS system in transmission configuration. Our SA-based THz imaging system will rely on the movement of a PCA along a scanning plane to create a synthetic array. We will choose to mobilize the emitter in order to create a planar synthetic array for practical reasons, which will be detailed later. We will use a BP algorithm to reconstruct 3D images of different objects under test. We will demonstrate the image reconstruction of three objects from transmitted signals through the object, rather than reflected waves. Each of the samples will be chosen to demonstrate an aspect of the imaging approach abilities. The first sample will be a reference “binary” sample that will allow us to assess the imaging capabilities of the system on the available bandwidth. The second sample will be a 3D dielectric sample, which will serve to demonstrate the 3D aspect of the imaging approach and the third and final sample will be a multi-material sample that will serve to see the evolution of the 3D image through different materials. A comparison between the proposed imaging approach and the classical raster scanning imaging method will be provided for each sample and the limitations of each method will be detailed.

We will further demonstrate that SA imaging will not mean a loss of spectral data. In fact, the amplitude and phase of the reconstructed data will carry the same amount of information on the spectral characteristics of the object under test as the classical scanning method. We will calculate the characteristics of the different materials of the multi-material sample by using the reconstructed data from the SA imaging approach. The efficiency of the approach in providing a novel context for THz imaging and spectroscopy will be demonstrated, which will be different from the classical configuration, without compromising the primary objective of utilizing THz

waves. Furthermore, we will demonstrate that sparse sampling will achieve similar performances in imaging and spectroscopy, using quantifiable comparison criteria, while significantly reducing the acquisition time compared to the previously demonstrated SA imaging approach and the raster scan classical approach.

In a second demonstration of the work, we will showcase another significant application of SA imaging in THz-TDS systems: We will demonstrate the characterization of a THz anti-resonant hollow core fiber. By following the same previously detailed procedure, 2D spectral-space maps will be generated of the propagated beam, and the transverse beam profile at the output of the fiber will be imaged at different frequencies of the THz band. This will represent an interesting step towards the understanding of THz fibers, by addressing numerous “practical” challenges encountered in their characterization using existing methods. Furthermore, a new approach to modal characterization of THz fibers will be introduced. Building on SA imaging results, a numerical treatment will be used to extract the spatial field distribution of the different modes supported by the fiber. The referred numerical treatment will be inspired from the spectrally and spatially resolved imaging technique, also referred to as S^2 imaging. S^2 imaging method is used in the optical domain to investigate high order modes supported by a fiber, and we will be interested in adapting it for THz fibers. Even though this new approach will face a multitude of challenges in the THz range, we will demonstrate its potential and provide an elaborate analysis of its future perspectives.

II.1. Introduction

The first chapter laid the groundwork by introducing fundamental concepts in THz imaging and spectroscopy and outlining existing techniques. Building upon this, this chapter delves into our work, focusing on adapting the SA imaging technique to the THz spectrum using the TDS system in a transmission configuration. The objective of our proposed system is to provide a novel imaging and spectroscopy configuration in the THz range. The novelty of the approach consists in imaging stationary samples in transmission configuration by taking advantage of the flexibility of fiber coupled PCAs, driven by a TDS system. Creating the SA involves the mechanical motion of a single antenna, and the resulting image is computationally generated from the transmitted field through the sample (Figure II-1).

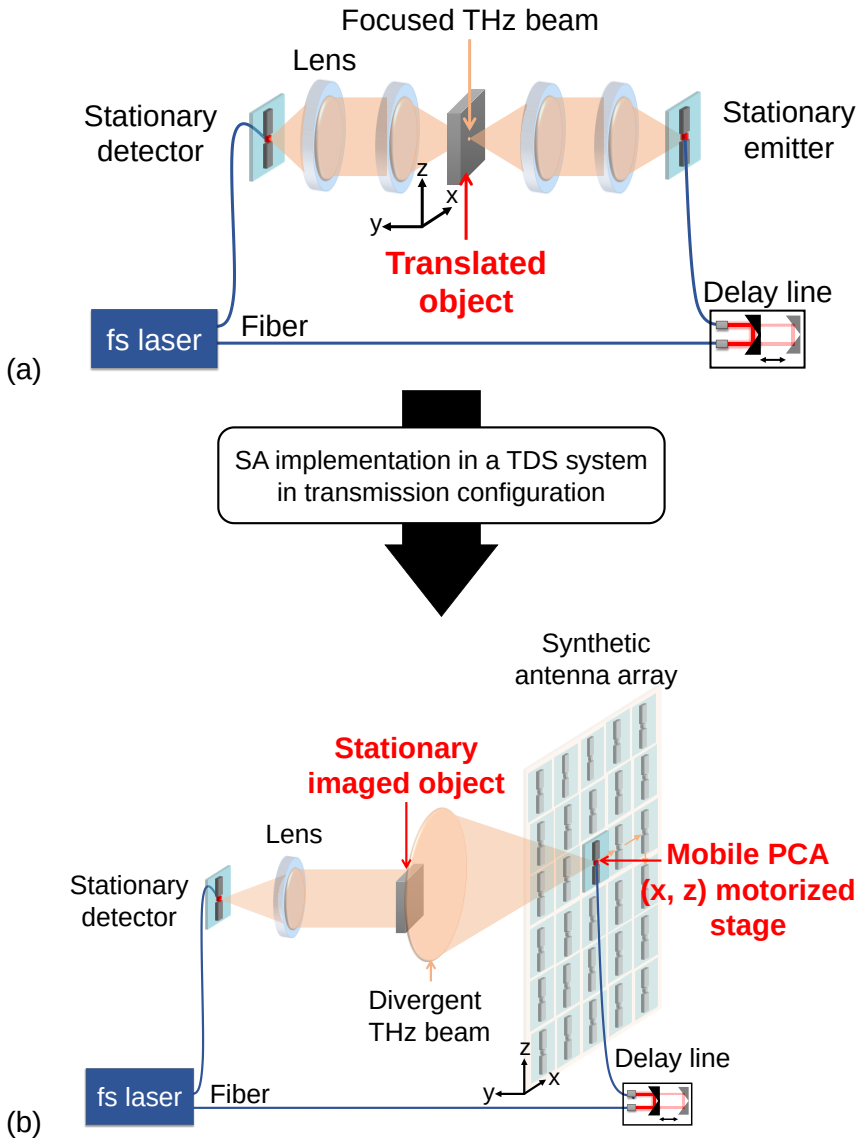

Figure II-1. SA implementation in a TDS system in transmission configuration. The transition from (a) the classical configuration to (b) the SA configuration involved the following modifications: three lenses are removed, and the emitter is attached to a mechanical translation arm to scan a planar surface in order to create a synthetic array of PCA emitters.

The first section will focus on our approach to SA imaging in the THz range, where we begin by revisiting the theoretical background of SA imaging and the BP algorithm employed for image reconstruction. Then, we examine the radiation pattern of the employed PCA and its impact on the reconstructed image. Subsequently, we integrate SA into the TDS system and experimentally assess its imaging performance. Finally, three different samples are tested for imaging in order to experimentally demonstrate the approach. Based on the findings, we draw a clear distinction between our method and raster scan imaging, which will serve as a reference for assessing the quality of the produced images.

In the second section of this chapter, we calculate the characteristics of the different materials of a multi-material sample by using the amplitude and phase of the complex reconstructed data from the SA imaging approach. In fact, the use of SA imaging preserves the material characterization ability of the TDS system similarly to the raster scanning imaging method. We provide a comparison of the obtained results using the full array and the sparse array. Moreover, to gain in acquisition time, we use sparsely sampled synthetic array for image reconstruction and material characterization. Spatial sparse sampling is not an option for raster scan imaging, which highlights an advantage of the proposed method in reducing the acquisition time. A subsection is dedicated to analyzing the effect of sparse sampling on the reconstructed image by comparing the results with the results obtained using a full array.

II.2. Synthetic aperture imaging in THz range

In this section of the chapter, we start by detailing the process of SA imaging and image reconstruction using BP algorithm. Then, we analyze the influence of PCA's radiation pattern on SA imaging. Finally, we present the experimental implementation in the TDS system.

II.2.1. Theoretical background

The proposed imaging technique draws inspiration from the stripmap SA Radar mode [149], a technique in which a sensor is fixed to a mobile platform moving at a constant velocity along a linear trajectory creating a 1D linear synthetic array. The antenna remains consistently pointing perpendicularly to the direction of the mobile platform's path, where the scene to be imaged is located. To adapt this method for 3D imaging, the SA has been extended into a planar 2D array.

Before detailing the image reconstruction process, it's essential to briefly outline the various simplifying assumptions necessary to implement SA. In order to model the scene being imaged, SA operates under the assumption that the illuminated object can be discretized into independent point sources that do not interact with each other (utilizing the Born first-order approximation). Additionally, SA assumes that the emitted field from each point source within the imaged object corresponds to the emitted field by the main source illuminating the object, convoluted with the impulse response of the local transmissivity of the object being tested. As SA imaging presupposes a linear relationship between the data and the scene, the convolution of the source field and the impulse response of the local transmissivity causes attenuation and temporal phase shifts in the emitted field, thereby represented as complex frequency transmissivity. The resulting reconstructed image is derived from this complex transmissivity, a process that will be elaborated on in this section.

Once these approximations are clarified, the exploration moves towards explaining SA imaging using a single point source. The schematic of the SA 3D imaging process is depicted in Figure II-2, illustrating both the acquisition and reconstruction procedures. The point source to be

imaged is positioned at coordinates (x_0, y_0=R, z_0). During the acquisition process, an antenna scans a 2D plane with a linear step dx and dz in x- and z-directions, respectively, to create a SA with dimensions D_x and D_z. For each antenna position (x_n, y_n = 0, z_n), with n ∈ [1, N] and N is the total number of spatial scanned points, the temporal signal $s_{mes}(t, x_n, z_n)$ is measured.

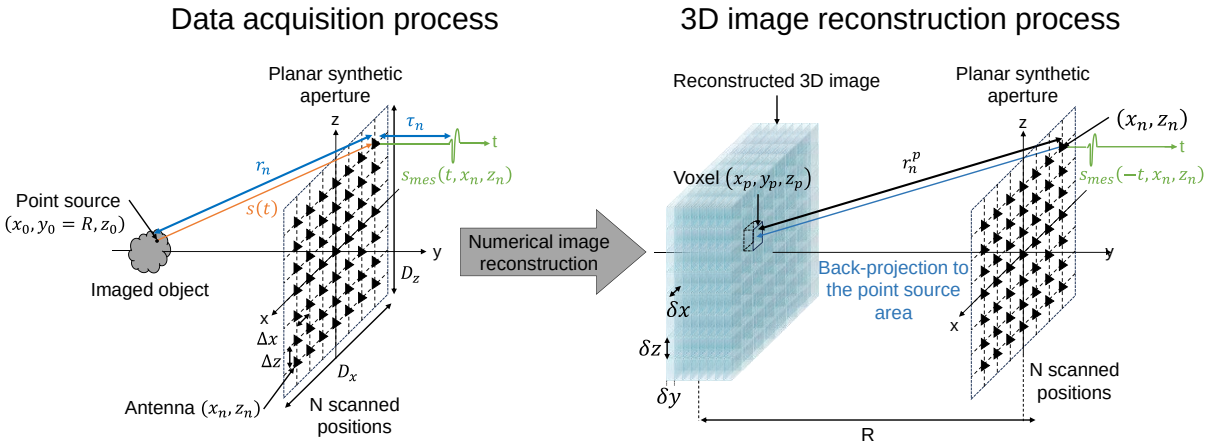

Figure II-2. SA imaging data acquisition process and Image reconstruction process through BP algorithm. During the acquisition, the moving detector antenna is mechanically scanning the plane XOZ to create a planar synthetic antenna array of N synthetic antennas. At each position n of the mobile antenna, the signal s(t) from the point source is measured with a delay τ_n. For image reconstruction, the region of interest is numerically segmented into a grid of voxels. Signals collected by antennas are collectively back projected into each voxel, which results in the reconstruction of a 3D image.

According to the aforementioned approximations, the received signal $s_{mes}(t, x_n, z_n)$ is essentially a time-delayed copy of the illuminating signal s(t) transmitted from the point source, with a delay time τ_n defined as:

Eq. 21.

$$\tau_n = \frac{r_n}{c}$$

Here, r_n is the range from an antenna position n on the SA to the point source, which is given by:

Eq. 22

$$r_n = \sqrt{(x_n - x_0)^2 + R^2 + (z_n - z_0)^2}$$

Image reconstruction is based on compensating this propagation temporal delay. In our case, the 3D image is reconstructed using the BP algorithm [150], [151], [152], which operates in the frequency domain. Consequently, temporal delays are translated into corresponding phase shifts. The BP algorithm acts as a digital lens by compensating the phase of the signals propagated from the antennas to the scene to be imaged, which is decomposed to a grid of voxels p, and p ∈ [1, P] with P is the total number of voxels of the reconstructed image. To compensate the phase shift due to the propagation from the point source to the array, the measured data is multiplied by the conjugate of the phase shift $\Psi_{n,m}^{p}$ corresponding to the travel distance between an antenna n of the array and a voxel p of the grid of the imaged scene, expressed as:

Eq. 23

$$\Psi_{n,m}^{p} = e^{-j\frac{2\pi}{c}f_m r_n^p}$$

With f_m the frequency, and m ∈ [1, M] with M is the total number of frequency points. The parameter r_n^p represents the distance between an antenna n of the planar synthetic array and a voxel p, expressed as:

Eq. 24

$$r_n^p = \sqrt{(x_p - x_n)^2 + (y_p - y_n)^2 + (z_p - z_n)^2}$$

When the conjugate of the phase shift is multiplied by the measured signals at each position, and then summed over all the antennas N of the array, the result is a frequency-dependent reconstructed complex transmittivity of each voxel p of the reconstructed image, which is expressed as:

Eq. 25

$$\tilde{T}_{re}(f_m, x_p, y_p, z_p) \approx \sum_{n=1}^{N} S_{mes}(f_m, x_n, z_n) \,.\, {\Psi_{n,m}^{p}}^{*}$$

The intensity of each voxel in the reconstructed 3D image is calculated by integrating the complex transmissivity at different frequencies and can be expressed as:

Eq. 26

$$I(x_p, y_p, z_p) = \left| \sum_{m=1}^{M} \tilde{T}_{re}(f_m, x_p, y_p, z_p) \right|$$

Eq. 25 can be written in the following matrix format for each frequency f:

Eq. 27

$$\mathrm{I_f} = \mathrm{S_f} \,.\, \Psi_{\mathrm{f}}^{\dagger}$$

With I_f: vector of dimension 1xP, representing the transmissivity intensity $|\tilde{T}_{re}|$ for each voxel, which must be reshaped in matrix form and summed in frequency to represent the 3D image. S_f: vector of measured signals, dimension 1xN (number of antennas). Ψ_f : Propagation matrix of dimension P x N with † conjugate transpose operator.

The adoption of a matrix-based approach leads to a simple and efficient backpropagation computation. However, it demands significant memory resources, particularly a substantial Random-Access Memory (RAM) to handle the computational load. The utilization of larger RAM capacities facilitates the creation and manipulation of extensive matrices, thereby enabling the reconstruction of larger images with enhanced numerical resolution. While iterative calculation approaches can also achieve this, they might entail significantly more computation time.

In summary, this overview of SA imaging remains general in nature as it overlooks various parameters, including antenna characteristics. Specifically, a fundamental requirement for this method to operate effectively is that the mobile antenna must consistently have the object under test within its range of view. Typically, SA principles are presented assuming that the mobile antenna is isotropic, i.e., radiating uniformly in all directions, ensuring it covers the

object under test from every angle. However, real antennas deviate from this assumption, unable to cover all spatial directions due to their limited divergence, which consequently restricts the effective array's size. These limitations manifest in the resulting image, which will be discussed in the subsequent section, right after the full characterization of the divergence of the antenna that will be used for the experimental demonstration of SA.

II.2.2. Analysis of the influence of PCA's radiation pattern on SA imaging

In the context of SA imaging, the characteristics of the employed antennas play a crucial role in determining the quality of the generated images and the overall performance of the system. An analysis of the equivalent circuit model of a typical PCA is provided in Appendix 1 (page 144), which allows the prediction of the generated available THz power as a function of the physical parameters of the antenna (substrate properties, photoconductive gap dimensions, etc.). This section focuses on the experimental analysis of the radiation pattern of the PCA used for SA imaging. The results of the experimental measurement of the radiation pattern will be subsequently used to predict experimental image reconstruction results.

II.2.2.1. Characterization of the radiation pattern of a PCA

In the context of SA imaging, the divergence (radiating aperture) of the beam dictates the achievable cross-range resolutions and FOV of the resulting image. In our specific scenario, both the emitter and receiver PCAs are commercially available fiber-coupled TERA15-FC [101] antenna modules paired with a high refractive index silicon (HR-Si) hyper-hemispherical lens on the output side. This section is dedicated to characterizing the unknown radiation beam emitted by these commercial PCAs.

At the moment, we don't know the structure of the antennas, so we need to directly examine experimental measurement results rather than depending solely on simulations. However, existing literature offers simulations for different PCA designs [153], [154], [155], [156], [157]. It's important to note that there aren't many experimental measurements available for a PCA's radiation pattern. While some studies have covered THz radiation in CW systems [158], there is a lack of experimental measurements focusing on the radiation pattern of a PCA within a THz pulsed system. Consequently, this section serves as a valuable guide for PCA characterization regarding beam profile analysis across both temporal and frequency domains, in addition to being instrumental for SA establishment later on.

To build the experimental setup that will be used for the measurement of the radiation pattern of the PCA, we should recall from the first chapter that SA imaging can be done without a set of focusing lenses (as SA processing acts as a digital lens). However, eliminating all TPX focusing lenses leads to a reduction in system's sensitivity and consequently, a decline in the dynamic range of the measured THz pulse. In the four-lens configuration (Figure II-3.a.), the dynamic range registers at 78 dB at 1 THz (Figure II-4, blue curve), whereas the lens-free configuration (Figure II-3.b.) results in a measured signal with a notable dynamic range drop, with the dynamic range falling to 30 dB at 1 THz (Figure II-4, yellow curve), accompanied by a reduction in the available bandwidth from 5.6 THz to 3 THz. However, the addition of one lens in front of the detector (Figure II-3.c.) elevates the dynamic range of the signal to 70 dB at 1 THz and provides a bandwidth of 4.5 THz (Figure II-4, orange curve). The lens is a PTFE (Polytetrafluoroethylene) plano-convex lens, with a focal length F = 10 cm and a diameter of 5 cm.

Nevertheless, the addition of a collimating lens is a compromise between dynamic range and FOV, because the collimating lens has a limited FOV which is around 4.25 cm (85% of the total diameter of the lens).

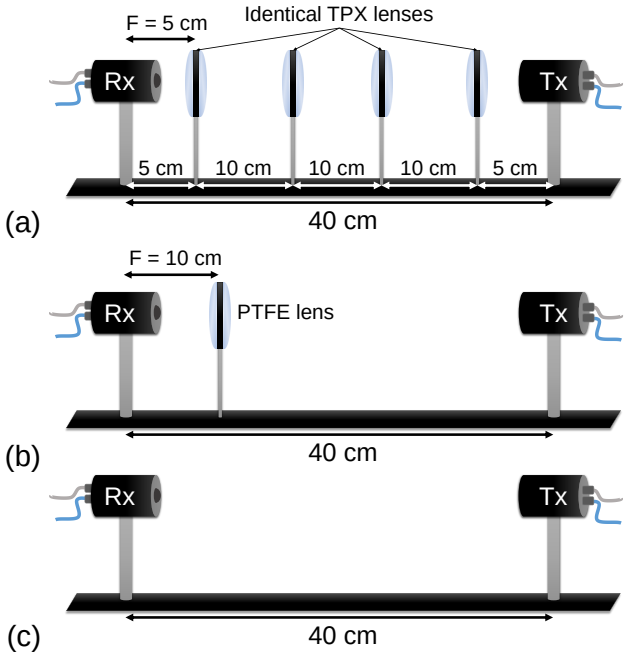

Figure II-3. Three configurations of TDS system, (a) the classical configuration with four TPX lenses. (b) with only one PTFE lens and (c) without any lenses.

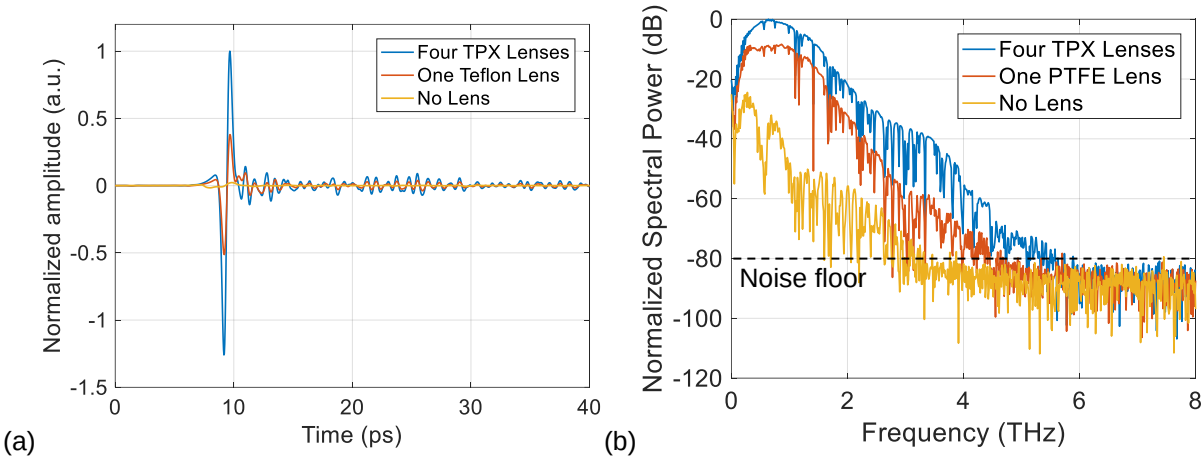

Figure II-4. (a) Normalized amplitude of the recorded THz temporal signals with the full optical system, as in a classical focused TDS system (blue curve), with one PTFE lens (orange curve) and without any focusing lenses (yellow curve). (b) Normalized amplitude of spectral power in dB recorded with the full optical system as in a classical focused TDS system (blue curve), with one PTFE lens (orange curve) and without any focusing lenses (yellow curve).

Interestingly, a dip in the data appears at around 0.5 THz when using the configuration without lenses. While the exact nature of this phenomenon requires further investigation, it's important to note that this issue does not impact the implementation of SA imaging. That is because the experimental data acquisition for SA imaging demonstration will be conducted using the PTFE lens (Figure II-3.b.). This choice ensures a higher dynamic range and larger available bandwidth, while also avoiding the dip around 0.5 THz. Moreover, positioning the antenna at the focal distance of the collimating lens (F = 10 cm) yields an infinitely collimated beam [159]. This results in the creation of a plane wave locally, thereby establishing far-field conditions.

The far field region is where the radiation pattern of the antenna should be measured. The far-field region is defined by the Fraunhofer criterion expressed as follows:

$$R_{ff} > 2\frac{A^2}{\lambda}$$

R_{ff} is the start of the far-field region. The parameter A represents the diameter of the emitter's largest aperture. The beginning of the far-field region depends on both the wavelength and the aperture size of the emitter. In our case, by adding the collimating lens, we are measuring the antenna's radiation pattern in the far field, even though we know that the antenna will illuminate the sample in the near field. The purpose of this analysis is to get a qualitative idea of the behavior of the antenna in order to estimate the overall limits of the system.

The next step is to measure the radiation pattern of the antenna before examining its impact on the image reconstruction process. The selected PCA exhibits linear polarization (Figure II-5). Consequently, characterizing the radiation pattern of the antenna necessitates assessment in both the E-plane (polarization direction) and the H-plane (perpendicular to the polarization direction).

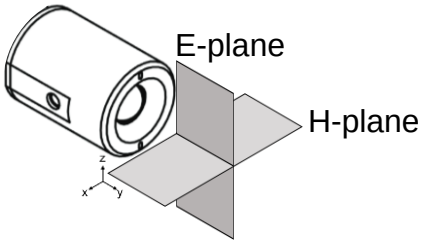

Figure II-5. Diagram showing the E and H planes for a vertically polarized commercial THz PCA [101].

The measurement setup is presented in Figure II-6.

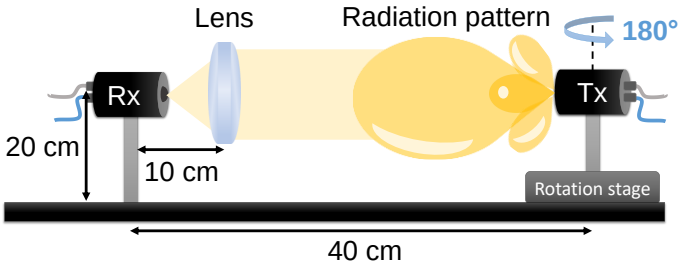

Figure II-6. Radiation pattern measurement setup. The detector remains fixed while the emitter is rotated through 180° in the horizontal plane, with a 5° step, to measure the E-plane radiation pattern. Subsequently, both antennas are turned 90° around their cylindrical symmetry to measure the radiation pattern in the H-plane using a similar procedure.

The detector PCA remains in a fixed position, while the emitter undergoes rotation. A PTFE lens is put in front of the detector at its focal distance F = 10 cm, thus resulting in infinitely collimating the THz beam. The antennas are positioned at a height of 20 cm above the table, with a 40 cm separation between them. The separation between the antennas could be taken between 40 cm and 60 cm, a range imposed by the delay line of the TDS system. We chose the smallest separation available to optimize signal attenuation knowing that the far-field condition is assured with the additional collimating lens. The emitter is mounted on a manual rotation stage and rotates from -90° to 90°, with 0° corresponds to direct alignment with the receiver. A temporal signal is measured with 500 times averaging at each antenna position. To ensure precision, the rotation axis coincides with the focal point of the hyper-hemispherical

lens attached to the antenna, positioned approximately 2.3 mm behind the front side of the emitter housing. Figure II-7 displays a map of the amplitude of the envelope of the raw temporal signals measured at each angle in E-plane and H-plane. This map is normalized to its maximum values and presented in dB to offer a clearer visualization of the signal's temporal evolution across all rotation angles.

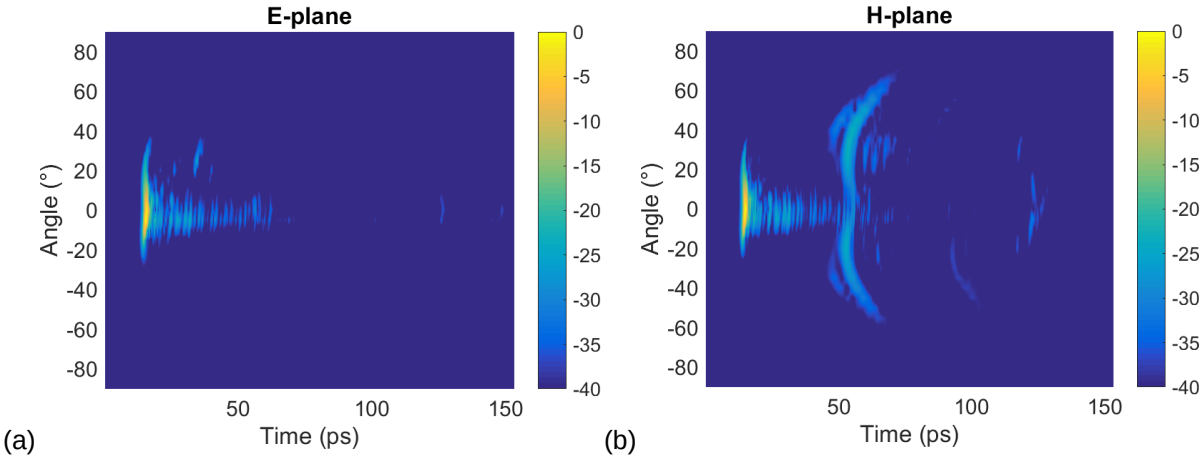

Figure II-7. 2D map of the amplitude of the envelop of the detected temporal signals within the angular range of -90° to 90° in both (a) E-plane and (b) H-plane. The complex envelops of each raw time-domain measurement is extracted and its module is normalized and presented in dB in at each rotation angle.

The maps depict the main pulse centered around 0° where the antennas align. Following the main pulse, numerous reflections appear in both the E-plane and H-plane, arising from reflections in the antennas' lenses. However, in the H-plane, a wing-like form emerges around 60 ps at approximately -25 dB. These reflections are suspected to result from the attached hyper-hemispherical lens, causing aberrations in the antenna's horizontal plane. However, further investigation into this behavior was not conducted.

From the measured temporal data, we present in Figure II-8 a time domain radiating pattern derived from maximum power values of the complex envelope of the temporal signal in dB at an instance t = 16 ps of the arrival of the temporal pulse. The antenna exhibits divergence of 11.25° and 13.15° in E-plane and H-plane, respectively, measured at -3 dB of the presented traces. The shift between the centers of the E- and H-plane radiation patterns is a result of a slight experimental miss-alignment.

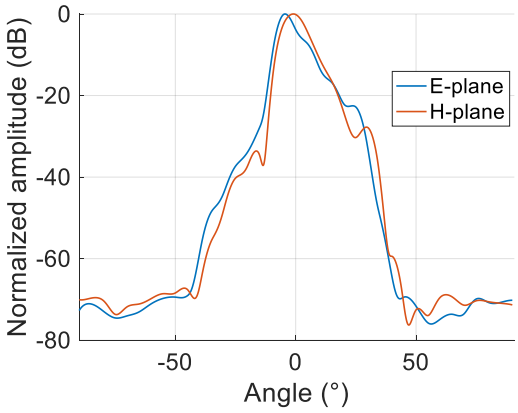

Figure II-8. Measured radiation pattern of the commercial PCA with the added collimating lens, extracted from the temporal data, in E-plane (blue trace) and H-plane (orange plane).

Next, we investigate the PCA's radiation pattern across the frequency range spanning from 0 to 4.5 THz. The objective is to observe how the antenna's radiation evolves across the available bandwidth (ranging from 0.1 to 4.5 THz). To achieve this, we employ an FFT on the previously measured temporal data shown in the aforementioned maps (from 0 ps to 130 ps). This process results in the 2D maps presented in Figure II-9 that illustrate the evolution of the normalized spectral power in dB as a function of frequency and rotation angle, in both E-plane and H-plane. As expected, these maps indicate a decrease in power amplitude level at higher frequencies, with the highest amplitudes consistently centered at 0°. The maps' gradient is limited to -80 dB to eliminate the noise floor in the maps. In both E-plane and H-plane, the maps reveal power levels above -40 dB for frequencies below 1 THz. Between 1 THz and approximately 2.5 THz, the power levels are ranging between -40 dB and -70 dB. Above 2.5 THz, the power gradually declines from -70 dB towards the noise floor at -80 dB. Notably, the H-plane displays secondary lobes within the 0 to 0.2 THz range.

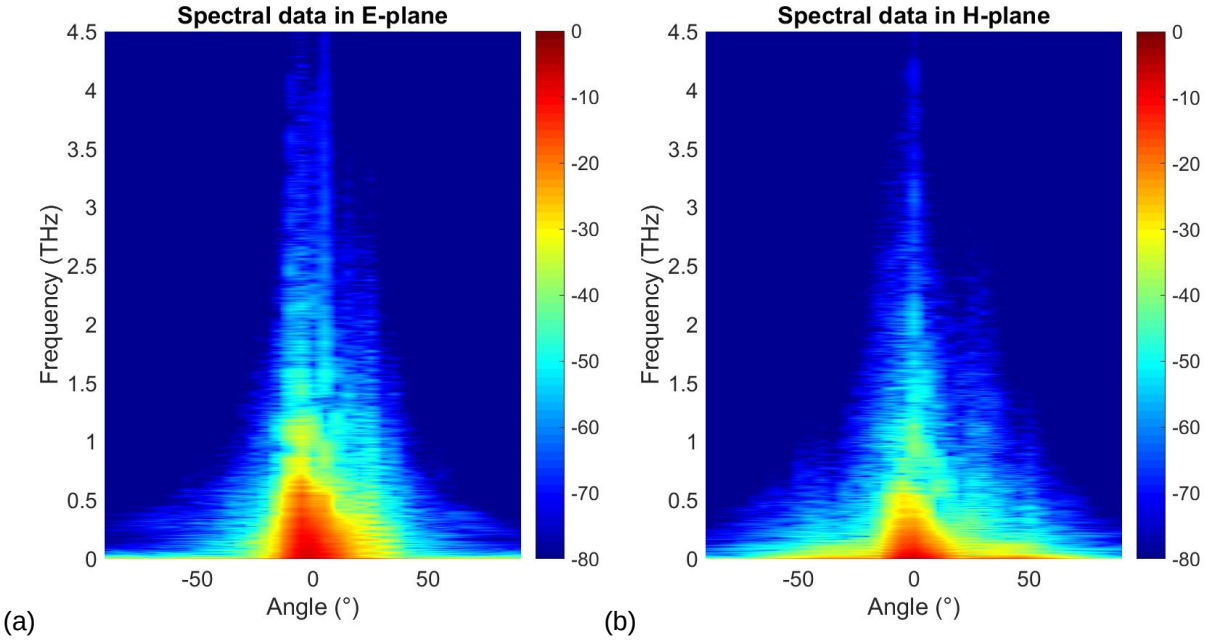

Figure II-9. 2D maps of the power of the measured spectral data between 0 and 4.5 THz at (a) E-plane and (b) H-plane, in dB. The maps are saturated to -80 dB to eliminate the noise floor and provide a better visibility.

Furthermore, to derive the spectral radiation pattern, we normalize to the maximum power at each frequency, thereby allowing the examination of the spatial distribution of the radiation pattern across the available bandwidth. The normalized maps are presented in Figure II-10 in dB. The radiation pattern displays a prominent band centered around 0°, reflecting the antenna's spectral radiation pattern.

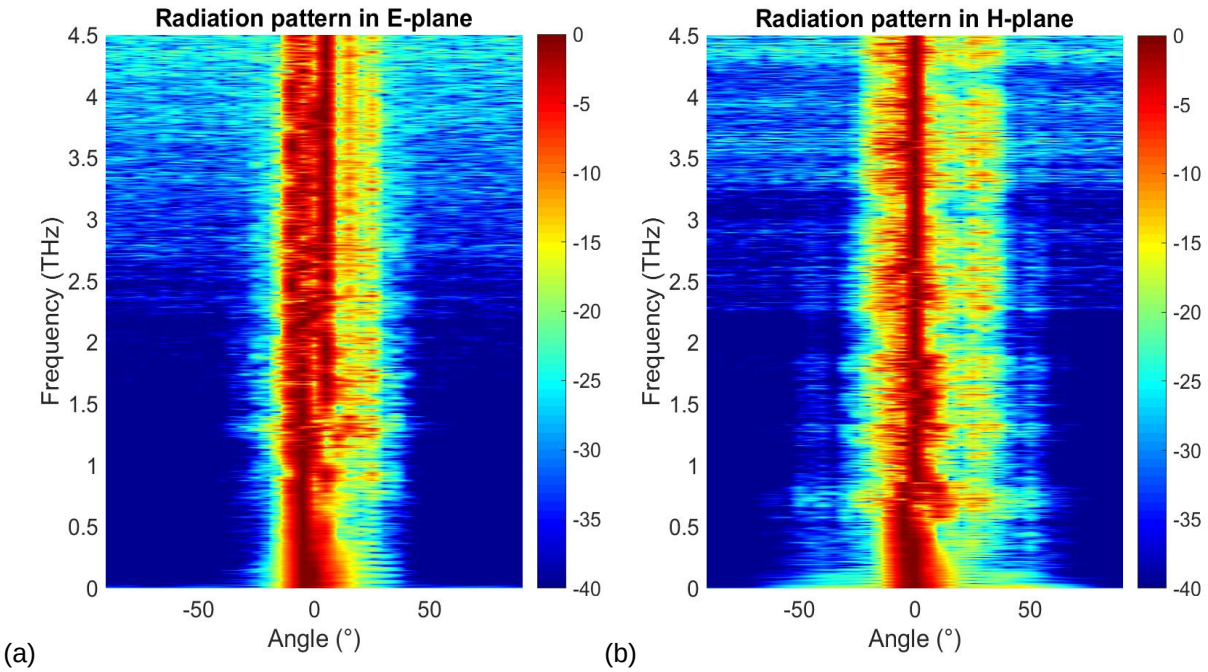

Figure II-10. Spectral radiation pattern of the antenna from 0 to 4.5 THz at (a) E-plane and (b) H-plane, in dB. The amplitude is normalized to the maximum at each frequency.

However, across the entire frequency spectrum in both the E-plane and H-plane, the radiating pattern appears asymmetrical in reference to the angle 0°. Specifically, on the left side of the radiation maps (positive angles on the x-axis), more irregularities and oscillations are noticeable, potentially due to possible miss-positioning of the hyper-hemispherical lens on the antenna. Despite this lack of symmetry, the radiation pattern demonstrates considerable uniformity before reaching 1 THz, observed in both the E-plane and H-plane. However, past 1 THz, aberrations at the center of the radiation pattern begin to appear. Above 2.25 THz, the noise level begins to rise above -40 dB. In the H-plane, the secondary lobes are always persistent between 0 and 0.2 THz.

If the radiation pattern projected onto the plane to be imaged is not uniform, this will generate amplitude errors in the image reconstruction. Therefore, ideally, the radiation pattern should be deconvoluted from the reconstructed image, but from a practical point of view this is very difficult to achieve, as the pattern projected onto each plane to be imaged must be perfectly known. Consequently, image quality will depend on the frequency band chosen and the level of fluctuation of the radiation pattern in the useful angle: the useful angle of the radiation pattern to image at 20 cm with an antenna displaced to the maximum of the size of the synthetic array is low.

On the other hand, we should note that on each pixel of the formed image, we average the contributions of each antenna that saw the scene from different angles, which will "smooth out" the intrinsic fluctuations of the radiation pattern. In addition, we perform a frequency summation, which will also average out all these imperfections. Which is why the time domain radiation diagram shown above (Figure II-8) is relatively uniform.

However, it’s important to acknowledge that imaging sub-bands will not lead to the same final quality. Below 1 THz, the diagrams are uniform, and the dynamic range is optimal, but resolution is low. Resolution can be increased by exploiting sub-bands around higher frequencies, but at the cost of a deterioration in image quality (linked to a reduction in dynamic range).

From a practical point of view, we therefore consider it usable as long as the dynamic range is greater than -40 dB, even if there are fluctuations. Which leads to a usable maximal frequency of 2.5 THz with this dynamic range.

II.2.2.2. Influence of the radiation pattern on the resolution

This section will provide a simulation-based analysis of the achievable performances using the imaging approach with the available TDS system, notably the resolution and Field of View (FOV). The simulation is based on the previously obtained information about the PCAs, including the radiation pattern and the exploitable bandwidth. The primary goal is to evaluate how the antenna's characteristics influence the reconstructed impulse response within the available bandwidth. By examining the simulation results, we aim to draw conclusions regarding the capabilities and limitations of the experimental imaging system. These conclusions will be essential considerations for imaging complex objects during subsequent testing phases.

We start by establishing the various parameters relevant to the discussion of the imaging system's resolution. In theory, the spatial resolutions of a 3D image, generated using a planar 2D synthetic array of isotropic antennas [160], are expressed as:

Eq. 28

$$\delta_x = \frac{\lambda . R}{D_x}, \delta_y = \frac{c}{BW}, \delta_z = \frac{\lambda . R}{D_z}$$

Here, δx and δz represent cross-range resolutions, and δy range resolution. λ is the central wavelength of the BW of the propagating beam. However, the theoretical resolutions mentioned above assume the use of an isotropic antenna. In reality, real antennas exhibit limited divergence, which limits their radiation to specific spatial directions.

So, to account for the complete form of the radiation pattern, which is previously demonstrated in our experimental findings, we approximate the radiation pattern to a Gaussian form (Figure II-11). The Gaussian function will be used to simulate the radiation pattern of the PCA through the analysis of the effect of the radiation pattern on the reconstructed image. Other approximations to the radiation pattern have been proposed in the context of analyzing the effect of the antenna's radiation pattern on the reconstructed image for non-destructive testing applications [161], [162]. The divergence of the Gaussian beam is set at 12° at -3 dB.

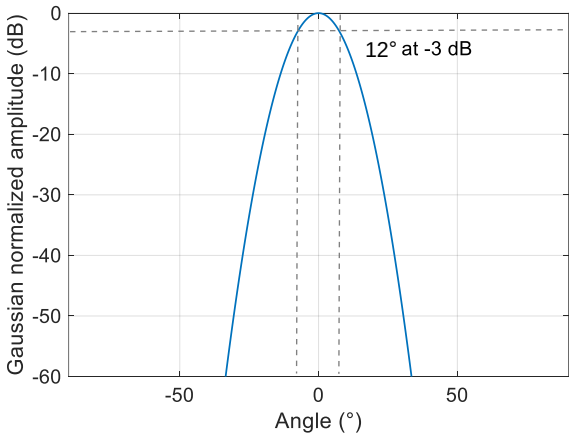

Figure II-11. Simulation of the radiation pattern of the antenna using a gaussian form. The divergence of the radiation pattern is 12° at -3 dB.

Generally, to assess the impact of the antenna's divergence on the imaging result, the Point Spread Function (PSF) of the imaging system is examined. The PSF quantifies the imaging system's response to an ideal point-like source and serves as the fundamental unit for image formation at a certain distance from the imaging antenna array [163], [164]. Mathematically, the image response in an observation plane at y = y_0, is the convolution product of the field diffracted by the illuminated object with the PSF of the antenna array:

Eq. 29

$$Image(x, y_0, z) = E_{Object}(x, y_0, z) * PSF(x, y_0, z)$$

The simulation used to reconstruct the PSF is set as follows, an array of detectors with a variable size D and a uniform inter-element step d is positioned at a distance R from a point source. The point source emits an isotropic THz beam in the frequency range 0.2-2.5 THz, towards the antenna array (with gaussian divergence). The point source is positioned at a range R = 20 cm which corresponds to the mean distance used on the experimental setup. The simulated time domain signals at each position of the antenna are shown in the figure below in a form of a 2D map for each array size D.

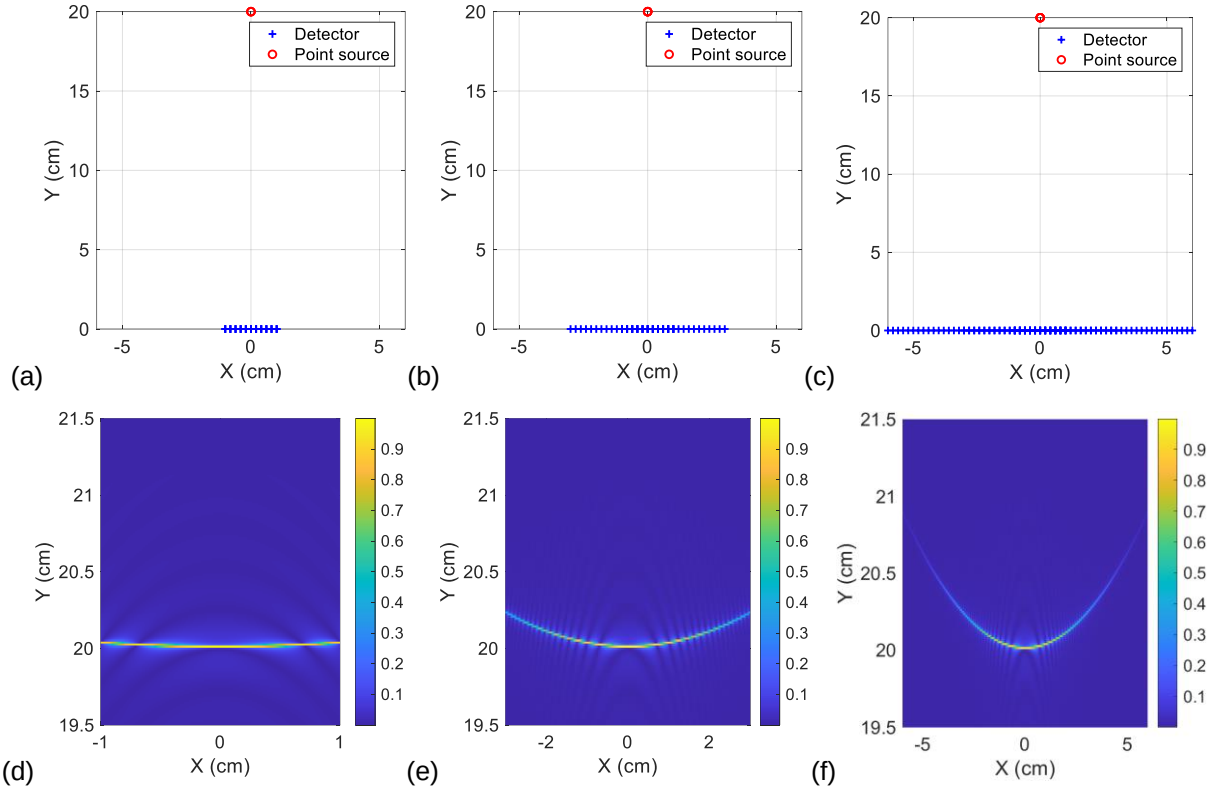

Figure II-12. Imaging simulation setup with a point source and an array of detectors. The size of the array varies to take three different values: (a) D = 1 cm, (b) D = 6 cm and (c) D = 12 cm. 2D maps of the normalized envelope of the time domain data using three arrays (d) D = 1 cm, (e) D = 6 cm and (f) D = 12 cm.

The curved shape created by the evolution of the maximum of the measured temporal peak is called the migration hyperbola and it is due to the delay of propagation between the central antenna of the array and the antenna at the extremities of the array. In Figure II-12.f., a difference in the intensity of the center of the hyperbola and the extremities is obvious, and it is due to the divergence of the antenna (in addition to attenuation related to the propagation distance in 1/R). A lower intensity at the extremities of the hyperbola means that the detectors

at the extremities of the array do not detect the emitted beam from the point source because they are limited by their divergence, thus not being able to see angles above what their divergence allows. This results in the fact that above a certain size of the array, the antenna pattern acts as a spatial filter, reducing resolution. To demonstrate that further, the 2D reconstructed PSF generated using the three arrays with varying sizes D are presented in

Figure II-13. The luminous spot's size in these images differs due to the influence of the array size and the divergence of the antenna.

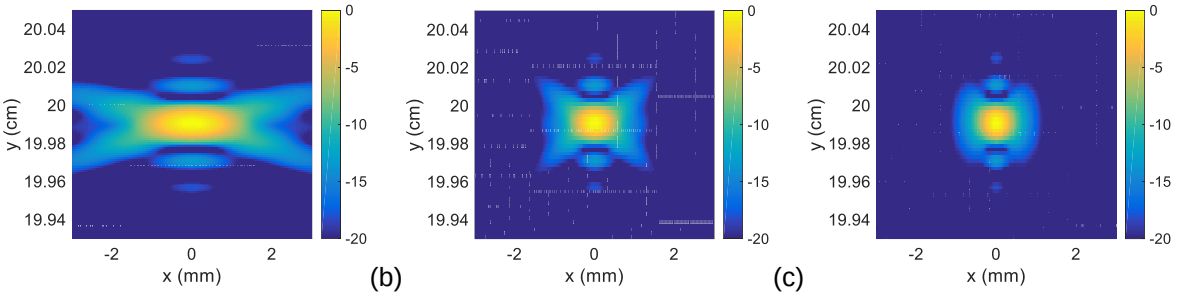

Figure II-13. Reconstructed 2D images in dB of the PSF using three different array sizes D. (a) D = 2 cm (b) D = 6 cm and (c) D = 12 cm. The reconstructed images are traced in modulus to the power of 2 ($|I|^2$) to improve the image's dynamic range.

Notably, employing a larger array enhances cross-range resolution along the x-axis, as confirmed by 1D cuts of the planar PSF, as shown in Figure II-14.a. The range resolution along the y-axis on the other hand remains unchanged at a value of 200 µm at FWHM, as it solely relies on the BW, as depicted in Figure II-14.b.

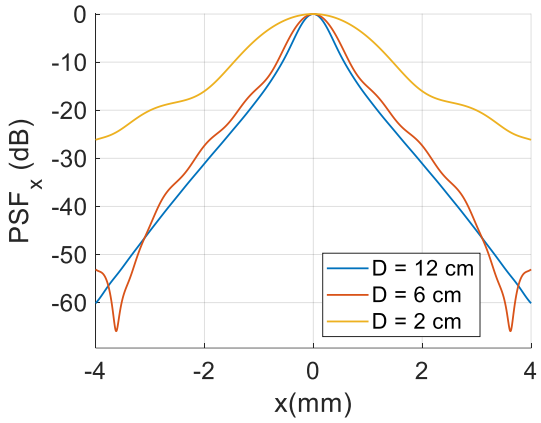

Figure II-14. 1D cuts of the reconstructed PSF in x-direction, using 3 different sizes of antenna array: D = 12 cm (blue trace), D = 6 cm (orange trace) and D = 2 cm (yellow trace).

The cross-range resolutions (i.e. δx and δz) obtained using 12 cm, 6 cm, and 2 cm arrays are 680 µm, 790 µm and 1700 µm, respectively. The disparity in resolution between an array with D = 2 cm and D = 6 cm is substantial. Nevertheless, resolution improvements are less significant when transitioning from an array of D = 6 cm to D = 12 cm, indicating a saturation point where antenna size no longer influences resolution. Our goal is to determine the maximum size D_{max} of the synthetic array at which the resolution ceases to improve. To achieve this, we reconstructed the PSF of a point source using various synthetic array sizes, ranging from 1 cm to 15 cm, and measure the size of the reconstructed spot at -3 dB is each array size D. Additionally, we compare the results using an array of divergent antennas to results using isotropic antennas and calculations using the theoretical approximation of cross-range resolution described by Eq. 28. The results of these simulations are presented in Figure II-15.

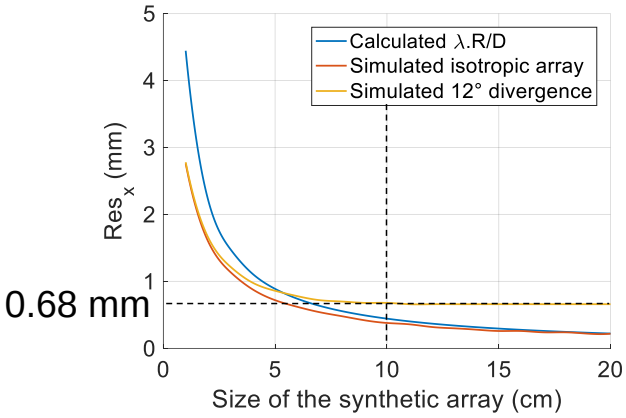

Figure II-15. Evolution of the cross-range resolution, measured at -3 dB of PSF in x-direction, as a function of D, the antenna array size. The theoretical value of the cross-range resolution is calculated using the formula (blue trace) and simulated in the case of an array of isotropic antennas (orange trace), and then in the case of an array with limited divergent antennas with 12° divergence (yellow trace).

A correlation is observed between the theoretical calculation of cross-range resolution using the theoretical equation (blue curve) and the simulation of image reconstruction utilizing an isotropic antenna with unrestricted divergence (orange curve).

However, the image reconstruction simulation conducted with an antenna with a 12° divergence angle results in a saturation of cross-range resolution values at 0.68 mm when using an array exceeding D = 10 cm. This outcome suggests that enlarging the synthetic array beyond this threshold does not yield improved resolution. This limitation stems from the intrinsic link between reconstruction resolution and object illumination.

We should note that the FOV however, depends solely on the step d_x and d_z in both directions following the equation:

Eq. 30

$$FOV = \frac{\lambda R}{d}$$

With d being d_x or d_z, which are the steps between two consecutive antennas in x- or z-direction, respectively. R is the range distance between the antennas and the imaged scene. Divergence also limits the FOV. We examine the evolution of the FOV with the size of the step d for the same antenna using the same simulation process above. We reconstruct maps using an array with a fixed size D = 10 cm according to the previous results. The 2D maps of the image of the point source are presented in Figure II-16 for three different step sizes between antennas d = 5 mm, 2 mm, and 1 mm and same array size D = 10 cm.

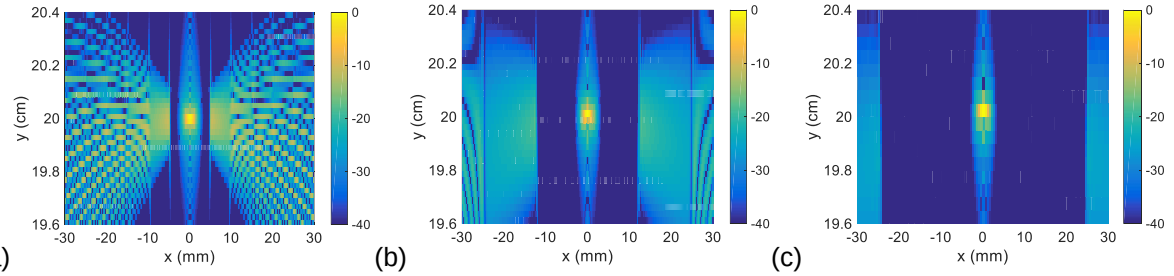

Figure II-16. Reconstructed 2D images ($|I_p|^2$) in dB of the PSF using three different arrays with three different step sizes d. (a) d = 5 mm, (b) d = 2 mm et (c) d = 1 mm.

The reconstructed map in Figure II-16.b shows that a step of 2 mm is needed to be able to image samples with a size of 2.5×2.5 cm² without aliasing. Reducing the step d to 1 mm results in an available FOV of 4×4 cm² as seen in Figure II-16.c.

To conclude, we established in the section, using simulation-based analysis, that the size of the array is limited to 10 cm in both directions. This value seems to be independent from the chosen frequency band. The size of the collimated beam is limited to 4.25 cm because of the collimating lens, which limits the size of the sample under test to the same size. To achieve the FOV = 4.25 cm, a step d = 1 mm between successive antennas of the synthetic array is required when f = 1.35 THz. However, the value of d changes with the central frequency of the chosen frequency bandwidth. We should note that, even if the lens fixes the FOV, spatial oversampling (i.e. a smaller array step d than necessary) helps to improve the overall SNR, as it allows the signal to be averaged when summed coherently over a voxel. For experimental demonstrations, the choice of frequency sub-band will be dictated by the required 3D resolution.

II.2.3. Experimental implementation in TDS system

II.2.3.1. Experimental setup

SA-TDS approach was implemented in broadband THz-TDS system (TERA K15 all fiber-coupled Terahertz Spectrometer from Menlo Systems GmbH). SA-TDS system was achieved by attaching the emitter antenna to a mechanical 2D translation arm to record the transmitted THz pulse at different spatial positions (Figure II-17). Both receiver or emitter antennas can be translated to create a synthetic antenna array as they are both lightweight, compact and fiber optic pigtailed PCAs. For simplicity, the emitter antenna was chosen because it is not attached to a current amplifier as in the case of the receiver, which otherwise restrains the range of movement and calls for a more complicated support system to securely move the amplifier together with the receiver.

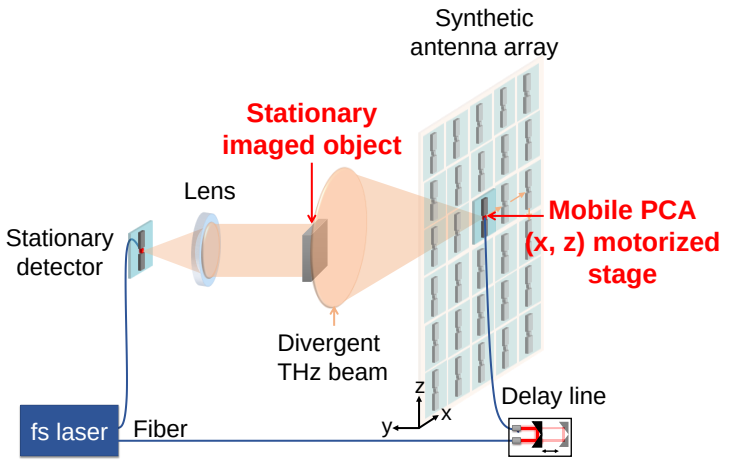

Figure II-17. SA imaging in transmission configuration. The moving divergent antenna is mechanically scanning the XOZ plane to create a planar synthetic antenna array. At each position of the mobile antenna, the emitted beam passing through the stationary object is focused on the fixed, detecting antenna. A PTFE lens is used to focus the beam onto the fixed detector.

The spacing between antennas will be adapted according to the chosen reconstruction frequency sub-bandwidth to always have a FOV of at least 2×2 cm². To enhance the DR, each signal is generated by averaging 40 time-domain traces, which is equivalent to an averaging for 5 seconds at each position. The size of the array and the averaging time results in a total

scanning time of 5 hours. All measurements are conducted under typical indoor atmospheric conditions at a room temperature of 23°C. A photograph of the experimental setup is presented in Figure II-18 below.

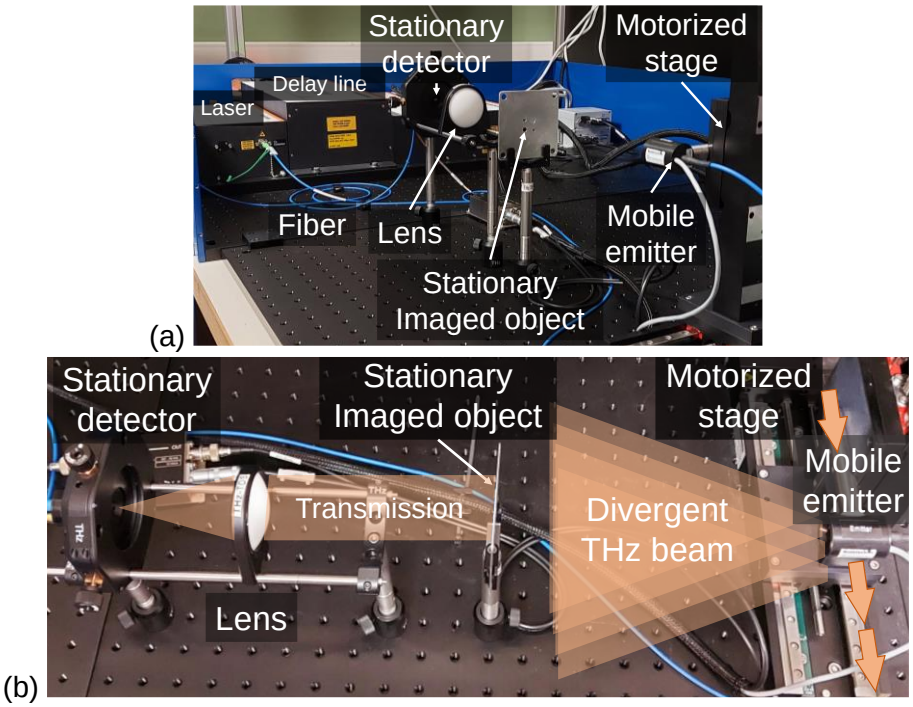

Figure II-18. Experimental setup used for SA imaging using the THz-TDS system, photographed from two different angles.

We start by measuring the PSF of the imaging system by employing a metallic plate with a small hole as imaged object. The hole diameter (250 µm) is chosen to be smaller than the resolution of the imaging system. The object was positioned at a range of R = 20 cm. As stated before, the target could be placed at any position between the lens and the mobile antenna. The synthetic array has a physical aperture of 10 × 10 cm², a size indicated by the previous simulation results on the PSF. Given the relatively small necessary FOV required to observe the target (1 cm), a step size of d = 5 mm in both directions proved adequate. To enhance the dynamic range of our measurements, signals at each antenna position were averaged over 40 measurements. The PSF is reconstructed using the bandwidth between 0.2 and 2.5 THz.

After the acquisition process, the BP algorithm was utilized to generate an image of the target according to the process explained above. The result is a 3D image of the point source (Figure II-19.a). Lateral 1D cuts in the horizontal and vertical planes (x- and z- directions on the XOZ plane) (Figure II-19.a) allows the experimental measurement of the resolution in each direction, respectively, at -3 dB (Figure II-20).

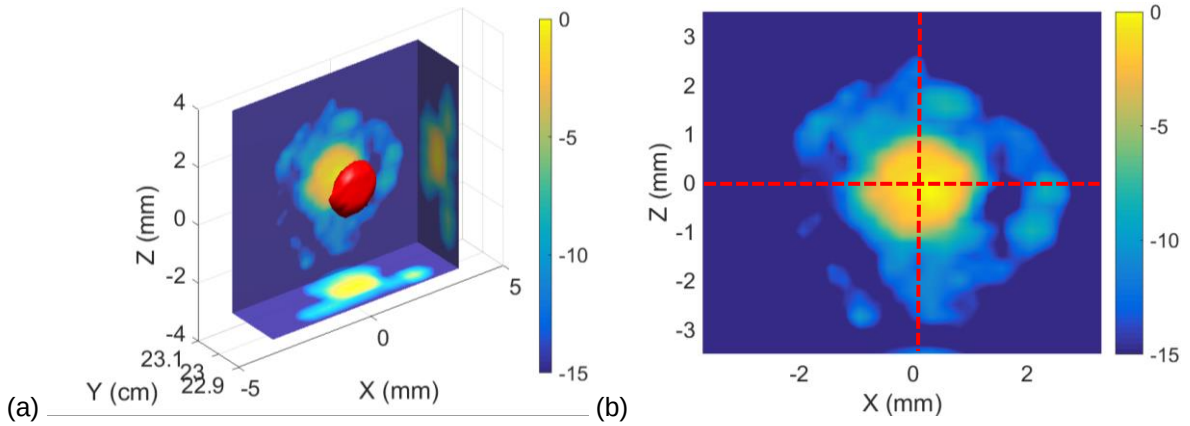

Figure II-19. Reconstructed (a) 3D image and (b) 2D image in the XOZ plane of the point source ($|I_p|^2$) in dB. The cuts in x-direction and z-direction are indicated with horizontal and vertical red lines, respectively.

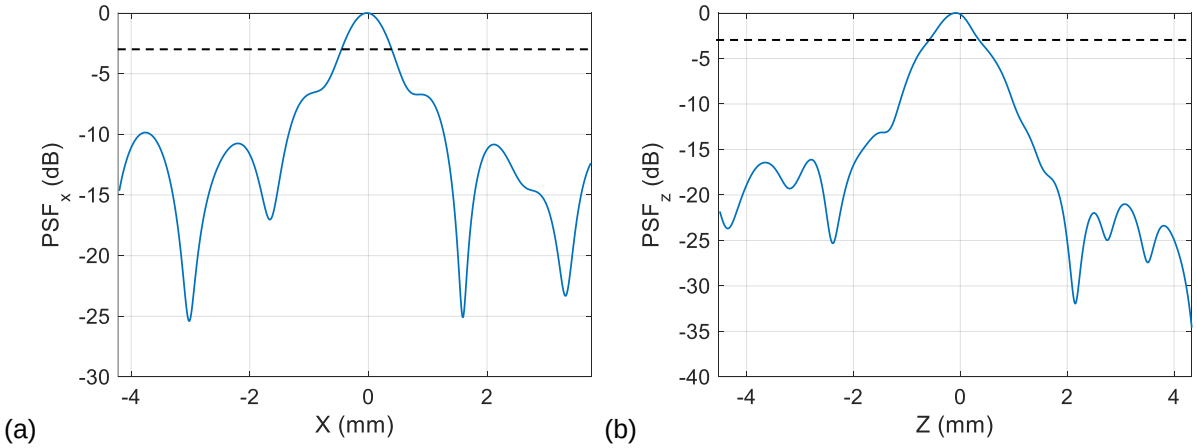

Figure II-20. 1D cuts of the experimental reconstructed PSF in (a) x-direction and (b) z-direction, in dB. The dashed line indicates the level of -3dB at which the value of the experimental resolution is extracted.

The measurement at – 3 dB revealed an experimental resolution of δ_x = 850 µm in the x-direction and δ_z = 930 µm in the z-direction, closely aligning with the simulated values ($\delta_x = \delta_z$ = 680 µm from Figure II-15). The difference between the PSF in x- and z-directions could be due to disparities in the radiation pattern of the antenna resulting in differences in illuminated zones of the point target.

The measured resolutions are close to the simulation results, with some disparity due to the fluctuations of the distribution of the radiation pattern in frequency domain.

II.2.4. Experimental imaging results

Imaging of a flat reference target:

The reference target is a thin metallic plate featuring 30 holes (Figure II-21). The 30 holes are distributed across 6 rows. Within each row, the holes have the same diameter, with the diameter progressively increasing from one row to the next. The holes maintain an equal center-to-center distance, resulting in a reduced metallic separation between successive rows. All dimensions are detailed in the figure below.

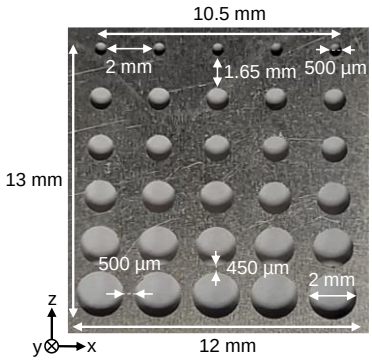

Figure II-21. A photograph of the flat reference target. The sample is a thin metallic plane with a thickness of 0.2 mm. The diameters of the holes and the distance between the holes are provided.

The main aim of this first experiment is to compare the performance of SA imaging with that of conventional raster scanning. The approaches are in fact quite different, since raster scan is based on localized illumination and reading (point focusing), whereas SA uses global illumination. Even though SA post-processing involves digital focused detection (digital lens by back projection), the image of each voxel is the result of the field diffracted by the object (in that voxel) initially illuminated in its entirety. To make this comparison with a good dynamic/ resolution compromise, the frequency reconstruction band has been fixed between 0.8 THz and 1.5 THz. The resolution of the SA imaging system in this band is $\delta_x \times \delta_y \times \delta_z = 750 \times 600 \times 750\ \mu m^3$. The antenna spacing is fixed at d = 2 mm, which provides a FOV of 2.73 cm. The image reconstruction result is presented in Figure I-22. Because the object is planar, we are not interested in looking into the depth of its reconstructed image, thus we present 2D images only.

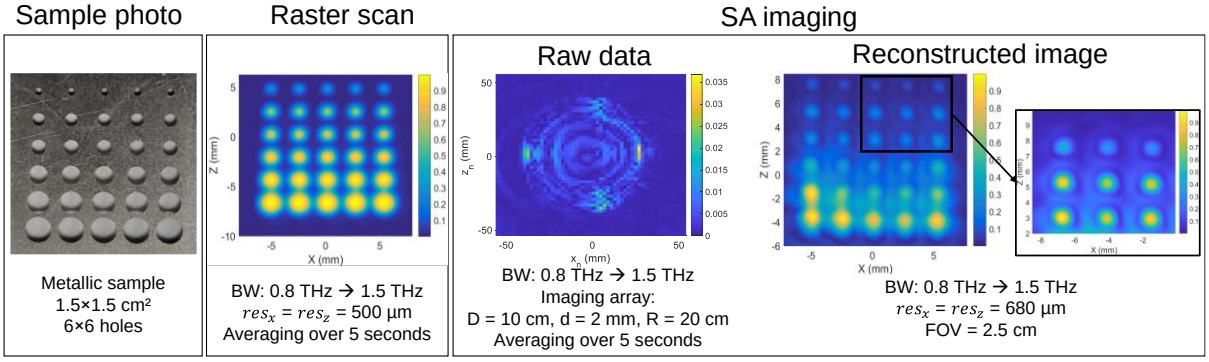

Figure II-22. Imaging results using raster scan and SA imaging approach of the flat reference target along the same frequency bandwidth. The image also shows the SA experimentally acquired raw data before numerical reconstruction.

The SA image shows the accurate number of holes (30 holes), with the smaller holes exhibiting less intensity than the larger ones. Which is due to the radiation efficiency of the hole. We are reconstructing the amplitude of the field transmitted through the hole, which means that a smaller opening result in lower radiation efficiency, thus lower reconstructed amplitude.

We conducted a comparative analysis between the SA imaging results and pixel-by-pixel imaging results achieved through raster scan imaging to provide a broader perspective. To enable this comparison, we re-adopted the classical configuration of the TDS system, employing four lenses to image the same object under test.

For this approach, the sample is attached to a mechanical arm and translated with a 0.5 mm step in the focal plane of the focused THz beam. This specific step size was chosen based on the system supplier's disclosure regarding the lateral resolution of the raster-scan TDS imaging system, which ranges between 1 mm and 0.5 mm. To ensure higher resolution, we opted for the smallest specified value of 0.5 mm. The bandwidth of the measured signals is filtered to the size of the chosen sub-bandwidth to accurately compare the results.

The amplitude of the scanned 2D image of the object under test is displayed in Figure II-23, accompanied by the necessary lateral cuts taken at the level of each row of holes, similarly to the previous SA results. This comparison aims to provide a comprehensive understanding of the differences and similarities between SA imaging and pixel-by-pixel raster scan imaging methodologies.

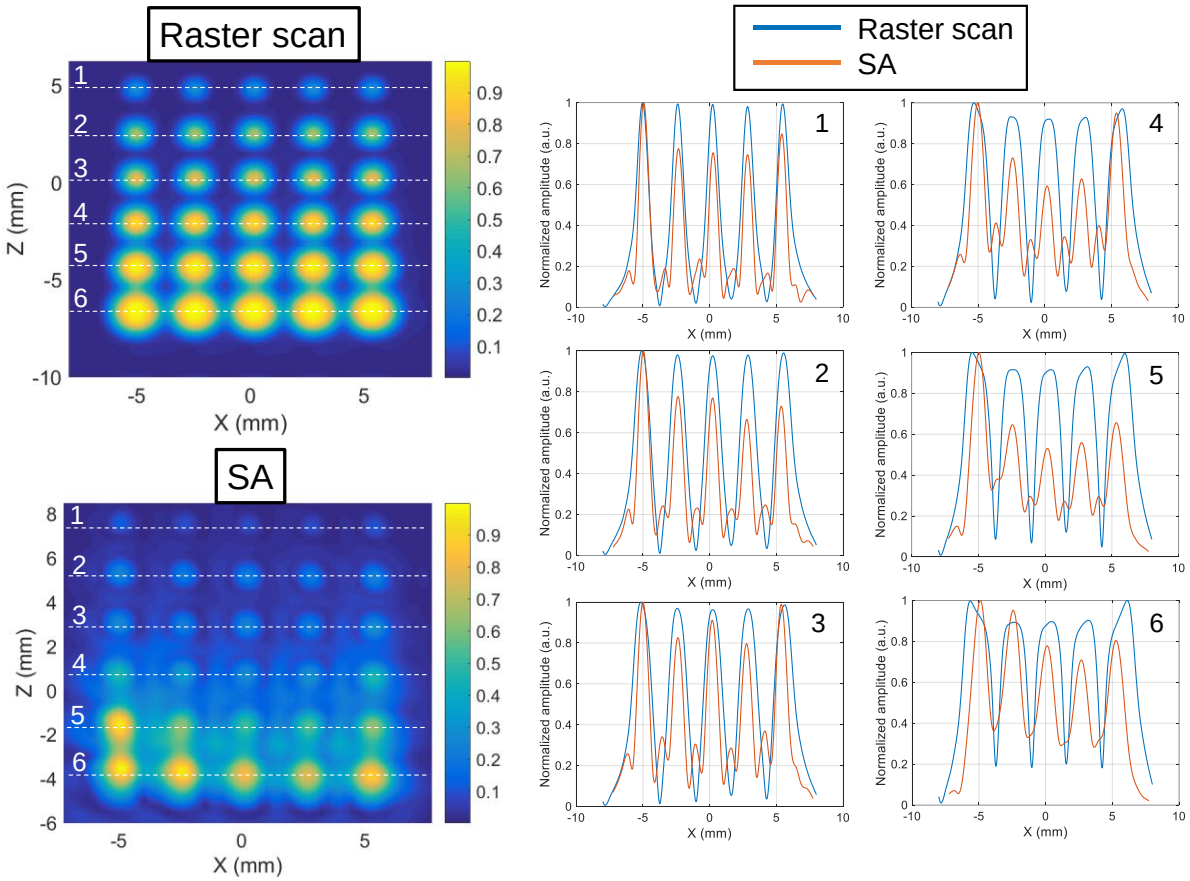

Figure II-23. (Left) 2D image of the sample generated using raster scanning approach, and 2D reconstructed image of the sample using SA imaging. (Right) Lateral 1D profiles of the reconstructed image at the level of each line of holes. The number on the 1D curves indicate its location on the 2D images on the 2D image. Blue curves are 1D profiles from the raster scanned image and orange curves are taken from the reconstructed image using SA.

The antenna array makes it possible to obtain all the elements of the test pattern, even those with intrinsic sub-resolution. The level of detail is virtually equivalent to that of a raster scan.

However, SA reveals amplitude differences and side lobes. Side lobes are directly related to the PSF (Eq. 29). Generally speaking, amplitude fluctuations can be due to the sensitivity of the lens-less system, interference between elements, since the field diffracted by the illuminated holes is imaged globally (but not significant in this imaging plane which is very close

to the object), transverse and frequency non-uniform illumination (radiation patterns, imperfect alignment of antennas and object, etc.).

This could be better corrected by solving the problem as a whole through matrix inversion, rather than simple phase conjugation through backpropagation. Side lobes could also be minimized by deconvoluting the PSF from the reconstructed image.

In conclusion, despite a few imperfections compared with raster scanning, we have just proved the feasibility of SA for transmission imaging, without moving the object.

Another important factor to discuss is the acquisition time. To obtain the SA image, the antenna has scanned an area of 10×10 cm² with a step d = 2 mm in both directions, resulting in a total of 2500 steps. Using the chosen bandwidth, this synthetic array resulted in a FOV of 2.73 cm and a resolution of 0.68 µm, thus an image with 40×40=1600 pixels. Theoretically, the generated image should have the same number of pixels as the steps taken to measure the data. However, it is not the case using the available PCA because its divergence limits the resolutions regardless of the size of the synthetic array. For the raster scan method, the supplier provides the information on the minimal resolution to be 0.5 mm, so to scan an area of 2.73 cm, one need 55×55=3025 steps to generate an image with the same number of pixels. The number of pixels of the raster scan image is higher than that of the SA result because the resolution is higher. Which means that raster scanning takes more time than SA to generate an image with higher resolution.

It is tricky to compare acquisition time of the imaging approaches in the case of different achievable resolutions. That is why we circle back to the previous demonstration where we demonstrated the performance of the SA imaging along the whole available frequency range. Using the frequency range 0.2-2.5 THz and creating a synthetic array of 10×10 cm² with a step d = 2 mm in both directions (2500 steps), we reconstruct an image with a cross-range resolution of 0.56 mm and a FOV of 2.55 cm (46×46=2116 pixels). To raster scan the same FOV = 2.55 cm with a resolution of 0.5 mm, one need 51×51=2601 steps (2601 pixels). Now that the resolutions are almost identical, the number of steps required to generate the SA image (2500 steps) and the raster scan image (2601 steps) are very close. Which means that the acquisition time is also very close. It actually takes a duration of 4.97 hours for SA acquisition and 5.11 hours for raster scanning with an averaging of 5 seconds at each position. To conclude, it is safe to say that SA imaging approach and raster scanning approach take almost the same amount of time to generate images of the same FOV achieving very close spatial resolutions.

To conclude on these results, the SA imaging approach successfully reproduces the image of the object under test. However, it does come with inherent limitations primarily associated with its imaging methodology. The illumination of the entire object under test results in more complex interactions between the object under test and the illuminating beam. Conversely, raster scan imaging approach relies on a focused beam to illuminate small parts of the object under test at a time, thus reporting information only at a scanned area at a time instead of the whole object. However, the raster scan approach required a mechanical arm to translate the object under test in the focus plane of the THz beam. Conversely to SA aperture imaging, where the object under test was stationary while the emitter was moving during acquisition. Moreover, without the need for lenses to focus the beam.

These disparities and variations offer distinct advantages, presenting diverse options suitable for their respective applications (heavy/ fragile objects such as art pieces and archeological

finds, liquid, or gas containers, etc.). The aim is to find a compromise between image “quality” and the constraints associated with the imaging setup to effectively address the specific requirements of each situation.

We demonstrated the imaging approach on a planar object and compared the results of SA imaging to raster scan imaging. In the next section, we look into the application of the proposed imaging method on a 3D sample.

Imaging of a 3D object:

The second object to be tested is a 3D circular staircase made with plexiglass (Figure II-24).

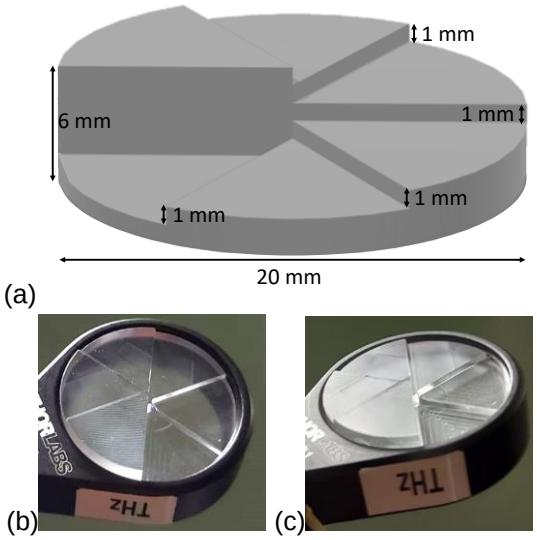

Figure II-24. A 3D plexiglass object under test with a 2 cm diameter. The object is featuring 6 triangular stairs with a thickness increment of 1 mm. (a) Schematic of the object and (b) and (c) photographs of the object under test inserted into its support from two different angles. The thin motifs observed on the surface of the triangles are relatively shallow and small in comparison to the experimental resolution.

The plexiglass material employed in the object exhibits a refractive index of approximately 1.6. Additionally, it demonstrates an absorption coefficient of roughly 10 cm^{-1} at 1 THz (Figure II-25). These characteristics of the plexiglass are experimentally measured on a 1 mm thick plexiglass sample using classical configuration of the TDS system.

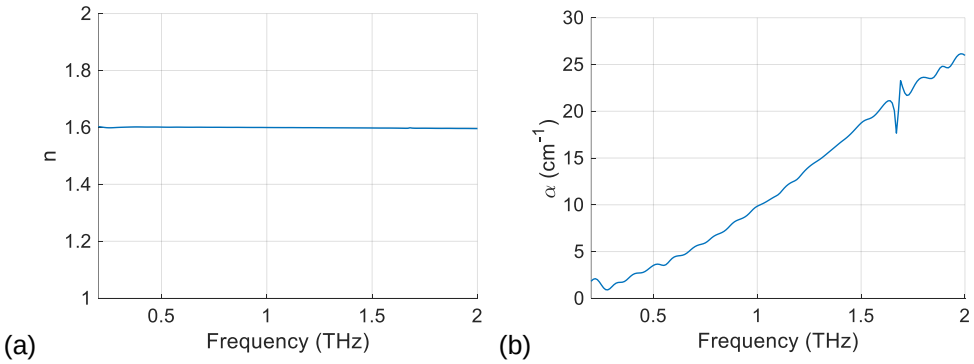

Figure II-25. (a) Refractive index and (b) absorption coefficient of Plexiglass. These parameters are measured for a plexiglass sample with thickness of 1 mm using the TDS system with 4 lenses.

As detailed in the first chapter, the exploitable bandwidth (or effective bandwidth) depends on the thickness of the substrate as the dynamic range is influenced by its absorption. That is why, an evaluation of the effective bandwidth available for this specific object under test is

necessary. The idea is to use the measured absorption coefficient α of the material to define the maximum useful frequency at which the wave is capable to propagate through all the layers of the object. To do that, we recall Eq. 10 from the first chapter, which indicates the evolution of the maximum measurable absorption as a function of the thickness of a material and the dynamic range of the signal.

Eq. 31

$$\alpha_{max}(f) = \frac{2}{e}\ln\left(D(f)\frac{4n(f)}{(n(f)+1)^2}\right)$$

The intersection between the trace of the measured absorption of the substrate and the maximum measured absorption calculated from Eq. 31 indicates the maximum frequency of the effective bandwidth. The calculated effective bandwidth will be subsequently used for the reconstruction of the image of the object 2.

We calculate the maximum measurable absorption α_{max} using the refractive index of the plexiglass, the different thicknesses e of the steps of the sample, and the dynamic range of the signal. The resulted α_{max} of each thickness value e are presented in Figure II-26 with the measured absorption coefficient of the plexiglass. We can see that α_{max} decreases for higher values of e. This results in the intersection of the trace of the absorption of the plexiglass and the trace of α_{max} to shift to lower frequencies. This indicates that the thicker the sample of plexiglass, the smaller the effective bandwidth.

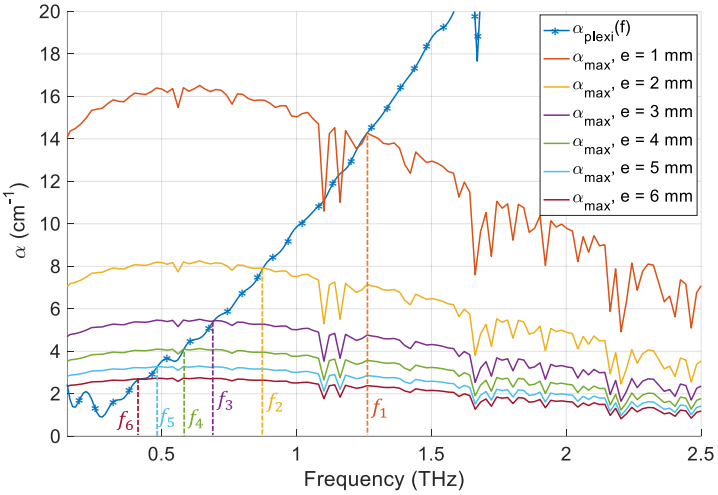

Figure II-26. The absorption coefficient of the plexiglass, and the maximum measurable absorption coefficient calculated using Eq. 31. The intersection between the absorption coefficient of the material and the maximum measurable absorption coefficient indicates the limit on the effective bandwidth for each of thickness value.

From the figure above, we see that the effective bandwidth for a sample of plexiglass with a thickness e = 1 mm is limited by the frequency f_1 = 1.25 THz. As the thickness increases to e = 6 mm, the upper boundary of the effective bandwidth decreases to f_6 = 0.42 THz. Which means that in order to examine all thicknesses of the sample, the chosen frequency band should be limited to the highest frequency limit which is f_1 = 1.25 THz. Additionally, to adequately assess the thickest layer, we must employ a frequency lower than f_6. In summary, our analysis indicates that the effective available bandwidth required to analyze this specific object under examination should ideally fall within the range of 0.2 THz to 1.25 THz.

In this frequency range, the SA imaging system reveals a cross-range resolution of 0.9 mm and a range resolution of 0.3 mm (calculated in air). These performances are theoretically sufficient to image the object under test. The result of image reconstruction is shown in the Figure II-27.

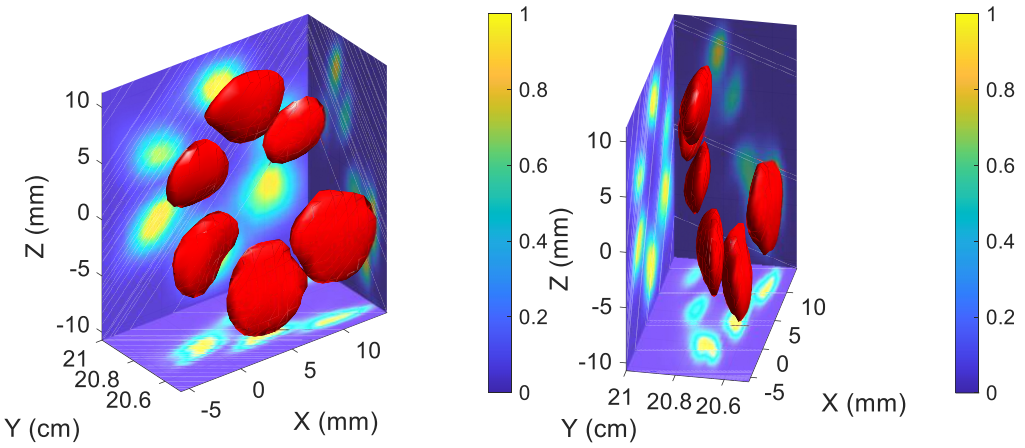

Figure II-27. 3D reconstructed image and the corresponding projections on XOY, XOZ, and YOZ planes, presented from two different angles to showcase the 3D expansion of the image. The 3D image is reconstructed in the frequency bandwidth 0.2 THz and 1.25 THz. The projection planes are normalized to the maximum value.

The result shows the isovalues reconstruction of the 3D image of the sample showing 6 spots with different sizes. The largest spot, which is also closer in depth at 20.55 cm, is the spot corresponding to the thinnest triangle. The spots become slightly smaller indicating thicker zones in the sample thus less energy is propagating through as many frequencies are being filtered out due to higher thicknesses. The thickest triangle is farther back in depth at y = 20.9 cm, which is due to the delay of the propagating wave due to the differences in thickness. In fact, the difference in depth between the thinnest triangle and the thickest triangle Δy = 3.5 mm, could be used to find the whole thickness e of the sample using the following equation:

Eq. 32

$$n_g = 1 + \frac{\Delta y}{e} \Rightarrow e = \frac{\Delta y}{n_g - 1}$$

With n_g the group refractive index of the substrate. Using Eq. 32, we find a thickness e = 5.83 mm, a value that closely aligns with the actual thickness of the sample.

Another significant result is the absence of the triangle form in the reconstructed image. Instead of a triangular shape, each step appears as a round spot. As explained previously, this deviation occurs because, during each antenna position, the complete illumination of the object prompts more scattering at the edges and corners of the triangles compared to their central areas. Moreover, the image is filtered by the PSF of the synthetic array. Consequently, the reconstructed image displays a rounded shape for each step.

This particular phenomenon is not present in raster scan imaging because each pixel in the image derives from an individual scan of a small area, effectively minimizing the scattering effect. The figure below illustrates the result of raster scanning the same object, with an image resolution of 0.5 mm in both directions. The measured signal's bandwidth is filtered to match the size of the bandwidth used to reconstruct the SA image, and the signals undergo the same amount of averaging as in the SA acquisition process.

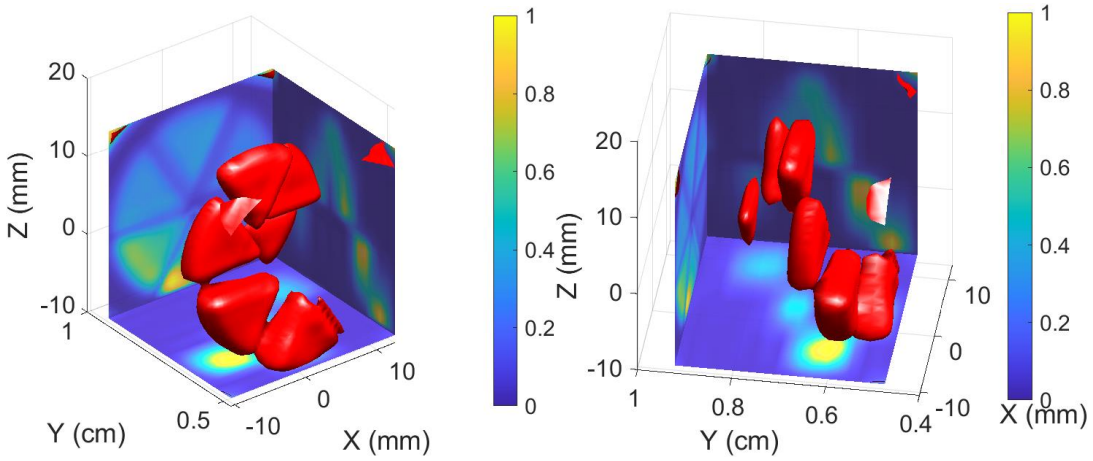

Figure II-28. 3D image acquired by raster scanning the object under test and the corresponding projections in the XOY, XOZ and YOZ planes, presented from two different angles to showcase the 3D expansion of the image. The spectrum is limited to the bandwidth between 0.2 THz and 1.25 THz. The scanning resolution is 0.5 mm.

In contrast to the diffraction effects observed in the SA reconstructed image, the raster scan image distinctly portrays the triangular shape for each step. On the other hand, similarly to the first demonstration, the SA approach involves maintaining the sample stationary, whereas raster scanning necessitates a suitable support for attachment to a mechanical arm to facilitate sample movement. Similar to before, the proposed method offers a complementary approach rather than advocating for the complete replacement of raster scanning imaging methodology. Both methods necessitate compromises to adapt to the constraints imposed by the object under examination.

II.3. Terahertz spectroscopy based on synthetic aperture imaging

II.3.1. Theoretical approach

In our application, we utilize the SA technique not only for imaging but also for spectroscopy purposes. The complex reconstructed data is used to extract the frequency-dependent refractive index $n(f)$ and the absorption coefficient $\alpha(f)$. Similar to classical THz-TDS measurements, our approach necessitates the acquisition of both reference and sample signals. In our study, we obtained the reference and sample data under identical conditions, employing an identical synthetic antenna array, much like the configuration employed for capturing the sample data. The reference measurements were conducted without the presence of the imaging object. Following the reference data acquisition, we independently reconstruct a reference complex transmittivity, denoted as $\tilde{T}_{re_{reference}}(f, x_p, z_p)$ by applying Eq. 25. This provides a frequency-dependent reconstructed spectrum at each pixel, serving as a reference spectrum for the corresponding pixel in the sample complex transmittivity $\tilde{T}_{re_{object}}(f, x_p, z_p)$.

Based on these reference and sample reconstructed transmittivities, we calculate the complex transmission coefficient of the object at each frequency f using the following equation:

Eq. 33

$$\frac{\tilde{T}_{re_{sample}}(f, x_p, z_p)}{\tilde{T}_{re_{reference}}(f, x_p, z_p)} = \rho_{re}(f, x_p, z_p) e^{-j\varphi_{re}(f, x_p, z_p)}$$

This ratio yields $\rho_{re}(f, x_p, z_p)$ and $\varphi_{re}(f, x_p, z_p)$, representing the amplitude ratio and phase difference, respectively, between the spectral components of the sample and the reference reconstructed transmittivities.
Consequently, we can derive the real part of the refractive index $n(f, x_p, z_p)$, its imaginary part $\kappa(f, x_p, z_p)$ and the absorption coefficient $\alpha(f, x_p, z_p)$ for every pixel of the reconstructed object image using the following equations [165]:

Eq. 34

$$n(f, x_p, z_p) = 1 + c\frac{\varphi_{re}(f, x_p, z_p)}{2\pi f e}$$

Eq. 35

$$\kappa(f, x_p, z_p) = -\frac{c}{4\pi f e}\ln\left(\tau(f, x_p, z_p)\rho_{re}(f, x_p, z_p)\right)$$

Eq. 36

$$\tau(f, x_p, z_p) = 1 - \frac{\left(n(f, x_p, z_p) - 1\right)^2}{\left(n(f, x_p, z_p) + 1\right)^2}$$

Eq. 37

$$\alpha(f, x_p, z_p) = \frac{4\pi f}{c}\kappa(f, x_p, z_p)$$

The thickness of the sample e is measured with a digital micrometer gauge (with a precision of +/- 1 µm) before conducting the imaging and spectroscopy experiments. The measured thickness serves as an input parameter for calculating the aforementioned parameters from the reconstructed data.

II.3.2. Experimental results

We present spectroscopy results for a multi-material planar object.

To demonstrate this capability, we present the imaging and spectroscopy of a planar multi-material object, which includes metal, quartz, and Magnesium oxide (MgO). Quartz and MgO are selected for this characterization due to their widespread popularity in the THz region, driven by their unique properties that find application in various fields. Quartz, made of silicon dioxide (SiO2) [166], serves as an excellent substrate for optically characterizing non-free-standing THz samples due to its minimal absorption and high transmission. Its applications extend to creating efficient dielectric THz devices like waveguides and polarization-converting components [167]. Additionally, under specific conditions, quartz exhibits birefringence, enabling its use in THz optics [168]. MgO, a widely used wide bandgap semiconductor, is integral to developing new materials and plays a crucial role in THz components, such as quasi-optic and nonlinear parametric devices, showing significant gains in applications like THz parametric amplifiers [169] and Cherenkov radiation-based THz pulse generation using MgO:LN [170], [171]. MgO is chosen for its ability to prevent crystal damage in the THz range.

The substrates are incorporated into a thin metallic plate, with a planar surface of 2 x 2 cm², featuring four open circular holes with varying diameters ranging from 3 mm to 6 mm (Figure

II-29). Specifically, the 530 µm-thick MgO sample is positioned behind the 6 mm diameter hole, while the quartz sample, also 530 µm thick, is placed behind the 5 mm diameter hole. For image reconstruction, the frequency range utilized was from 0.6 THz to 1 THz, employing an array size of 10×10 cm². This resulted in a cross-range resolution of $\delta_z \approx \delta_x = 1.05$ mm and a range resolution of $\delta_y = 750$ µm. The spacing between antennas (step d = 2 mm) was determined to ensure a FOV that adequately covers the object's surface under examination.

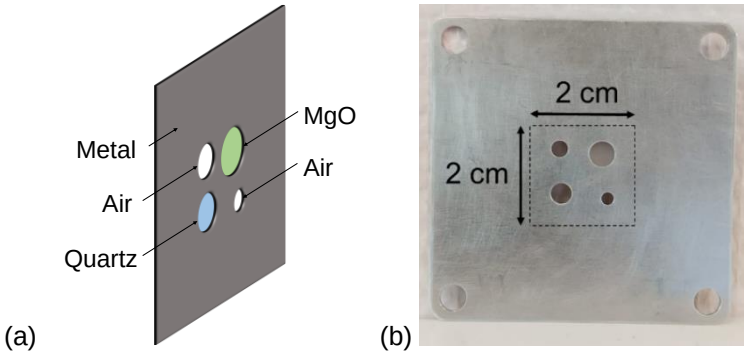

Figure II-29. (a) Schematic and (b) photograph of the object under test: a metallic plate of 2x2 cm² with four holes, two holes with diameters 6 mm and 5 mm containing MgO (false-colored in green) and quartz (false-colored in blue) respectively. The other smaller holes of 3 and 4 mm contain air. The thickness of the two substrates is e = 530 µm.

The intensity of the reconstructed 3D image, shown in Figure II-30, effectively reproduces the shapes of the four holes, accurately representing their spatial positions on the metallic plate.

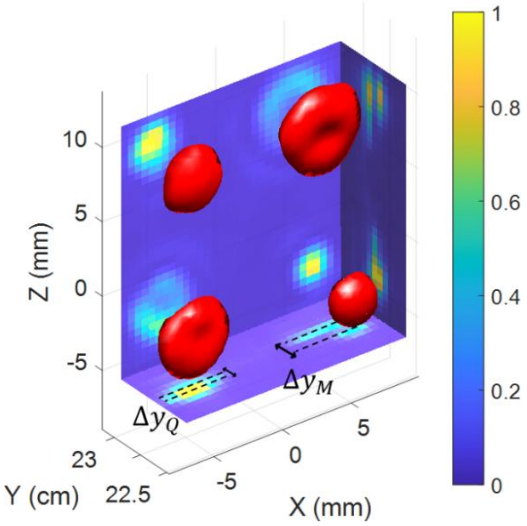

Figure II-30. reconstructed 3d of the sample under test I the frequency bandwidth between 0.6 THz and 1 THz, and the associate projections on XOY, XOZ, and YOZ planes.

The 2D projection of the 3D image on the XOZ plane shows a disparity in the reconstructed amplitude at each hole. This is due to the differences in the refractive index of the different materials. In fact, the reconstruction process operates under the assumption that THz wave propagation occurs solely in air, disregarding the distinct properties of each material. Moreover, even if the layers of materials share the same depth and thickness, this assumption results in evident depth delays observed in the projection of the 3D image onto the XOY plane.

The distinct spatial depths between the reconstructed zones of different materials allow for retrieving the group refractive index values using Eq. 32. For instance, considering a distance $\Delta y_Q = 0.5$ mm between the reconstructed quartz area and air, the group refractive index of

quartz is determined as n_{gQ} = 1.94. Similarly, for MgO (Δy_M = 1 mm), the group refractive index is calculated as n_{gM} = 2.88. In Figure II-30, the projections onto the XOY and YOZ planes originating from the areas of MgO and air are visibly distinct, with a spatial depth between the two reconstructed zones surpassing the depth resolution of our synthetic array (δ_y = 0.75 mm). Conversely, the separation corresponding to the projections of quartz and air is less visible (Δy_Q < 0.75 mm).

To further demonstrate the capabilities of the proposed approach for material characterization, the reconstructed data is used to extract the refractive index and absorption coefficient as indicated in the previous section. Based on the reference and sample reconstructed transmittivities, a complex transmission coefficient of the object is calculated at each frequency. Using an inverse Fourier transform, the time domain reconstructed signals of the reference time domain signal through air and through the quartz and MgO samples after the reconstruction of the image are presented in Figure II-31.

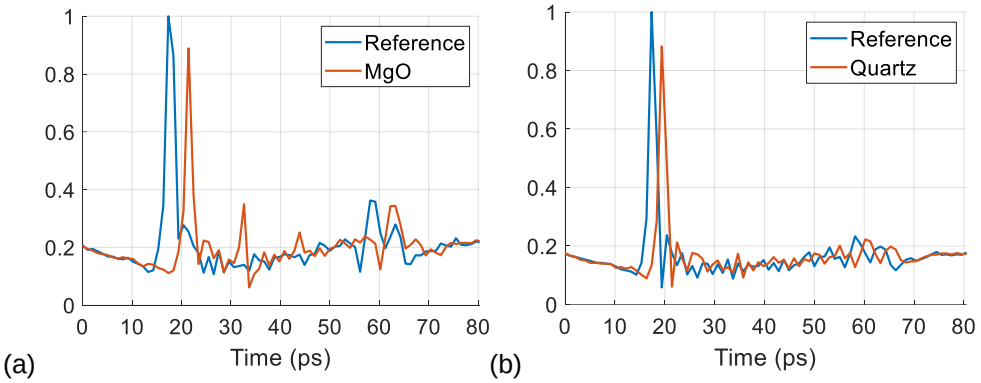

Figure II-31. The normalized amplitude of the complex envelope of the reconstructed temporal signals through the MgO and quartz samples: (a) MgO at x_p = 6 mm and z_p = 5 mm (orange curve) and the reference temporal signal corresponding to the same reconstructed coordinates (blue curve). (b) Quartz at x_p = -3mm and z_p = -3mm (orange curve) and the corresponding reference reconstructed temporal signal (blue curve).

The selected materials are non-dispersive and each of them have a thickness of 530 µm, which is thick enough for the propagated short pulse to create an isolated echo pulse from the main signal. The transmitted temporal signal through the quartz does not display any visible multiples, while MgO exhibits one reflection peak after a trip in the substrate since it has a higher refractive index than quartz. In this particular case, the echo on the temporal signal can be removed using simple windowing techniques in the same way echoes could be removed when using a classical THz-TDS set up for material characterization.

After computing $n(f, x_p, z_p)$ using Eq. 34, the frequency dependent refractive index, taken at the center pixel of the holes containing quartz (blue curve) and MgO (orange curve), are presented in Figure II-32.a from 0.6 THz to 1 THz (which is the frequency band chosen beforehand for image reconstruction). The average refractive index on the investigated frequency band of MgO is $n_{M_{avg}} = 3.01$ and the average refractive index of quartz is $n_{Q_{avg}} = 2.07$, values which are consistent with previous reports [166], [172].

The absorption coefficient of each pixel of the reconstructed image of the object is calculated using Eq. 37. In Figure II-32.b, the absorption coefficient of the center pixel of the hole containing quartz (blue curve) and the center pixel of the hole containing MgO (orange curve) are presented from 0.6 THz to 1 THz. The absorption coefficient of quartz is extremely low, less than 1.5 cm^{-1} in magnitude, the material being nearly transparent between 0.6 THz and

1 THz [166]. The MgO sample also presents a very low absorption coefficient of less than 3 cm^{-1} between 0.6 THz and 1 THz [172].

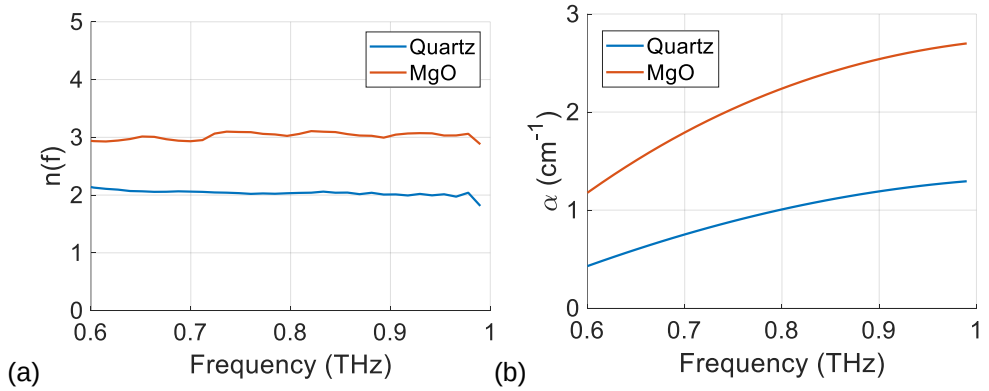

Figure II-32. (a) Frequency dependent refractive index computed from reconstructed data using Eq. 34 at two different coordinates: quartz at x=-3mm and z=-3mm (blue curve) and MgO at x=6mm and z=5mm (orange curve). (b) Frequency dependent absorption coefficient computed from reconstructed data using equation (9) at the same coordinates of quartz (blue curve) and MgO (orange curve). The reference measurement for the absorption coefficient is obtained using the metallic object without the dielectric substrates.

From the computed $n(f, x_p, z_p)$, 2D maps of the refractive index of the object could be reconstructed at each frequency of the reconstruction frequency band. As shown in Figure II-33, the index of the areas of the air holes, quartz and MgO samples are correctly reconstructed at 0.6 THz and 1 THz, emphasizing the interest of SA-TDS for imaging and material characterization in the THz rang. A higher resolution could be attained by placing the system in a dry air chamber to access higher frequencies of the THz spectrum generated by the TDS.

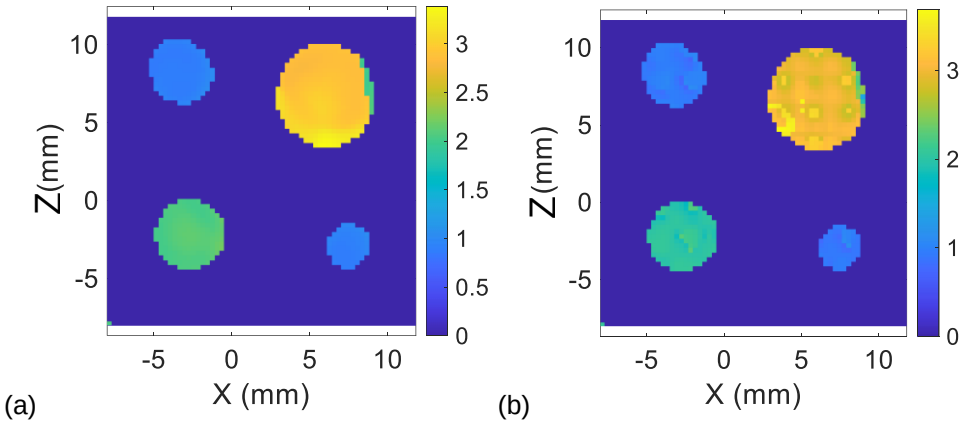

Figure II-33. 2D maps of the reconstructed refractive index of the dielectric samples within the imaged object at two different frequencies (a) at 0.6 THz and (b) at 1 THz. The 3D imaging performed beforehand is used to define the areas of interest, in which the refractive index reconstruction could be performed. The area of the metallic plate is set with a null refractive index for the visual aspect.

We further demonstrate the pairing of SA technique and spectroscopy analysis of the object under test, by using the reconstructed amplitude and phase to obtain the refractive index and the absorption coefficient, which enables 2D spectroscopy mapping for each frequency of the investigated reconstruction band.

Having established the efficacy of SA imaging and spectroscopy, we aim to further enhance a crucial aspect of this approach: the acquisition time. Our demonstration revealed that despite

performance differences between SA imaging and raster scan imaging, the required acquisition time for both methods remains very close for the same FOV and resolution settings.

This leads us to propose building on the SA approach to optimize the acquisition time, which is not a possible option in the case of raster scan imaging. We demonstrate that numerical image reconstruction offers a degree of “flexibility”, allowing a reduction in acquisition time while maintaining comparable image quality to that achieved with a complete dataset. This reduction in collected data is achieved through sparse sampling, a technique that will be elaborated upon in the subsequent section, outlining its implementation and benefits.

II.4. Sparse sampling for shorter acquisition time

2D mechanical scanning is time-consuming, presenting a significant drawback. Sparse 2D arrays offer an alternative approach by reducing the number of active elements within antenna systems. This reduction is achieved by scanning only a portion of the positions covered by a full planar 2D array. For effective data acquisition and subsequent image reconstruction, this subset of scanned positions must adhere to specific spatial distribution conditions. These conditions are primarily related to the size of the array and the acceptable spacing between antennas within the sparse array configuration.

Traditionally, sparse arrays have been based on many distributions, including random distributions and motif-based distributions, such as circular [144] or spiral arrays and square matrix arrays [141]. While numerous optimization algorithms are available in the literature to select array elements that produce the most suitable image based on given constraints [173], [174], [175], our work focuses on demonstrating the feasibility of sparse sampling using a planar synthetic array of PCAs powered by the TDS system. Our goal is to determine a minimal number of antennas needed to maintain certain performance levels compared to a full array, based on relevant parameters. In this study, we do not delve into optimizing the spatial distribution of the proposed sparse array.

In our specific application context, and with the same number of antennas, we observed no significant differences when experimenting with various array architectures, ranging from random distributions to rectangular spiral and circular spiral arrays. For this demonstration, we selected a spiral synthetic array, specifically the Archimedes spiral (Figure II-34) (also known as the arithmetic spiral), due to its straightforward mathematical formula [176]. In polar coordinates, the Archimedes spiral is represented as follows:

Eq. 38

$$r(\theta) = a + b.\theta$$

where r refers to the distance from the sampling point to the origin of polar coordinates, θ refers to the angle between the line from the sampling point to the origin and the polar axis, a is the distance from the central position of spiral-sampling pattern to the origin, i.e., when θ = 0°, and b is the increment of r for unit angular. This equation can be converted to Cartesian coordinates, as presented in Figure II-34, calculated as follows:

Eq. 39

$$\begin{cases} x = r(\theta).\cos(\theta) \\ z = r(\theta).\sin(\theta) \end{cases}$$

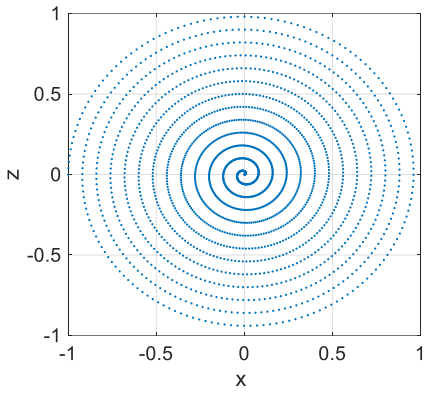

Figure II-34**.** Classical Archimedes spiral-pattern.

To derive a sparse array in the shape of a spiral from a full planar array, all the sampling points of the spiral must cover all the rows and columns of the full array. In other words, the diameter of the largest circle within the spiral must precisely match the size of the full array D. Each point on the spiral function is then associated with the nearest grid point on the rectangular grid within the full-sampling pattern.

Preserving the full-size D ensures the retention of the same cross-range resolution achieved with the full array. This is validated by Figure II-35 which illustrates the reconstruction of the PSF using previously acquired experimental data using the array of 10×10 cm² and d = 2 mm in the frequency range between 0.6 THz and 1 THz. By maintaining the largest circle's diameter at D = 10 cm, we reconstruct the PSF of multiple arrays with three different sampling rates Figure II-35. 100% sampling rate means we kept the full planar array (blue trace). 40% sampling rate means we chose the appropriate number of turns of the spiral form to keep 40% of the antennas active and eliminate 60% of the antennas (orange trace). 8% sampling means the spiral was chosen to keep only 8% of antennas active and eliminate 92% (yellow trace). We can confidently achieve the same cross-range resolution for different sampling rates, as the size of the PSF at -3 dB is identical for all traces.

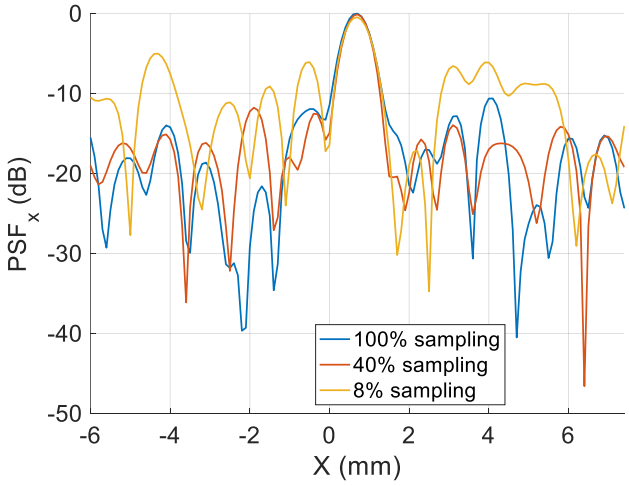

Figure II-35. Reconstructed PSF in x-direction in dB using three different synthetic arrays with three different sampling ratios, 100% as in full array (blue trace), 40% sampling (orange trace) and 8% sampling (yellow trace).

Nevertheless, the side lobes level increases significantly when reconstructing the PSF using only 8% of the full array (Figure II-35, yellow trace).

To evaluate the performances of sparse sampled array, we employ the calculation of the Normalized Root Mean Square Error (NRMSE) [177] between the PSF derived from the full 2D array and that obtained from the sparse array. This parameter enables the assessment of the overall structural similarity between the two images, considering the entire image as a whole rather than emphasizing a single parameter.

NRMSE measures the amount of change per pixel and normalizes it by the root mean of the reference image, which, in this case, is the PSF reconstructed using the full array. NRMSE values range from 0 to 1, with 0 indicating identical images and 1 indicating completely different images. The NRMSE between a reference image I_{ref}, and the sparse image I is given by:

Eq. 40

$$NRMSE = \frac{\sqrt{\frac{1}{P}\sum_{p=1}^{P}\left(I(p) - I_{ref}(p)\right)^2}}{\sqrt{\frac{1}{P}\sum_{i=1}^{N} I_{ref}(p)^2}}$$

With P the total number of pixels of the PSF images.

To generate various sampling ratios, we vary the number of turns of the spiral while keeping the diameter of the largest circle constant. Experimentally, for each sampling ratio, we reconstruct and store the 2D PSF for comparison with the PSF of the full array using the NRMSE. Figure II-36 illustrates the evolution of the NRMSE across different sampling ratios, ranging from 10% to 55%.

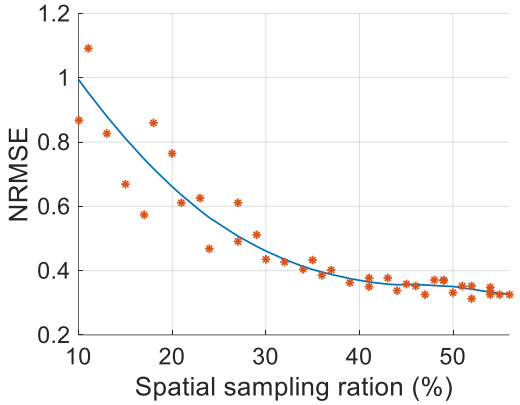

Figure II-36. Calculated NRMSE of reconstructed PSF images using sparse arrays with different sampling ratios in reference to a reference PSF image reconstructed using a full planar array. The blue trace is an indication of the tendency of the points, which is used to evaluate the evolution of the NRMSE more clearly.

The NRMSE decreases for higher sampling ratios and demonstrates stabilization at around a 40% sampling ratio. As a result, the subsequent experimental demonstration will be based on a sparse array with a 40% sampling ratio.

Furthermore, the reduction in the number of antennas leads to a decrease in the amplitude of the reconstructed signal. Indeed, as mentioned at the beginning of this chapter, each voxel in the image is the sum of the back-propagated signals from the antenna array. This summation (when coherent) increases the signal-to-noise ratio as a function of the number of antennas used. Although theoretically a limited number of antennas could give the same image quality at infinite SNR, this quality can be strongly affected under experimental conditions. This is demonstrated in Figure II-37, where the spectral amplitude in dB of the central pixel of the PSF

reconstructed using three arrays with different sampling rates are presented. Specifically, the presented amplitudes depict a higher SNR for the full array (100% sampling rate), exhibiting a decrease when reconstructing the PSF using a sparse array with 40% sampling. The SNR further diminishes with an array having an 8% sampling rate.

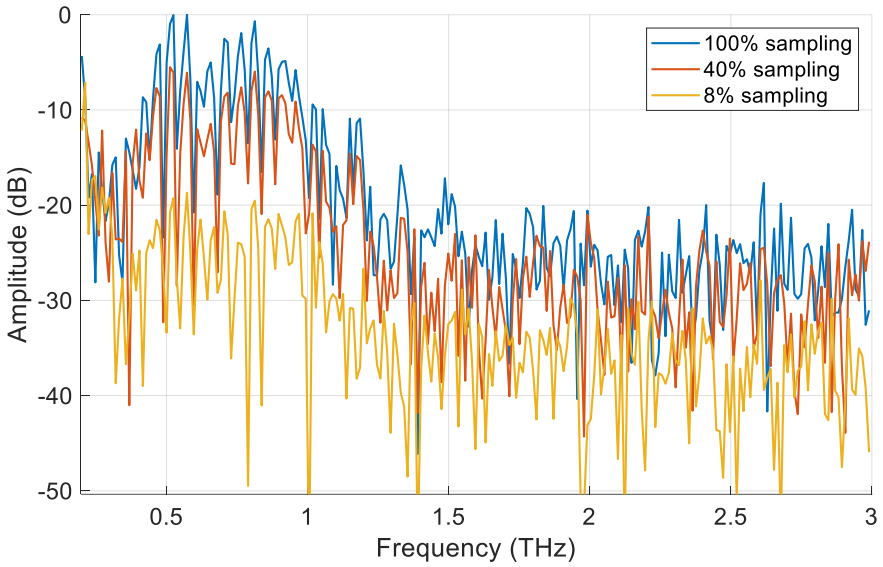

Figure II-37. Amplitude in dB of the central pixel of the PSF between 0.6 THz and 1 THz, reconstructed using three different synthetic arrays with three different sampling ratios, 100% as in full array (blue trace), 40% sampling (orange trace) and 8% sampling (yellow trace).

II.4.1. Imaging results and comparison with a full array

In our experimental setup, we achieved sparsity in the spiral array by selectively removing temporal signals detected from positions in the full array. Alternatively, it's possible to directly move the motorized stage to follow a specific pattern and create a sparse array without scanning the entire plane (Figure II-38).

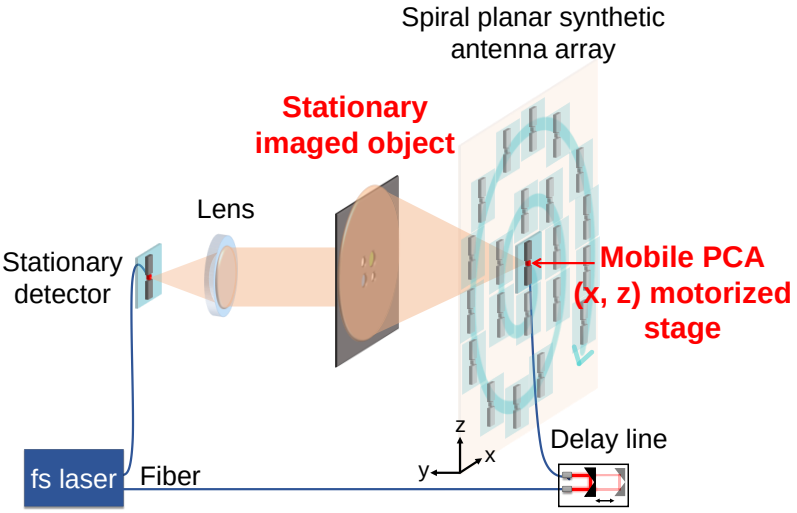

Figure II-38. Schematic of SA imaging in a transmission configuration using a sparse synthetic array.

In Figure II-39, we present the reconstruction results using a full array as a reference, and the array with 40% sampling, as recommended by the NRMSE parameter result. We chose to present the results for this object under test as we are interested in testing the sparse array for spectroscopy, not just imaging.

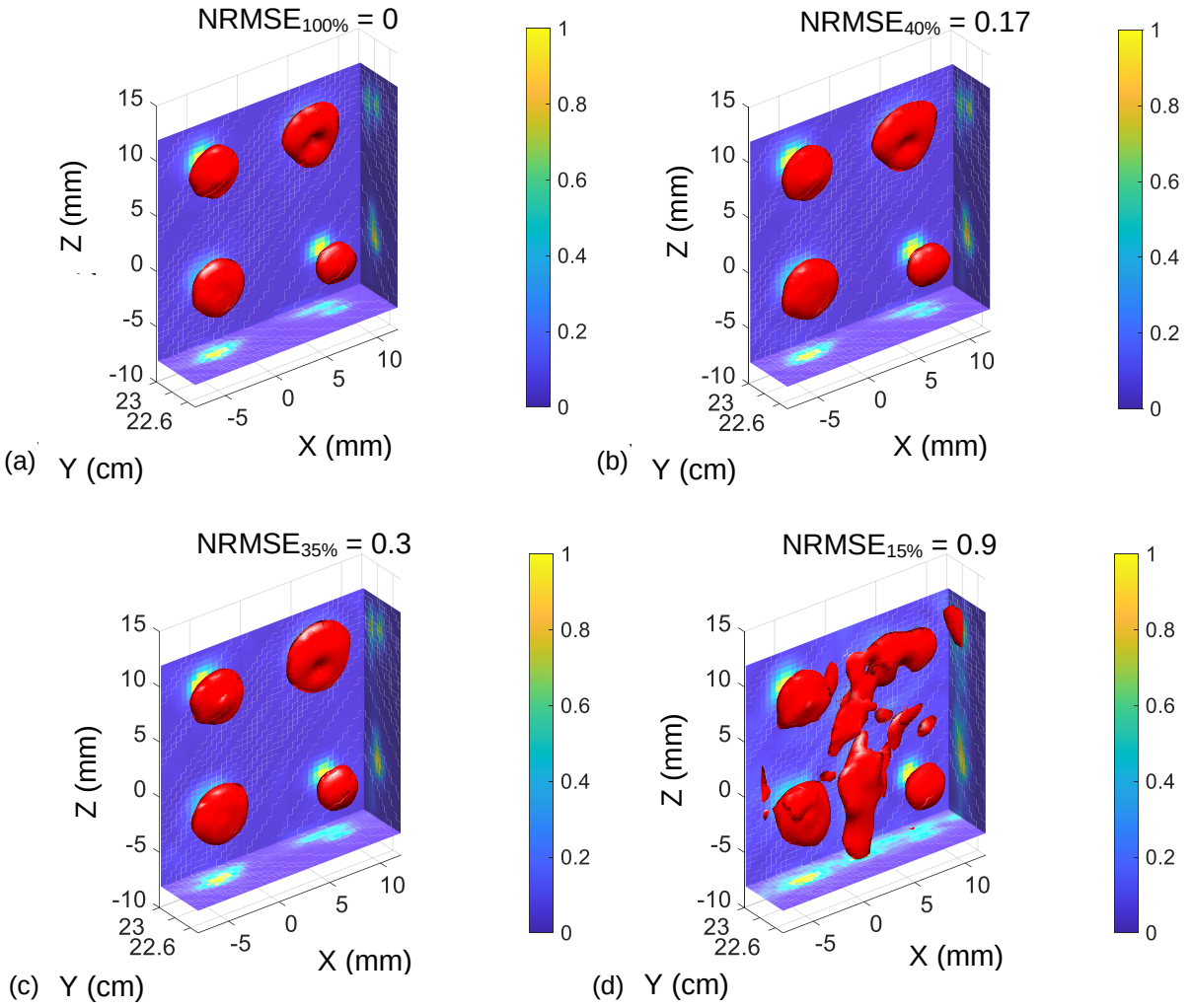

Figure II-39. 3D images and associate projections on XOY, XOZ, and YOZ planes, reconstructed between 0.6 THz and 1 THz using a (a) full sampled array (b) an array with 40% sampling rate, (c) an array with 35% sampling rate and (d) an array with 15% sampling rate.

We also include the reconstruction results using sparse arrays with lower sampling rates to demonstrate the effect of under-sampling on the reconstruction outcome. While the impact is evident with the 15% sampling, we observe minimal differences in the 35% sampling array, highlighting the need for quantifying parameters of the effect of the sampling rate.

To quantify these differences, we introduce the Structural Similarity Index Measure (SSIM), which quantifies image quality degradation based on visible structures in the image [177]. SSIM measures the perceptual difference between two similar images and has values ranging from -1 to 1, where 1 indicates perfect structural similarity:

Eq. 41

$$SSIM(x,y) = \frac{(2\mu_x\mu_y + c_1)(2\sigma_{xy} + c_2)}{(\mu_x^2 + \mu y^2 + c_1)(\sigma_x^2 + \sigma_y^2 + c_2)}$$

With μ_x the pixel sample mean of x, μ_y the pixel sample mean of y, σ_x^2 the variance of x, σ_y^2 the variance of y, σ_{xy} the covariance of x and y, $c_1 = (k_1 L)^2$, $c_2 = (k_2 L)^2$ two variables to stabilize the division with weak denominator with L the dynamic range of the pixel-values, $k_1 = 0.01$ and $k_2 = 0.03$ by default [178].

MATLAB provides a pre-built SSIM function that will be employed for the subsequent analysis. We calculate SSIM for each pixel of the image to create 2D maps indicating zones of similarity and dissimilarity between the image reconstructed with the sparse array and the reference image, as shown in the Figure II-40 for different arrays.

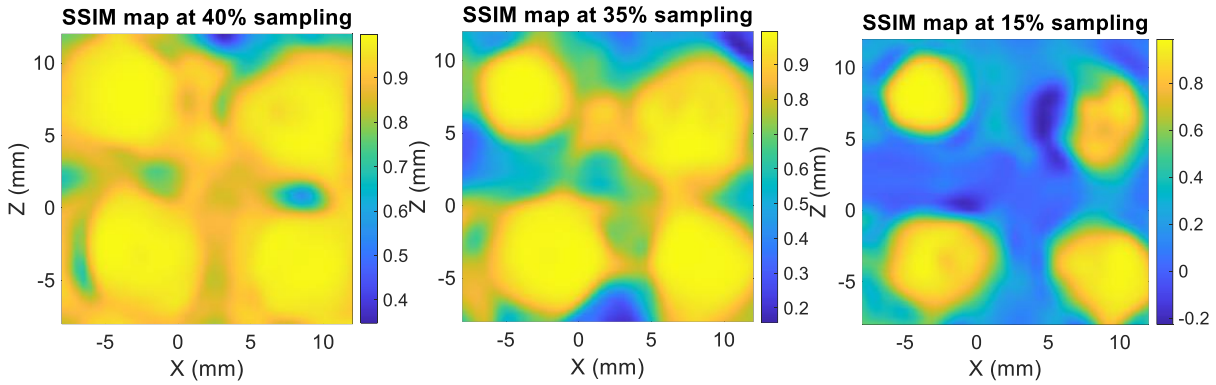

Figure II-40. Structural Similarity Index Map calculated for three different resulted reconstructed images using three different sparse arrays with 40%, 35% and 15% sampling rate. Pixels with higher intensity (yellow) show the zones where the reconstructed image using the sparse array and the full array are similar. The lower intensity values (blue) show where the reconstructed images are not similar indicating the regions where the image quality degrades in comparison to the reference image.

Based on the SSIM maps, the high intensity in the first maps indicates a high similarity between the two reconstructed images, confirming the sufficiency of 40% sampling. However, as the sampling rate decreases, the local SSIM values decrease, indicating increased dissimilarity due to low sampling. We can also calculate a global SSIM value for the entire image rather than pixel-by-pixel local values. The global SSIM values for the images reconstructed using 40%, 35%, and 15% sampling are 0.9, 0.77, and 0.42, respectively.

We conclude that a sparse array was able to produce very similar results to a full linear array. Quantitative parameters effectively demonstrated the level of disparities between the outcomes. However, the sparse spatial sampling approach cannot be adapted in the raster scan approach due to its reliance on direct pixel acquisition, wherein any missed pixels would appear as dark areas on the image. This fundamental distinction represents a critical and conclusive contrast between raster scan imaging and SA imaging, highlighting a significant advantage offered by SA imaging in reducing acquisition time. It's important to note that diffraction phenomenon and the related issues associated with SA imaging are always present using sparse sampling. Hence, adopting this approach necessitates a compromise based on the specific imaging scenario and the intended application context.

II.4.2. Terahertz spectroscopy based on sparse synthetic aperture imaging

We demonstrate that using a sparse array with 40% sampling does not affect the calculated refractive index and absorption coefficient of the materials. Following the same previously detailed procedure, we obtain the results in Figure II-41.

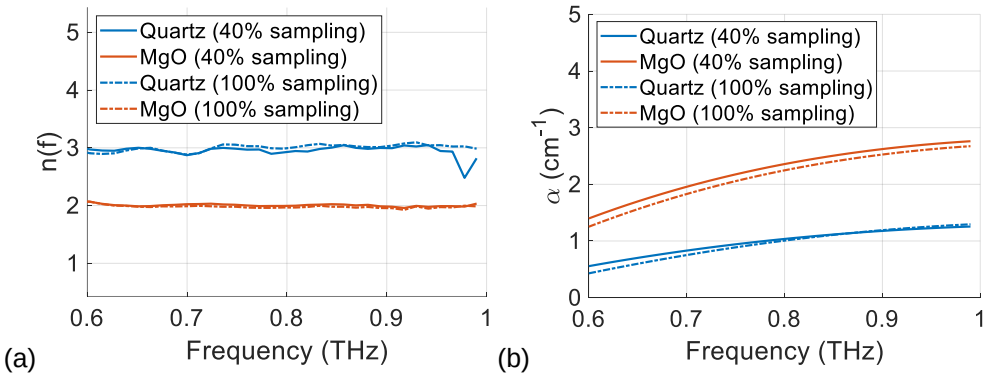

Figure II-41. Material characterization results using a sparse array with 60% less antennas. (a) Frequency dependent refractive index computed from reconstructed data using equation (6) at two different coordinates: quartz at x=-3mm and z=-3mm (blue curve) and MgO at x=6mm and z=5mm (orange curve). (b) Frequency dependent absorption coefficient computed from reconstructed data using equation (9) at the same coordinates of quartz (blue curve) and MgO (orange curve). The reference measurement for the absorption coefficient is obtained using the metallic object without the dielectric substrates.

In the same way, 2D maps of the reconstructed refractive index could be assembled, and we can see that the same results as with the full array are obtained.

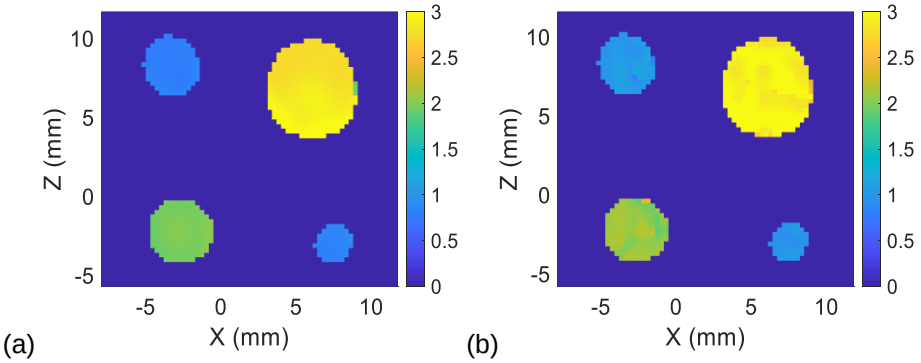

Figure II-42. 2D maps of the reconstructed refractive index of the dielectric samples within the imaged object at two different frequencies (a) at 600 GHz and (b) at 1 THz. The 3D imaging performed beforehand is used to define the areas of interest, in which the refractive index reconstruction could be performed. The area of the metallic plate is set with a null refractive index for the visual aspect.

Thus, for similar results, we are able to reduce acquisition time with 60% for both imaging and spectroscopy purposes.

II.5. Conclusions and discussions

This study has introduced a novel approach, employing SA imaging in transmission configuration within a broadband TDS system for both 3D imaging and spectroscopy. The objective was to create a versatile imaging configuration capable of accommodating the diverse samples encountered across various domains. To achieve this, our work involved several stages, ensuring the system's functionality and optimizing its performance using available experimental components.

Prior to the experimental demonstration, measurements were conducted on the radiation patterns emitted by a broadband PCA powered by the TDS. This aimed to optimize SA creation, involving comprehensive assessments of the emitter antenna's radiation pattern. The results revealed a smooth E-plane radiation resembling a Gaussian distribution, while the H-

plane exhibited secondary lobes. Through rigorous analysis, we identified an optimal bandwidth range from 0.2 THz to 2.5 THz, strategically balancing various factors such as secondary lobes, noise, high frequencies, and dynamic range.

The impact of radiation patterns and frequency bandwidth on image reconstruction was thoroughly analyzed. Simulations highlighted that resolutions reached a saturation point when using arrays of 10 cm and above due to the inherent relationship between resolution and object illumination. Experimental implementation using the TERA K15 THz-TDS system validated simulated resolutions closely, yielding cross-range resolutions of δx = 850 µm and δz = 930 µm. To manage computational load, intricate object imaging was performed within sub-frequency bands after establishing fundamental performance metrics across the bandwidth.

SA imaging successfully reconstructed planar and 3D object images. A comparative analysis between our proposed SA imaging and the traditional raster scanning approach revealed nuanced differences and similarities. The primary distinctions stemmed from the methodology: SA imaging illuminates the entire object, leading to complex interactions, while raster scanning focuses on small sections at a time. However, the raster scan approach requires mechanical translation of the object, contrasting with SA aperture imaging, where the object remains stationary while the emitter moves during acquisition, catering to a wide range of samples. However, both approaches exhibited similarities in acquisition time under equivalent settings and produced 3D images influenced by material characteristics in depth due to propagation in air.

A significant outcome of this work is the application of SA for spectroscopy, yielding consistent calculations of refractive index and absorption coefficients from reconstructed data. Spectroscopy results for multi-material planar objects utilizing the reconstructed data highlighted the potential of this approach.

Moreover, introducing sparse sampling into our methodology marked a crucial milestone, reducing acquisition time by 60% while maintaining performance standards. This achievement was further substantiated by consistent spectroscopy results, affirming the efficacy of sparse sampling in obtaining accurate material characteristics.

In summary, this chapter underscores the effectiveness of SA imaging using a TDS system in transmission configuration, showcasing its advantage in reducing acquisition time compared to raster scan imaging via sparse sampling implementation. However, the choice between methodologies requires careful consideration of trade-offs and specific application demands. Nonetheless, SA imaging has demonstrated robustness in providing accurate spectroscopic data, affirming its potential in material characterization.

Looking forward, the proposed system could be used for polarimetric imaging to understand the polarization properties of an imaged sample. Polarization filters are integrated into a TDS system to allow multiple configurations of polarization imaging [179]. Polarimetry imaging using SA technique will allow the inspection of polarization characteristics of a wider range of objects under test. In addition to that, our study presents promising prospects for real-time THz imaging by exploring sparse sampling with real planar arrays of PCAs, potentially reducing system costs while delivering instantaneous imaging in the THz range with acceptable performance. Moreover, the development of PCAs with wider divergence and higher efficiency at higher frequencies holds promise for enhancing cross-range resolution using SA imaging, expanding the capabilities of THz imaging technology.

Chapter III. Synthetic aperture for terahertz fibers characterization

III.1. Introduction

In the previous chapter, we have demonstrated a THz imaging and spectroscopy approach in transmission configuration, that allows the object under test to remain stationary. This chapter is dedicated to the demonstration of an interesting application of this approach where the object under test will benefit greatly from this experimental disposition provided by SA technique applied with the TDS system. This object under test is a THz fiber (could also be called a THz waveguide). The work presented in this chapter is divided into two distinct sections, illustrated in the schematic in Figure III-1.

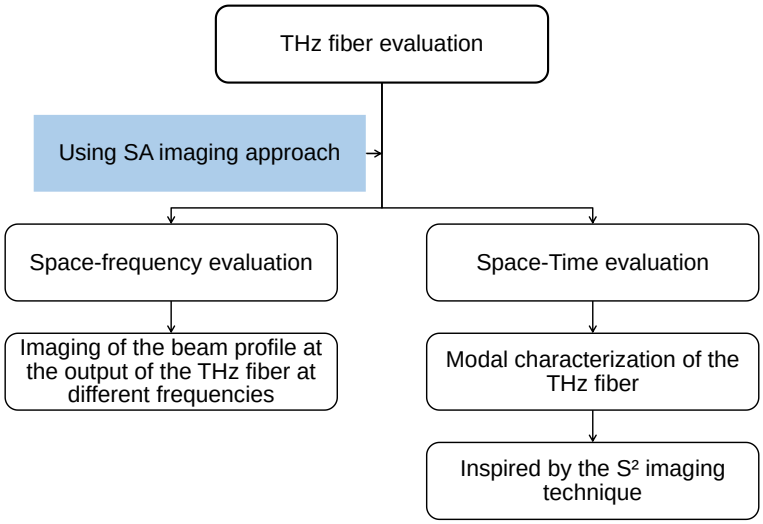

Figure III-1. Schematic summarizing the content of this chapter.

Our work aims to demonstrate the use of SA in imaging both time domain and spectral distributions of a propagated beam at the THz fiber output.

This chapter starts with the spectral evaluation, where we reconstruct 2D transverse images (beam profile) of the THz fiber output at various frequencies within the THz band. We also evaluate the evolution of the spectral beam across frequency to conclude on the modal behavior of the fiber.

The second part of our work involves the temporal assessment of the propagated THz beam within the fiber. Here, we use SA imaging with an approach inspired by a method known as spectrally and spatially resolved imaging (S^2 imaging), commonly used in the optical domain. This method allows to experimentally extract the modal content of optical fibers, identified from their respective group delays.

III.2. Context

THz fibers predominantly feature hollow-core structures [180], where light is essentially guided within an air channel, while the outer cladding serves as a confining structure. This preference stems from the distinct characteristics of THz waves that cause most dielectric materials to be absorbent in the THz domain [181]. Notably, the absorption coefficient of TOPAS rises from about 35 dB/m at 0.5 THz up to 190 dB/m at 1.5 THz [182]. However, dry air stands out as the primary transparent medium viable for use at THz frequencies. Consequently, opting for a hollow core fiber stands out as the optimal choice for guiding THz radiations, effectively minimizing propagation losses. A hollow pipe with a thin cladding is an example of a hollow

core guiding structure of THz waves, which is based on the anti-resonance guiding mechanism. Using the pipe fiber, the dielectric cladding of the hollow fiber acts as a Fabry-Perot resonator where the wave crosses the dielectric layer at resonance frequencies, while it reflects under the anti-resonance condition leading to wave confinement in the air channel.

The beam profile at the output of a fiber plays a crucial role in determining its performance. Analyzing this profile is essential to understand the fiber's guiding properties [183]. TDS system-based techniques for imaging the beam profile of a THz fiber are based on near-field microscopy imaging approach. The experimental setup of this approach is presented in Figure III-2:

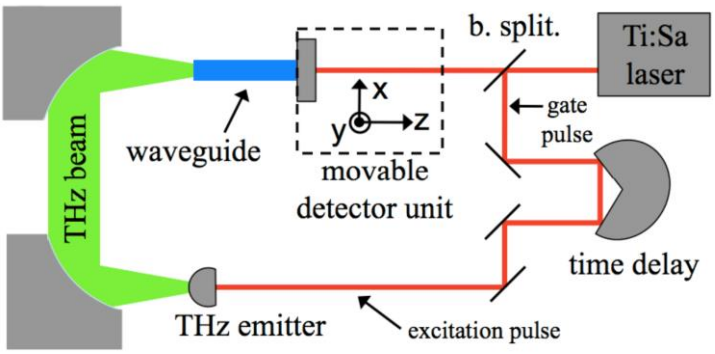

Figure III-2. Schematic of the THz near-field microscopy setup for fiber mode profiling.

A THz near-field microscopy system is based on the implementation of PCA acting as the coherent THz pulse source and as a near-field probe. The PCA near-field probe is a concept borrowed from near-field scanning optical microscopy (NSOM) [184]. At optical frequencies, a silver coated optical fiber with a tip window of tens of nanometers wide is placed close to objects and collects and deliveries light in the near field Figure III-3.

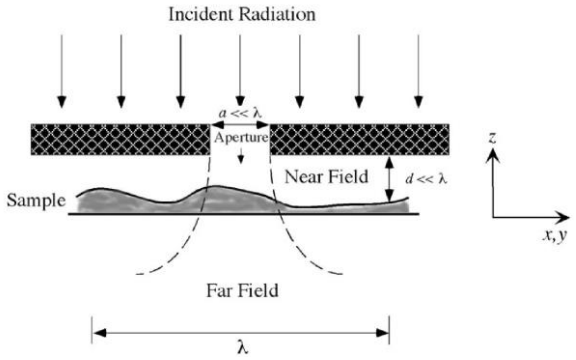

Figure III-3. A sketch showing the basic principles of sub-wavelength resolution in near-field optics. The two critical requirements are: (1) a sub-wavelength light source (radiation source + sub-wavelength aperture), and (2) placing the sample in the near-field zone of the light source [184].

At THz frequencies, an opaque screen with a subwavelength aperture is placed a few micrometers in front of a PCA to improve the spatial resolution. The electric field at the aperture can be mapped by moving the receiver and aperture together (movable detector unit) at the output of the fiber. Near-field information can be obtained by placing the fiber close to the focus of the near-field probe. After Fourier transform of the mapped time-domain data, frequency-dependent, two-dimensional near-field maps of the transverse field are captured. This characterization technique provides subwavelength spatial resolution images with timeframes of sub-picosecond temporal precision. However, a rigorous alignment of the sub-wavelength

aperture with the output end of the fiber is necessary. Additionally, when a fixed sample is raster scanned by moving the detector, one has to take care that the detector is precisely translated together with the excitation laser beam and the focusing optics to maintain the necessary alignment of the components. Moreover, the near-field probe must be placed in close proximity to an object (a few tens of micrometers) to collect transmitted waves and obtain good spatial resolution. The small separation between the probe and the sample causes operational problems. Extreme care has to be taken because the probe can be damaged by contact with samples. Achieving parallelism between the sample plane and the probe scanning plane is also critical to avoid changes in signal strength and resolution due to changes in sample-probe separation.

We propose to explore the SA imaging approach for imaging and characterizing the distribution of the THz beam propagated within the fiber. Our proposed approach does not call for a near-field probe. Instead, we use the previously used PCAs to create a SA at a distance of few centimeters from the output of the fiber. To address the free-space alignment in raster scanning, the development of PCAs at 1550 nm made it possible to have access to fiber-coupled PCAs. The adaptation of the previously demonstrated method to a fiber is quite straightforward as the object under test is replaced with the fiber under test without major technical changes.

On a second note, THz fibers intrinsically support many modes because they usually feature large cores. To image the modes, we propose a new approach based on the integration of SA imaging technique with an additional technique called Spatially and Spectrally (S^2) resolved imaging [6]. This method, typically applied for optical fibers, enables the imaging of modes supported by fibers within their available transmission band.

To demonstrate these propositions, we have selected an antiresonant hollow core THz pipe fiber. It is essential to clarify that our objective in this study is not centered on discussing the fiber's guiding capabilities within the THz region or validating its performance against other fiber structures. Instead, our focal point lies in presenting a novel imaging and characterization approach for a THz fiber in both the frequency and temporal domains. This method holds potential for future application in the testing and development of different THz fibers or radiative structures. The following section is dedicated to the introduction of the antiresonant hollow core THz pipe fiber, which will undergo further analysis in subsequent sections. Our objective is to present a comprehensive theoretical background on the THz fiber's guiding mechanism, accompanied by characterization experimental results.

III.3. Antiresonant hollow core THz pipe fiber

The transverse cross section of an antiresonant hollow-core pipe fiber is presented in Figure III-4. The pipe waveguide has a large air-core (n_{air} = 1) with a diameter A, and a thin ring cladding with a thickness e. Material of the cladding is a dielectric with a uniform refractive index n_d. Polymeric materials such as Topas, Zeonex and PMMA are used to make the cladding of the hollow-core fibers, due to their desirable properties such as the lowest absorption coefficient (reported) and cost-effectiveness [185]. The medium outside the cladding is air.

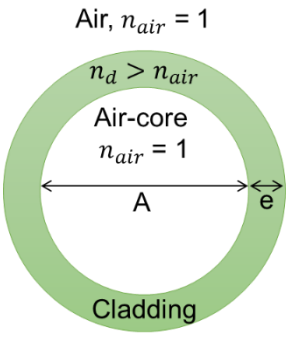

Figure III-4. Transverse cross-section of the pipe fiber

The confinement of the THz wave within the hollow core of the waveguide relies on the antiresonant guiding mechanism that can be briefly described by viewing the cladding as a Fabry-Perot resonator [186], [187] as shown in Figure III-5. The transmission spectrum of a Fabry-Perot resonator is composed of periodic narrow peaks corresponding to transmission maximums occurring at the frequencies at which the Fabry-Perot resonates (called resonance frequencies). That is to say, at or near the frequencies at which the cladding of the pipe waveguide resonates, nearly no reflection takes place at the core-cladding interface and thus fields could hardly exist inside the core region (Figure III-5.a). On the other hand, under the "antiresonant" conditions of the cladding, i.e., at the frequencies away from the resonant ones, the wave is reflected at the core-cladding interface (Figure III-5.b). Thus, resulting in a confinement of the incident wave and guiding it to the output of the fiber.

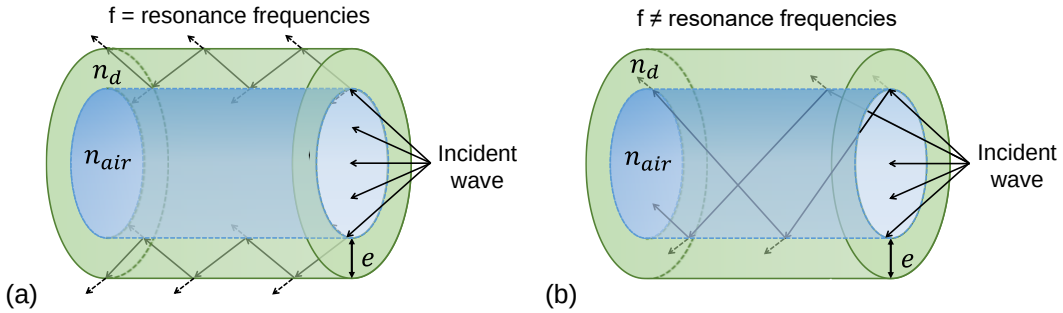

Figure III-5. 3D schematic of a pipe waveguide. The dielectric cladding surrounding the air core acts as a Fabry Perot resonator. (a) At resonance frequencies, the confined wave leaks through the dielectric structure. (b) At antiresonance frequencies, the waves are confined and guided through the pipe.

The waves are confined and guided within frequency-delimited transmission windows Δf in the air channel of the pipe (Figure III-6), which satisfy the Fabry-Perot resonance condition for the dielectric layer, represented by the following equation:

Eq. 42

$$f_q = \frac{qc}{2e\sqrt{n_d^2 - 1}}, q = 1, 2, 3, \ldots$$

with q the resonance order.

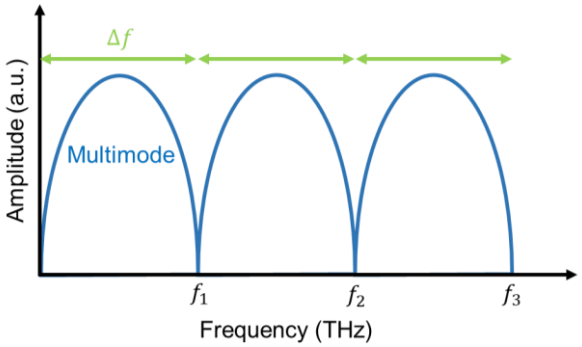

Figure III-6. Schematic of the transmission spectrum of the pipe fiber. The electric field is transmitted through frequency windows determined by the properties of the cladding.

The bandwidth of the transmission windows Δf can be calculated using the following relation:

Eq. 43

$$\Delta f = \frac{c}{2e\sqrt{n_d^2 - 1}}$$

A lower refractive index and/or a thinner wall leads to broader transmission windows (Figure III-7).

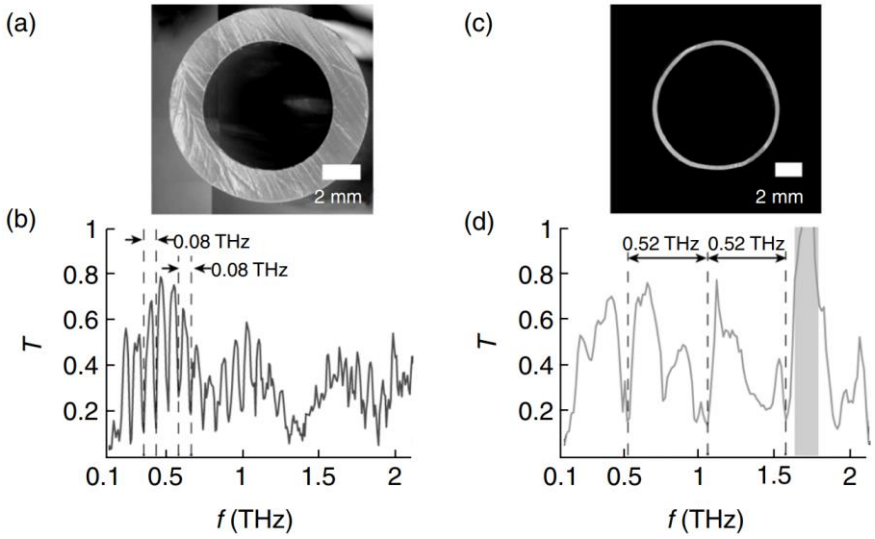

Figure III-7. Images of cross-sections of (a) 1.6 mm thick PE pipe and (c) 0.30 mm thin PTFE pipe. Transmission intensity through the (b) thick-walled and (d) thin-walled fibers. [25]

We conduct the experimental characterization on a plastic pipe of diameter A = 6 mm, a thickness e = 0.12 mm and a refractive index n_d = 1.55. As a result, we anticipate a transmission frequency band of Δf = 1.06 THz. The pipe's length is set at L = 20 cm. To measure the transmission spectrum, we employ the setup illustrated in Figure III-8. The fixed detector antenna (Rx) is positioned 46 cm from the emitter antenna (Tx). The collimating lens, situated at its focal distance F = 10 cm from the detector, collects the beam from the pipe and improves the dynamic range.

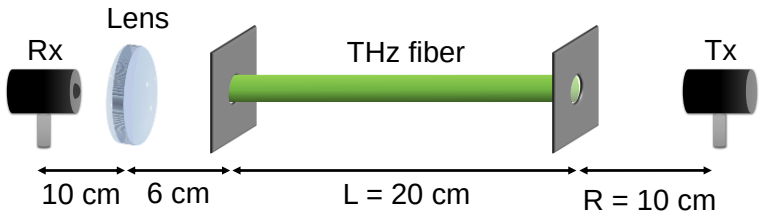

Figure III-8. The experimental setup used to measure the transmission spectrum of the THz fiber under test.

Prior to measuring the transmitted THz pulse through the fiber and metallic holes, a reference measurement was conducted without these elements (Figure III-9). Another measurement was then performed with the metallic holes only to observe their impact on the transmitted pulse and spectrum (Figure III-10). Results showed that the addition of the metallic holes caused a 40 dB degradation in the signal amplitude compared to the reference signal, attributed to the larger size of the illuminated area compared to that of the metallic hole. This resulted in the diffraction of the beam after the first hole.

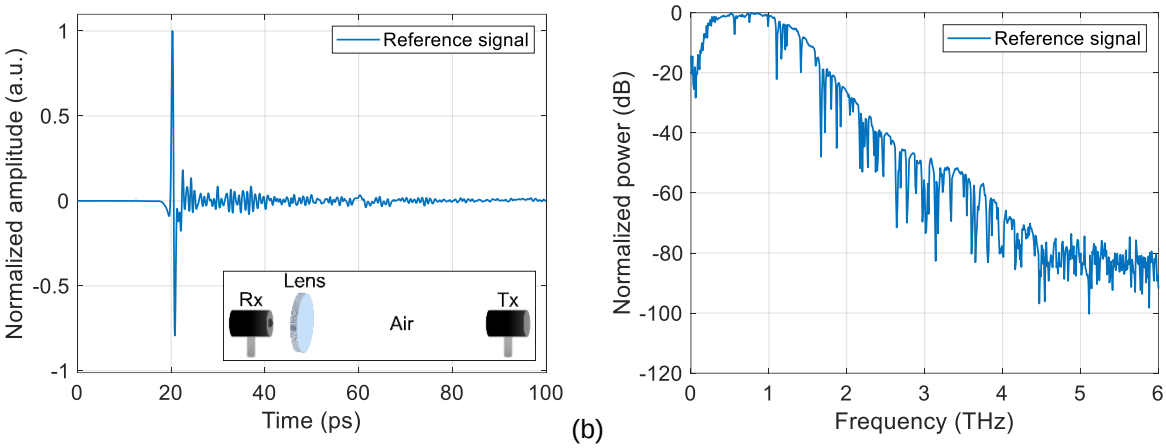

(a) (b)

Figure III-9. Measured reference temporal signal and its frequency spectrum with one Teflon lens in front of the detector. The temporal amplitude and spectral power are normalized to the maximum of the reference signal.

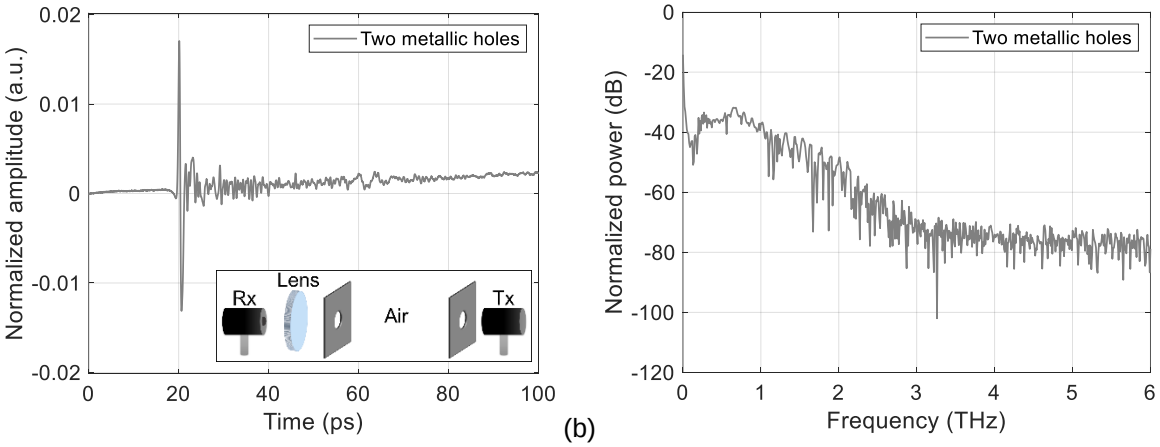

(a) (b)

Figure III-10. Measured temporal signal through two metallic holes spaced with 20 cm, and the amplitude of its frequency spectrum. The metallic hole will serve as the support for the THz fiber during acquisition. The temporal amplitude and spectral power are normalized to the maximum of the reference signal.

However, the addition of the THz fiber led to a gain, notably in the first transmission window, as the pulse was guided rather than dispersed between the two holes (Figure III-11).

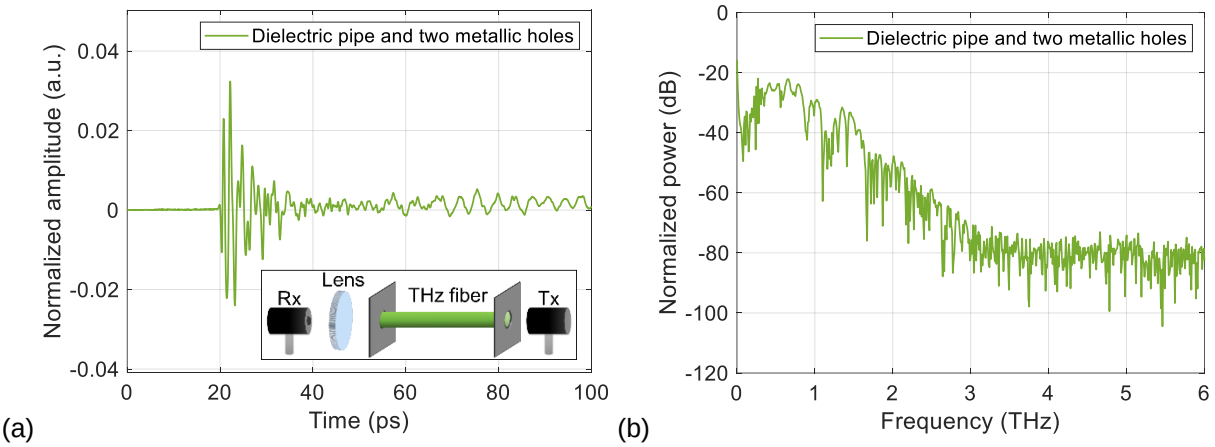

Figure III-11. Measured temporal signal through two metallic holes and the 20 cm long THz fiber, and the amplitude of its frequency spectrum. The temporal amplitude and spectral power are normalized to the maximum of the reference signal.

The Figure III-12 showcases, on the same graph, the transmitted spectrum through the two metallic holes and the spectrum measured with the fiber supported by the said metallic holes.

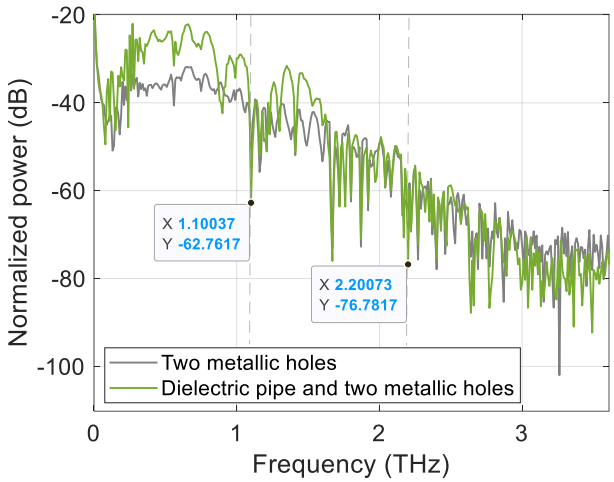

Figure III-12. Measured spectra through the waveguide (green trace), and through the supporting holes without the waveguide (grey trace). The spectra are normalized to the maximum value of the reference measurement.

The spectral amplitude of the transmitted pulse displays a first transmission window delimited by the first resonance frequencies at 1.1 THz. A second transmission window is expected between 1.1 THz and 2.2 THz. However, the graphical representation indicates an absence of this second transmission window; instead, it demonstrates a diminishing amplitude around 1.5 THz, registering at -50 dB. This reduction in amplitude may be attributed to limitations in the dynamic range specifically within this frequency range. For that reason, we focus on imaging the beam profile at frequencies of the first transmission window.

Compared with the theoretical value of the resonance frequency, a slight shift of the experimental resonance frequency can be observed. The resonance frequency has shifted from 1.06 THz to 1.1 THz. This is unavoidable owing to cladding-thickness variations in the commercial polymer pipes. Cladding thickness could vary with up to ± 20 µm. Hence the frequency mismatch could be partially attributed to the nonuniform cladding thickness. Other discrepancy source includes frequency-dependent cladding refractive index which is generally found between 1.54 and 1.58. Compared to the signal transmitted through the holes, we

observe an improvement in transmission over the first transmission window due to waveguiding through the fiber. A measured power increase of 10 dB is observed at 0.5 THz.

The experimental real part of the effective refractive index of the THz fiber is calculated using the following equation:

Eq. 44

$$n_{eff}(f) = 1 + c\frac{\varphi_{ref}(f) - \varphi_{fiber}(f)}{2\pi f L}$$

With φ_{ref} and φ_{fiber} are the signal phases measured through air and fiber, respectively.

We find an effective refractive index inferior to 1 which is expected as the propagation of the THz wave is done in the air core (Figure III-13).

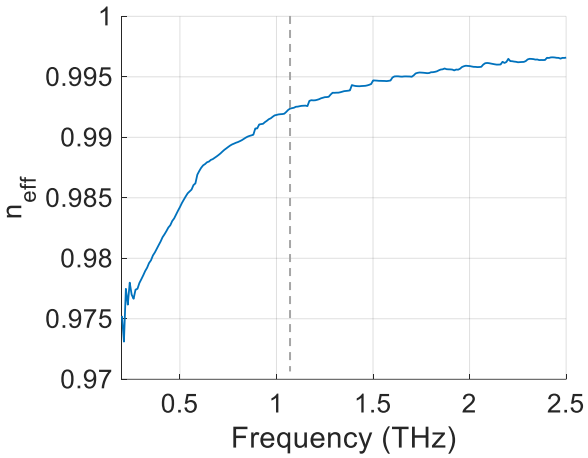

Figure III-13. Frequency-dependent effective refractive index of the THz fiber under test.

The variation of the effective index is typical of an anti-resonant propagation.

After experimentally acquiring information on the transmission spectrum of THz fiber, we investigate the beam profile at its output using the SA imaging approach. The goal is to reconstruct the beam's transverse distribution at different frequencies of the THz spectrum.

III.4. SA imaging of beam profile delivered by antiresonant hollow core THz pipe fiber

We demonstrated in the previous chapter how SA imaging provides spectral information over a large frequency bandwidth, and also over a larger spatial area without having to move the object under test, which is advantageous for the characterization of a THz fiber.

In our implementation, the THz fiber is positioned between the mobile antenna and the collimating lens (Figure III-14). The mobile antenna scans an area $D^2 = 10 \times 10$ cm² of the XOZ plane with a step d = 2 mm. As the emitter moves, it creates a synthetic array that illuminates the end of the fiber at various spatial positions.

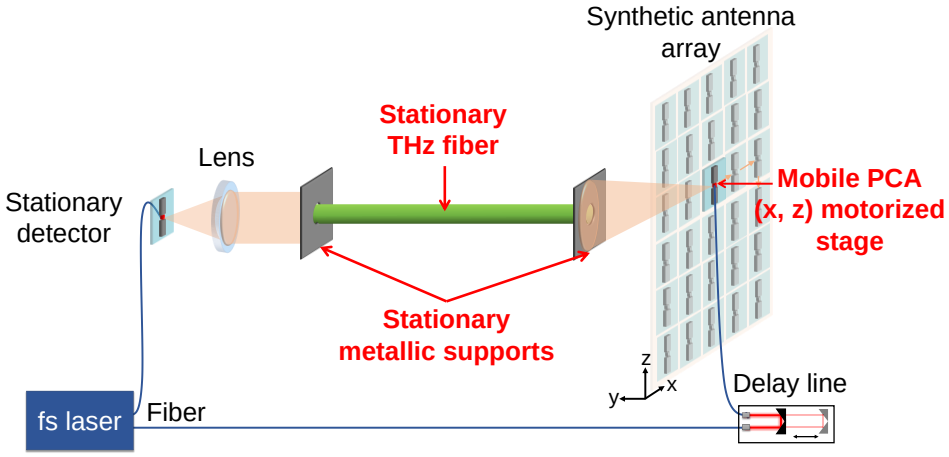

Figure III-14. Transmission based SA configuration using a THz-TDS for the characterization of a THz fiber.

This reconstruction process forms a spectral matrix, which amplitude $\left|\tilde{T}_{re}(f_m, x_p, y_p, z_p)\right|$ represents the frequency-dependent image of the output of the fiber located at a range y_p, thus resulting in a 2D transverse image of the beam profile. The lateral resolution is determined by the overall size D of the SA, and the reconstruction frequency f_m, as previously detailed.

A photograph of the experimental setup is provided in Figure III-15.

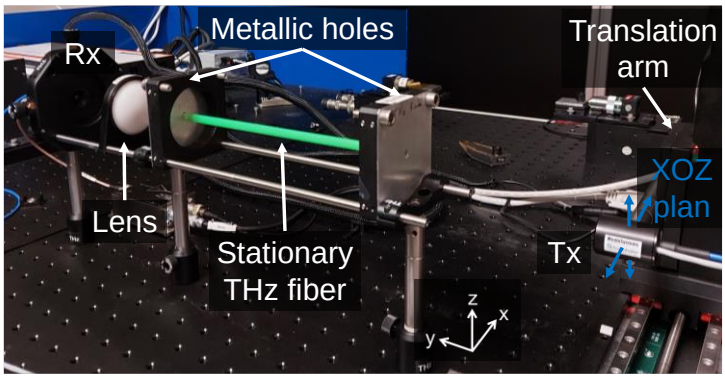

Figure III-15. SA imaging experimental setup of the THz fiber. The mobile scanning antenna is attached to the translation arm. The THz fiber is supported in a stationary position using the two metallic holes. The detector, lens and the supported fiber are stationary during the acquisition process and aligned with the center of the fiber under test.

The same measurement dataset will be used for reconstructing the beam profile maps within the fiber across distinct frequencies. Consequently, the resulting images' cross-range resolutions and FOV will vary in accordance with the equations stated in the previous chapter. The measured experimental resolution shows a variation ranging from 2.5 mm to 0.76 mm when imaging at frequencies between 0.2 and 1.1 THz. Simultaneously, the FOV will span from 7.5 cm to 25 cm across the same frequency range. In light of these variations, the SA method is expected to effectively produces adequate maps across this spectrum of frequencies.

We present the reconstructed data in the form of space-frequency maps in the horizontal (x-axis) and vertical (z-axis) sections of the output of the fiber under test (Figure III-16). This space-frequency representation highlights the variation in the lateral horizontal and vertical directions of the confined beam as a function of frequency (within the transmission window). The maps are presented in frequency domain, using normalized spectral reconstructed electric

field magnitude maps in dB ($20*\log_{10}\left(\frac{|T_{re}|}{max(|T_{re}|)}\right)$, T_{re} from equation Eq. 25) at the horizontal and vertical cuts at the center of the output of the fiber.

The discontinuities observed at 0.55 THz, 0.75 THz, and 0.9 THz, marked by white arrows in both 2D maps, are dips in the spectrum due to water absorption indicated by arrows on the transmission spectrum trace. Moreover, distinctive periodic patterns are observed between 0.2 THz and 0.5 THz, and between 0.6 THz and 0.75 THz in both maps.

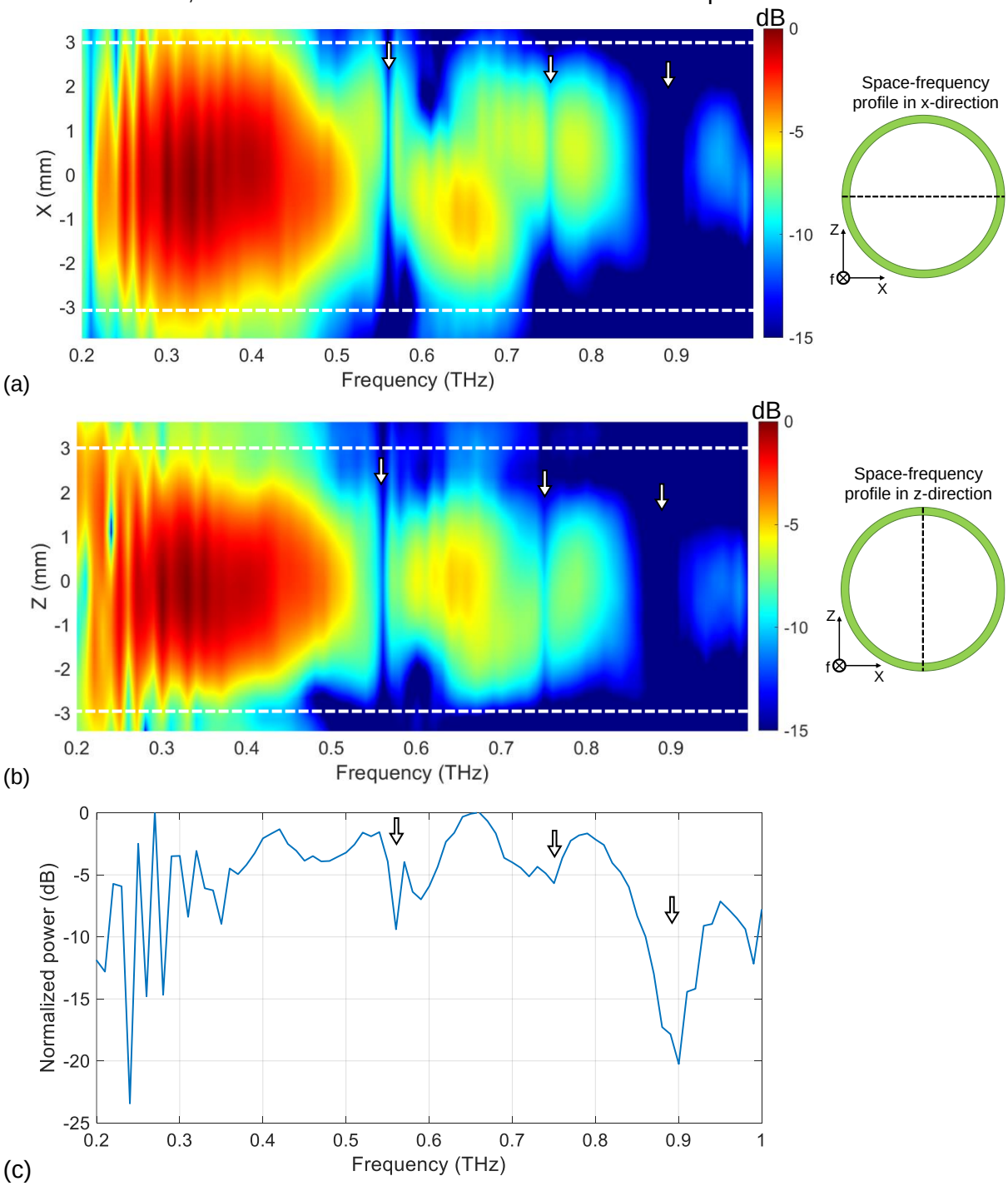

Figure III-16. Space-frequency maps of the normalized squared modulus of reconstructed data ($|T_{re}|^2$) in dB at the waveguide output along (a) x-direction and (b) z-direction. The dashed white lines show the inner waveguide wall. (c) Normalized amplitude (in dB) of the transmission spectrum though the fiber between 0.2 THz and 1 THz.

Figure III-17 below depicts transverse maps of the output of the THz fiber at different frequencies of the first transmission window of the fiber, including at the frequencies marked on the maps above. Each individual map portrays the beam's lateral spatial distribution at a single frequency. The maps are presented in the XOZ plane, using normalized spectral reconstructed electric field magnitude in dB ($20^{*}\log_{10}\left(\frac{|T_{re}|}{max(|T_{re}|)}\right)$, T_{re} from equation Eq. 25) at the THz fiber end.

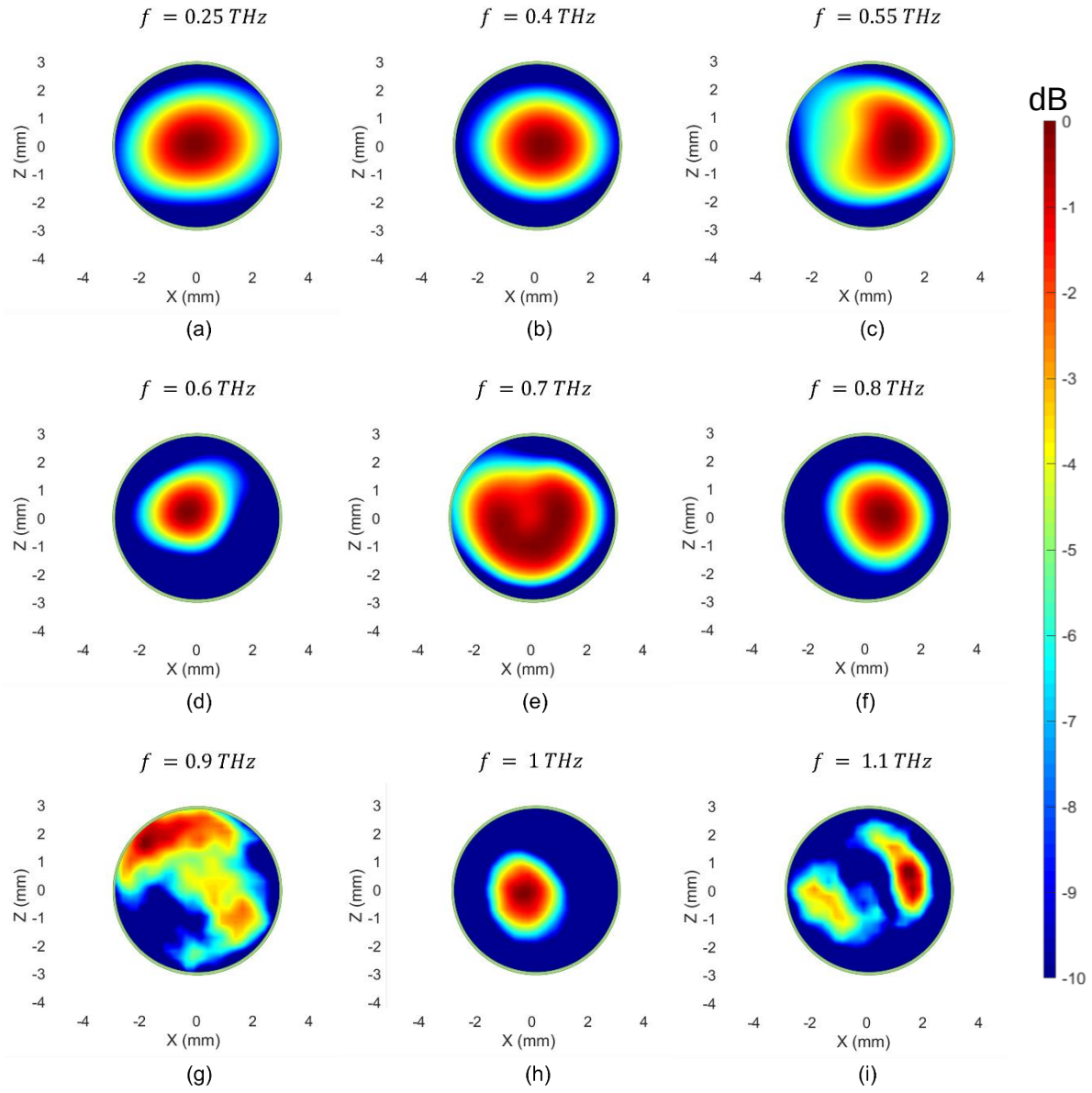

Figure III-17. Spectral distribution of the squared modulus of electric field ($|E|^2$) at the output of the pipe waveguide reconstructed at (a) 0.25 THz, (b) 0.4 THz, (c) 0.55 THz, (d) 0.6 THz, (e) 0.7 THz, (f) 0.8 THz, (g) 0.9 THz, (h) 1 THz and (i) 1.1 THz.

According to experimental results, at 1.1 THz, the beam profile exhibits a distinct distribution, which is due to the resonance effect causing the beam to leak through the fiber at this particular frequency. Within the transmission window, the propagated beam is certainly composed of different modes, as this seems observable on the transverse spatial distribution of the beam.

The experimental results have demonstrated the imaging of the output of the THz fiber without needing to move or interact with the fiber under test during the acquisition process. The fiber

under test was positioned at a distance yp = 10 cm from the imaging synthetic array, providing sufficient distance to insure the absence of any damage of the antenna or the fiber during the scanning process. The proposed approach enables the generation of spatial-frequency maps of the propagated beam. In addition to that, it allows the imaging of the spatial distribution of the propagating beam at each frequency without any input parameters on the diameter of the antenna, its length, effective refractive index, or absorption coefficient. We should note that the imaging setup could adapt to longer THz fibers in the limitation of the delay line available with the TDS system. Moreover, the SA setup offers flexibility in the position of the output of the fiber in reference to the center of the synthetic array, as back projection algorithm allows the recovery of the phase information thus the ability to locate the output of the fiber. These performances make the SA imaging approach, in conjunction with the TDS system, a significant initial step toward the development of adaptable imaging systems suitable for a wide range of THz fibers with significantly less complications.

The obtained results from this initial step to fiber characterization highlights the need for a modal characterization method in order to decompose the modal content of the fiber under test. In the next section, we propose a novel approach to modal characterization of THz fibers.

III.5. Spectrally and spatially (S^2) imaging technique for THz fiber characterization

This section details the second part of our work, which is the modal characterization of the THz fiber.

The previous measurement gives the reconstructed amplitude distribution ($|T_{re}|^2$) of the THz field propagated in the waveguide for each frequency. Nevertheless, the field can be propagated in different modes, depending on the waveguide under test. It is interesting to be able to measure the modal content of the propagated field. To this end, we will present the various methods developed in the field of optics, and then study the possibility of using the SA method to obtain the modal decomposition of the field propagated in a THz pipe. The limitations of this method will then be discussed.

III.5.1. S^2 imaging in the optical domain

In recent years many techniques have been developed to measure the modal content of multimode optical fibers, for example based on selective mode launch [188], modal weight solvers [189] and time of flight [190]. In order to acquire modal information on the fiber, these methods measure the interference that arises from the different group velocity of the various optical modes. Several variants have been proposed, in which the interference is probed in the frequency domain [191], time domain [192], or in the spatial domain [193].

The S^2 imaging technique is another popular tool for identifying modes and imaging multiple higher-order modes propagating simultaneously in fiber-based devices in the optical domain. It differs from most of the others as it does not require any prior knowledge about the refractive index profile, guidance mechanism or modal properties of the fiber under test [194]. One of the earliest works on S^2 imaging of modal content in fibers was published in 2008 by J.W. Nicholson et al. [195].

S^2 imaging exploits the difference in group velocity of the propagated modes that leads to a spectral interference pattern at the fiber output. The spectrum is converted in time domain through a Fourier transform that enables to distinguish the different modes located at different group delay. The transmitted spectrum is measured at several locations in the transverse plan of the fiber (plane (x, z) perpendicular to the propagation axis (y)) for reconstructing (after a

Fourier transform) the intensity distribution of the different modes (having the same group delay).

The S^2 imaging setup is shown in Figure III-18. Light from a broadband source is coupled into a single mode fiber (SMF), which delivers the source beam into the fiber under test. The near field of the fiber under test is imaged using a microscope objective (MO) aligned in a 4-f configuration (magnification configuration) with a lens L. A 50/50 beam splitter (BS) split and direct the measured beam on a CCD, and on the collection fiber (CF, a 50 µm graded index fiber). The CCD enables a real time visual check on the input alignment conditions. The S^2 measurement is then performed as the CF scans the fiber under test across the plane perpendicular to the propagation axis on a 2D translation stage while the optical spectrum analyzer (OSA) measures at each location the delivered beam.

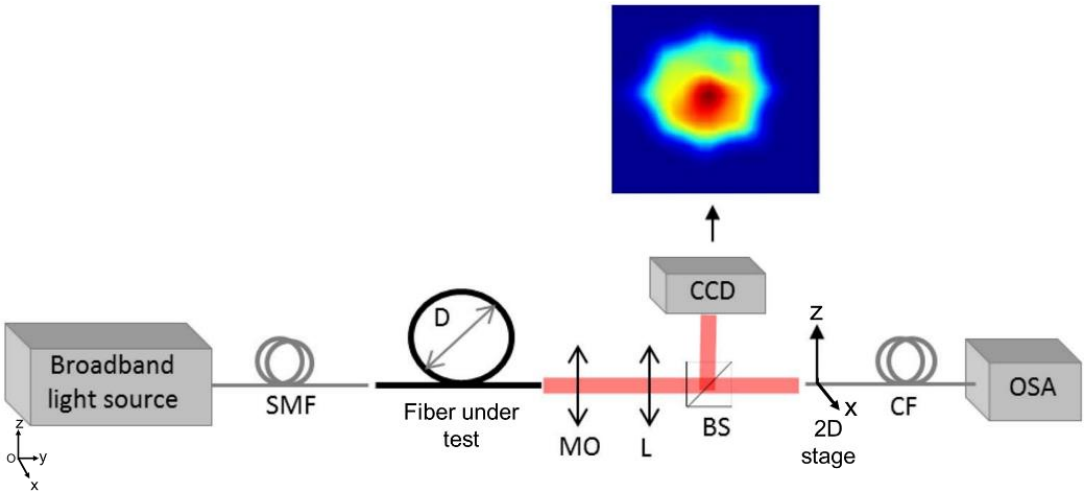

Figure III-18. Experimental setup used for S^2 measurement on optical fibers. The image of the electric field propagating inside the fiber under test is shown above the CCD (adapted from [196]).

If different modes overlap spatially at that (x, z) point, the delivered beam will have a spectral interference pattern due to group delay differences between the modes in the fiber under test (figure 3.a.). A Fourier transform applied to the optical spectra reveals narrow peaks at various group delays corresponding to the different modes (figure 3.b.). The zero of group delay is defined as the time when the wave is entering into the fiber.

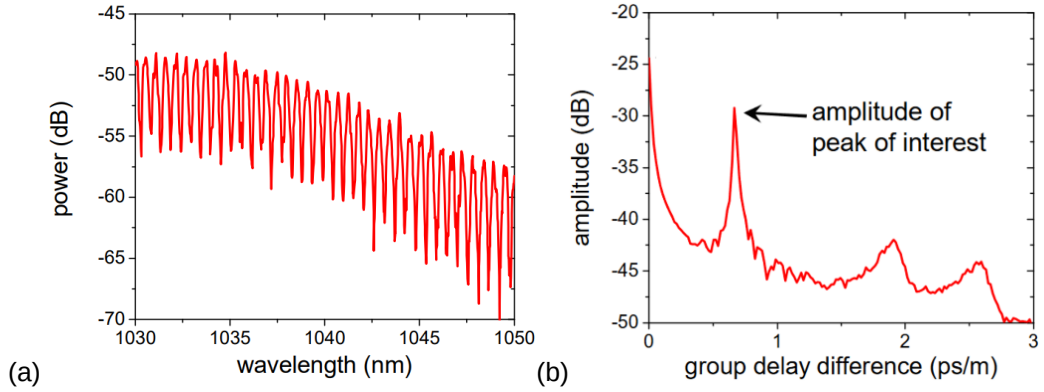

Figure III-19. (a) Typical optical spectrum measured at an (x, z) location, (b) the inverse Fourier transform of the optical spectrum showing multiple beat frequencies. The horizontal axis of the Fourier transform is normalized to the fiber length to obtain group delay difference in units of ps/m [195].

This measurement process is repeated at different points in the xoz plane thus mapping the transverse profile of different modes and identifying them. Intensity images of high order modes

are obtained at their corresponding group delay (Figure III-20). No prior knowledge of fiber properties is required to identify the supported modes.

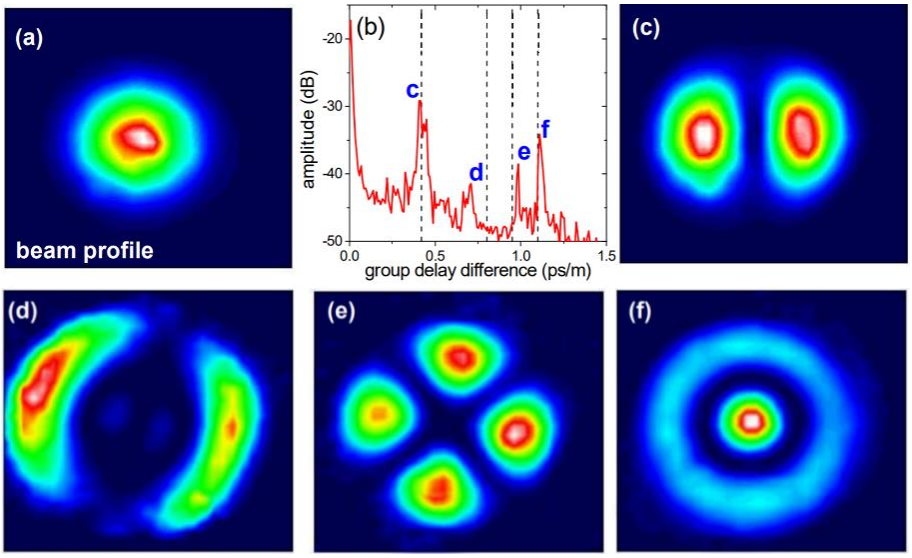

Figure III-20. Measurement results on a 20 m long multi-mode optical fiber, with a core diameter of 27 µm. (a) The beam profile was obtained by integrating the optical spectrum at each pixel. (b) The inverse Fourier transform of the optical spectra showing the beat frequencies of interest. Also shown as dashed lines are group delay differences between the higher order modes, obtained from a calculation based on the measured index profile. (c)-(f) Assembled images of the higher-order modes images corresponding to the indicated peaks in (b) (adapted from [195]).

The S² method's effectiveness in the optical domain is well-established. Its performance relies on different key parameters.

The temporal resolution of the inverse Fourier transform showing the different modes: the delay between the peaks in the time-domain trace calculated from the inverse FFT of the measured interference pattern is equal to the difference in group delay between the modes. The group delay (τ_g) of each mode is defined as follows:

Eq. 45

$$\tau_g = \frac{L}{c} n_g = \frac{L}{c}\left(n_{eff} - \lambda \frac{dn_{eff}}{d\lambda}\right)$$

With L, the fiber length, n_g the group index of the mode, which is determined by the variation of effective refractive index n_{eff} with the wavelength λ.

Consequently, to be able to differentiate successive modes, the spectrum needs to be measured with a temporal resolution τ_{res} of at least half of the smallest time difference between two consecutive modes along a frequency window. This ensures that the instrument can accurately capture and differentiate between the changing modes as they occur over time.

The measured spectral bandwidth: in addition to the measurement instrument's resolution, another significant factor impacting the ability to differentiate the propagating modes is the available transmission bandwidth of the fiber under test. In fact, the modal analysis is performed within a single transmission window BW_f of the fiber, in order to prevent interference with modes supported across multiple transmission windows. However, this limitation will result in a decrease in the temporal resolution τ_{res}, which is now determined by the fiber's

transmission bandwidth BW_f instead of the measurement instrument, as dictated by the equation:

Eq. 46

$$\tau_{\mathrm{res}} = \frac{1}{BW_f}$$

A reported work used a bandwidth of 10 nm, ranging from 1050 nm to 1060 nm, within the transmission window of an examined anti-resonant hollow core optical fiber [196]. This bandwidth is equivalent to a frequency band of BW_f = 2.7 THz, thus allowing a temporal resolution of $\tau_{res} = 0.37\,ps$, which was proven to be sufficient to differentiate between the peaks of the modes [195].

Our objective is to investigate the possibility to take advantage of the SA imaging technique for developing this method in the THz range. That is because SA imaging technique will allow to image the pipe output without the constraints of raster scanning at small distance from the output. In fact, SA aperture will allow data acquisition at a distance of tens of centimeters from the output of the fiber. In addition to that, using SA imaging technique will eliminate the need for an MO and a CF, and the size of the pixel will be linked to the imaging resolution of the SA technique (as presented in the previous chapter).

Using SA imaging, a matrix of spectral signals is reconstructed at multiple pixels to produce an image that contains both spatial and spectral data as demonstrated in the previous chapter. This data can then be analyzed to extract temporal peaks through an Inverse Fourier Transform. Consequently, SA imaging provides the necessary set of data as the classical approach but in an effective manner that is adapted to the THz range.

However, it's crucial to consider the limitations imposed by our measurement instrument, the TDS system, as well as the limitations imposed by the THz fiber under test. Therefore, the upcoming chapter will delve into simulating the modal behavior of the fiber under test. Through simulation, we will replicate the S^2 time domain trace with the mode peaks by calculating the group delay of the supported modes of the selected fiber. These simulation results will provide the value of the necessary temporal resolution, which we'll be compared with the capabilities of our experimental setup.

III.5.2. Simulation results of the modal content in the investigated THz fiber

We investigate the modes propagated in a pipe fiber shown in Figure III-21. The material's permittivity and magnetic permeability are represented by ε and μ_0. Those of air are represented by ε_0 and μ_0, respectively. The cylindrical coordinate system (r, φ, y) is established for analysis. The dependences of the electric field of a mode in an optical waveguide have the form [197]:

Eq. 47

$$\vec{E}(r,\phi,y,t) = \vec{E}(r)e^{i(\beta y + m\phi - \omega t)} = [E_r(r)\vec{e}_r + E_\phi(r)\vec{e}_\phi + E_y(r)\vec{e}_y]e^{i(\beta y + m\phi - \omega t)}$$

Where $\vec{e}_r$, $\vec{e}_\phi$ and $\vec{e}_y$ are the unity vectors in cylindrical coordinates. The components of the electric field are found by solving the scalar Helmholtz equations [198].

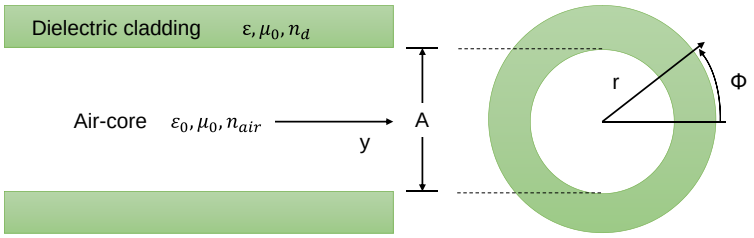

Figure III-21. The model of the hollow-core antiresonant fiber.

In the TE mode, and after solving all components of the electric field, the longitudinal component E_y of electric field equal zero, and thus the transverse electric field components in air core region can be written as:

Eq. 48

$$E_r = -\frac{\mu_0 k_0}{k_r^2} B J_m(k_r r)$$

$$E_\phi = -i\frac{\mu_0 k_0}{k_r} B J'_m(k_r r)$$

With k_r the radial wave vector, expressed as follows:

Eq. 49

$$k_r = \sqrt{n_0^2 k_0^2 - \beta^2}$$

And k_0 is the vacuum wavenumber, expressed as:

Eq. 50

$$k_0 = \frac{\omega}{c}$$

Where B is a constant real number, J_m and J'_m are the Bessel function of m^{th} order and its first derivative, m is the azimuthal mode index, and β is the radial wave vector.

The expression of the effective refractive indexes of supported modes is extracted for the approximation of low-order modes [198], and expressed as follows:

Eq. 51

$$n_{eff}^{mn} \approx 1 - \frac{1}{2}\left(\frac{u_{mn}}{\pi}\right)^2 \left(\frac{\lambda}{A}\right)^2$$

where u_{mn} is the n^{th} root of the $(m-1)^{th}$-order Bessel function of the first kind, A is the diameter of the air-core of the pipe, and m and n represent the subscripts of the vector modes.

Numerical tools, based on the analytical model described above, are available in order to accurately assess the theoretical distribution of the supported modes and calculate the effective refractive index of each mode. Finite Element Method (FEM) featured in COMSOL Multiphysics © software is a popular tool used to provide the simulation results. The cross section of fiber structure has been considered for 2D analysis. A circular perfectly matched layer (PML) was used as a boundary condition in the simulation of the proposed fiber. By using the FEM, the whole simulating domain will be divided into smaller sub-domains (meshing) which can be the geometric primitives such as quadrilaterals and triangles in 2D. Meshing with a triangular shape was chosen due to its best structure alignment inside the circular structure

of the fiber. Size of the mesh element is also an important parameter because the accuracy of the FEM solution can be varied with the mesh size. The small mesh sizes provide accurate simulation results. However, the simulation time will be increased drastically with the decreasing of the mesh size. To optimize the calculation time, the smaller mesh size was only used in the area of interest (i.e. fiber core region) and a larger mesh size was chosen for the rest (i.e. cladding region). In order to obtain accurate results, extremely fine meshes with maximum element sizes of λ/10 and λ/5 in air-core and cladding, respectively, were used.

We will focus on one component of the simulated electric field, the component E_z following z direction in Cartesian coordinates ($\vec{e}_z = sin\phi.\vec{e}_r + cos\phi.\vec{e}_\phi$ in cylindrical coordinate system). This feature is due to the linear polarization in the z direction of both the emitter and detector used in the TDS setup, which will be employed in the upcoming experimental demonstration.

The parameters of the simulated pipe fiber are the same as the parameters of the previously characterized pipe fiber. We recall the numerical values: diameter A = 6 mm, thickness of dielectric cladding e = 0.12 mm with a refractive index n_d = 1.55. the first transmission window is Δf = 1.1 THz.

The calculations indicate the presence of five higher-order core modes in addition to the fundamental mode in the simulated pipe fiber. Figure III-22 illustrates the modal and vector distributions of the E_z component of the electric field for both the fundamental mode (a) and five subsequent high-order modes (b)-(f), sorted by their effective refractive index. The fundamental mode exhibits the refractive index closest to 1. The modes are calculated at 0.55 THz, the central frequency of the transmission window of the THz pipe tested, with the first transmission window limited at 1.1 THz.

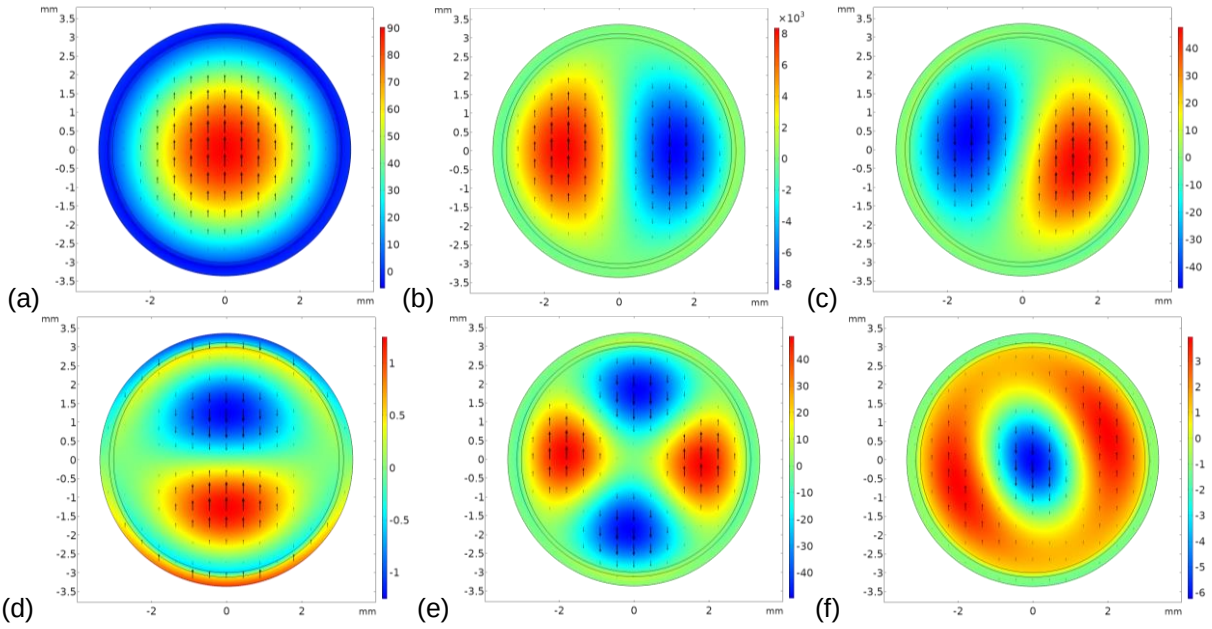

Figure III-22. E_z component of six modes supported by the fiber. (a) Fundamental mode HE_{11}. (b)-(f) Depict higher-order modes TE_{01}, HE_{21}, TM_{01}, HE_{31} and HE_{12} in ascending order of effective refractive index, with the fundamental mode HE_{11} possessing the highest effective refractive index. The small black arrows in the figure indicate the polarization direction of the field for each mode.

We have simulated their effective refractive index between 0.2 and 1 THz, as illustrated in Figure III-23.

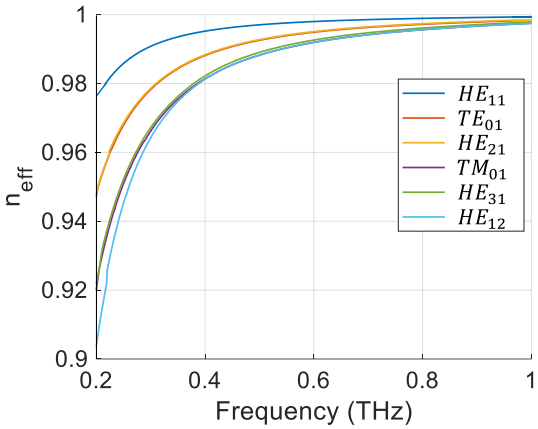

Figure III-23. Effective refractive index of the fundamental mode (HE_{11}) and 5 high-order modes supported by the simulated THz fiber within the range 0.2 THz to 1 THz.

These results reveal a slight difference between the effective refractive indexes of each mode across the bandwidth. The fundamental mode (HE_{11}) is the mode with the effective refractive index closer to 1 (dark blue trace). A diminishing difference between the effective refractive indices is apparent at higher frequencies, aligning with Eq. 51's indication that n_{eff} approaches 1 for shorter wavelengths.

The group delay is calculated for each mode along the frequency bandwidth from their corresponding effective refractive index, according to Eq. 45. The result for a THz pipe L = 20 cm is shown in Figure III-24.

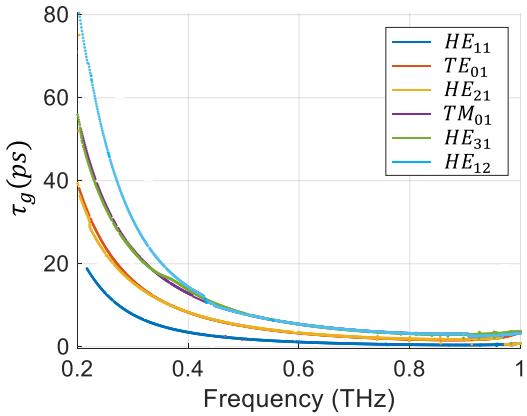

Figure III-24. Group delay of the fundamental mode and 5 high-order modes supported by the simulated THz fiber between 0.2 THz and 1 THz, calculated using Eq. 45 for a 20 cm long pipe fiber, from n_{eff} presented in Figure III-23.

As expected, the fundamental mode (dark blue trace) has the minimum group delay over the frequency range. Which indicates that the fundamental mode propagates faster than the high-order modes. The following modes have higher group delay which is more apparent at lower frequencies.

We calculate the mean group delay of each mode in order to trace the S^2 time domain trace. The mean of the group delay $\mathrm{mean}(\tau_g)$ of each mode is calculated over the transmission bandwidth according to the following equation:

Eq. 52

$$\mathrm{mean}(\tau_g) = \frac{\sum_{i=1}^{N_f} \tau_g(f_i)}{N_f}$$

With f_i the frequency and $i \in [1, N_f]$ with N_f the total number of frequency points in the transmission bandwidth.

Calculation results indicate that the fundamental mode arrives with a mean group delay of 2.28 ps, and then 2 modes arrive at 4.37 ps and 4.47 ps. Subsequently, a third batch consisting of 3 modes arrives at 6.47 ps, 6.54 ps and 6.55 ps, respectively.

We base the choice of the resolution of this simulated temporal trace on the smallest difference between the group delays. The smallest group delay difference is 0.01 ps, between HE_{31} and HE_{12}. So, the minimum appropriate temporal resolution is 0.01 ps divided by 2 to adhere to the Nyquist-Shannon sampling theorem [199]. For this purpose, the chosen temporal resolution $\tau_{res} = 0.005\ ps$ was sufficient for the discrimination between the closely propagating modes.

To generate the time-domain S^2 trace from the calculated group delay values obtained from simulation results of a THz pipe, a time-domain linear vector is numerically created with multiple points covering a temporal window of 10 ps. This window could take any size above 6.55 ps, which represents the highest calculated mean group delay. The difference between each point in this vector is set to the previously chosen temporal resolution $\tau_{res} = 0.005\ ps$. Then, the vector points corresponding to the calculated group delays are assigned a value of 1, in contrast to all other vector points assigned a value 0. The resulting time-domain trace, depicted in Figure III-25 displays peaks at the respective mean group delays of each mode.

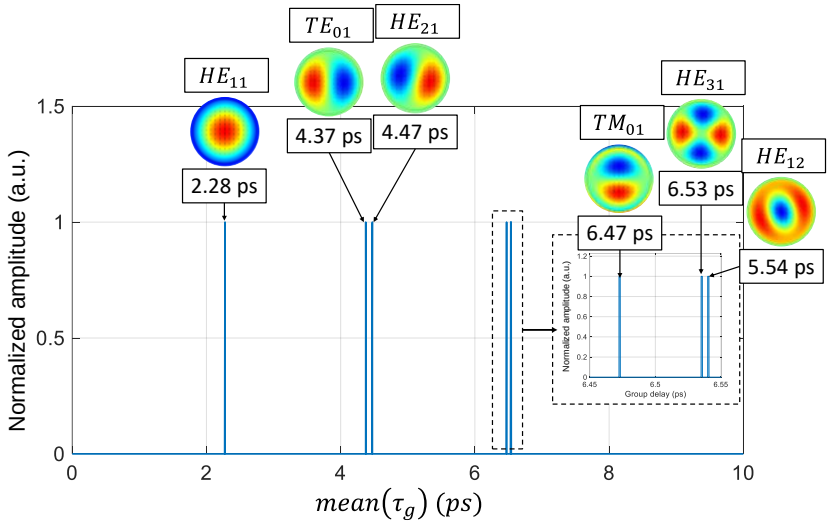

Figure III-25. Simulation results of mode peaks presented over a temporal window of 10 ps for a pipe 20 cm long pipe fiber. Zoom on a smaller temporal window of 0.12 ps in order to clearly see the peaks. The simulation is performed with a 0.005 ps temporal resolution. The spatial distributions of the simulated modes are provided at each corresponding group delay.

However, as stated before, in order to avoid the interference with modes supported across multiple transmission windows the available temporal resolution using the experimental setup for SA imaging is limited to the transmission band of the THz fiber. The temporal resolution available using a reconstruction bandwidth between 100 GHz and 1 THz is $\tau_{res_{SA}} = 1{,}12\ ps$ (from Eq. 46, with BW_f = 0.9 THz).

The experimental resolution is lower than the resolution necessary to discern between the peaks. In fact, it will not be enough to differentiate between the closer mean group delays of the high-order modes specifically, as their temporal difference is smaller than 1.12 ps. This is

confirmed with Figure III-26 where the temporal trace is presented with a resolution of $\tau_{res} = 1.12\ ps$.

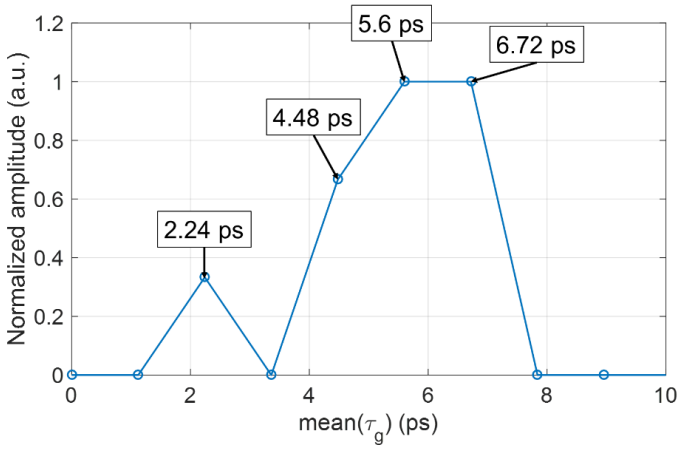

Figure III-26. Simulation results of mode interference presented over a temporal window of 10 ps, for a 20 cm long fiber. The simulation is performed with a 1.12 ps temporal resolution, which is the temporal resolution available within the THz transmission window of the simulated fiber. The points highlight the temporal resolution.

This result is a simulation of the experimental S^2 temporal trace indicating that with the available parameters, the temporal resolution will not enable the discernment of the modes, and the modal content of the fiber cannot be fully analyzed. Nevertheless, the resulting temporal trace shows a first peak at 2.24 ps that corresponds to the fundamental mode. Its position is shifted from 2.28 ps to 2.24 ps because of the resolution. Consequently, it is possible to differentiate the fundamental mode from the high-order modes, which could be useful for evaluating the single mode property of the waveguide. In the next section, we are interested in the confirmation of the proposed approach using the experimental setup.

III.5.3. Experimental results

The objective of this section is to experimentally demonstrate the modal imaging approach and comparing them to the simulation outcomes. The spatial distributions of the modes are reconstructed over the frequency range between 0.1 to 1 THz, as this range is located inside the first transmission window of the THz fiber.

The Point Spread Function (PSF) of the synthetic array configuration used for imaging is measured beforehand over the reconstruction frequency band in x- and z-directions. The cross-range resolution is estimated at 857 µm and 879 µm is x- and z-directions, respectively.

In order to reconstruct the images of the modes, the same setup presented in Figure III-14 is used. The same reconstructed data used to image the beam profile is further exploited as follows: an inverse Fourier transform is applied to the reconstructed spectral data to extract temporal information for each pixel in the image:

Eq. 53

$$\tilde{T}_{re}(t_m, x_p, y_p, z_p) = TF^{-1}\left(\tilde{T}_{re}(f_m, x_p, y_p, z_p)\right)$$

At the position of the output of the fiber y_p = 10 cm from the synthetic array, the mean of the amplitude of the time domain traces $mean(|\tilde{T}_{re}(t_m, x_p, y_p, z_p)|)$ over all pixels (x_p, z_p) of the reconstructed image is presented in the Figure III-27 below (blue trace). The temporal trace

shows multiple peaks at distinct mean group delays. A comparison between experimental and simulation results is provided on the same figure.

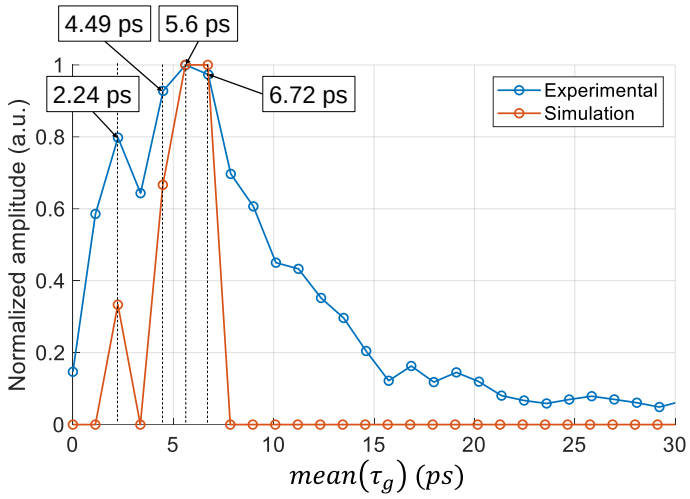

Figure III-27. The mean of the temporal traces from the S² experimental result (blue) with the simulation trace (orange). The amplitude is normalized to its maximum value. The points highlight the temporal resolution.

Figure III-27 exhibits a notable alignment in the first part of the graph, reflecting a strong correspondence between the simulation and the experimental outcomes. However, the experimental time-trace (blue trace) continue to slowly decrease after 6.72 ps, an aspect not found in the simulated results (orange trace). This difference is due to pipe modes and other lossy modes.

At the indicated group delays on the Figure III-27, we assemble the following 2D maps:

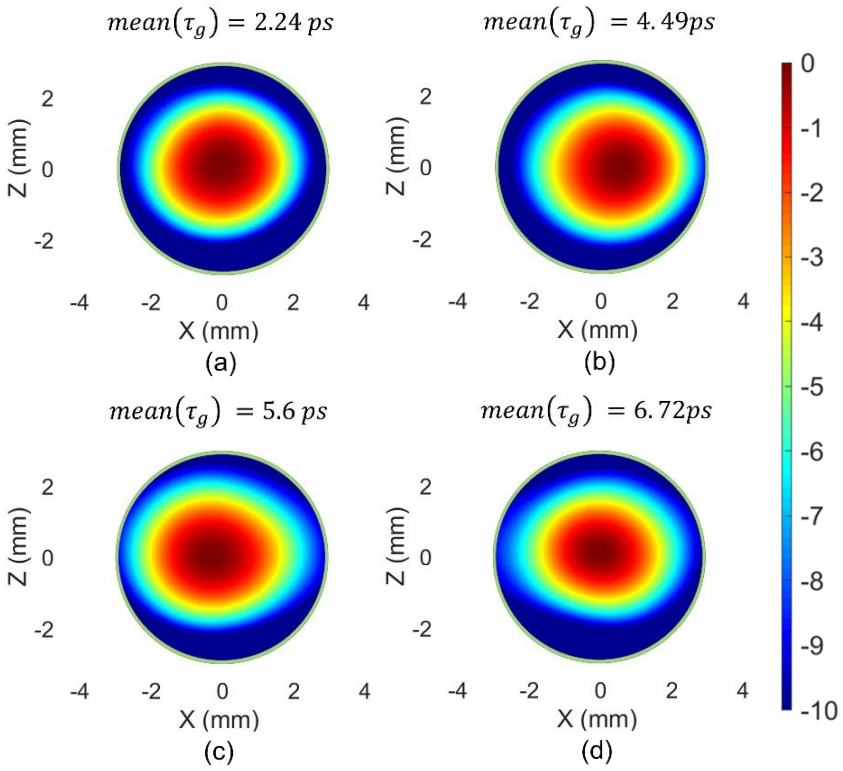

Figure III-28. Reconstructed amplitude images in dB obtained by processing the peaks in Figure III-27.

The map at 2.24 ps is the map of the fundamental mode, which displays a Gaussian pattern. A 1D lateral cut of the reconstructed image in x-direction and z-direction are shown in Figure III-29. The lateral cuts have a gaussian form according to the fitting of the curves.

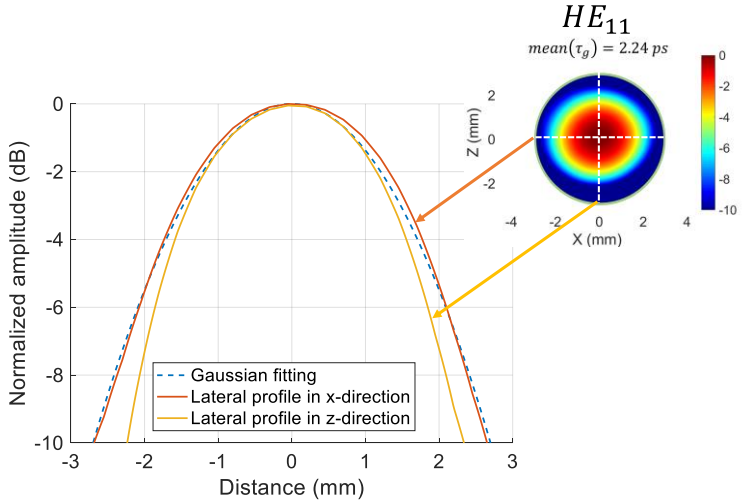

Figure III-29. 1D cuts in the plane XOZ, in x-direction and z-direction, of the fundamental mode HE_{11}, compared to a Gaussian fitting.

For the rest of the maps, the mode profile seems to take a gaussian shape also, as confirmed with the following lateral profile cuts in x- and z-directions of the reconstructed modes.

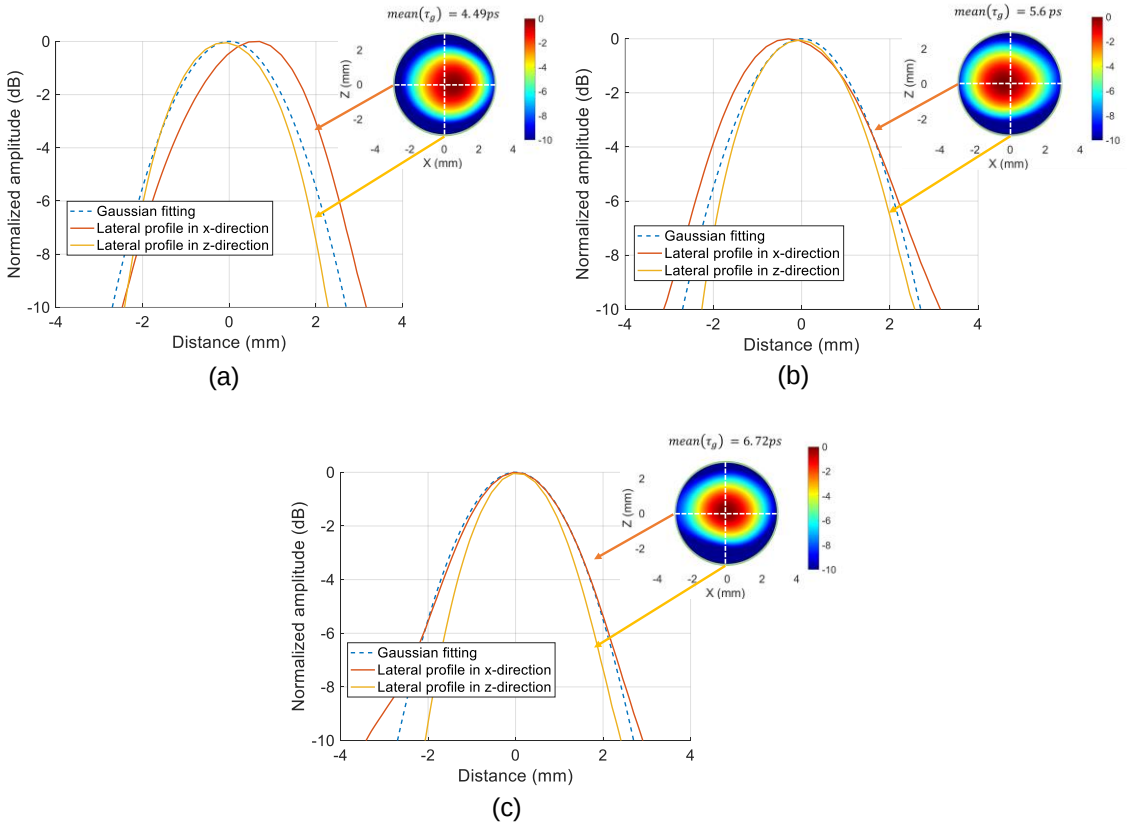

Figure III-30. 1D cuts in the plane XOZ, in x-direction and z-direction of the profiles reconstructed at mean group delay of (a) 4.49 ps, (b) 5.6 ps and (c) 6.72 ps. The lateral profiles are compared to a gaussian fitting for reference.

The gaussian profile of the reconstructed modal maps could be a consequence of a domination of the mode HE11 over the higher order modes showing a quasi-single mode regime of the THz wave propagation. This could also be a consequence of the variation of the group delay of the HE11 within the measured frequency range 0.1-1 THz yielding a measure and analysis of meanly this mode. Indeed, the of the group delay of the mode HE11 at 0.3 THz is 8.19 ps, while its value at 0.5 THz is 2.25 ps. We need to investigate furthermore these two hypotheses.

The combination of the S^2 method and the SA imaging technique demonstrated its potential for modal characterization of a THz fiber. However, the method did not deliver on the anticipated distinction of modes. In the discussion section, an in-depth exploration of parameters that directly influence the efficacy of the S^2 characterization method will be conducted. This comprehensive analysis aims to shed light on the limitations of the proposed approach in the THz domain.

III.5.4. Discussion

In this chapter, we have successfully demonstrated the imaging of a beam profile at the output of a THz fiber employing the SA imaging approach. Our method is based on a transmission THz-TDS system generating a SA for characterizing the fiber's output. Through numerical reconstruction, we generated a space-frequency map of the propagated beam across the first transmission window of the pipe fiber under test. Moreover, we achieved transversal images of the beam profile at different frequencies, from 0.2 THz to 1.1 THz, which indicated the possibility of multimodal propagation in the pipe fiber. This result highlights the versatility of our proposed imaging techniques for the analysis of radiative beam that were previously challenging to assess within the THz range. It also contributes to bridging the expertise gap needed for characterizing THz fibers. This work opens the door for further exploration, including the investigation of different types of hollow-core THz fibers, as well as the examination of various THz guiding components such as resonators or radiative structure. To improve the capabilities of the proposed approach, the use of a dry box can significantly reduce water absorption lines, thereby improving the analysis over a broader bandwidth and enabling access to higher THz frequencies through the TDS system.

Additionally, modal characterization of the THz pipe waveguide has been experimentally demonstrated to a certain extent. However, significant improvements remain necessary to achieve an efficient and exhaustive modal characterization of the fiber. The temporal resolution is currently limited at 1.12 ps. This temporal resolution was achieved using a frequency band 0.1-1 THz (0.9 THz), which is almost the entire first transmission window of the pipe fiber. This bandwidth is too large for the pipe’s transmission window, since it gives a single averaged point of the delay group of the supported modes. It would be necessary to improve resolution while reducing the reconstruction bandwidth also (in reference to the transmission of the pipe).

To improve the resolution, the first factor is the length of the fiber. In fact, looking at Eq. 45, we can see that for a given fiber, its length L dictates the group delay of the mode at the output of the fiber. The longer the fiber, the larger the delay between the different modes. Which means that for a fixed temporal resolution, the choice of fiber length L can be optimized to provide a more substantial delay between modes, thus facilitating their differentiation using the SA-S^2 method proposed and taking advantage of the available TDS equipment.

In fact, by using the same simulated effective refractive index presented in Figure III-23, we calculate the group delay time for multiple lengths L of the fiber using Eq. 45. Simulation results indicate that we can achieve a temporal delay of 3 ps (~2 × 1.12 ps) between the closest

propagating modes with a fiber length L = 150 m. Due to the length of the fiber, propagating modes have a higher group delay resulting in larger delay difference between the modes. However, it's important to acknowledge that experimental confirmation of this outcome is difficult given the limitations of the current TDS system. This limitation arises from the restricted distance between the antennas. In our setup, the optical delay line permits scanning over a limited distance of 70 cm between the PCAs. To accommodate the collimating lens and maintain a 10 cm gap between the output of the fiber and the scanning antenna, only a fiber with a length of around 50 cm can be measured within the available space. Consequently, the mean group delay of modes propagated along a 50 cm fiber is depicted in Figure III-31.

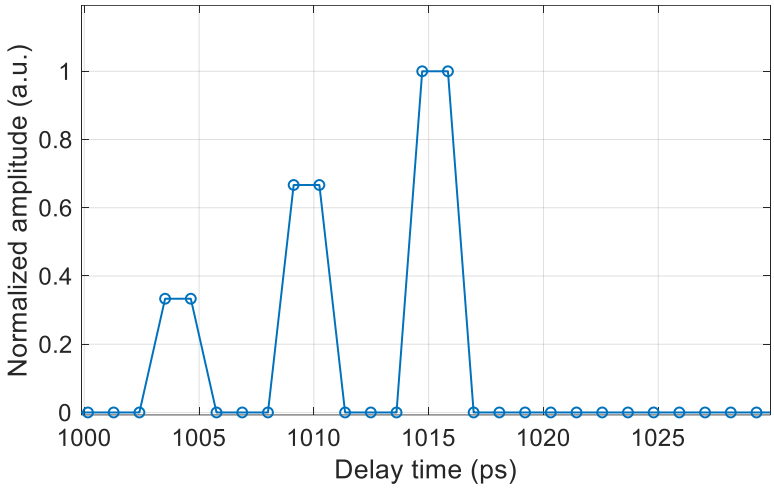

Figure III-31. Simulation of propagating modes as a function of mean group delay, for a 50 cm long fiber. The results are presented over a temporal window of 30 ps. The simulation is realized with a 1.12 ps temporal resolution, which is the temporal resolution available with the transmission window of the fiber.

The modes have a higher delay due to the length of the fiber; the fundamental mode is distinguishable from the higher order modes. The higher order modes have enough differential delay to arrive in two separate batches. However, the peaks of high order modes are not distinguishable individually.

Under the constraints of our experimental setup, we can distinguish the fundamental mode, but it is not feasible to distinguish between the propagating high order modes. To address this limitation and enable the differentiation of propagating modes, a TDS system equipped with a sufficiently long delay line would be essential. Such a system would allow for greater separation between the antennas, providing space for the characterization of longer fibers.

Conclusion

The research presented in this thesis manuscript demonstrates an imaging and spectroscopy approach in the THz frequency range for stationary objects in a transmission configuration. To implement this approach, we adapted the SA imaging technique to a TDS system in a transmission setup.

In a typical configuration, the TDS system uses four lenses to focus a THz beam and generates a pixel-by-pixel image of the object under test, which is mechanically translated within the focused beam. The objective behind our proposed system is to offer an alternative setup where the object under test remains stationary.

Similar SA approaches of THz imaging and spectroscopy have been dominated by reflection-based setups which are better suited for reflective solid materials, highly absorbent objects or objects with thicknesses exceeding the optimal range for TDS systems in transmission configuration. However, the transmission configuration is more appropriate for evaluating transparent materials such as inorganic materials, ceramics, polymers, or gases, as the low-intensity reflected beam from these materials creates a challenge for reconstruction and analysis for reflection SA-based approaches. This highlights the need for an alternative setup where the object under test is evaluated in transmission configuration. Furthermore, the reported studies on SA imaging using coherent generation and detection systems have not extensively used the reconstructed amplitude and phase information to extract the real refractive index and absorption coefficient of the objects under test. Another main objective behind our proposed approach is to demonstrate the effectiveness of SA technique in material characterization.

This thesis details the several stages of our research. The first part was introducing SA imaging in transmission configuration to a broadband TDS system. To achieve that, we modified the classical configuration of the TDS system into a suitable setup that enabled the creation of a SA. These modifications consist of attaching the emitter antenna to a mobile platform and removing the lenses. Measurements were conducted on the radiation pattern emitted by the broadband PCA in order to determine the limitations of the system. The divergence of the emitter was found to be around 12° at -3 dB. Simulations highlighted that resolution reached a saturation point when using synthetic array of 10 cm and above due to the inherent relationship between resolution and the illumination of the object. Experimental implementation of SA using the TERA K15 THz-TDS commercial system validated simulated resolutions closely, yielding cross-range resolutions of δx = 850 µm and δz = 930 µm, along with a range resolution of δy = 200 µm across the available bandwidth (0.2 - 2.5 THz).

Using this SA imaging technique, we successfully reconstructed images of planar and 3D objects. A comparative analysis between our proposed SA imaging and the classical raster scanning (pixel-by-pixel imaging) revealed differences and similarities. The primary distinctions stemmed from the differences in the methodologies: SA imaging illuminates the entire object, leading to complex interactions, while raster scanning focuses on small sections of the object at a time. However, the raster scan approach requires mechanical translation of the object, contrasting with SA aperture imaging, where the object remains stationary while the emitter moves during acquisition. However, both approaches exhibited similarities in acquisition time under equivalent settings (resolution and FOV). To reduce the acquisition time, we integrated sparse sampling into our methodology, thus reducing acquisition time by 60% while maintaining performance standards. In contrast, in raster scanning, the sparse sampling

produces 'dark' pixels in the resulting image due to the lack of numerical treatment to compensate for missing data.

We further demonstrated the application of SA for spectroscopy, yielding consistent calculations of refractive index and absorption coefficients from reconstructed data of a multi-material planar object, and demonstrated that sparse sampling yields the same spectroscopy result as the full planar array.

In summary, this part of the manuscript underscores the effectiveness of SA using TDS system in image reconstruction, showcasing its advantage in reducing acquisition time compared to raster scan imaging via sparse sampling implementation. However, the choice between methodologies requires careful consideration of trade-offs and specific application demands. Nonetheless, SA imaging has demonstrated robustness in providing accurate spectroscopic data, affirming its potential in material characterization.

In the last chapter, we have demonstrated an application of the proposed imaging and spectroscopy approach: the spectral and time domain mapping of the output field profiles of a THz fiber. We have found in previous research that imaging of the output field profiles of THz waveguides has been explored using a THz near-field microscopy system based on the implementation of PCA as a coherent THz pulse source and as a near-field probe. This characterization technique provides high resolution images, but the waveguide has to be positioned at less than a millimeter from the near-field probe and the approach was demonstrated using a free space TDS system (antennas activated through free-space laser beam propagation) thus requiring complex experimental setups and careful alignment of multiple moving elements.

Our proposed approach provides a simpler imaging setup using SA and fiber coupled PCAs and positioning the fiber in the place of the object under test. Through the same numerical reconstruction process demonstrated in the previous chapter, we achieved images of the THz beam profile propagating within the waveguide, spanning a frequency range from 0.2 THz to 1.1 THz. This result highlights the versatility of our proposed imaging techniques for the analysis of objects that were previously challenging to characterize in the THz range.

Moreover, the obtained spectral images call for a modal characterization method to break-down the modal content of the fiber, which we explored in the next section of this chapter. The objective was to analyze the propagation of the THz beam in the fiber in the time domain, and extract the modal content based on the propagation delay of the supported modes. With an available time-domain resolution of 1.12 ps, we have been able to identify and generate the image of the fundamental mode propagating in the fiber, however we could not identify the high order modes separately. Preliminary results have been presented although, significant improvements remain necessary to achieve an efficient and exhaustive modal characterization of the fiber. We discussed the different factors that could be improved in order to successfully achieve modal characterization of fibers, or other propagation related devices in the THz range. The length L of the fiber which dictates the group delay of the mode at the output of the fiber and can be optimized to provide a more substantial delay between modes, thus facilitating their differentiation using the SA-S^2 method proposed and taking advantage of the available TDS equipment. However, in our setup, the optical delay line permits scanning over a limited distance of 70 cm between the PCAs. To address this limitation and enable the differentiation of propagating modes, a TDS system equipped with a sufficiently long delay line would be essential.

In conclusion, SA technique provides a valuable approach to THz imaging and spectroscopy when paired to a TDS system. Imaging and material characterization in transmission configuration of stationary objects provides a useful variety of techniques which is instrumental in the development of THz technologies. One of the notable applications of this approach is the characterization of THz waveguides. This approach relies on commercial TDS components without the need to purchase or develop additional components that would be less versatile compared to the commercial fiber coupled PCAs. This is critical to facilitate access to THz waveguides properties and exploit these findings to move forward in their development process. Moreover, this characterization approach could be extended to study guided waves propagation in other types of THz waveguides, resonators, filters, etc.

The proposed approach could be adapted for THz polarimetry, i.e., the measurement of the polarization state of THz waves transmitted through samples. Polarimetric techniques are used to estimate fine details of a material or to help resolve the orientation of small structures in the sample. Using our proposed imaging system based on SA imaging, multiple 3D images of an object under test could be reconstructed with multiple polarizations by attaching the emitter and detector to an automated rotational arm. Even though the experimental execution of this proposition would add to the acquisition time, additional information about the polarization state of the object under test will be provided, which could be useful in the case of the characterization of birefringent materials or components (birefringent THz hollow-core fibers), or providing additional polarization state distribution characteristics for information extraction on concealed objects, etc.

SA approach could be carried out using a sub-array of photoconductive antennas to reduce scanning time. The previously presented array of 8×8 antenna (Figure I-36) is an example of a sub array that could be mechanically scanned to scan 64 positions at the same time, thus significantly reducing acquisition time (scanning only 40 positions instead of 2500 in the case of our demonstration).

Our study presents promising prospects for real-time THz imaging, by integrating a real PCA array instead of relying on mechanically moving the antenna to create a synthetic array (Figure III-32). The implementation of a real PCA array will give rise to a multitude of challenges. However, seeing the impressive advancements achieved in the THz-SA imaging domain in the last three years, when this PhD took place, in addition to the arising commercial competition to provide affordable, compact, and user-friendly THz imaging and spectroscopy systems, these future perspectives will probably come to reality in the near future.

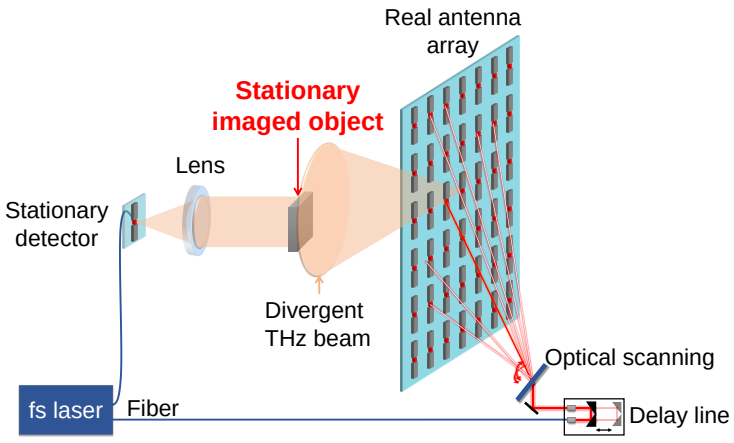

Figure III-32. Real PCA array for real-time THz imaging and spectroscopy.

Published work and conferences:

Journal article (In preparation): M. A. Assou, G. Humbert, A. Crunteanu and C. Decroze, "Synthetic aperture imaging of Terahertz hollow-core pipe fibers", peer reviewed publication, XLIM research institute, University of Limoges (2024).

Journal article: M. A. Assou, G. Humbert, A. Crunteanu and C. Decroze, "Synthetic Photoconductive Antenna Array for Terahertz 3-D Imaging and Spectroscopy," in IEEE Transactions on Terahertz Science and Technology, vol. 13, no. 5, pp. 440-447, Sept. 2023, doi: 10.1109/TTHZ.2023.3281771.

Conference paper* (Invited speaker)*: M. A. Assou, G. Humbert, A. Crunteanu, and C. Decroze, “Spectral imaging of Terahertz Waveguide using Synthetic Aperture", 2024 IEEE International Symposium on Antennas and Propagation and ITNC-USNC-URSI Radio Science Meeting 14-19 July 2024. Florence, Italy

Conference paper* (Poster)*: M. A. Assou, G. Humbert, A. Crunteanu and C. Decroze, "Sparse Synthetic Antenna Array for 3D Imaging and Spectroscopy in the Terahertz range," 2023 48th International Conference on Infrared, Millimeter, and Terahertz Waves (IRMMW-THz), Montreal, QC, Canada, 2023, pp. 1-2, doi: 10.1109/IRMMW-THz57677.2023.10298934.

Conference paper* (Oral presentation)*: M. A. Assou, G. Humbert, A. Crunteanu and C. Decroze, "Synthèse d'ouverture en spectroscopie THz dans le domaine temporel pour l'imagerie 3D". XXIIèmes Journées Nationales Microondes, Limoges 8-10 juin 2022, Jun 2022, Limoges, France.

Conference paper* (Oral presentation)*: M. A. Assou, G. Humbert, A. Crunteanu, and C. Decroze, " Sparse Synthetic Antenna Array for 3D Imaging and Spectroscopy in the Terahertz Range”. GDR NanoTeraMIR Meeting 2023, Dunkerque – 2023 May 24-26th.

Conference paper* (Poster)*: M. A. Assou, G. Humbert, A. Crunteanu and C. Decroze, "Synthèse d’ouverture en spectroscopie THz dans le domaine Temporel pour l’imagerie 3D", Neuvième Conférence Plénière du GDR ONDES, Pôle évènementiel de LILLIAD, Université de Lille 30 novembre et 1er décembre 2021, Nov 2021, Lille, France.

Conference paper* (Poster)*: M. A. Assou, G. Humbert, A. Crunteanu and C. Decroze, "Antenna array for real-time 3D imaging in terahertz domain", 3rd edition of the Σ-Tech Days. Explore the world of biomaterials with advanced photonics and artificial intelligence, Oct 2021, Limoges, France.

Bibliography

[1] L. Sun, L. Zhao, and R.-Y. Peng, “Research progress in the effects of terahertz waves on biomacromolecules,” *Mil. Med. Res.*, vol. 8, no. 1, p. 28, Dec. 2021, doi: 10.1186/s40779-021-00321-8.

[2] B. Wang, S. Zhong, T.-L. Lee, K. S. Fancey, and J. Mi, “Non-destructive testing and evaluation of composite materials/structures: A state-of-the-art review,” *Adv. Mech. Eng.*, vol. 12, no. 4, p. 168781402091376, Apr. 2020, doi: 10.1177/1687814020913761.

[3] M. van Exter, C. Fattinger, and D. Grischkowsky, “Terahertz time-domain spectroscopy of water vapor,” *Opt. Lett.*, vol. 14, no. 20, pp. 1128–1130, Oct. 1989, doi: 10.1364/OL.14.001128.

[4] E. K. Rahani, T. Kundu, Z. Wu, and H. Xin, “Mechanical Damage Detection in Polymer Tiles by THz Radiation,” *IEEE Sens. J.*, vol. 11, no. 8, pp. 1720–1725, Aug. 2011, doi: 10.1109/JSEN.2010.2095457.

[5] P. Mousavi, F. Haran, D. Jez, F. Santosa, and J. S. Dodge, “Simultaneous composition and thickness measurement of paper using terahertz time-domain spectroscopy,” *Appl. Opt.*, vol. 48, no. 33, p. 6541, Nov. 2009, doi: 10.1364/AO.48.006541.

[6] T. Yasui, T. Yasuda, K. Sawanaka, and T. Araki, “Terahertz paintmeter for noncontact monitoring of thickness and drying progress in paint film,” *Appl. Opt.*, vol. 44, no. 32, p. 6849, Nov. 2005, doi: 10.1364/AO.44.006849.

[7] S. Wietzker, C. Jördens, N. Krumbholz, B. Baudrit, M. Bastian, and M. Koch, “Terahertz imaging: a new non-destructive technique for the quality control of plastic weld joints,” *J. Eur. Opt. Soc. Rapid Publ.*, vol. 2, p. 07013, Apr. 2007, doi: 10.2971/jeos.2007.07013.

[8] E. Nguema, V. Vigneras, J. L. Miane, and P. Mounaix, “Dielectric properties of conducting polyaniline films by THz time-domain spectroscopy,” *Eur. Polym. J.*, vol. 44, no. 1, pp. 124–129, Jan. 2008, doi: 10.1016/j.eurpolymj.2007.10.020.

[9] D. Banerjee, W. von Spiegel, M. D. Thomson, S. Schabel, and H. G. Roskos, “Diagnosing water content in paper by terahertz radiation,” *Opt. Express*, vol. 16, no. 12, p. 9060, Jun. 2008, doi: 10.1364/OE.16.009060.

[10] J.-W. Park, K.-H. Im, D. K. Hsu, J.-A. Jung, and I.-Y. Yang, “Terahertz spectroscopy approach of the fiber orientation influence on CFRP composite solid laminates,” *J. Mech. Sci. Technol.*, vol. 26, no. 7, pp. 2051–2054, Jul. 2012, doi: 10.1007/s12206-012-0513-5.

[11] K. Kawase, T. Shibuya, S. Hayashi, and K. Suizu, “THz imaging techniques for nondestructive inspections,” *Comptes Rendus Phys.*, vol. 11, no. 7–8, pp. 510–518, Aug. 2010, doi: 10.1016/j.crhy.2010.04.003.

[12] S.-T. Han, W. K. Park, Y.-H. Ahn, W.-J. Lee, and H. S. Chun, “Development of a compact sub-terahertz gyrotron and its application to t-ray real-time imaging for food inspection,” in *2012 37th International Conference on Infrared, Millimeter, and Terahertz Waves*, Wollongong, NSW, Australia: IEEE, Sep. 2012, pp. 1–2. doi: 10.1109/IRMMW-THz.2012.6380390.

[13] C. Jördens, “Detection of foreign bodies in chocolate with pulsed terahertz spectroscopy,” *Opt. Eng.*, vol. 47, no. 3, p. 037003, Mar. 2008, doi: 10.1117/1.2896597.

[14] C. Wang, R. Zhou, Y. Huang, L. Xie, and Y. Ying, “Terahertz spectroscopic imaging with discriminant analysis for detecting foreign materials among sausages,” *Food Control*, vol. 97, pp. 100–104, Mar. 2019, doi: 10.1016/j.foodcont.2018.10.024.

[15] B. Qin, Z. Li, Z. Luo, H. Zhang, and Y. Li, “Feasibility of Terahertz Time-Domain Spectroscopy to Detect Carbendazim Mixtures Wrapped in Paper,” *J. Spectrosc.*, vol. 2017, pp. 1–8, 2017, doi: 10.1155/2017/6302868.

[16] X. Sun, J. Liu, K. Zhu, J. Hu, X. Jiang, and Y. Liu, “Generalized regression neural network association with terahertz spectroscopy for quantitative analysis of benzoic acid additive in wheat flour,” *R. Soc. Open Sci.*, vol. 6, no. 7, p. 190485, Jul. 2019, doi: 10.1098/rsos.190485.

[17] X. Sun, K. Zhu, J. Hu, X. Jiang, and Y. Liu, “Nondestructive Detection of Melamine in Milk Powder by Terahertz Spectroscopy and Correlation Analysis Algorithm,” *J. Appl. Spectrosc.*, vol. 86, no. 4, pp. 661–665, Sep. 2019, doi: 10.1007/s10812-019-00875-5.

[18] C. Han *et al.*, “Terahertz Spectroscopy and Imaging Techniques for Herbal Medicinal Plants Detection: A Comprehensive Review,” *Crit. Rev. Anal. Chem.*, pp. 1–15, Mar. 2023, doi: 10.1080/10408347.2023.2183077.

[19] J. Liang, Q. Guo, T. Chang, K. Li, and H.-L. Cui, “Reliable origin identification of Scutellaria baicalensis based on terahertz time-domain spectroscopy and pattern recognition,” *Optik*, vol. 174, pp. 7–14, Dec. 2018, doi: 10.1016/j.ijleo.2018.08.050.

[20] N. P. Yadav, G. Hu, and R. K. Singh, “Investigation of Tablet Defects by AI Based Terahertz Technology,” *Open J. Antennas Propag.*, vol. 11, no. 02, pp. 26–35, 2023, doi: 10.4236/ojapr.2023.112003.

[21] A. Moradikouchi, A. Sparén, O. Svensson, S. Folestad, J. Stake, and H. Rodilla, “Terahertz frequency-domain sensing combined with quantitative multivariate analysis for pharmaceutical tablet inspection,” *Int. J. Pharm.*, vol. 632, p. 122545, Feb. 2023, doi: 10.1016/j.ijpharm.2022.122545.

[22] K. Ajito *et al.*, “Nondestructive Multicomponent Terahertz Chemical Imaging of Medicine in Tablets,” *J. Electrochem. Soc.*, vol. 161, no. 9, pp. B171–B175, 2014, doi: 10.1149/2.0201409jes.

[23] E. Abraham, A. Younus, J. C. Delagnes, and P. Mounaix, “Non-invasive investigation of art paintings by terahertz imaging,” *Appl. Phys. A*, vol. 100, no. 3, pp. 585–590, Sep. 2010, doi: 10.1007/s00339-010-5642-z.

[24] F. Zidane *et al.*, “Artificial Intelligence-Based Low-Terahertz Imaging for Archaeological Shards’ Classification,” *IEEE Trans. Antennas Propag.*, vol. 70, no. 8, pp. 6300–6312, Aug. 2022, doi: 10.1109/TAP.2022.3189553.

[25] D. Saeedkia, *Handbook of terahertz technology for imaging, sensing and communications*. Woodhead Publishing Limited, 2013. doi: 10.1533/9780857096494.

[26] K. Krügener *et al.*, “Terahertz meets sculptural and architectural art: Evaluation and conservation of stone objects with T-ray technology,” *Sci. Rep.*, vol. 5, no. 1, p. 14842, Oct. 2015, doi: 10.1038/srep14842.

[27] H. Hoshina, Y. Sasaki, A. Hayashi, C. Otani, and K. Kawase, “Noninvasive Mail Inspection System with Terahertz Radiation,” *Appl. Spectrosc.*, vol. 63, no. 1, 2009.

[28] A. V. Shchepetilnikov *et al.*, “New Ultra-Fast Sub-Terahertz Linear Scanner for Postal Security Screening,” *J. Infrared Millim. Terahertz Waves*, vol. 41, no. 6, pp. 655–664, Jun. 2020, doi: 10.1007/s10762-020-00692-4.

[29] J.-L. Coutaz and F. Garet, “Les ondes électromagnétiques térahertz au service de la sécurité et de la défense,” *Photoniques*, no. 55, pp. 34–39, Sep. 2011, doi: 10.1051/photon/20115534.

[30] I. V. Il’ina, D. S. Sitnikov, and M. B. Agranat, “State-of-the-Art of Studies of the Effect of Terahertz Radiation on Living Biological Systems,” *High Temp.*, vol. 56, no. 5, pp. 789–810, Sep. 2018, doi: 10.1134/S0018151X18050127.

[31] Y. Cheng, L. Qiao, D. Zhu, Y. Wang, and Z. Zhao, “Passive polarimetric imaging of millimeter and terahertz waves for personnel security screening,” *Opt. Lett.*, vol. 46, no. 6, p. 1233, Mar. 2021, doi: 10.1364/OL.418497.

[32] S. Gui, J. Li, F. Zuo, and Y. Pi, “Analysis of Security Imaging Method for Walking Human Screening With Single Channel Synthetic Aperture Radar,” *IEEE Access*, vol. 7, pp. 111363–111374, 2019, doi: 10.1109/ACCESS.2019.2931413.

[33] A. D’Arco, M. D. Di Fabrizio, V. Dolci, M. Petrarca, and S. Lupi, “THz Pulsed Imaging in Biomedical Applications,” *Condens. Matter*, vol. 5, no. 2, p. 25, Apr. 2020, doi: 10.3390/condmat5020025.

[34] O. P. Cherkasova *et al.*, “Cellular effects of terahertz waves,” *J. Biomed. Opt.*, vol. 26, no. 09, Sep. 2021, doi: 10.1117/1.JBO.26.9.090902.

[35] G. J. Wilmink *et al.*, “In vitro investigation of the biological effects associated with human dermal fibroblasts exposed to 2.52 THz radiation,” *Lasers Surg. Med.*, vol. 43, no. 2, pp. 152–163, Feb. 2011, doi: 10.1002/lsm.20960.

[36] Z. Yan, L.-G. Zhu, K. Meng, W. Huang, and Q. Shi, “THz medical imaging: from in vitro to in vivo,” *Trends Biotechnol.*, vol. 40, no. 7, pp. 816–830, Jul. 2022, doi: 10.1016/j.tibtech.2021.12.002.

[37] K. I. Zaytsev *et al.*, “In vitro terahertz spectroscopy of gelatin-embedded human brain tumors: a pilot study,” in *Saratov Fall Meeting 2017: Optical Technologies in Biophysics and Medicine XIX*, V. V. Tuchin, D. E. Postnov, E. A. Genina, and V. L. Derbov, Eds., Saratov, Russian Federation: SPIE, Apr. 2018, p. 187. doi: 10.1117/12.2316302.

[38] Q. Cassar *et al.*, “Terahertz refractive index-based morphological dilation for breast carcinoma delineation,” *Sci. Rep.*, vol. 11, no. 1, p. 6457, Mar. 2021, doi: 10.1038/s41598-021-85853-8.

[39] Q. Cassar *et al.*, “Pilot study of freshly excised breast tissue response in the 300 – 600 GHz range,” *Biomed. Opt. Express*, vol. 9, no. 7, p. 2930, Jul. 2018, doi: 10.1364/BOE.9.002930.

[40] M. Gezimati and G. Singh, “Terahertz Imaging and Sensing for Healthcare: Current Status and Future Perspectives,” *IEEE Access*, vol. 11, pp. 18590–18619, 2023, doi: 10.1109/ACCESS.2023.3247196.

[41] A. I. Nikitkina *et al.*, “Terahertz radiation and the skin: a review,” *J. Biomed. Opt.*, vol. 26, no. 04, Feb. 2021, doi: 10.1117/1.JBO.26.4.043005.

[42] A. Sadeghi, S. M. H. Naghavi, M. Mozafari, and E. Afshari, “Nanoscale biomaterials for terahertz imaging: A non-invasive approach for early cancer detection,” *Transl. Oncol.*, vol. 27, p. 101565, Jan. 2023, doi: 10.1016/j.tranon.2022.101565.

[43] M. Gezimati and G. Singh, “Advances in terahertz technology for cancer detection applications,” *Opt. Quantum Electron.*, vol. 55, no. 2, p. 151, Feb. 2023, doi: 10.1007/s11082-022-04340-0.

[44] K. Tekbıyık, A. R. Ekti, G. K. Kurt, and A. Görçin, “Terahertz band communication systems: Challenges, novelties and standardization efforts,” *Phys. Commun.*, vol. 35, p. 100700, Aug. 2019, doi: 10.1016/j.phycom.2019.04.014.

[45] Z. Chen *et al.*, “A survey on terahertz communications,” *China Commun.*, 2019.

[46] H.-J. Song and N. Lee, “Terahertz Communications: Challenges in the Next Decade,” *IEEE Trans. Terahertz Sci. Technol.*, vol. 12, no. 2, pp. 105–117, Mar. 2022, doi: 10.1109/TTHZ.2021.3128677.

[47] C. Lin and G. Y. Li, “Indoor Terahertz Communications: How Many Antenna Arrays Are Needed?,” *IEEE Trans. Wirel. Commun.*, vol. 14, no. 6, pp. 3097–3107, Jun. 2015, doi: 10.1109/TWC.2015.2401560.

[48] X. Ma *et al.*, “Intelligent reflecting surface enhanced indoor terahertz communication systems,” *Nano Commun. Netw.*, vol. 24, p. 100284, May 2020, doi: 10.1016/j.nancom.2020.100284.

[49] S. Ju *et al.*, “Scattering Mechanisms and Modeling for Terahertz Wireless Communications,” in *ICC 2019 - 2019 IEEE International Conference on Communications (ICC)*, Shanghai, China: IEEE, May 2019, pp. 1–7. doi: 10.1109/ICC.2019.8761205.

[50] Y. Amarasinghe, W. Zhang, R. Zhang, D. M. Mittleman, and J. Ma, “Scattering of Terahertz Waves by Snow,” *J. Infrared Millim. Terahertz Waves*, vol. 41, no. 2, pp. 215–224, Feb. 2020, doi: 10.1007/s10762-019-00647-4.

[51] S. Sabchevski and M. Glyavin, “Development and Application of THz Gyrotrons for Advanced Spectroscopic Methods,” *Photonics*, vol. 10, no. 2, p. 189, Feb. 2023, doi: 10.3390/photonics10020189.

[52] P. Tan, J. Huang, K. Liu, Y. Xiong, and M. Fan, “Terahertz radiation sources based on free electron lasers and their applications,” *Sci. China Inf. Sci.*, vol. 55, no. 1, pp. 1–15, Jan. 2012, doi: 10.1007/s11432-011-4515-1.

[53] H. Johnson, “Backward-Wave Oscillators,” *Proc. IRE*, vol. 43, no. 6, pp. 684–697, 1955, doi: 10.1109/JRPROC.1955.278054.

[54] M. Y. Glyavin, G. G. Denisov, V. E. Zapevalov, M. A. Koshelev, M. Y. Tretyakov, and A. I. Tsvetkov, “High-power terahertz sources for spectroscopy and material diagnostics”.

[55] A. Fisher, “Single-pass high-efficiency terahertz free-electron laser,” *Nat. Photonics*, vol. 16, 2022.

[56] M. Asada and S. Suzuki, “Terahertz Emitter Using Resonant-Tunneling Diode and Applications,” *Sensors*, vol. 21, no. 4, p. 1384, Feb. 2021, doi: 10.3390/s21041384.

[57] C. Dalle, F. Dessenne, and J.-L. Thobel, “Theoretical Investigation of Terahertz GaN Mesa Transferred-Electron Device by Means of Time-Domain Energy/Momentum Modeling,” *IEEE Trans. Electron Devices*, vol. 59, no. 12, pp. 3321–3326, Dec. 2012, doi: 10.1109/TED.2012.2218111.

[58] A. Acharyya and P. Das, Eds., *Advanced Materials for Future Terahertz Devices, Circuits and Systems*, vol. 727. in Lecture Notes in Electrical Engineering, vol. 727. Singapore: Springer Singapore, 2021. doi: 10.1007/978-981-33-4489-1.

[59] H. Ito, F. Nakajima, T. Furuta, and T. Ishibashi, “Continuous THz-wave generation using antenna-integrated uni-travelling-carrier photodiodes”.

[60] H.-J. Song, K. Ajito, Y. Muramoto, A. Wakatsuki, and T. Nagatsuma, “Uni-Travelling-Carrier Photodiode Module Generating 300 GHz Power Greater Than 1 mW”.

[61] A. V. Raisanen, “Frequency multipliers for millimeter and submillimeter wavelengths,” *Proc. IEEE*, vol. 80, no. 11, pp. 1842–1852, Nov. 1992, doi: 10.1109/5.175259.

[62] A. Maestrini *et al.*, “Schottky diode-based terahertz frequency multipliers and mixers,” *Comptes Rendus Phys.*, vol. 11, no. 7–8, pp. 480–495, Aug. 2010, doi: 10.1016/j.crhy.2010.05.002.

[63] “Quantum Cascade Laser,” vol. 264, 1994.

[64] S. Fathololoumi *et al.*, “Terahertz quantum cascade lasers operating up to ∼ 200 K with optimized oscillator strength and improved injection tunneling,” 2012.

[65] R. Sharma, H. Kaur, and M. Singh, “Recent Advances of Efficient Design of Terahertz Quantum-Cascade Lasers,” *Plasmonics*, vol. 16, no. 2, pp. 449–461, Apr. 2021, doi: 10.1007/s11468-020-01295-4.

[66] P. Chevalier *et al.*, “Widely tunable compact terahertz gas lasers,” *Science*, vol. 366, no. 6467, pp. 856–860, Nov. 2019, doi: 10.1126/science.aay8683.

[67] E. Bründermann, H.-W. Hübers, and M. F. Kimmitt, *Terahertz Techniques*, vol. 151. in Springer Series in Optical Sciences, vol. 151. Berlin, Heidelberg: Springer Berlin Heidelberg, 2012. doi: 10.1007/978-3-642-02592-1.

[68] A. Pagies, G. Ducournau, and J.-F. Lampin, “Continuous wave terahertz molecular laser optically pumped by a quantum cascade laser,” in *2016 41st International Conference on Infrared, Millimeter, and Terahertz waves (IRMMW-THz)*, Copenhagen, Denmark: IEEE, Sep. 2016, pp. 1–2. doi: 10.1109/IRMMW-THz.2016.7758379.

[69] A. V. V. Nampoothiri *et al.*, “Hollow-core Optical Fiber Gas Lasers (HOFGLAS): a review [Invited],” *Opt. Mater. Express*, vol. 2, no. 7, p. 948, Jul. 2012, doi: 10.1364/OME.2.000948.

[70] Granite, “Terahertz Molecular Lasers: Introduction & Applications,” Edinburgh Instruments. Accessed: Jun. 25, 2023. [Online]. Available: https://www.edinst.com/terahertz-molecular-lasers-introduction-applications/

[71] R. Safian, G. Ghazi, and N. Mohammadian, “Review of photomixing continuous-wave terahertz systems and current application trends in terahertz domain,” *Opt. Eng.*, vol. 58, no. 11, p. 1, Nov. 2019, doi: 10.1117/1.OE.58.11.110901.

[72] S. Preu, G. H. Döhler, S. Malzer, L. J. Wang, and A. C. Gossard, “Tunable, continuous-wave Terahertz photomixer sources and applications,” *J. Appl. Phys.*, vol. 109, no. 6, p. 061301, Mar. 2011, doi: 10.1063/1.3552291.

[73] M. Bass, P. A. Franken, J. F. Ward, and G. Weinreich, “Optical Rectification,” *Phys. Rev. Lett.*, vol. 9, no. 11, pp. 446–448, Dec. 1962, doi: 10.1103/PhysRevLett.9.446.

[74] D. H. Auston, A. M. Johnson, P. R. Smith, and J. C. Bean, “Picosecond optoelectronic detection, sampling, and correlation measurements in amorphous semiconductors,” *Appl Phys Lett*, vol. 37, 1980.

[75] N. Arora, A. Bandyopadhyay, and A. Sengupta, “Modeling and Optimization of THz Photoconductive Antenna,” p. 7.

[76] S. Mondal, N. F. B. Edwin, and V. Rathinasamy, “Interdigitated Photoconductive Antenna for Efficient Terahertz Generation and Detection,” in *Terahertz Technology*, B. You and J.-Y. Lu, Eds., Rijeka: IntechOpen, 2022. doi: 10.5772/intechopen.102379.

[77] A. Alizadeh, M. Nazeri, and A. Sajedi Bidgoli, “Enhancement of the frequency peak of terahertz photoconductive antennas using metamaterial (MTM) superstrate structures,” *J. Comput. Electron.*, vol. 19, no. 1, pp. 451–456, Mar. 2020, doi: 10.1007/s10825-019-01407-2.

[78] S. Mondal, N. F. B. Edwin, V. Rathinasamy, S. Mondal, N. F. B. Edwin, and V. Rathinasamy, “Interdigitated Photoconductive Antenna for Efficient Terahertz Generation and Detection,” in *Terahertz Technology*, IntechOpen, 2022. doi: 10.5772/intechopen.102379.

[79] X. Chen and X. Liu, “Terahertz Antennas and Measurement,” in *Handbook of Antenna Technologies*, Z. N. Chen, D. Liu, H. Nakano, X. Qing, and T. Zwick, Eds., Singapore: Springer Singapore, 2016, pp. 619–659. doi: 10.1007/978-981-4560-44-3_47.

[80] Y. He, Y. Chen, L. Zhang, S.-W. Wong, and Z. N. Chen, “An overview of terahertz antennas,” *China Commun.*, vol. 17, no. 7, pp. 124–165, Jul. 2020, doi: 10.23919/J.CC.2020.07.011.

[81] X. He *et al.*, “Carbon Nanotube Terahertz Detector,” *Nano Lett.*, vol. 14, no. 7, pp. 3953–3958, Jul. 2014, doi: 10.1021/nl5012678.

[82] F. Simoens and J. Meilhan, “Terahertz real-time imaging uncooled array based on antenna- and cavity-coupled bolometers,” *Philos. Trans. R. Soc. Math. Phys. Eng. Sci.*, vol. 372, no. 2012, p. 20130111, Mar. 2014, doi: 10.1098/rsta.2013.0111.

[83] Q. Wu and X. -C. Zhang, “Free-space electro-optic sampling of terahertz beams,” *Appl. Phys. Lett.*, vol. 67, no. 24, pp. 3523–3525, Dec. 1995, doi: 10.1063/1.114909.

[84] T. K. Nguyen and I. Park, “EFFECTS OF ANTENNA DESIGN PARAMETERS ON THE CHARACTERISTICS OF A TERAHERTZ COPLANAR STRIPLINE DIPOLE ANTENNA,” *Prog. Electromagn. Res. M*, vol. 28, pp. 129–143, 2013, doi: 10.2528/PIERM12112401.

[85] Y. Huang, N. Khiabani, Y. Shen, and D. Li, “Terahertz photoconductive antenna efficiency,” in *2011 International Workshop on Antenna Technology (iWAT)*, Hong Kong, China: IEEE, Mar. 2011, pp. 152–156. doi: 10.1109/IWAT.2011.5752384.

[86] J. Prajapati, M. Bharadwaj, A. Chatterjee, and R. Bhattacharjee, “Circuit modeling and performance analysis of photoconductive antenna,” *Opt. Commun.*, vol. 394, pp. 69–79, Jul. 2017, doi: 10.1016/j.optcom.2017.03.004.

[87] S. B. Amlashi, A. Araghi, and G. Dadashzadeh, “Design of a Photoconductive Antenna for Pulsed-Terahertz Spectroscopy with Polarization Diversity,” in *2018 International Symposium on Networks, Computers and Communications (ISNCC)*, Rome: IEEE, Jun. 2018, pp. 1–5. doi: 10.1109/ISNCC.2018.8530985.

[88] I. Malhotra, P. Thakur, S. Pandit, K. R. Jha, and G. Singh, “Analytical framework of small-gap photoconductive dipole antenna using equivalent circuit model,” *Opt. Quantum Electron.*, vol. 49, no. 10, p. 334, Oct. 2017, doi: 10.1007/s11082-017-1175-4.

[89] F. Garet, L. Duvillaret, and J.-L. Coutaz, “Evidence of frequency-dependent THz beam polarization in time-domain spectroscopy,” presented at the Optoelectronics ’99 - Integrated Optoelectronic Devices, M. S. Sherwin, Ed., San Jose, CA, Apr. 1999, pp. 30–37. doi: 10.1117/12.347128.

[90] D. M. Mittleman, R. H. Jacobsen, and M. C. Nuss, “T-ray imaging,” *IEEE J. Sel. Top. Quantum Electron.*, vol. 2, no. 3, pp. 679–692, Sep. 1996, doi: 10.1109/2944.571768.

[91] M. Scheller, C. Jansen, and M. Koch, “Applications of Effective Medium Theories in the Terahertz Regime,” in *Recent Optical and Photonic Technologies*, K. Young, Ed., InTech, 2010. doi: 10.5772/6915.

[92] J. Dong, “Nondestructive evaluation of forced delamination in glass fiber-reinforced composites by terahertz and ultrasonic waves,” *Compos. Part B*, 2015.

[93] V. M. Ustinov and A. E. Zhukov, “GaAs-based long-wavelength lasers,” *Semicond. Sci. Technol.*, vol. 15, no. 8, pp. R41–R54, Aug. 2000, doi: 10.1088/0268-1242/15/8/201.

[94] “Ultrafast Femtosecond Fiber Laser, 1550 nm.” Accessed: Jun. 22, 2023. [Online]. Available: https://www.thorlabs.com

[95] “Application of Optical Delay Line in Terahertz Time-Domain Spectroscopy | Neon.” Accessed: Jun. 22, 2023. [Online]. Available: https://www.neoncq.com/application-of-optical-delay-line-in-terahertz-time-domain-spectroscopy.html

[96] J. Van Rudd and D. M. Mittleman, “Influence of substrate-lens design in terahertz time-domain spectroscopy,” *J. Opt. Soc. Am. B*, vol. 19, no. 2, p. 319, Feb. 2002, doi: 10.1364/JOSAB.19.000319.

[97] J. A. Murphy and S. Withington, “Perturbation analysis of Gaussian-beam-mode scattering at off-axis ellipsoidal mirrors,” *Infrared Phys. Technol.*, vol. 37, no. 2, pp. 205–219, Mar. 1996, doi: 10.1016/1350-4495(95)00047-X.

[98] W. Withayachumnankul and M. Naftaly, “Fundamentals of Measurement in Terahertz Time-Domain Spectroscopy,” 2014.

[99] M. Naftaly, “Metrology Issues and Solutions in THz Time-Domain Spectroscopy: Noise, Errors, Calibration,” *IEEE Sens. J.*, vol. 13, no. 1, pp. 8–17, Jan. 2013, doi: 10.1109/JSEN.2012.2208624.

[100] W. Withayachumnankul, B. M. Fischer, and D. Abbott, “Material thickness optimization for transmission-mode terahertz time-domain spectroscopy,” *Opt. Express*, vol. 16, no. 10, p. 7382, May 2008, doi: 10.1364/OE.16.007382.

[101] “All fiber-coupled Terahertz Spectrometer | Menlo Systems.” Accessed: Jun. 26, 2023. [Online]. Available: https://www.menlosystems.com/products/thz-time-domain-solutions/terak15-terahertz-spectrometer/

[102] A. Leitenstorfer *et al.*, “The 2023 terahertz science and technology roadmap,” *J. Phys. Appl. Phys.*, vol. 56, no. 22, p. 223001, Jun. 2023, doi: 10.1088/1361-6463/acbe4c.

[103] S. M. Eaton *et al.*, “Quantum Micro–Nano Devices Fabricated in Diamond by Femtosecond Laser and Ion Irradiation,” *Adv. Quantum Technol.*, vol. 2, no. 5–6, p. 1900006, Jun. 2019, doi: 10.1002/qute.201900006.

[104] W. Jia, M. Lou, W. Gao, and B. Sensale-Rodriguez, “Design and fabrication of a terahertz dual-plane hologram and extended-depth-of-focus diffractive lens,” *Opt. Contin.*, vol. 1, no. 8, p. 1722, Aug. 2022, doi: 10.1364/OPTCON.466008.

[105] D. Wang *et al.*, “Extended depth of field in continuous-wave terahertz computed tomography based on Bessel beam,” *Opt. Commun.*, vol. 432, pp. 20–26, Feb. 2019, doi: 10.1016/j.optcom.2018.09.031.

[106] A. I. Hernandez-Serrano and E. Pickwell-MacPherson, “Low cost and long-focal-depth metallic axicon for terahertz frequencies based on parallel-plate-waveguides,” *Sci. Rep.*, vol. 11, no. 1, p. 3005, Feb. 2021, doi: 10.1038/s41598-021-82503-x.

[107] B. Ding, G. Wen, C. Ma, and X. Yang, “Target recognition in synthetic aperture radar images using binary morphological operations,” *J. Appl. Remote Sens.*, vol. 10, no. 4, p. 046006, Oct. 2016, doi: 10.1117/1.JRS.10.046006.

[108] R. Bürgmann, P. A. Rosen, and E. J. Fielding, “Synthetic Aperture Radar Interferometry to Measure Earth’s Surface Topography and Its Deformation,” *Annu. Rev. Earth Planet. Sci.*, vol. 28, no. 1, pp. 169–209, May 2000, doi: 10.1146/annurev.earth.28.1.169.

[109] S. W. Paek, S. Balasubramanian, S. Kim, and O. de Weck, “Small-Satellite Synthetic Aperture Radar for Continuous Global Biospheric Monitoring: A Review,” *Remote Sens.*, vol. 12, no. 16, p. 2546, Aug. 2020, doi: 10.3390/rs12162546.

[110] T. Ager, “An Introduction to Synthetic Aperture Radar Imaging,” *Oceanography*, vol. 26, no. 2, Jun. 2013, doi: 10.5670/oceanog.2013.28.

[111] V. K. Dang, T. D. Nguyen, N. H. Dao, T. L. Duong, X. V. Dinh, and C. Weber, “Land subsidence induced by underground coal mining at Quang Ninh, Vietnam: persistent scatterer interferometric synthetic aperture radar observation using Sentinel-1 data,” *Int. J. Remote Sens.*, vol. 42, no. 9, pp. 3563–3582, May 2021, doi: 10.1080/01431161.2021.1875513.

[112] M. Cheney, “Fundamentals of Radar Imaging”.

[113] H. Cruz, M. Véstias, J. Monteiro, H. Neto, and R. P. Duarte, “A Review of Synthetic-Aperture Radar Image Formation Algorithms and Implementations: A Computational Perspective,” 2022.

[114] G. Wang, F. Qi, Z. Liu, C. Liu, C. Xing, and W. Ning, “Comparison Between Back Projection Algorithm and Range Migration Algorithm in Terahertz Imaging,” vol. 8, 2020.

[115] D. Pritsker, “Efficient Global Back-Projection on an FPGA,” *IEEE Radar Conf. RadarCon*, 2015.

[116] K. Hu, X. Zhang, S. He, H. Zhao, and J. Shi, “A Less-Memory and High-Efficiency Autofocus Back Projection Algorithm for SAR Imaging,” *IEEE Geosci. REMOTE Sens. Lett.*, vol. 12, no. 4, 2015.

[117] Y. Cao *et al.*, “Parallel Optimisation and Implementation of a Real-Time Back Projection (BP) Algorithm for SAR Based on FPGA,” 2022.

[118] “SAR Imagery for Civil, Commercial & Defense.” Accessed: Jun. 26, 2023. [Online]. Available: https://www.maxar.com/products/sar-imagery

[119] W. M. Brown and L. J. Porcello, “An introduction to synthetic-aperture radar”.

[120] M. Soumekh, *Synthetic Aperture Radar Signal Processing*, vol. 7. New York : Wiley, 1999.

[121] V. Krozer and T. Loffler, “Terahertz Imaging Systems With Aperture Synthesis Techniques,” *IEEE Trans. Microw. THEORY Tech.*, vol. 58, no. 7, 2010.

[122] K. McClatchey, M. T. Reiten, and R. A. Cheville, “Time resolved synthetic aperture terahertz impulse imaging,” *Appl. Phys. Lett.*, vol. 79, no. 27, pp. 4485–4487, Dec. 2001, doi: 10.1063/1.1427745.

[123] T. Bryllert *et al.*, “A 600 GHz imaging radar for concealed objects detection,” in *2009 IEEE Radar Conference*, Pasadena, CA, USA: IEEE, 2009, pp. 1–3. doi: 10.1109/RADAR.2009.4977038.

[124] X. Zhang, T. Chang, Z. Wang, and H.-L. Cui, “Three-Dimensional Terahertz Continuous Wave Imaging Radar for Nondestructive Testing,” *IEEE Access*, vol. 8, pp. 144259–144276, 2020, doi: 10.1109/ACCESS.2020.3014170.

[125] S. Saqueb, N. K. Nahar, and K. Sertel, “Fast two-dimensional THz imaging using rail-based synthetic aperture radar (SAR) processing,” *Electron. Lett.*, vol. 56, no. 19, pp. 988–990, Sep. 2020, doi: 10.1049/el.2020.0847.

[126] A. Batra, M. Wiemeler, D. Gohringer, and T. Kaiser, “Sub-mm Resolution 3D SAR Imaging at 1.5 THz,” in *2021 Fourth International Workshop on Mobile Terahertz Systems (IWMTS)*, Essen, Germany: IEEE, Jul. 2021, pp. 1–5. doi: 10.1109/IWMTS51331.2021.9486780.

[127] A. Bandyopadhyay *et al.*, “Terahertz interferometric and synthetic aperture imaging”.

[128] S. C. Henry, “Three-dimensional broadband terahertz synthetic aperture imaging,” *Opt. Eng.*, vol. 51, no. 9, p. 091603, May 2012, doi: 10.1117/1.OE.51.9.091603.

[129] S. Henry, “3-D Terahertz Synthetic-Aperture Imaging and Spectroscopy,” Jan. 2000. doi: 10.15760/etd.693.

[130] D. Damyanov *et al.*, “High Resolution Lensless Terahertz Imaging and Ranging,” *IEEE Access*, vol. 7, pp. 147704–147712, 2019, doi: 10.1109/ACCESS.2019.2934582.

[131] D. Damyanov, T. Kubiczek, K. Kolpatzeck, A. Czylwik, T. Schultze, and J. C. Balzer, “3D THz-TDS SAR Imaging by an Inverse Synthetic Cylindrical Aperture,” *IEEE Access*, vol. 11, pp. 9680–9690, 2023, doi: 10.1109/ACCESS.2023.3240101.

[132] B. Pradarutti *et al.*, “Terahertz line detection by a microlens array coupled photoconductive antenna array,” *Opt. Express*, vol. 16, no. 22, p. 18443, Oct. 2008, doi: 10.1364/OE.16.018443.

[133] R. Henri *et al.*, “Fabrication and Characterization of an 8 × 8 Terahertz Photoconductive Antenna Array for Spatially Resolved Time Domain Spectroscopy and Imaging Applications,” *IEEE Access*, vol. 9, pp. 117691–117702, 2021, doi: 10.1109/ACCESS.2021.3106227.

[134] A. Nadgir, R. Thurston, K. A. Larsen, M. M. Brister, and D. S. Slaughter, “SILIA: Software Implementation of a Multi-Channel, Multi-Frequency Lock-in Amplifier for Spectroscopy and Imaging Applications”.

[135] J. J. M. deWit, A. Meta, and P. Hoogeboom, “Modified Range-Doppler Processing for FM-CW Synthetic Aperture Radar,” *IEEE Geosci. Remote Sens. Lett.*, vol. 3, no. 1, pp. 83–87, Jan. 2006, doi: 10.1109/LGRS.2005.856700.

[136] J. M. Lopez-Sahcnez and J. Fortuny-Guasch, “3-D radar imaging using range migration techniques,” *IEEE Trans. Antennas Propag.*, vol. 48, no. 5, pp. 728–737, May 2000, doi: 10.1109/8.855491.

[137] C. Xing, F. Qi, Z. Liu, Y. Wang, and S. Guo, “Terahertz compressive imaging: understanding and improvement by a better strategy for data selection,” *Int. J. Numer. Model. Electron. Netw. Devices Fields*, vol. 34, no. 5, Aug. 2021, doi: 10.1002/jnm.2863.

[138] W. L. Chan, K. Charan, D. Takhar, K. F. Kelly, R. G. Baraniuk, and D. M. Mittleman, “A single-pixel terahertz imaging system based on compressed sensing,” *Appl. Phys. Lett.*, vol. 93, no. 12, p. 121105, Sep. 2008, doi: 10.1063/1.2989126.

[139] L. Liu, Z. Zhang, L. Gan, Y. Shen, and Y. Huang, “Terahertz imaging with compressed sensing,” in *2016 IEEE 9th UK-Europe-China Workshop on Millimetre Waves and Terahertz Technologies (UCMMT)*, Qingdao, China: IEEE, Sep. 2016, pp. 50–53. doi: 10.1109/UCMMT.2016.7873958.

[140] P. Hillger, J. Grzyb, R. Jain, and U. R. Pfeiffer, “Terahertz Imaging and Sensing Applications With Silicon-Based Technologies,” *IEEE Trans. Terahertz Sci. Technol.*, vol. 9, no. 1, pp. 1–19, Jan. 2019, doi: 10.1109/TTHZ.2018.2884852.

[141] H. Yoon and T.-K. Song, “Sparse Rectangular and Spiral Array Designs for 3D Medical Ultrasound Imaging,” *Sensors*, vol. 20, no. 1, p. 173, Dec. 2019, doi: 10.3390/s20010173.

[142] K. Y. Reddy, R. B. Kumar, M. Jijenth, K. K. Suman, V. S. Gangwar, and A. K. Singh, “Synthesis of randomly spaced planar antenna array with low peak side lobe level (PSLL) using Modified Genetic Algorithm,” in *2017 IEEE International Conference on Antenna Innovations & Modern Technologies for Ground, Aircraft and Satellite Applications (iAIM)*, Bangalore, India: IEEE, Nov. 2017, pp. 1–4. doi: 10.1109/IAIM.2017.8402567.

[143] K. Chen, Y. Li, and J. Shi, “Optimization of Sparse Concentric Ring Arrays for Low Sidelobe,” *Int. J. Antennas Propag.*, vol. 2019, pp. 1–8, Jun. 2019, doi: 10.1155/2019/1485075.

[144] K. Chen, H. Chen, L. Wang, and H. Wu, “Modified Real GA for the Synthesis of Sparse Planar Circular Arrays,” *IEEE Antennas Wirel. Propag. Lett.*, vol. 15, pp. 274–277, 2016, doi: 10.1109/LAWP.2015.2440432.

[145] B. Baccouche *et al.*, “Illumination aspects of sparse line arrays for 3D terahertz imaging,” in *2016 41st International Conference on Infrared, Millimeter, and Terahertz waves (IRMMW-THz)*, Copenhagen, Denmark: IEEE, Sep. 2016, pp. 1–2. doi: 10.1109/IRMMW-THz.2016.7758825.

[146] B. Baccouche *et al.*, “Three-Dimensional Terahertz Imaging With Sparse Multistatic Line Arrays,” *IEEE J. Sel. Top. Quantum Electron.*, vol. 23, no. 4, pp. 1–11, Jul. 2017, doi: 10.1109/JSTQE.2017.2673552.

[147] A. M. Molaei, S. Hu, V. Skouroliakou, V. Fusco, X. Chen, and O. Yurduseven, “Fast Processing Approach for Near-Field Terahertz Imaging With Linear Sparse Periodic Array,” *IEEE Sens. J.*, vol. 22, no. 5, pp. 4410–4424, Mar. 2022, doi: 10.1109/JSEN.2022.3145324.

[148] X. Chen, H. Wang, Q. Yang, Y. Zeng, and B. Deng, “An Efficient mmW Frequency-Domain Imaging Algorithm for Near-Field Scanning 1-D SIMO/MIMO Array,” *IEEE Trans. Instrum. Meas.*, vol. 71, pp. 1–12, 2022, doi: 10.1109/TIM.2022.3189631.

[149] R. Yang *et al.*, “Sliding Spotlight Synthetic Aperture Radar,” in *High-Resolution Microwave Imaging*, Singapore: Springer Singapore, 2018, pp. 297–321. doi: 10.1007/978-981-10-7138-6_9.

[150] ia gov awdoerr@s and J. M. Edward.Bishop@ga-asi.com, “Basics of Backprojection Algorithm for Processing Synthetic Aperture Radar Images”.

[151] M. I. Duersch, “Backprojection for Synthetic Aperture Radar”.

[152] G. Wang, F. Qi, Z. Liu, C. Liu, C. Xing, and W. Ning, “Comparison Between Back Projection Algorithm and Range Migration Algorithm in Terahertz Imaging,” *IEEE Access*, vol. 8, pp. 18772–18777, 2020, doi: 10.1109/ACCESS.2020.2968085.

[153] N. Arora, A. Bandyopadhyay, and A. Sengupta, “Modeling and Optimization of THz Photoconductive Antenna”.

[154] N. Khiabani, Y. Huang, Y.-C. Shen, and StephenJ. Boyes, “Theoretical Modeling of a Photoconductive Antenna in a Terahertz Pulsed System,” *IEEE Trans. Antennas Propag.*, vol. 61, no. 4, pp. 1538–1546, Apr. 2013, doi: 10.1109/TAP.2013.2239599.

[155] N. Khiabani, Y. Huang, and Y. Shen, “Discussions on the main parameters of THz photoconductive antennas as emitters,” p. 5.

[156] N. Zhu and R. W. Ziolkowski, “Photoconductive THz Antenna Designs With High Radiation Efficiency, High Directivity, and High Aperture Efficiency,” *IEEE Trans. Terahertz Sci. Technol.*, vol. 3, no. 6, pp. 721–730, Nov. 2013, doi: 10.1109/TTHZ.2013.2285568.

[157] A. Garufo *et al.*, “Norton Equivalent Circuit for Pulsed Photoconductive Antennas—Part II: Experimental Validation,” *IEEE Trans. Antennas Propag.*, vol. 66, no. 4, pp. 1646–1659, Apr. 2018, doi: 10.1109/TAP.2018.2800704.

[158] J. Smith, S. Nellen, S. Lauck, B. Globisch, and M. Naftaly, “Beam Profile Investigation of an Optoelectronic Continuous-Wave Terahertz Emitter,” in *2019 44th International Conference on Infrared, Millimeter, and Terahertz Waves (IRMMW-THz)*, Paris, France: IEEE, Sep. 2019, pp. 1–2. doi: 10.1109/IRMMW-THz.2019.8874086.

[159] “Collimator,” *Wikipedia*. Nov. 26, 2023. Accessed: Dec. 09, 2023. [Online]. Available: https://en.wikipedia.org/w/index.php?title=Collimator&oldid=1186884048

[160] K. Tomiyasu, “Tutorial review of synthetic-aperture radar (SAR) with applications to imaging of the ocean surface,” *Proc. IEEE*, vol. 66, no. 5, pp. 563–583, May 1978, doi: 10.1109/PROC.1978.10961.

[161] C. Liu and R. Zoughi, “Influence of Antenna Pattern on Synthetic Aperture Radar Image Sidelobe Level in NDE Applications,” *IEEE Trans. Instrum. Meas.*, vol. 70, 2021.

[162] C. Liu and R. Zoughi, “Influence of Antenna Pattern on Synthetic Aperture Radar Resolution for NDE Applications,” *IEEE Trans. Instrum. Meas.*, vol. 70, 2021.

[163] K. Ahi, “Mathematical Modeling of THz Point Spread Function and Simulation of THz Imaging Systems,” *IEEE Trans. Terahertz Sci. Technol.*, vol. 7, no. 6, pp. 747–754, Nov. 2017, doi: 10.1109/TTHZ.2017.2750690.

[164] M. Di Fabrizio, A. D’Arco, S. Mou, L. Palumbo, M. Petrarca, and S. Lupi, “Performance Evaluation of a THz Pulsed Imaging System: Point Spread Function, Broadband THz Beam Visualization and Image Reconstruction,” *Appl. Sci.*, vol. 11, no. 2, p. 562, Jan. 2021, doi: 10.3390/app11020562.

[165] M. Naftaly and R. E. Miles, “Terahertz Time-Domain Spectroscopy for Material Characterization,” *Proc. IEEE*, vol. 95, no. 8, pp. 1658–1665, Aug. 2007, doi: 10.1109/JPROC.2007.898835.

[166] C. L. Davies, J. B. Patel, C. Q. Xia, L. M. Herz, and M. B. Johnston, “Temperature-Dependent Refractive Index of Quartz at Terahertz Frequencies,” *J. Infrared Millim. Terahertz Waves*, vol. 39, no. 12, pp. 1236–1248, Dec. 2018, doi: 10.1007/s10762-018-0538-7.

[167] H. Amarloo and N. Ranjkesh, “Terahertz Silicon–BCB–Quartz Dielectric Waveguide: An Efficient Platform for Compact THz Systems,” *IEEE Trans. TERAHERTZ Sci. Technol.*, vol. 8, no. 2, 2018.

[168] A. K. Kaveev *et al.*, “Terahertz polarization conversion with quartz waveplate sets”.

[169] Y. Taira *et al.*, “A Terahertz Wave Parametric Amplifier With a Gain of 55 dB”.

[170] K. Takeya, T. Minami, H. Okano, S. R. Tripathi, and K. Kawase, “Enhanced Cherenkov phase matching terahertz wave generation via a magnesium oxide doped lithium niobate ridged waveguide crystal,” *APL Photonics*, 2016.

[171] M. Theuer *et al.*, “Efficient generation of Cherenkov-type terahertz radiation from a lithium niobate crystal with a silicon prism output coupler,” *Appl Phys Lett*.

[172] J. Han, B. K. Woo, W. Chen, M. Sang, X. Lu, and W. Zhang, “Terahertz Dielectric Properties of MgO Nanocrystals,” *J. Phys. Chem. C*, vol. 112, no. 45, pp. 17512–17516, Nov. 2008, doi: 10.1021/jp805880p.

[173] Z. Zhang and T. Buma, “Improved terahertz imaging with a sparse synthetic aperture array,” L. P. Sadwick and C. M. M. O’Sullivan, Eds., San Francisco, California, Feb. 2010, p. 760103. doi: 10.1117/12.841756.

[174] K. Chen, H. Chen, L. Wang, and H. Wu, “Modified Real GA for the Synthesis of Sparse Planar Circular Arrays,” *IEEE Antennas Wirel. Propag. Lett.*, vol. 15, pp. 274–277, 2016, doi: 10.1109/LAWP.2015.2440432.

[175] K. Chen, Y. Li, and J. Shi, “Optimization of Sparse Concentric Ring Arrays for Low Sidelobe,” *Int. J. Antennas Propag.*, vol. 2019, pp. 1–8, Jun. 2019, doi: 10.1155/2019/1485075.

[176] C. Lv, B. Deng, Y. Zhang, Q. Yang, and H. Wang, “Terahertz Spiral SAR Imaging Algorithms and Simulations,” in *2020 IEEE 4th Information Technology, Networking, Electronic and Automation Control Conference (ITNEC)*, Chongqing, China: IEEE, Jun. 2020, pp. 1746–1750. doi: 10.1109/ITNEC48623.2020.9085036.

[177] N. Ekhtiari, “Comparing ground truth with predictions using image similarity measures”.

[178] “Structural similarity,” *Wikipedia*. Sep. 03, 2023. Accessed: Oct. 11, 2023. [Online]. Available: https://en.wikipedia.org/w/index.php?title=Structural_similarity&oldid=1173601662

[179] S.-X. Huang *et al.*, “Terahertz Multi-Spectral Mueller Matrix Polarimetry on Leaf Using Only Orthogonal-Polarization Measurements,” *IEEE Trans. Terahertz Sci. Technol.*, vol. 11, no. 6, pp. 609–619, Nov. 2021, doi: 10.1109/TTHZ.2021.3090111.

[180] G. Humbert, “Optical Fibers in Terahertz Domain,” in *Handbook of Optical Fibers*, G.-D. Peng, Ed., Singapore: Springer Singapore, 2019, pp. 1–49. doi: 10.1007/978-981-10-1477-2_33-1.

[181] G. Humbert *et al.*, “Hollow core photonic crystal fibers for beam delivery,” 2004.

[182] K. Nielsen, H. K. Rasmussen, A. J. L. Adam, M. Planken, O. Bang, and P. U. Jepsen, “Bendable, low-loss Topas fibers for the terahertz frequency range,” 2009.

[183] S. Wielandy, “Implications of higher-order mode content in large mode area fibers with good beam quality,” *Opt. Express*, vol. 15, no. 23, p. 15402, Nov. 2007, doi: 10.1364/OE.15.015402.

[184] J. W. P. Hsu, “Near-field scanning optical microscopy studies of electronic and photonic materials and devices,” *Mater. Sci. Eng.*, 2001.

[185] G. Sun *et al.*, “Anti-resonant fiber with nested U-shape tubes for low-loss terahertz waveguides,” *Opt. Laser Technol.*, vol. 163, p. 109424, Aug. 2023, doi: 10.1016/j.optlastec.2023.109424.

[186] Y.-J. Rao, Z.-L. Ran, and Y. Gong, *Fiber-optic Fabry-Perot sensors: an introduction*. in Series in fiber optic sensors. Boca Raton: CRC Press, Taylor & Francis Group, 2017.

[187] G. Humbert, J.-L. Auguste, G. Ducournau, and J.-F. Lampin, “Low-loss, 1-m long length, hollow-core THz waveguide operating at 1 THz, based on anti-resonant guiding mechanism”.

[188] T. G. Euser *et al.*, “Dynamic control of higher-order modes in hollow-core photonic crystal fibers,” 2008.

[189] O. Shapira, A. F. Abouraddy, J. D. Joannopoulos, and Y. Fink, “Complete Modal Decomposition for Optical Waveguides,” *Phys. Rev. Lett.*, 2005.

[190] D. R. Gray *et al.*, “Complementary Analysis of Modal Content and Properties in a 19-cell Hollow Core Photonic Band Gap Fiber using Time-of- Flight and S2 Techniques,” 2012.

[191] J. Demas and S. Ramachandran, “Sub-second mode measurement of fibers using C2 imaging,” 2014.

[192] Y. Z. Ma *et al.*, “Fiber-modes and fiber-anisotropy characterization using low-coherence interferometry,” *Appl. Phys. B*, vol. 96, no. 2–3, pp. 345–353, Aug. 2009, doi: 10.1007/s00340-009-3517-9.

[193] M. Paurisse, L. Lévèque, M. Hanna, F. Druon, and P. Georges, “Complete measurement of fiber modal content by wavefront analysis,” 2012.

[194] D. R. Gray *et al.*, “Accurate calibration of S2 and interferometry based multimode fiber characterization techniques,” 2015.

[195] J. W. Nicholson, A. D. Yablon, S. Ramachandran, and S. Ghalmi, “Spatially and spectrally resolved imaging of modal content in large-mode-area fibers,” *Opt. Express*, vol. 16, no. 10, p. 7233, May 2008, doi: 10.1364/OE.16.007233.

[196] A. V. Newkirk *et al.*, “Modal analysis of antiresonant hollow core fibers using S^2 imaging,” *Opt. Lett.*, vol. 41, no. 14, p. 3277, Jul. 2016, doi: 10.1364/OL.41.003277.

[197] M. A. Kaliteevskiĭ, V. V. Nikolaev, and R. A. Abram, “Calculation of the mode structure of multilayer optical fibers based on transfer matrices for cylindrical waves,” *Opt. Spectrosc.*, vol. 88, no. 5, pp. 792–795, May 2000, doi: 10.1134/1.626880.

[198] S. Yan, Z. Lian, S. Lou, X. Wang, W. Zhang, and Z. Tang, “The expression for calculating mode effective indices of hollow-core anti-resonant fibers in non-resonant wavelength regions”.

[199] “Nyquist–Shannon sampling theorem,” *Wikipedia*. Oct. 14, 2023. Accessed: Dec. 05, 2023. [Online]. Available: https://en.wikipedia.org/w/index.php?title=Nyquist%E2%80%93Shannon_sampling_theorem&oldid=1180085259

[200] O. A. Castañeda-Uribe, C. A. Criollo, S. Winnerl, M. Helm, and A. Avila, “Comparative study of equivalent circuit models for photoconductive antennas,” *Opt. Express*, vol. 26, no. 22, p. 29017, Oct. 2018, doi: 10.1364/OE.26.029017.

Appendices

Appendix 1. Equivalent Circuit Model of a PCA

Despite not being directly involved in the PCA's fabrication, an equivalent circuit model (ECM) of the antenna is proposed and analyzed in order to conclude on the impact of the physical parameters of the antenna on its generated THz power.

PCA equivalent circuit model

The PCA has gained popularity for its effectiveness in pulsed THz generation and detection applications [88], [200]. Typically, a PCA comprises a metallic antenna pattern on a semiconductor substrate. The dipole structure is a prevalent choice for the antenna pattern due to its relatively simple fabrication process and impedance matching capabilities. During operation, a biased voltage source and an optical laser source drive the photoconductive gap G, inducing a current that generates THz radiation.

To achieve higher THz emission efficiency, small-gap PCAs are often preferred for THz generation. A small-gap PCA is one with a gap narrower than the wavelength (3 to 50 µm), resulting in THz radiation across a broad frequency spectrum, delimited by the resonance frequency f_r of the metallic antenna structure.

Successful generation of the desired THz radiation via a PCA depends on overcoming challenges like field breakdown, thermal breakdown, and low antenna efficiency due to insufficient charge acceleration. This necessitates sufficient incoming laser power, a suitable photoconductive material, an appropriate bias voltage, and a well-designed antenna. Thus, a systematic analysis procedure is crucial to comprehensively understand the antenna's behavior concerning its various triggering elements. However, analyzing THz antennas differs significantly from microwave antennas due to their optoelectronic characteristics, originating from the optical excitation of photoconductive material responses. This necessitates a different simulation and analysis procedure that incorporates both optical excitation and antenna geometrical effects.

Various physical models have been explored by researchers, among them the Equivalent Circuit Model (ECM) in which the PCA is represented as a combination of lumped elements, with time-varying resistance, capacitance, voltage or current source and the antenna impedance. The ECM approach leverages existing antenna theory to analyze the photoconductive antenna, in addition to carrier dynamics theory, thus including all antenna-related aspects. This approach provides a realistic depiction of the antenna, establishing a direct link between ECM parameters, material properties, and the THz antenna's structure which could be used for designing PCAs with improved performances.

An analytical framework for modeling small-gap photoconductive dipole antennas based on an ECM is proposed in the following section. The proposed approach provides a first simulation, to our knowledge, of a fiber coupled 1560 nm input THz PCA, as for the previously reported work exclusively on free space 800 nm input THz PCA. This framework aims to determine factors contributing to the antenna's generated THz power as a function of gap size G, dipole width W, bias voltage and excitation optical power.

Analytical frame work

When the antenna electrodes are externally biased, a static field is built inside the bulk semiconductor. Under the influence of a fixed DC bias voltage, the charge carriers (electrons and holes) flow in a certain direction and a current is produced. When the input energy from

the optical pulse into the photoconductive semiconductor substrate is larger than that of its bandgap, it separates the electrons and holes creating electron–hole pairs. The input energy changes rapidly on applying an ultra-short optical pulse on the photoconductive gap G which vary the carrier density n(t) across the gap which intrinsically generates a time-varying electric field leading to electromagnetic waves generation dur to the variation of the current intensity.

We consider a Gaussian beam distribution of a laser pulse incident on the gap G, thus the laser intensity could be described as:

Eq. 54

$$I_l(r,t) = I_l(1-R)e^{\left(\frac{-2r^2}{\omega_0^2}\right)}e^{\left(\frac{-2t^2}{\tau_l^2}\right)}$$

Where I_l is the peak laser intensity, R is the power reflection coefficient, w_0 is the optical beam waist at 1/e of the peak amplitude, r is the radius of the beam and τ_l is the laser pulse duration.

With the photo-illumination of the small-gap photoconductive dipole antenna, the time-dependent carrier density n(t) is generated and is determined using the following equation:

Eq. 55

$$n(t) = \frac{\sqrt{2\pi}\tau_l \alpha I_l}{4hf_l}(1-R)e^{-2}e^{\left(\frac{\tau_l^2}{8\tau_c^2}-\frac{t}{\tau_c}\right)}\left[\mathrm{erf}\left(\frac{\sqrt{2}t}{\tau_l}-\frac{\sqrt{2}\tau_l}{4\tau_c}\right)+1\right]$$

Where α the optical absorption coefficient of the substrate, h the Planck's constant, τ_c the carrier lifetime, and f_l the optical pulse repetition frequency.

The separation of electron–hole pairs and their immigration to the antenna electrodes due to the bias voltage results in the THz radiation. However, when the residual space-charge pairs near the metal contacts are unable to find the opposite sign pair for recombination, they remain static near the dipole antenna electrodes, which results in the formation of a time-dependent capacitance C(t), which is influenced by the generated carrier density n(t) in the photoconductive gap and the recombination time τ_r of photoconductive material.

Eq. 56

$$C(t) = \left(\frac{\tau_r}{Z_a}\right)\left(1+\frac{e\mu_e Z_a S n(t)}{G}\right)$$

Where S is cross-sectional area of the active volume that is normal to the DC bias electric field, τ_r is the recombination time, Z_a is the antenna impedance, e the electron charge and μ_e the electron mobility in the photoconductive substrate.

This time-varying capacitance C(t) and the time-dependent voltage source controlled by the voltage across capacitance $\beta(t)V_c(t)$ reflects the screening effect across the gap of dipole PCA. The screening effect refers to the phenomenon where the generated carriers in the photoconductive material reduce the electric field within the material itself by creating an opposing electric field that partially cancels the externally applied bias field. As a result, the screening effect leads to a reduction in the photocurrent by limiting the acceleration of new charge carriers. This effect becomes more prominent as the photocarriers accumulate and saturate the photoconductive material. This self-generated electric field could be quantified by calculating both β(t) and $V_c(t)$. The expression of β(t) is defined as:

Eq. 57

$$\beta(t) = \frac{e\mu_e\tau_r n(t)}{\epsilon\xi}$$

Where ϵ is the dielectric permittivity of the substrate and ξ the geometrical factor of the substrate.

The photoconductive gap acts as a current source for the antenna and its resistance is considered as the source resistance $R_S(t)$ of the antenna. The time-dependent source conductance $G_S(t)$ can be expressed as:

Eq. 58

$$G_S(t) = \frac{S}{G} e\mu_e n(t)(1 - e^{-\alpha T_{sub}})$$

Where T_{sub} is the laser skin depth at the excitation region.

The time-dependent voltage $V_C(t)$ across the capacitance of the antenna electrodes is determined from the following equation which is a first order differential equation and is solved for $V_C(t)$ using Runge–Kutta numerical analysis method for fourth order:

Eq. 59

$$\frac{dV_{c(t)}}{dt} + \left[\left(\frac{1+\beta(t)}{Z_a C(t)}\right) + \frac{G_s(t)}{C(t)} + \frac{1}{C(t)}\frac{dC(t)}{dt}\right] V_c(t) = \frac{E_{bias}}{Z_a C(t)}$$

where E_{bias} is the constant biased voltage applied across the biased lines of photoconductive dipole antenna.

The THz photocurrent induced at the photoconductive gap (G) is computed using the equation:

Eq. 60

$$I_{ph}(t) = e\,\mu_e n(t) V_C(t) \frac{S}{G}$$

The rise time of photocurrent is determined by laser pulse duration τ_l and its decay time is influenced by the carrier lifetime τ_c of the photoconductive material.

The antenna radiated power $P_{THz}(t)$ and the total efficiency of antenna η_t shows their dependence on the radiated voltage $V_{rad}(t)$ and optical laser source parameters:

Eq. 61

$$P_{THz}(t) = \frac{V_{rad}^2(t)}{Z_a}$$

With

Eq. 62

$$V_{rad}(t) = Z_a I_{ph}(t)$$

And

Eq. 63

$$\eta_t = \frac{P_{THz_{peak}}}{P_{opt_{peak}}}$$

With

Eq. 64

$$P_{opt_{peak}} = \frac{P_{av}}{\tau_l \, f_{rep}}$$

With $P_{THz\ peak}$ the peak radiated power, P_{av} the average optical power provided by the laser and f_{rep} the repetition frequency of the laser pulse.

Thus, the lumped elements of the ECM of the PCA could be assembled as shown in the following Figure A-1.

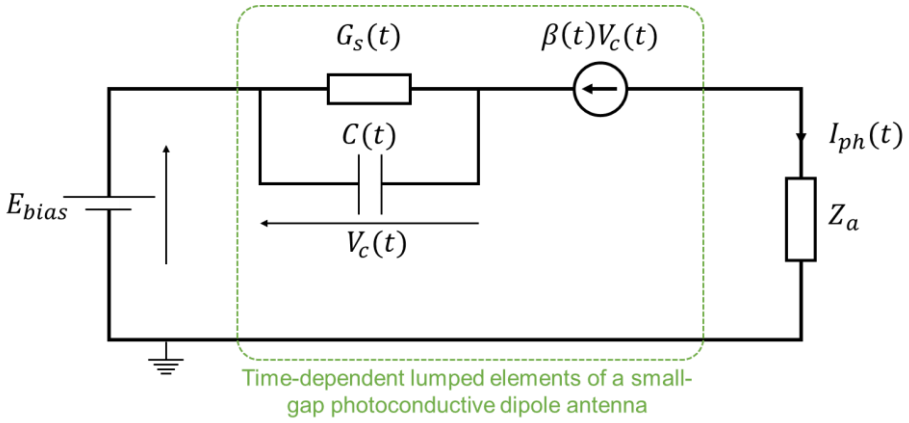

Figure A-1. The proposed equivalent circuit model of a dipole PCA. The circuit is composed of time-dependent lumped elements reflecting the opto-electronic physical reaction to a laser beam excitation and electrical bias.

Simulation results and discussions

The analyzed PCA is a commercial fiber coupled THz antenna supplied by Menlo Systems. Even though the structure of the metallic radiation part of the antenna is unknown to us, the rest of the information about the substrate, the used laser excitation and the bias voltage is available to the user of the antenna thus making is feasible to execute this simulation and compare the obtained results with the measured experimental data.

The substrate of the PCA, according to the supplier, is multilayered Iron doped Gallium Arsenide and Indium Aluminum Arsenide (Fe:GaAs/InAlAs) which parameters are detailed in the Table. A-1. The simulation accounts for a dipole antenna Figure A-2, which will provide a decent approximation of the experimental results, however, noticeable difference might appear on the part of the BW of the emitted signal, as it is larger for bowtie and spiral antennas for example.

Table. A-1. Physical parameters and constants used in the proposed PCA dipole simulation

Parameter	**Value**	**Unity**
Speed of light in vacuum c	3×10^{8}	m/s
Permittivity of free space ε_0	8.85×10^{-12}	F/m
Permeability of free space μ_0	1.25×10^{-6}	$N.A^{-2}$

Planck's constant h	6.62×10^{-34}	m^2. Kg / s
Electron charge e	1.602×10^{-19}	C
Bias voltage E_{bias}	100	V
Excitation laser parameters		
Light wavelength λ_l	1560	µm
Laser pulse duration ζ_l	100	ps
Optical pulse repetition frequency f_l	100	MHz
Average optical power P_{av}	30	mW
PCA parameters		
Permittivity of thin layer-substrate ε	13.26	NaN
Conductivity of metal σ_C	5.81×10^7	S/m
Electron mobility in thin-layer substrate μ_e	2395	cm^2 / V / s
Optical absorption coefficient α	6×10^6	m^{-1}
Power reflection coefficient R	0.318	NaN
Carrier lifetime ζ_c	0.3	ps
Recombination lifetime ζ_r	100	ps
Geometrical factor of the substrate ξ	900	NaN
Laser skin depth at the excitation region T_{sub}	1	µm
Antenna impedance Z_a	50	Ω

The dimensions of the dipole G and W are not specified in the table above as they will be varied across different values to evaluate their effect of the ECM elements and the generated THz power eventually.

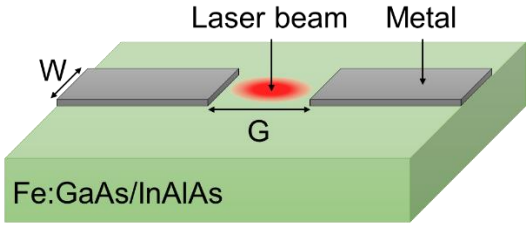

Figure A-2. A simple dipole PCA.

The influence of antenna gap size G is investigated with values between 3 µm and 13 µm with a 2 µm step, a range accounting for the usually found values of G on PCAs. The Figure A-3 shows the effect of change in photoconductive gap size G on time dependent carrier density n(t), capacitance C(t), Source conductance $G_S(t)$, the voltage across the antenna gap $V_C(t)$ and the generated photocurrent $I_{ph}(t)$.

Figure A-3.a show an increasing carrier density with a decreasing gap size because the optically excited area shrinks for smaller G values resulting in a larger carrier number in smaller space compared to a bigger gap size. The capacitance C(t) in Figure A-3.b shows that for the small gap-size, the capacitance is higher because it is inversely proportional to the gap size as shown in Eq. 56. This result means that the opposing effect of the screening effect is smaller in larger gap antennas.

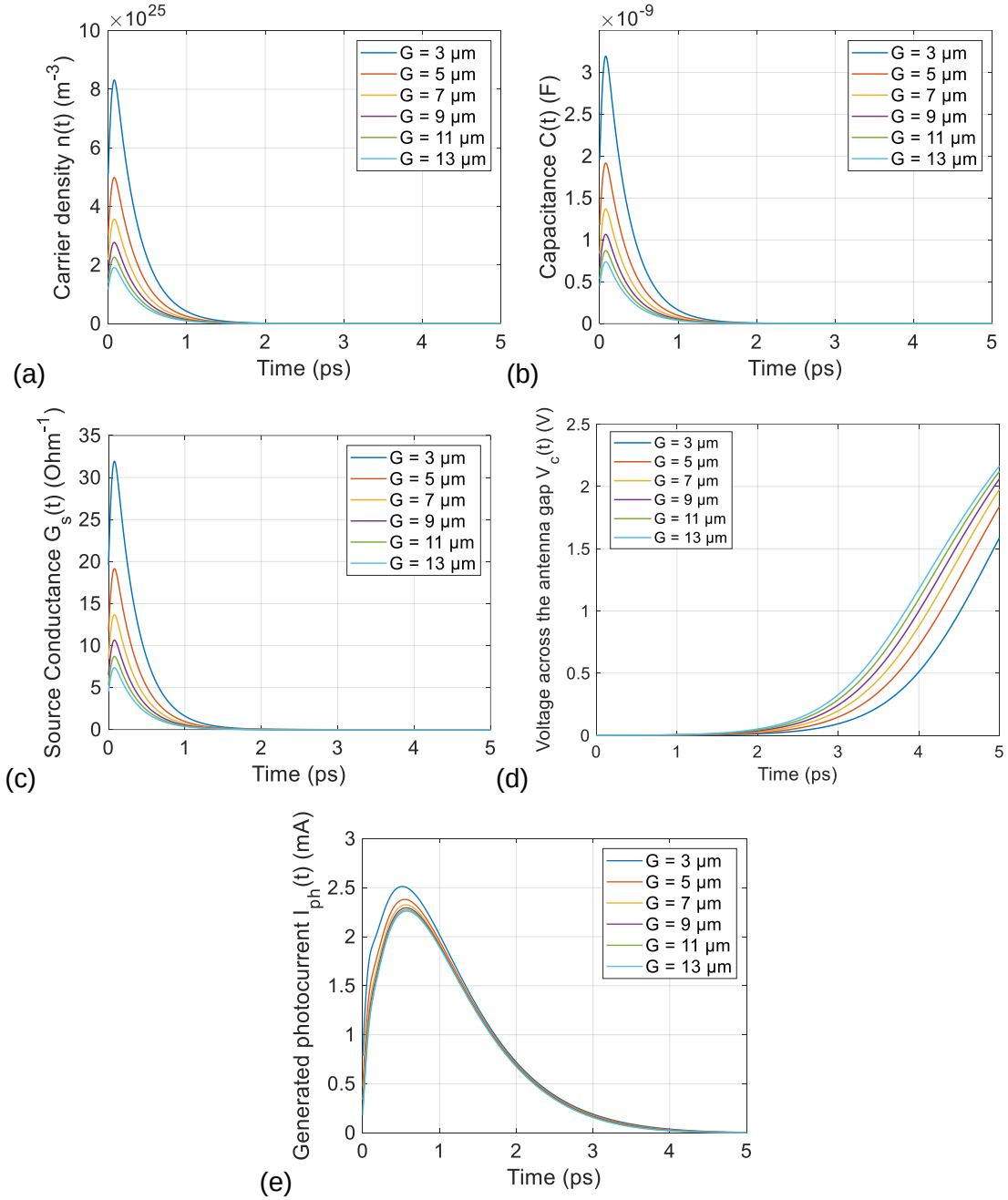

Figure A-3. The effect of change in photoconductive gap size G on time dependent (a) carrier density n(t), (b) capacitance C(t), (c) Source conductance $G_S(t)$, (d) the voltage across the antenna gap $V_C(t)$, and (e) the generated photocurrent I_{ph}.

The variation in source conductance with photoconductive gap size and width of antenna electrodes is shown in Figure A-3.c and it is observed that with the increase of photoconductive gap, the value of source conductance $G_s(t)$ decreases. This is because for a constant optical excitation power, an increase in the gap size G results an increase in the distance between

the generated photo-carriers and therefore there is a decrease in the carrier density n(t) in the antenna gap. The decrease in n(t) results in significant decrease in source conductance due to decrease in time-dependent bulk conductivity.

The time dependent generated photocurrent $I_{ph}(t)$ depicted in Figure A-3.e also varies with change in photoconductive gap size, the photocurrent seems to increase with smaller gap sizes. That is because with decreasing gap size G, the carrier density n(t) increases, and the source resistance decreases which results in an increase of the photocurrent. This could also be confirmed with the $V_C(t)$ shown in Figure A-3.d, where the simulated voltage across the capacitance decreases with smaller gap sizes indicating a weaker screening effect across the photoconductive gap which finally means an increase in the photocurrent.

From the simulated parameters, the THz radiated power could be calculated. The variation of the time-dependent THz radiated power for the different value of G is shown in Figure A-4.a and its Fourier transform is calculated to show the spectral radiated THz power in Figure A-4.b as a function of frequency up to 10 THz in dB.

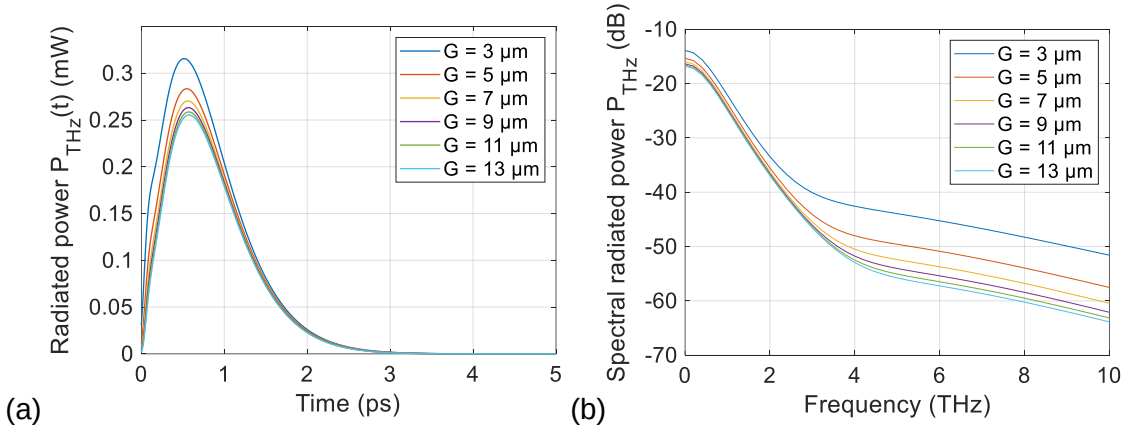

Figure A-4. The effect of change in photoconductive gap size G on (a) time dependent radiated THz power Calculated from the generated photocurrent and (b) the spectral radiated THz power as a function of frequency.

As it could be expected from the previously shown photocurrent results, the radiated power $P_{THz}(t)$ is increasing with smaller gap sizes due to increasing carrier density n(t) and weaker screening effect due to decreasing voltage across the capacitance. The spectral radiated power predicts a BW up to 4 THz with decreases with smaller gap sizes.

The same analysis procedure was executed with a variable W between 4 µm and 16 µm with a 3 µm step. The results for the effect of change in dipole width W on time dependent carrier density n(t), capacitance C(t), Source conductance $G_S(t)$, the voltage across the antenna gap $V_C(t)$ and the generated photocurrent $I_{ph}(t)$ are shown in Figure A-5.

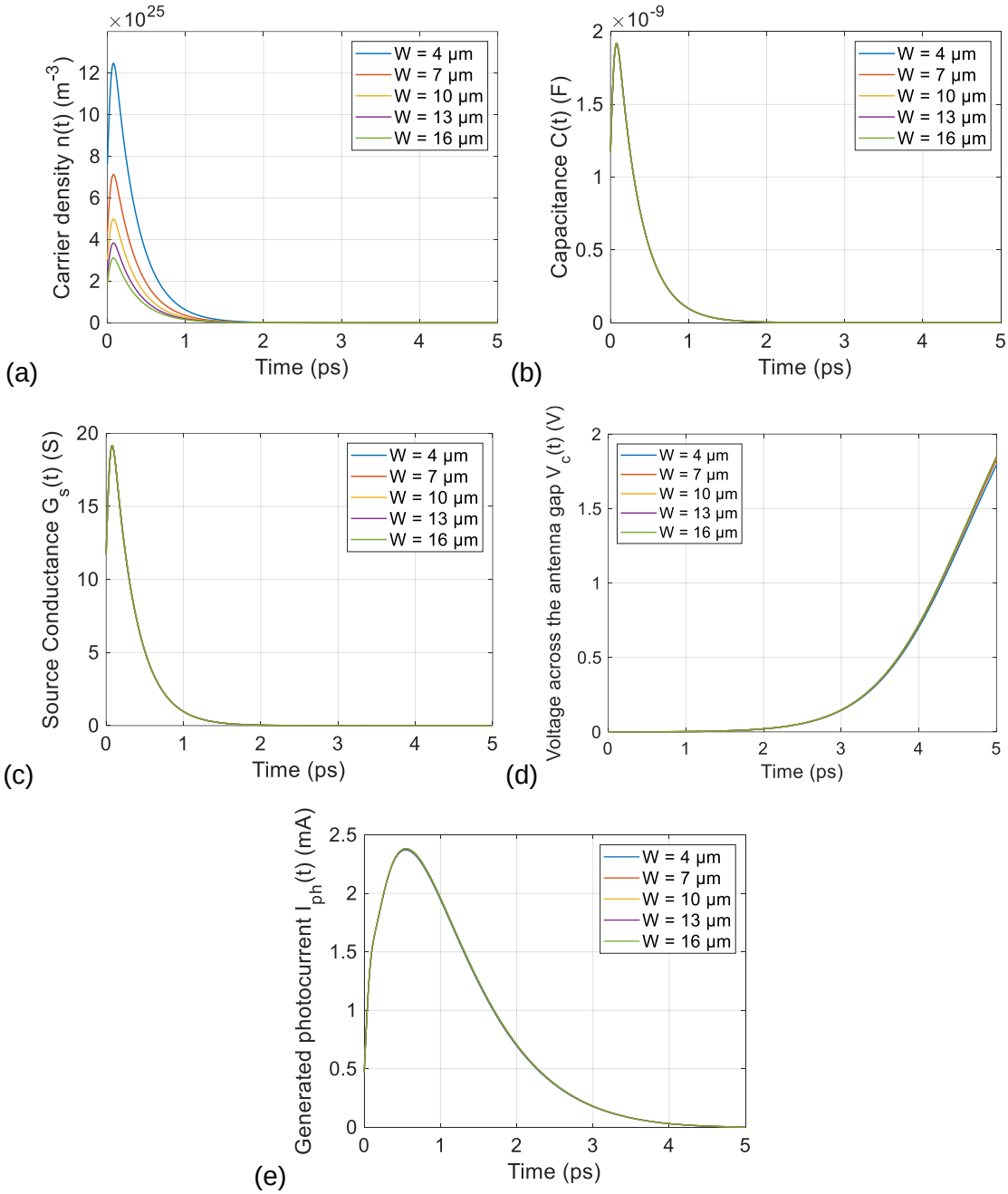

Figure A-5. The effect of change in the width of antenna electrodes W on time dependent (a) carrier density n (b) capacitance C (c) Source conductance G_S (d) the voltage across the antenna gap V_C and (e) the generated photocurrent I_{ph}.

Figure A-5.a show a decreasing carrier density with decreasing W for the same reason stated for the G variation. The larger the W, the larger the optically excited surface thus decreasing the density of carrier generated in the area. However, the rest of the parameters do not seem to vary much with the W values. That is due to the fact the larger electrodes do not affect the number of carriers stuck next to the electrodes for a fixed G. In other word, even if the electrodes are larger, the same number of carriers always participate in the capacitance creation next to the electrode. This could be confirmed with the Eq. 56 where the W and n(t) compensate each other's variation. The same thing could be said on the lack of observable variation of the source conductance, voltage across the capacitance and the generated photocurrent with the variation of W. In fact, the variation of the electrode width does not seem

to affect the performances of the antenna under test as confirmed with the radiated power shown in Figure A-6.

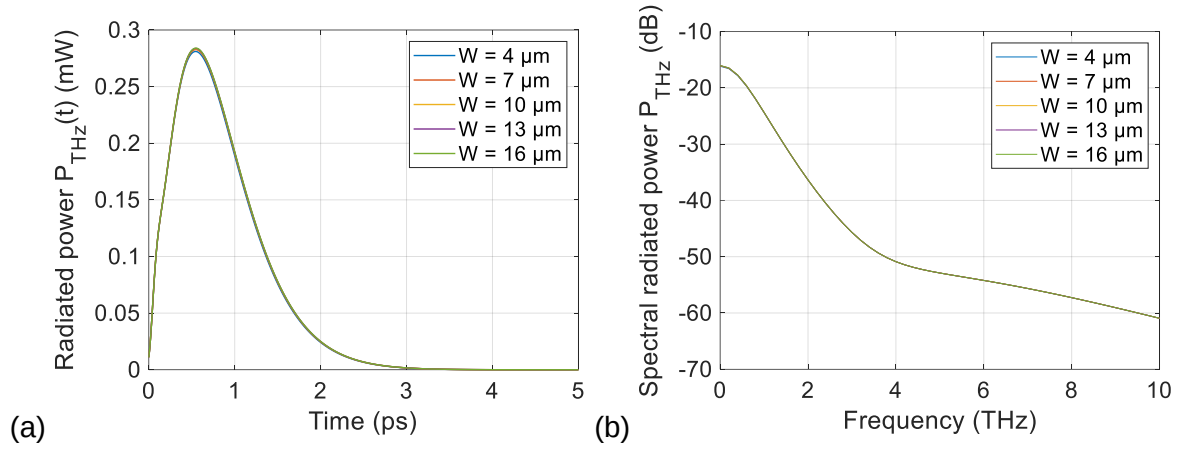

Figure A-6. The effect of change in the width of antenna electrodes W on (a) time dependent radiated THz power Calculated from the generated photocurrent and (b) the spectral radiated THz power as a function of frequency.

Further, the variation of the excitation optical power is also investigated in parallel to the variation of G, W and E_{bias} in order to have a broader view on the effect of these different parameters. The results are shown in Figure A-7.

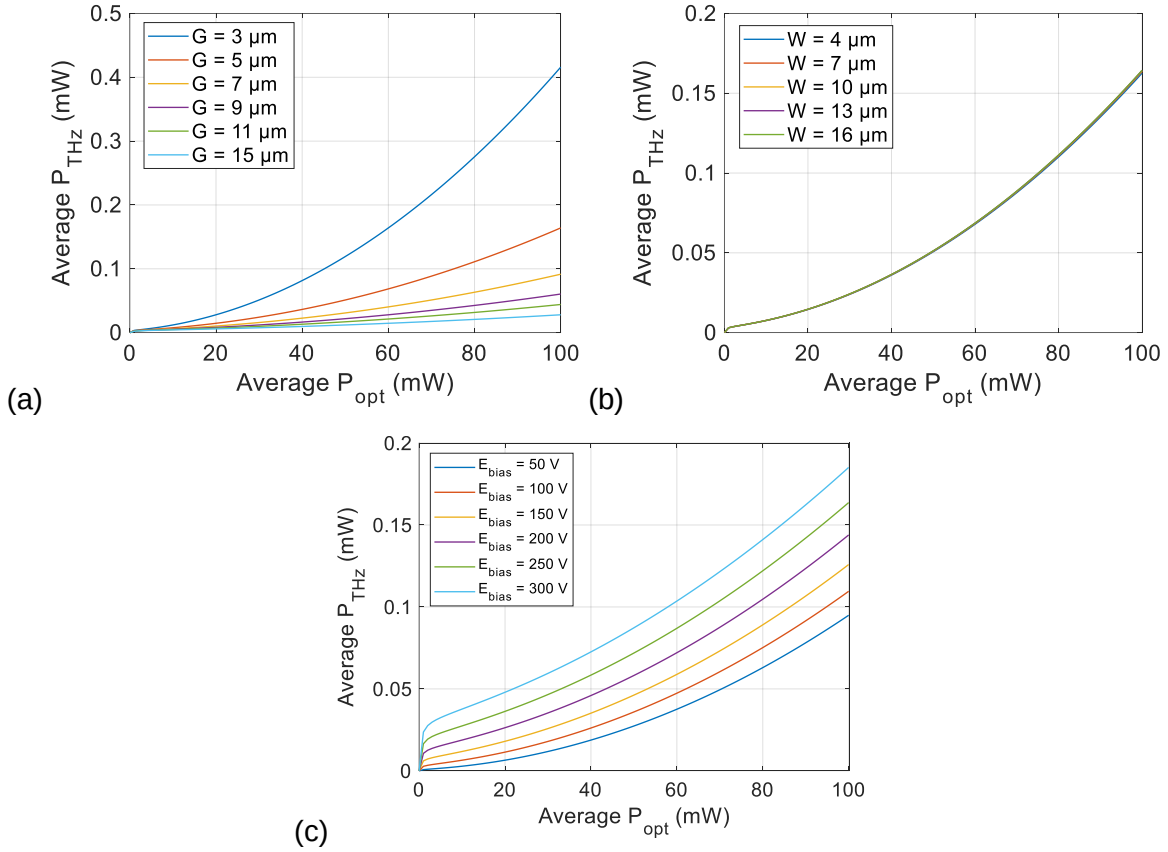

Figure A-7. The average radiated power over the average optical power for different values of (a) photoconductive gap size G, (b) widths of antenna electrodes W and (c) bias voltages E_{bias}.

In Figure A-7.a, the average radiated power increases with the injected average optical power, but not in same rate for each value of G as the average generated THz power seem to increase

slower with average optical power for larger gap sizes G. That is the saturation effect taking place as with the increase of the gap size comes the increase of the screening effect and the decrease of the carrier density. That is why the increase of average optical power will only provide result in the case of smaller values of the photoconductive gap.

Figure A-7.b. shows that the variation of the electrode width W does not result in any variation of the average generated power with increasing average optical power. And finally, Figure A-7.c. depicts the variation of average generated THz power with the variation of the average optical power for different applied bias voltage values. The results show a linear increase in the average generated THz power with increasing bias voltage because the screening voltage itself depends directly on the bias voltage, thus with increasing bias voltage, the photoexcited carriers are accelerated but the screening field is increased linearly for all injected optical powers. By increasing the bias voltage, the higher THz output power can be obtained, however, the breakdown voltage of device limits to yield maximum radiation power. The multilayered Fe:GaAs/InAlAs substrate was developed to overcome the limit of breakdown voltage of a GaAs substrate.

In conclusion, this analytical study delved into the characterization of THz generation processes using a standard PCA, despite the unavailability of precise specifications regarding the commercial PCA antennas used in the preceding chapters. Although these findings haven't been directly applied to acquisition processes or image reconstruction, they present avenues for enhancing PCAs, particularly for SA imaging. They shed light on crucial parameters for PCA optimization, notably in terms of generated power, a critical factor given the absence of physical lenses in the SA-TDS setup. This analysis lays the groundwork for potential advancements in PCA design and conception, serving as a valuable resource in tandem with wave propagation simulations. Together, these tools can offer robust guidelines for tailoring PCAs to specific applications across diverse contexts.

Synthetic Aperture Imaging and Spectroscopy in the Terahertz Range Using Time Domain Spectroscopy System

Les techniques d'imagerie et de spectroscopie térahertz offrent de vastes applications dans le control non destructif ou le contrôle de qualité dans la manufacture industrielle, la pharmaceutique et la biologie, l'archéologie ou encore le monde de l'art. Pour ces applications, la technique de spectroscopie térahertz dans le domaine temporel (THz-TDS) permet une analyse sur une bande passante instantanée très large (0.1-6 THz), mais nécessite généralement de déplacer mécaniquement l'échantillon à imager dans le plan focal du faisceau THz. Le travail de cette thèse porte sur l'adaptation d'un banc THz-TDS pour l'imagerie et la spectroscopie des échantillons fixes, en se basant sur le principe d'un radar à synthèse d'ouverture (SAR), en transmission. En utilisant cette technique, on démontre une reconstruction d'image en 3D avec une résolution inférieure au millimètre de plusieurs échantillons différents. Pour remédier au temps d'acquisition prolongés, un échantillonnage spatial lacunaire est proposé, réduisant les éléments du réseau synthétique et améliorant la vitesse d'acquisition. De plus, les données reconstruites ne sont pas uniquement utilisées pour l'imagerie mais permettent également la caractérisation des paramètres optiques matériaux (l'indice de réfraction et le coefficient d'absorption) constituant l'objet imagé dans la bande de fréquence de reconstruction. Ainsi, la technique proposée permet la cartographie spectrale 2D de l'indice de réfraction à diverses fréquences térahertz. Enfin, la méthodologie proposée est appliquée à l'imagerie de sortie de guide d'ondes térahertz, illustrant sa grande flexibilité et ses vastes domaine potentielles d'utilisation.

Mots-clés : Imagerie térahertz, spectroscopie térahertz, caractérisation des matériaux, système de spectroscopie dans le domaine temporelle, synthèse d'ouverture, rétroprojection, reconstruction d'image 3D, guide d'onde térahertz, fibre térahertz.

Synthetic Aperture Imaging and Spectroscopy in the Terahertz Range Using Time Domain Spectroscopy System

Terahertz (THz) imaging and spectroscopy techniques offer a wide range of non-destructive testing applications in many industries, such as industrial manufacturing, pharmaceuticals, biology, archaeology, and the art world. For these applications, THz time-domain spectroscopy system (THz-TDS) allows analysis over a very wide instantaneous bandwidth (0.1- 6 THz), but generally requires mechanical displacement of the sample to be imaged in the focal plane of the THz beam. This thesis focuses on the adaptation of a THz -TDS system for imaging and spectroscopy of fixed samples, based on the principle of Synthetic Aperture Radar (SAR), in transmission configuration. Using this technique, we demonstrate sub-millimeter resolution 3D image reconstruction of three different samples. To overcome long acquisition times, sparse spatial sampling is proposed, reducing synthetic array elements, and improving the acquisition speed. Moreover, the reconstructed data are not only used for imaging purposes; they can also be employed to characterize the optical parameters of the materials - the refractive index and absorption coefficient of the object's constituents in the reconstruction frequency band. Consequently, the proposed technique enables 2D spectral mapping of refractive index at various terahertz frequencies. Finally, the proposed methodology is applied to the imaging of the output of THz waveguides, illustrating its wide flexibility and additional application domains.

Keywords: Terahertz imaging, terahertz spectroscopy, material characterization, terahertz time-domain spectroscopy system, synthetic aperture, back-projection, 3D image reconstruction, terahertz waveguide, terahertz fiber.